frontiers | Research Topics

Methods in cell therapy and regenerative medicine

Edited by
Anna Lange-Consiglio, Charlotte Riviere, V. Prasad Shastri
and Amiq Gazdhar

Published in
Frontiers in Bioengineering and Biotechnology

ISSN 1664-8714
ISBN 978-2-83251-887-8
DOI 10.3389/978-2-83251-887-8

About Frontiers

Frontiers is more than just an open access publisher of scholarly articles: it is a pioneering approach to the world of academia, radically improving the way scholarly research is managed. The grand vision of Frontiers is a world where all people have an equal opportunity to seek, share and generate knowledge. Frontiers provides immediate and permanent online open access to all its publications, but this alone is not enough to realize our grand goals.

Frontiers journal series

The Frontiers journal series is a multi-tier and interdisciplinary set of open-access, online journals, promising a paradigm shift from the current review, selection and dissemination processes in academic publishing. All Frontiers journals are driven by researchers for researchers; therefore, they constitute a service to the scholarly community. At the same time, the *Frontiers journal series* operates on a revolutionary invention, the tiered publishing system, initially addressing specific communities of scholars, and gradually climbing up to broader public understanding, thus serving the interests of the lay society, too.

Dedication to quality

Each Frontiers article is a landmark of the highest quality, thanks to genuinely collaborative interactions between authors and review editors, who include some of the world's best academicians. Research must be certified by peers before entering a stream of knowledge that may eventually reach the public - and shape society; therefore, Frontiers only applies the most rigorous and unbiased reviews. Frontiers revolutionizes research publishing by freely delivering the most outstanding research, evaluated with no bias from both the academic and social point of view. By applying the most advanced information technologies, Frontiers is catapulting scholarly publishing into a new generation.

What are Frontiers Research Topics?

Frontiers Research Topics are very popular trademarks of the *Frontiers journals series*: they are collections of at least ten articles, all centered on a particular subject. With their unique mix of varied contributions from Original Research to Review Articles, Frontiers Research Topics unify the most influential researchers, the latest key findings and historical advances in a hot research area.

Find out more on how to host your own Frontiers Research Topic or contribute to one as an author by contacting the Frontiers editorial office: frontiersin.org/about/contact

Methods in cell therapy and regenerative medicine

Topic editors
Anna Lange-Consiglio — University of Milan, Italy
Charlotte Riviere — Université Claude Bernard Lyon 1, France
V. Prasad Shastri — University of Freiburg, Germany
Amiq Gazdhar — University Hospital of Bern, Switzerland

Citation
Lange-Consiglio, A., Riviere, C., Shastri, V. P., Gazdhar, A., eds. (2023). *Methods in cell therapy and regenerative medicine*. Lausanne: Frontiers Media SA.
doi: 10.3389/978-2-83251-887-8

Table of contents

frontiers
in Bioengineering and Biotechnology

REVIEW
published: 10 February 2022
doi: 10.3389/fbioe.2022.831477

Recent Advances in Liver Engineering With Decellularized Scaffold

Qingqing Dai [1,2†], ***Wei Jiang*** [3†], ***Fan Huang*** [1], ***Fei Song*** [4], ***Jiqian Zhang*** [5]* ***and Hongchuan Zhao*** [1]*

[1]Department of Hepatopancreatobiliary Surgery and Organ Transplantation Center, Department of General Surgery, The First Affiliated Hospital of Anhui Medical University, Hefei, China, [2]Department of Internal Medicine IV (Gastroenterology, Hepatology, and Infectious Diseases), Jena University Hospital, Jena, Germany, [3]Department of Burns, The First Affiliated Hospital of Anhui Medical University, Hefei, China, [4]Department of Urology, Jena University Hospital, Jena, Germany, [5]Department of Anesthesiology, The First Affiliated Hospital of Anhui Medical University, Hefei, China

Liver transplantation is currently the only effective treatment for patients with end-stage liver disease; however, donor liver scarcity is a notable concern. As a result, extensive endeavors have been made to diversify the source of donor livers. For example, the use of a decellularized scaffold in liver engineering has gained considerable attention in recent years. The decellularized scaffold preserves the original orchestral structure and bioactive chemicals of the liver, and has the potential to create a *de novo* liver that is fit for transplantation after recellularization. The structure of the liver and hepatic extracellular matrix, decellularization, recellularization, and recent developments are discussed in this review. Additionally, the criteria for assessment and major obstacles in using a decellularized scaffold are covered in detail.

Keywords: liver engineering, scaffold, decellularization, recellularization, implantation

Edited by:
V. Prasad Shastri,
University of Freiburg, Germany

Reviewed by:
Chiara Magliaro,
University of Pisa, Italy
Elizabeth Stahl,
University of California, Berkeley, United States

****Correspondence:***
Jiqian Zhang
jiqianzh@mail.ustc.edu.cn
Hongchuan Zhao
zhc0117@sina.com

†These authors have contributed equally to this work

Specialty section:
This article was submitted to Tissue Engineering and Regenerative Medicine, a section of the journal Frontiers in Bioengineering and Biotechnology

Received: *08 December 2021*
Accepted: *24 January 2022*
Published: *10 February 2022*

Citation:
Dai Q, Jiang W, Huang F, Song F, Zhang J and Zhao H (2022) Recent Advances in Liver Engineering With Decellularized Scaffold. Front. Bioeng. Biotechnol. 10:831477. doi: 10.3389/fbioe.2022.831477

1 INTRODUCTION

Globally, end-stage liver disease is a primary cause of morbidity and mortality, accounting for more than one million deaths per year (Cheemerla and Balakrishnan, 2021). End-stage liver disease is a growing public health hazard for which liver transplantation is the only available remedy.

Since Thomas Starzl conducted the first liver transplantation in 1963, liver transplantation has evolved significantly over the last 50 years. Along with the renewal of immunosuppressive drugs, liver transplantation technology has increasingly advanced, resulting in the survival of numerous patients with end-stage liver disease (Song et al., 2014). Unfortunately, donor scarcity continues to be a significant issue. Aside from increasing citizen donation rates and marginal liver utilization, efforts are required to develop alternative viable treatments (Muller et al., 2020; Yagi et al., 2020).

In recent years, the use of decellularized scaffolds in liver engineering has garnered considerable attention (**Figure 1**). Decellularized scaffolds from xenogeneic animals (such as pigs, sheep, and cattle) and discarded human livers preserve the multifaceted extracellular matrix (ECM) of the liver and serve as a reservoir for growth factors, cytokines, and signaling molecules that are critical and indispensable for cellular growth, proliferation, differentiation, and neovascularization (Choudhury et al., 2020). Decellularized scaffolds are subsequently repopulated with primary hepatocytes, endothelial cells, and stem cells, which ultimately develop new livers that can be transplanted into patients with end-stage liver disease to replace the original decompensated livers. Increasing evidence suggests that decellularized scaffolds can sustain implanted cells for extended periods, enabling subsequent implantation (Kakabadze et al., 2018; Yang et al., 2018; Liu et al., 2019; Everwien et al., 2020b; Shaheen et al., 2020).

Therefore, the recellularization of decellularized scaffolds holds great therapeutic potential for creating transplantable grafts for treating end-stage liver disease. This review provides an overview of

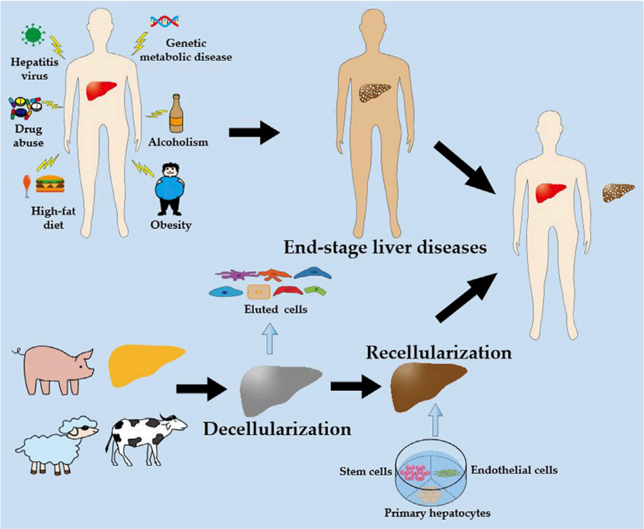

FIGURE 1 | A schematic illustration of the liver engineering based on decellularized scaffold. Livers obtained from xenogeneic animals (such as pigs, sheep and cattle) and discarded human livers are decellularized to produce decellularized scaffolds. The decellularized scaffolds are then recellularized with hepatocytes, endothelial cells, and stem cells, which are perfused *in vitro* to obtain a new liver. Ultimately, the new liver is transplanted into the patient with end-stage liver disease to replace the original decompensated liver.

the liver, hepatic ECM, decellularization, recellularization, and recent advances in liver engineering. Additionally, the review presents the detailed evaluation criteria and main obstacles for utilizing decellularized scaffolds.

2 LIVER AND HEPATIC ECM

2.1 Liver Structure

The liver is the largest internal organ in the body and is composed of various cell types, including hepatocytes, liver sinusoidal endothelial cells (LSECs), Kupffer cells, stellate cells, and cholangiocytes (Gordillo et al., 2015; Trefts et al., 2017; Stamataki and Swadling, 2020). These cells function in tandem to regulate liver function.

The liver receives a dual blood supply from the hepatic artery (HA) and portal vein (PV), and transports the bile that is synthesized by hepatocytes to the gallbladder and duodenum *via* the common bile duct (**Figure 2A**). The liver lobule (**Figure 2B**) is the anatomical structural unit of the liver and comprises hexagonal cords of hepatocytes, which are the principal parenchymal cells of the liver; these cells account for approximately 80% of the cellular composition of the liver. The central vein is located in the middle of each liver lobule, while the portal triad is located on the periphery and is composed of closely bundled branches of the HA, PV, and bile duct.

The hepatic sinusoid is a capillary-like channel lined with LSECs and flanked by hepatocyte plates and drains blood from the terminal branches of HA and PV into the central vein (**Figure 2C**) (McQuitty et al., 2020). Kupffer cells are resident macrophages that are localized in the hepatic sinusoid and adhere to LSECs. These cells are responsible for the uptake and destruction of foreign materials that are transported to the liver, such as bacteria, endotoxins, and microbial debris. The sinusoidal endothelium is primarily composed of LSECs, which are highly specialized endothelial cells and the most abundant non-parenchymal cells in the liver. These cells are located at the interface between the liver parenchyma and circulatory system (Poisson et al., 2017; Gracia-Sancho et al., 2021). Unlike other endothelial cells, LSECs have a unique phenotype because they lack the basement membrane and have a profusion of fenestrations (**Figure 2E**) (Li et al., 2020). Consequently, LSEC fenestrations and slow blood flow in the hepatic sinusoid enable hepatocytes to exchange sufficient substances with the blood in the space of Disse to perform essential functions, such as the uptake of toxins for processing and the secretion of synthesized serum proteins. Stellate cells are present in the space of Disse and allow the liver to respond to injury and heal certain types of damage. The surface of hepatocytes, which face the hepatic sinusoid, consists of a basolateral membrane with many microvilli, which dramatically increase the contact area between hepatocytes and plasma (**Figure 2E**). The smooth lateral membrane connects to adjacent hepatocytes and forms a narrow, tubular channel, which drains toxins, bile, and other digestive molecules secreted by hepatocytes to the bile duct. Cholangiocytes are epithelial cells of the bile duct that release bicarbonate and water, which contribute to bile secretion.

2.2 Hepatic ECM

The hepatic ECM is a well-organized non-cellular tridimensional scaffold composed of collagens, proteoglycan, fibronectin, laminin and several other glycoproteins, all secreted by resident cells in liver, and provides a microenvironment for adhesion, growth, replication, migration, differentiation, and other vital activities of the surrounding cells (**Figure 2D**). The hepatic ECM consists of the interstitial matrix, which fills in the intercellular space, and a basement membrane, which separates the endothelium from the underlying connective tissue. The basement membrane, which is composed of laminin, collagen type IV, and perlecan, is mainly distributed around the portal triad and central vein (**Figure 2C**) (Mak and Mei, 2017; Zhang et al., 2018). The liver parenchyma lacks a complete basement membrane, and the fibronectin and collagen I in the space of Disse separate the hepatocytes and hepatic sinusoids. The interstitial matrix comprises collagen types I, III, VI, and fibronectin, which provides a place for cells to attach and reside, and buffers against compression that is placed on the liver. Likewise, integrin is a transmembrane receptor that acts as a cement and modulator by binding to ligands, such as fibronectin, collagen, laminin, and cell surface proteins, and promotes cell-cell or cell-matrix adhesion and interaction (**Figure 2D**).

The composition of the hepatic ECM fluctuates with age. For example, older livers tend to have greater amounts of total collagen, sulfated glycosaminoglycans (GAGs), and lower levels of growth factors. Therefore, donor age should be considered as a critical component in determining the quality of the neo-liver during liver engineering (Acun et al., 2021).

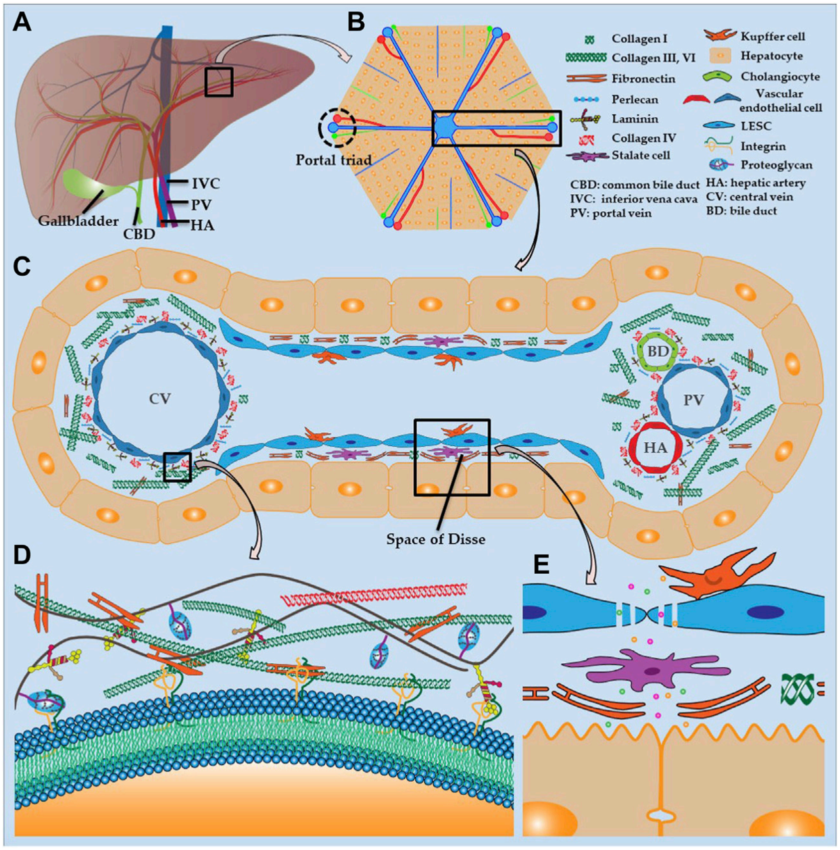

FIGURE 2 | Liver structure and hepatic ECM **(A)** Distribution of hepatic vasculature and bile ducts **(B)** Histology of liver lobule **(C)** Composition of hepatic sinusoids and ECM **(D)** ECM structure **(E)** Fenestration of LSECs and structure of space of Disse.

3 DECELLULARIZATION

Liver engineering is presently considered a promising alternative strategy for organ scarcity. Additionally, the use of synthetic and decellularized scaffolds in liver engineering has emerged as a research hotspot in liver engineering. The decellularized scaffold is more advantageous than the synthetic scaffold because it preserves the natural microscopic structures and microenvironment, retains bioactive molecules, and allows for implantation of the liver through directly anastomosing the native vessels of the scaffold and the vessels of the recipient (McCrary et al., 2020). Decellularization is the elimination of cellular components from native tissues or organs, while conserving the ECM and bioactive molecules. Physical methods, chemical reagents, and enzymatic treatments are commonly used for decellularization.

3.1 Physical Methods

3.1.1 Sonication

Sonication uses an ultrasonic bath or probe to transfer acoustic power into a solvent containing tissues or organs to disrupt cell membranes; an ultrasonic bath is preferred for decellularization. The collapse of microscopic vacuum bubbles generated during sonication releases violent shockwaves that shear the cell; the resulting cellular debris is removed by perfusion. The energy generated from the collision of the sound waves generates heat in the solution. Therefore, monitoring the temperature during sonication and cooling in a chiller are necessary to avoid heating and denaturation of the proteins and molecules. Sonication is mainly used with detergents to decellularize dense tissues, such as tendons, ligaments, and cartilage, as well as thin tissues, such as skin and blood vessels, where sonication allows the detergents to penetrate the tissues more effectively (Yusof et al., 2019; Shen et al., 2020; Dang et al., 2021; Lin et al., 2021; Suss et al., 2021). Sonication has only been used to decellularize whole parenchymal organs in the kidney, and has likely not been used in the liver because of the colossal size of liver and the need for high power to disrupt the hepatic microstructure (Say et al., 2019; Manalastas et al., 2021).

3.1.2 Freeze-Thaw

Rapid thermal changes in the freeze-thaw effectively lyse cells and aid in their subsequent removal (Tao et al., 2021). Hence, a single freeze-thaw cycle is commonly used as the first step to reduce the quantities of chemical reagents for liver decellularization (Cheng et al., 2019). However, a single freeze-thaw cycle can still impact the microstructure and mechanical properties of the ECM due to the formation of ice crystals (Cheng et al., 2019). As a result, some researchers have advocated the use of cryoprotectants in perfusion-mediated decellularization to mitigate the detrimental effects of the freeze-thaw cycle without affecting cell lysis. For example, Pulver reported that pretreatment with 5% trehalose achieved the same result as an overnight freeze-thaw cycle, but with lower microstructural damage (Pulver. et al., 2014).

3.1.3 Immersion and Agitation

Immersing tissues or organs in a reagent is the most straightforward method of decellularization, and when paired with agitation, the outcomes of decellularization are improved. The reaction efficiency depends on the reagent type, duration of immersion, and intensity of agitation. A reagent for the removal of the cellular components is required, and the total duration should be minimized to avoid damaging the ECM scaffold (Mattei et al., 2014). However, this approach is usually only appropriate for epidermal tissues and smaller organs, such as the small intestine submucosa, blood vessels, trachea, cornea, nerve, and thyroid gland, and is not appropriate for larger parenchymal organs (Syed et al., 2014; Guimaraes et al., 2019; Visscher et al., 2021; Changchen et al., 2021; Weng et al., 2021). The required DNA content of 50 ng/mg in the decellularized tissue is only achieved when the thickness of the liver slices or discs is less than 5 mm (Mattei et al., 2014; Mazza et al., 2019).

3.2 Chemical Methods

3.2.1 Detergents

Ionic, non-ionic, and zwitterionic detergents are commonly used for decellularization. The most extensively used ionic detergents are sodium dodecyl sulfate (SDS) and sodium deoxycholate (SDC), which solubilize cellular membranes and denature proteins (Zhang et al., 2018; Willemse et al., 2020; Felgendreff et al., 2021). Triton X-100 is the most widely used non-ionic detergent and is capable of breaking lipid-lipid, lipid-protein, and DNA-protein interactions. Triton X-100 is considered a gentler detergent than SDS. Furthermore, Jeong reported that SDS and SDC significantly disrupted GAGs and elastin, albeit more efficiently than Triton X-100 (Jeong et al., 2021). Additionally, the protocol using Triton X-100 alone conserved 1.5-fold more collagen and 2.5-fold more GAGs in the liver than that using Triton X-100 + SDS (Willemse et al., 2020). Zwitterionic detergents (such as 3-[(3-cholamidopropyl) dimethylammonio]-1-propanesulfonate (CHAPS)) exhibit both non-ionic and ionic characteristics, and are less harmful to proteins because of the net-zero electrical charge on the hydrophilic groups (O'Neill et al., 2013). Because of its low permeability, CHAPS is frequently used in thin tissues and organs, and its use in the liver has been rarely reported (O'Neill et al., 2013; Tajima et al., 2018; Shimoda et al., 2019).

Although diverse detergents are frequently combined for optimal decellularization, the efficiency of detergents nonetheless varies linearly with the exposure time and concentration, and varies inversely with the tissue thickness and density. Prolonged exposure times and high detergent concentrations can maximize the extent to which the ECM of the scaffold approaches the cell-free state. However, the ECM can also be disrupted and residual detergents may be present, particularly if SDS is used, which can penetrate deeply into the tissue and slowly dissipate. The disruption of the ECM and residual detergents may result in the formation of thrombi and cytotoxicity after recellularization and implantation, particularly in the liver because of its abundant blood flow and metabolic importance.

3.2.2 Hypertonic and Hypotonic Solutions

Hypertonic and hypotonic solutions promote cell shrinkage and swelling due to osmosis and ultimately induce lysis, while having a negligible effect on the ECM (Kim et al., 2016). Although osmosis can kill cells, it is inefficient and must be coupled with detergents or enzymes to obliterate the cellular components in the liver (Kobes et al., 2018; Lewis et al., 2018). Joseph reported that the sequential treatment of mouse liver with a hypotonic solution and Triton X-100 resulted in a scaffold that was devoid of cells and maintained its structural integrity, as confirmed by the scanning electron microscopy (SEM) images (Kobes et al., 2018).

3.2.3 Acids and Bases

Although acids remove DNA by dissolving cytoplasm and breaking nucleic acids during decellularization, they are more currently and popularly used as disinfectants because they are strong oxidants (Vishwakarma et al., 2019; Gao et al., 2020; Hussein et al., 2020). In a highly alkaline solution, double-stranded DNA denatures low-viscosity single-stranded DNA, which is easily removed by perfusion (Sengyoku et al., 2018). Relevant studies have demonstrated that a highly alkaline NaOH-PBS solution could achieve the same effect as SDS and CHAPS during decellularization while also enhancing biocompatibility and vascular regeneration of scaffolds (van Steenberghe et al., 2017; Sengyoku et al., 2018; van Steenberghe et al., 2018). Additionally, highly alkaline solutions with a pH of 12 or more can inactivate conventional bacteria and viruses, as well as unconventional prions, which are pathogens that are often associated with the use of biomaterials (van Steenberghe et al., 2017; Sengyoku et al., 2018). However, acids and bases can damage collagen and undermine protein-protein bonds, leading to microstructural destruction and decreased viscoelasticity (Reing et al., 2010). In addition, sodium hydroxide cleaves nearly all the growth factors, such as fibroblast growth factor and vascular endothelial growth factor (Reing et al., 2010).

3.2.4 Alcohols

Because of the polar hydroxyl groups, alcohols can diffuse into cells and resultantly dehydrate and lyse cells (Flynn, 2010). Because alcohol is more efficient at removing lipids than lipase, alcohols (such as glycerol) are frequently used to extract lipids from adipose tissue (Flynn, 2010; Brown et al., 2011). Alcohols can precipitate proteins and destroy the ultrastructure of the ECM; therefore, care must be taken when they are used to remove cellular components. Compared to acids, alcohols are more routinely used to sterilize decellularized matrix materials. Ethanol (4%) and peracetic acid (0.1%) are frequently used to sterilize decellularized scaffolds in liver engineering

(Xiang et al., 2016; Devalliere et al., 2018; Nishiguchi and Taguchi, 2021; Sassi et al., 2021).

3.2.5 Chelates

Chelates (such as ethylenediaminetetraacetic acid (EDTA) and ethylene glycol tetraacetic acid (EGTA)) bind metallic ions that are essential for protein interaction, resulting in the disconnection of intercellular integral proteins and disruption of cellular adhesion in the ECM. However, chelates alone are unable to completely remove cells and should be combined with detergents or enzymes (Zhao C et al., 2020; Faccioli et al., 2020; Lorvellec et al., 2020). Additionally, using EDTA in the decellularization technique reduces the residual DNA and produces more intact ECM (Maghsoudlou et al., 2016).

3.3 Enzymatic Treatments

Nucleases, trypsin, dispase, lipase, and collagenase are commonly used in decellularization, whereas nucleases and trypsin are most frequently used in liver decellularization. Enzymes can precisely remove cellular components, prevent unfavorable immune responses, and improve the efficacy of detergent-based decellularization.

Nucleases are enzymes that cleave the phosphodiester bonds between nucleotides in nucleic acids. They typically expedite the removal of nucleotides and minimize the risk of immune responses during decellularization. Endonucleases, such as DNase and RNase, are frequently used to remove nucleic acids during liver decellularization (Ahmed et al., 2020; Everwien et al., 2020b; Wu et al., 2020). Trypsin is a serine protease that hydrolyzes the proteins involved in cellular attachment; consequently, trypsin dissociates cells from adhering tissue. The regular replacement of trypsin is necessary because protease inhibitors that are released from broken cells restrict trypsin activity after prolonged circulation (Prasertsung et al., 2008). Additionally, the enzymes can penetrate deeper into the tissue under pressurized conditions to increase the reaction between the enzyme and the substrate, which aids in cellular removal and shortens the reaction time (Prasertsung et al., 2008).

3.4 Combination

Each of the aforementioned methods (**Sections 3.1–3.3**) has advantages and disadvantages. Although physical methods are less disruptive to the microstructure of the tissue, they do not remove cellular components. Comparatively, although chemical agents can significantly remove cellular components, they inevitably destroy the microstructure and ECM. The preferred method of decellularization varies tremendously among different tissues and organs, and the ideal protocol should include at least two of the aforementioned methods to maximize their respective advantages and minimize the disruption of the ECM. Currently, the most frequently used protocol for liver decellularization is a freeze-thaw cycle followed by a combination of detergents, enzymes, and chelating agents (details presented in **Table 1**).

Perfusion *via* the HA and PV is the preferred method for whole liver decellularization. To lyse and remove cells in the liver, detergents, enzymes, and other reagents are perfused into the vasculature of the liver; this approach ensures that the maximal integrity of the ECM is maintained. For example, decellularized liver contained less residual DNA, with a more homogeneous ECM, under oscillatory pressure and pressure-controlled perfusion; this approach also required a relatively short time, and more collagen and GAGs were retained in the decellularized liver (Struecker et al., 2017; Shaheen et al., 2020). Benjamin first reported that applying oscillatory pressure to rat livers that were perfused with 1% Triton X-100 and 1% SDS further enhanced microperfusion and the homogeneity of decellularization by simulating intra-abdominal conditions during respiration (Struecker et al., 2017). Shaheen noted that porcine livers decellularized by PV perfusion of 1x Triton X-100 and 0.6% SDS maintained a perfusion pressure of 8–12 mm Hg and preserved the parenchymal liver lobule structures when compared with the native liver (Shaheen et al., 2020).

3.5 Evaluation of Decellularized Liver ECM

The ultimate goal of decellularization is to remove all the cellular components while retaining an intact ECM for recellularization. However, no method has been able to satisfy this standard. Following recellularization, the remaining cellular components in the ECM create an unfavorable host immune response, and the deterioration of the ECM will also compromise the bioactivity of the implanted cells. Thus, establishing a quality standard for decellularization and scaffolds can facilitate the rapid and organized development of liver engineering and better satisfy the requirements for clinical applications.

3.5.1 Evaluation of Decellularization Efficiency

Presently, the degree of decellularization is primarily determined by the residual DNA, which is ubiquitous in tissues and cells and is directly associated with the host immune response. The generally acknowledged criteria are as follows: 1) DNA content <50 ng/mg dry ECM weight; 2) DNA fragment length <200 base pairs; and 3) lack of visible nuclear content with DAPI and HE staining. Narciso et al. lately described a novel method that combines phase-contrast images of decellularized tissues and fluorescent images of DNA staining of cell nuclei, allowing faster and easier quantification of DNA content (Narciso et al., 2021). However, investigations have shown that the cytoplasm and components of the cell membrane can also cause immune responses and inflammation (Chakraborty et al., 2020). Therefore, these aforementioned criteria should be upgraded and modernized to ensure accuracy and uniformity.

Although the abovementioned criteria have been widely adopted, they all lead to destructive end-points in analyses of the scaffold, and the degree of decellularization cannot be determined in real-time. Consequently, it is difficult to tailor decellularization to the distinctive attributes of each liver. Therefore, it is essential to develop a new non-invasive method to monitor and adjust decellularization in real-time to achieve individualization (Hulsmann et al., 2015; Geerts et al., 2016).

Akhyari et al. employed rheological evaluation and biomass compositional analysis of the perfusate for the real-time and non-invasive monitoring of heart decellularization. They discovered that the total protein, DNA, and biomass content in the perfusate

TABLE 1 | Common methods and combinations used in liver decellularization.

Common methods	Advantages	Disadvantages
Freeze-thaw	Effectively disrupts cell membrane and lyses cell Less disruptive to ECM	Does not remove cellular components Ice crystal formation disrupts microstructure of ECM and reduces mechanical strength
Detergents	Effectively lyse cells inside the organs Effectively remove cellular and nuclear components	Disrupt proteins and microstructure of ECM Reduce the contents of growth factors Residual detergents cause thrombus and cytotoxicity
Chelates	Effectively disrupt cell adhesion to ECM Reduce the residual DNA Produce more intact ECM	Do not actually lyse cells Denature proteins of ECM Ineffective when used alone
Enzymes	Precisely remove cellular components Reduce immune responses	Regular replacement Disrupt proteins and distort ECM structure

Common combinations	Overview	References
Freeze-thaw + detergents + chelates + enzymes	Free-thaw + Triton X-100 + EGTA + trypsin	Miyauchi et al. (2017) Minami et al. (2019) Takeishi et al. (2020)
	Free-thaw + Triton X-100/SDC + EDTA + trypsin	Coronado et al. (2017)
	Free-thaw + Triton X-100 + EDTA + trypsin	Faccioli et al. (2020)
Freeze-thaw + detergents + chelates	Free-thaw + Triton X-100/SDS + EGTA	Gao et al. (2020)
	Free-thaw + Triton X-100/SDS/CHAPS + EGTA	Shimoda et al. (2019)
	Free-thaw + Triton X-100/SDS/SDC + EDTA	Thanapirom et al. (2021)
Freeze-thaw + detergents + enzymes	Free-thaw + Triton X-100/SDS + DNase/RNase	Lu et al. (2018) Wu et al. (2020)
	Free-thaw + Triton X-100/SDS + DNase	Everwien et al. (2020b) Willemse et al. (2020)
	Free-thaw + SDS + DNase	Buhler et al. (2015)
Detergents + chelates + enzymes	SDC + EDTA + DNase	Lorvellec et al. (2020)
	Triton X-100 + EGTA + trypsin	Watanabe et al. (2019) Zhao C et al. (2020)
	Triton X-100 + EDTA + DNase	Caires-Junior et al. (2021)

was proportional to its viscosity. Based on this finding, the decellularization protocol could be adapted for a single organ. Furthermore, this finding demonstrated that the adverse effects of reagents on the ECM could be minimized if the pump profile, perfusion pressure, and revolution speed in the feedback control system were controlled (Hulsmann et al., 2015). Geerts et al. found that the HU value in CT scans was positively correlated with the quantity of DNA remaining in the scaffold during liver decellularization. These results suggest that the residual DNA could be used to predict the extent of decellularization. This established methodology when combined with characterization of the perfusate could be optimized to create a well-preserved scaffold (Geerts et al., 2016).

3.5.2 Quality Assessment of Decellularized Liver Scaffold

As the mold for liver engineering, the quality of the decellularized scaffold is crucial for successful liver recellularization and transplantation. However, there is currently no unified criteria for assessing the quality of the scaffold. The majority of qualitative and semi-quantitative studies have used morphological and molecular characteristics to assess the decellularized scaffold. The morphological assessment uses the appearance, HE staining, and SEM of the scaffold to evaluate its remaining microscopic anatomy and three-dimensional structure. The molecular assessment includes quantitative assessment of the residual DNA, cytokines, and ECM proteins. In addition, many studies have compared the mechanical strength, tension resistance, and other physical properties of the decellularized liver with those of the native liver (Everwien et al., 2020a).

Philipp et al. recently used macroscopic, microscopic, and morphological assessments to develop a morphological workflow for analyzing the microstructure of decellularized mouse liver scaffolds with mild histological damage (hepatic steatosis, hepatic fibrosis, and nodular regenerative hyperplasia) (details presented in **Table 2**). The results indicated that this procedure aided in evaluating the quality of decellularized scaffolds and in identifying the tissues with the best-preserved microstructure and matrix components; these results are also fundamental for future repopulation and transplantation trials (Felgendreff et al., 2021).

However, morphological scoring methods vary depending on the expertise and subjectivity of the observer. Therefore, it is necessary to create digital image analysis to decrease this variance and achieved increased accuracy. Magliaro et al. developed a faster and more intuitive open-source image analysis software, HisTOOLogy, and applied it to analyze the effects of different decellularization protocols, showing a positive linear relationship between cell count and eosin staining area with total DNA and total protein quantification (Magliaro et al., 2015). The results demonstrated HisTOOLogy's ability to analyze and provide quantitative information on histological sections, which aids in the efficiency and accuracy of evaluating decellularized scaffolds (Mattei et al., 2017). Besides, Moulisová et al. combined

TABLE 2 | The sequential morphological workflow to identify liver scaffold-sections with well-preserved microarchitecture.

–	Grading	Structure	Score
Macroscopic assessment	Good	Complete removal of hepatic tissue of the whole liver lobe	4
	Moderate	Incomplete removal of hepatic tissue in less than half of the parenchyma of a single liver lobe, predominantly at the edges of the liver lobes	3
	Limited	Incomplete removal of hepatic tissue in more than half of a single liver lobe	2
	Poor	No removal of hepatic tissue within one or more liver lobes	1
Microscopic assessment	The microscopic assessment was applied to all samples without macroscopically visible tissue remnants. Only sections without evidence of residual cell nuclei or cytoplasmic glycogen were subjected to further analysis		

–	–	Parameter	Structure	Present	absent
Morphological assessment	Histological score	Portal vein integrity	Presence of portal vein in HE staining	1	0
			Presence of continuous elastic fibers of the portal vein in EvG staining	1	0
		Central vein integrity	Presence of central vein in HE staining	1	0
			Presence of continuous elastic fibers of the central vein in EvG staining	1	0
		Sinusoidal network integrity	Presence of sinusoidal network	1	0
			If present, continuity of network structure*	1	0
	Immunohistochemical score	Portal vein integrity	Presence of collagen I and collagen IV signals in the portal vein	1	0
			Presence of continuous elastic fibers and basal membrane of the portal vein in elastin as well as laminin staining	1	0
		Central vein integrity	Presence of collagen I and collagen IV staining in the central vein	1	0
			Presence of continuous elastic fibers and basal membrane of the central vein in elastin as well as laminin staining	1	0
		Sinusoidal network integrity	Presence of sinusoidal network in collagen I and collagen IV staining	1	0
			Continuity of the sinusoidal network in collagen I and collagen IV staining, if present*	1	0

** Continuous: 1, interrupted: 0*

TABLE 3 | Morphological multi-scale evaluation system.

	Method	Magnification	Parameter	Structure	Score
conventional semiquantitative assessment	HE staining	5×	Lobular shape	Compression to 1/3 of the original shape	0
				Compression to 2/3 of the original shape	1
				Preservation of lobular shape	2
	HE staining	5×	Sinusoidal network presence	Present in less than 50% of lobules	0
				Present in 50–90% of lobules	1
				Present in more than 90% of lobules	2
	HE staining	10×	Septa and triad structures	Destroyed septa and triad structures	0
				Ruptured septa and/or separation into layers	1
				No rupture, no separation of the septa into layers, vessels well defined in triads	2
	HE staining	15×	Sinusoidal network integrity	Large differences in distance between individual sinusoids	0
				Some network irregularities	1
				Regular distribution and consistent network structure	2
	SEM	2000×	Sinusoidal wall integrity	Complete loss of integrity	0
				Some loss of integrity (loosening of the protein fibers, holes)	1
				Integrity maintained (compact protein wall, protein fibers well organized)	2
New Quantitative assessment	Scaffan/HE staining	40× (Whole slide scan)	Structure length per area (mm/mm^2)	<20	0
				20–60	1
				>60	2
			Number of branches per mm^2	<10,000	0
				10,000–30,000	1
				>30,000	2

semiquantitative histological analysis with a newly developed software application (ScaffAn), which uses automated image analysis (details presented in **Table 3**) (Moulisova et al., 2020), to create a novel multi-scale morphological evaluation system for determining the quality of decellularized liver scaffolds. Comparatively, the conventional semi-quantitative histological analysis is based on seven criteria and a matching three-level grading system, which uses the morphological quality based on HE staining and SEM. In the quantitative analysis, the length of the sinusoidal structure and number of sinusoidal network branches are calculated based on high-resolution slide scans of the HE stains by using the newly developed software. Therefore, this approach complements the conventional analysis and effectively improves the discriminative power.

Along with morphological and molecular characteristics, mechanical properties also play a significant role in hepatic homeostasis. Likewise, the viscoelastic properties of the scaffold are critical to the morphology, viability, and metabolic activities of the implanted cells in liver engineering. For example, stiff or floppy scaffolds and substrates resulted in decreased vitality, spreading, and albumin (ALB) expression in repopulated HepG2 cells and hepatocytes (You et al., 2013; Mattei et al., 2018). Thus, establishing comprehensive and integrated decellularization assessment criteria will improve the quality and clinical translation of decellularized liver scaffolds.

4 RECELLULARIZATION

The decellularized scaffold must be repopulated with functional cells to execute various physiological functions. The most vital cells are hepatic parenchymal cells, hepatocytes; however, the long-term *in vitro* survival of hepatocytes remains challenging. In addition, loss of the typical morphology and liver-specific functions provide evidence that the prolonged culturing of hepatocytes results in de-differentiation. Nonetheless, different stem cells and endothelial cells that have been applied in recellularization show great potential.

4.1 Primary Hepatocyte

Healthy livers can regenerate rapidly to maintain their standard size and function after a hepatectomy of 70%. However, primary hepatocytes scarcely proliferate *in vitro*. Therefore, obtaining sufficient viable hepatocytes is the biggest impediment to using primary hepatocytes for recellularization. The primary hepatocytes in a decellularized liver scaffold, cultured in a dynamic perfusion system, have higher viability, function, and can most crucially, proliferate, when compared to those cultured under static conditions (Kojima et al., 2018; Yang et al., 2018; Debnath et al., 2020; Sassi et al., 2021). Nonetheless, the prolonged culturing of primary hepatocytes results in the onset of apoptosis and a persistent decline in the function of certain cells. For example, the synthetic and metabolic abilities of primary hepatocytes were severely diminished after 1 week of recellularization, although histologically viable hepatocytes could still be observed (Butter et al., 2017; Debnath et al., 2020). Fetal hepatocytes have strong proliferative capacity and are a promising cell source for recellularization because of the progenitor cells in the fetal liver (Gridelli et al., 2012; Ogiso et al., 2016). Proliferation markers of fetal hepatocytes are 45-fold higher than those of adult hepatocytes, and reach the level of immortalized HepG2 cells. However, their hepatic function is relatively limited, and their use has generated much ethical concern (Gridelli et al., 2012; Ogiso et al., 2016).

4.2 Stem Cells

4.2.1 Embryonic Stem Cell

Embryonic stem cells (ESCs) are pluripotent cells that are derived from the blastocyst stage of early mammalian embryos and can differentiate into various cell types and are capable of self-renewal (Damdimopoulou et al., 2016; Zhao H. et al., 2020). Under certain culture conditions, ESCs can differentiate into functional hepatocytes, cholangiocytes, and endothelial cells. Therefore, they are a promising source of cells for liver engineering (Touboul et al., 2010; Dianat et al., 2014; Lorvellec et al., 2017; Zhao H. et al., 2020). In contrast with static cultures, ESCs differentiate more efficiently in the liver scaffold, expressing less of the fetal hepatocyte marker, alpha fetoprotein (AFP), and more of the adult hepatocyte indicators, ALB, and lipid, as well as increased production of glycogen; however, ECSs have only half the level of ALB expressed in induced pluripotent stem cells (iPSCs) (Lorvellec et al., 2017). The primary concern for implanting ESCs into a scaffold is tumorigenicity, namely the development of teratoma and teratocarcinoma (Ben-David and Benvenisty, 2011; Damdimopoulou et al., 2016). The primary strategies for improving the safety of ESCs include ensuring ultimate differentiation, eliminating remnant pluripotent stem cells, interfering with the genes associated with tumor progression, and routine post-transplant monitoring (Ben-David and Benvenisty, 2011; Damdimopoulou et al., 2016).

Furthermore, ESCs research is ethically controversial because the extraction of ESCs necessitates the destruction of embryos (Damdimopoulou et al., 2016). It has instead been proposed that ESCs can be obtained from surplus embryos that are used for *in vitro* fertilization with the consent of the donor (Damdimopoulou et al., 2016). It is also feasible to isolate ESCs from cloned embryos using donor eggs and patient cells, and even individual blastocyst cells without harming the embryos (Rodin et al., 2014; Damdimopoulou et al., 2016).

4.2.2 Induced Pluripotent Stem Cells

IPSCs can be obtained from adult tissue cells, where each pluripotent stem cell line is unique and would not cause an immune rejection response (Ben-David and Benvenisty, 2011; Vasylovska et al., 2020). IPSCs and derived hepatocyte-like cells (iPSC-HLCs) are likely cell sources for liver engineering. For example, human iPSC-HLCs and rat decellularized liver scaffolds were used to develop an artificial liver that could express ALB and CYP3A4. The new liver exhibited characteristic hepatic functions, such as protein synthesis and drug metabolism (Minami et al., 2019; Lorvellec et al., 2020). Nonetheless, AFP was still expressed in the recellularized liver, and the level of ALB in the recellularized liver was approximately 1/5 that of human iPSC-HLCs *in vitro* and 1/100 that of the recellularized liver with adult rat primary hepatocytes (Minami et al., 2019; Lorvellec et al., 2020). These results indicate that the HiPSC-HLCs in the *de novo* liver were immature, and induction and isolation of the HiPSC-HLCs caused cellular damage and reduced the functioning of hepatocytes. Takeishi implanted human iPSC-derived hepatocytes, endothelial cells, and cholangiocytes into rat liver scaffolds to generate a mini liver, which achieved 75% coverage of the liver vasculature and 66% coverage of the bile ducts (Takeishi et al., 2020). The human iPSC-derived mini liver had cell-cell and cell-ECM molecules, and functioned in immunocompromised rats for 4 days after auxiliary liver transplantation (Takeishi et al., 2020). Therefore, it is feasible to create a patient-specific bioengineered liver without immunogenicity. Additionally, the tumorigenic properties of iPSCs are roughly comparable to those of ESCs, and even iPSCs are more tumorigenic than ESCs because of genetic and epigenetic reasons (Ben-David and Benvenisty, 2011).

4.2.3 Mesenchymal Stem Cells

Mesenchymal stem cells (MSCs) are multipotent stem cells with high proliferative capacity for self-renewal and can differentiate into the cell lines of the resident tissues (Li et al., 2017; Alfaifi et al., 2018; Kang et al., 2020). MSCs were initially identified and isolated from bone marrow. However, this approach requires invasive procedures, yields limited cell numbers, and the differentiation ability declines with aging. MSCs have also been isolated from the umbilical cord, adipose tissue, placenta, synovial membrane, and amniotic fluid (Alfaifi et al., 2018; Kang et al., 2020). The umbilical cord is the ideal source of MSCs because these cells are easily accessible and are more primitive, abundant, and proliferative than cells from other tissues (Alfaifi et al., 2018). Adipose tissue is also an alternative source of MSCs, where these cells have high proliferative capacity and are easily obtained by adiposuction (Kang et al., 2020). For example, after cultivation with human umbilical MSCs, a porcine liver scaffold expressed liver-specific proteins ALB, CK-18, and glycogen, and successfully differentiated from the hUC-MSC phenotype to the primary human hepatocyte phenotype (Li et al., 2017). More importantly, unlike ESCs and iPSCs, MCSs are devoid of ethical and tumorigenic issues, making them potential sources of cells for liver engineering (Xiang et al., 2016; Li et al., 2017).

4.3 Endothelial Cells

The daedal vasculature system of the liver is indispensable in metabolite transport and homeostasis. Therefore, endothelialization of the decellularized scaffold is crucial for successfully reconstructing a bioengineered liver. Currently, human umbilical vein endothelial cells (HUVECs) and LSECs are the most frequently used endothelial cells. To create an ideal whole liver scaffold, Verstegen et al. decellularized human discarded liver and demonstrated that implanting HUVECs into the scaffold effectively rebuilt the endothelial system (Verstegen et al., 2017). Similarly, recellularized livers with HUVECs, which were implanted in immunosuppressed pigs, supported perfusion for up to 15 days (Shaheen et al., 2020). Instillation of LSECs in rat decellularized livers forms an endothelial layer that reduces platelet deposition and improves the function of the co-implanted hepatocytes (Kojima et al., 2018).

The vasculature in the liver has a hierarchy, which involves the hepatic sinusoids to the larger vessels. However, most studies on revascularization have focused on larger vessels, instead of the

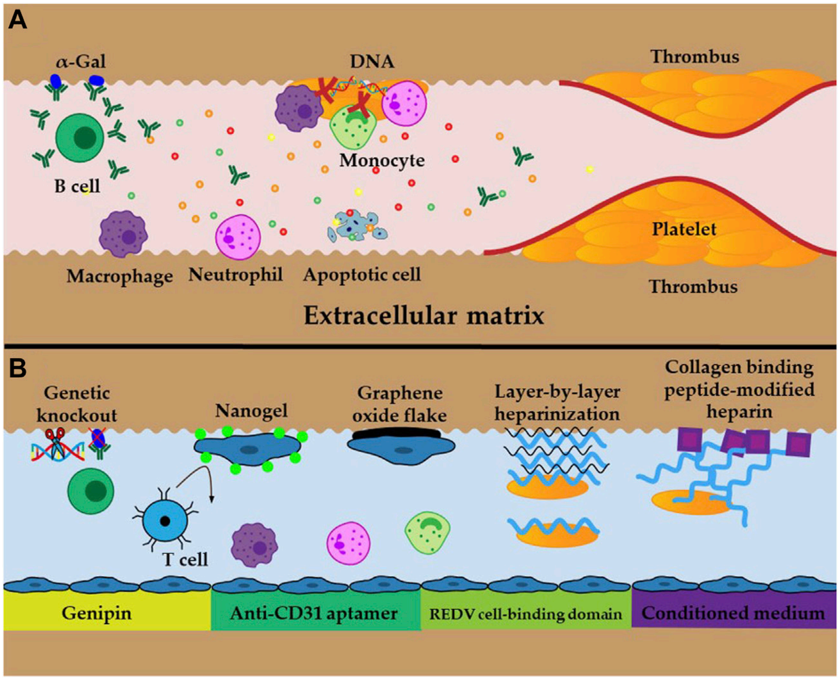

FIGURE 3 | Schematic illustration of obstacles and approaches **(A)** Inflammatory response, oxidative stress, cell apoptosis, and thrombosis caused by residual DNA and Gal epitopes and exposed ECM **(B)** Examples of cross-linking and techniques to improve immunogenicity and thrombosis.

microvasculature in the hepatic sinusoids. The absence of basement membrane resulted in severe damage to the microstructure of the hepatic sinusoids during decellularization. As previously mentioned (**Section 2.1**), the hepatic sinusoids and space of Disse are the sites of substance exchange between the liver and the blood, making microvascular revascularization at the sinusoids top-drawer to the new liver function. Watanabe et al. successfully used HUVECs coated with fibronectin and flow-induced mechanical stimulation to reconstruct the microvessels of the hepatic sinusoids (Watanabe et al., 2019). However, HUVECs and LSECs have distinct cell surface markers and permeability as aforementioned (**Section 2.1**), and LSECs are the preferred cells for re-endothelialization (Poisson et al., 2017; Shetty et al., 2018).

4.4 Combination

Several cells collaboratively accomplish hepatic functions; therefore, the liver cannot be recellularized with only 1 cell type to perform complicated hepatic functions. To generate a competent liver, the decellularized scaffold must be methodically infused with various cells, and these cells grow in the right site. A combination of the HA, PV, vena cava, and common bile ducts can be used for recellularlization. The common bile duct guides the hepatocytes to their anatomical sites, and re-endothelialization of the HA or PV can prevent thrombosis and guarantee sufficient blood perfusion to the rebuilt liver.

Cholangiocytes and hepatocytes that are perfused into the liver *via* the common bile duct and PV, respectively, can rebuild bile duct-like structures, while hepatocytes can settle in the liver parenchyma (Chen et al., 2019). In addition, hepatocytes and LSECs can be distributed in the hepatic parenchymal region and PV lumen after perfusion *via* the common bile duct and PV, respectively (Kojima et al., 2018). Takeishi demonstrated that the implantation of human iPSC-derived hepatocytes, endothelial cells, and cholangiocytes could cover the liver vasculature and bile ducts of decellularized rat liver (Takeishi et al., 2020). Anderson et al. implanted primary porcine hepatocytes into liver scaffolds previously reendothelialized with HUVECs could achieve ALB production, ammonia detoxification, and urea synthesis. Additionally, they found that the ectopic transplantation of engineered livers into pigs that have undergone a portocaval shunt can slow the accumulation of ammonia in the blood (Anderson et al., 2021). Kakabadze et al. discovered that the perfusion of liver tissue fragments that contained all cell types successfully hepatized decellularized placenta, resulting in the expression of ALB and glycogen (Kakabadze et al., 2018). The histological results also revealed that the hepatic cord and hepatic sinusoids were lined with endothelial cells, Kupffer cells, and other types of cells. The animal experimental results also indicated that the implantation of a hepatized placenta could prevent acute liver failure caused by excessive hepatectomy (Kakabadze et al., 2018). Multi-step perfusion and pressure control have also been shown to improve the implantation efficiency, cellular function, and microvascular formation in hepatic sinusoids (Soto-Gutierrez et al., 2011; Watanabe et al., 2019; Anderson et al., 2021).

5 MAIN OBSTACLES

5.1 Thrombogenicity

The primary advantage of whole decellularized liver scaffolds is that the intact vascular network is preserved. However, this advantage is at the expense of losing the endothelial layer (Shaheen et al., 2020). In the absence of an endothelial layer, the exposed components of the ECM, especially collagen, trigger platelet activation and aggregation, and generate thrombin and fibrin, which initiates the formation of a thrombus (**Figure 3A**). Additionally, residual DNA may activate platelets and exert significant pro-inflammatory and pro-thrombotic effects in the extracellular space, hence promoting the development of immunothrombosis (Fuchs et al., 2010; Shi et al., 2020). The resultant thrombosis contributes to an inadequate supply of nutrients and oxygen to the implanted cells, which impedes the long-term survival of the neo-liver (Sassi et al., 2021). Thus, re-establishing blood flow to the new liver entails inhibiting thrombosis and constructing a new endothelial layer. Heparin is the most prevalent anticoagulant and is extensively used in the lining of grafts to improve their hemocompatibility (**Figure 3B**) (Wu et al., 2021). Both *in vivo* and *in vitro* studies have shown that the layer-by-layer deposition of heparin onto decellularized scaffolds immobilizes heparin, which effectively prevents thrombosis, and neither recellularization nor the function of the hepatocytes is affected (Bruinsma BG et al., 2015; Liu et al., 2019). Jiang reported an easy-to-implement method for covalently binding collagen-binding peptides to heparin, where the modified heparin was selectively bound to collagen and dramatically reduced the adhesion of platelets and formation of thrombi (Jiang et al., 2016). Furthermore, scaffolds that were recellularized with HUVECs maintained stable blood perfusion under physiological stress when ectopically implanted in immunosuppressed pigs (Shaheen et al., 2020; Anderson et al., 2021). However, no study to date has achieved long-term *in vivo* perfusion because of imperfect revascularization, which remains a critical problem that must be addressed.

5.2 Anoikis

Anoikis is a particular type of apoptosis that results from the disruption of cell adhesion to the ECM (Chiarugi and Giannoni, 2008). *Ex vivo* perfusion and restoration of blood flow after transplantation generate reactive oxygen species (ROS) that hamper cell adhesion to the ECM and induce anoikis (**Figure 3A**), leading to low engraftment and survival of the implanted cells (Park et al., 2015). In addition, oxidative stress and inflammation suppress cell proliferation and enhance cellular senescence and death, which further reduce the success of the engrafted cells (Panahi et al., 2020). Therefore, it has been proposed that the transplant should be supplemented with antioxidants to scavenge ROS to increase the tolerance of the implanted cells to apoptosis. In addition, cross-linking approaches, such as the use of nanogels, graphene oxide sheets, anti-CD31 inducers, conditioned media, and REDV cell binding domains, also significantly improve cell adhesion to the ECM and increase engraftment in the implant (**Figure 3B**) (Park et al., 2015; Tang et al., 2017; Devalliere et al., 2018; Caires-Junior et al., 2021; Kim et al., 2021). These approaches are promising for the long-term survival of bioengineered livers because they increase cell engraftment and survival rates, which accelerate and improve vasculature reconstruction.

5.3 Immunogenicity

The prerequisite for the long-term *in vivo* survival of recellularized livers is low immunogenicity, which can be determined from the critical indicators of xenoantigenic residues (**Figure 3A**), such as residual DNA and galactose-a1,3-galactose (a-Gal) (Liu et al., 2018; Stahl et al., 2018). Reducing residual DNA and a-Gal involves improving the decellularization protocol and genetic knockout of a-Gal; these are proven approaches that diminish the immune response after implantation (**Figure 3B**) (Liu et al., 2018; Stahl et al., 2018). When sections of the liver scaffold were implanted subcutaneously in live animals, no immunogenicity was observed after 3 weeks, and there was low immunogenicity after 10 weeks (Mirmalek-Sani et al., 2013). Conversely, significant lymphocytic infiltration was observed 1 week after implantation, whereas at 3 weeks, the graft was almost completely degraded, and therefore, the inflammatory response was significantly reduced (Wang et al., 2016). Cross-linking the decellularized scaffolds with genipin and glutaraldehyde could minimize exposure of the immune cells to the ECM and increase cell adhesion of the implanted cells to the ECM (**Figure 3B**). When this approach is combined with immunosuppressive therapy, it can further improve the biocompatibility and long-term survival of the graft (Wang et al., 2016). Compared with glutaraldehyde, the genipin-crosslinked liver ECM exhibited superior biocompatibility and mechanical characteristics, and the *in vivo* immune responses of the host were lower (Gao et al., 2019). The graft from recellularized whole livers that was transplanted into living pigs was lost within 3 days without immunosuppression. Comparatively, this time period increased to more than 15 days when an immunosuppressive regimen was applied to the decellularized liver, and can potentially last longer if the immunosuppressive treatment is sustained (Shaheen et al., 2020). Therefore, more research into the concrete mechanism of immune rejection and strategies for suppressing immune rejection are critical for the long-term survival of bioengineered livers.

5.4 Shortage of Human Liver Scaffolds

Due to the shortage of discarded human livers, some researchers have proposed to populate human cells into the decellularized animal liver scaffolds to mimic human livers for transplantation. Xenotransplantation of genetically modified pig organs has attracted significant attention in recent years, particularly following the recent transplantation of a genetically modified pig kidney into a brain-dead human (Lu et al., 2019; Cooper, 2021). In contrast to the unsatisfactory microstructure of discarded human livers, animal livers are ideal and readily available. Human cells can colonize, proliferate, differentiate, and express ALB and glycogen in animal liver scaffolds (Li et al., 2017; Shaheen et al., 2020). However, the use of xenogeneic liver in human transplantation raises concerns due to the presence of the a-Gal. It has been shown that decellularized a-Gal knockout pig tissues behaved comparably to decellularized wild-type pig tissues (Stahl et al., 2018). Removing the a-Gal gene epitope reduced the adverse immune response of the recipient associated with prolonged exposure to decellularized xenografts (Stahl et al., 2018). Nevertheless, substantial concern has been expressed regarding the possibility of transmitting porcine endogenous retroviruses to the recipient and caregivers (Cooper, 2021).

Because of the risk of transmitting zoonosis, and immunological rejection of the xenogeneic liver, it is worthwhile to seek alternative human organs to replace the liver scaffold. The spleen and placenta are suitable alternative sources of scaffolds for bioengineered livers because they are readily available, have a vascular network for arterial and venous blood exchange, and contain ECM with diverse growth factors that support cell implantation (Maltepe and Fisher, 2015; Xiang et al., 2015; Liu et al., 2019). Decellularized spleen and placenta that are repopulated with primary hepatocytes and fresh liver fragments showed a characteristic hepatic cord structure, and expressed notable levels of ALB, urea, and glycogen after their ectopic transplantation into rats and sheep (Kakabadze et al., 2018; Liu et al., 2019). Moreover, this approach can mitigate against acute liver failure caused by extensive hepatectomy and promote regeneration of the original impaired liver. Consequently, other organs, such as the spleen and placenta, should be further explored as options to diversify the supply of organs for liver engineering (Kakabadze et al., 2018).

6 CONCLUSION AND PROSPECTS

This review discusses the structure of liver and hepatic ECM, and highlights the recent advances in decellularization and recellularization of the liver. An evaluation of decellularized scaffolds and obstacles is also presented. Although scaffold-based liver is a promising option for addressing the scarcity of donor liver, there are many limitations to the practical application of decellularized scaffolds: 1) ineluctable damage and denaturation of ECM proteins during decellularization, which hinders adhesion and proliferation of implanted cells; 2) imperfect revascularization, which lowers the hemocompatibility of the scaffold and increases the risk of thrombosis; and 3) elusory immune response, which causes inflammatory and rejection responses, resulting in loss of the graft. Future research that concentrates on these limitations will be valuable. Additionally, a better understanding of decellularization and recellularization of the liver is fundamental for producing transplantable liver grafts and ensuring the long-term survival of these grafts, especially if these insights are coupled with a deeper understanding of the mechanisms of the immune response.

AUTHOR CONTRIBUTIONS

QD and WJ summarized and wrote the article. FH, FS, JZ, and HZ commented and revised the submitted version.

FUNDING

This work was funded by the National Natural Science Foundation of China (grant number 81701073).

REFERENCES

Acun, A., Oganesyan, R., Uygun, K., Yeh, H., Yarmush, M. L., and Uygun, B. E. (2021). Liver Donor Age Affects Hepatocyte Function through Age-dependent Changes in Decellularized Liver Matrix. *Biomaterials* 270, 120689. doi:10.1016/j.biomaterials.2021.120689

Ahmed, E., Saleh, T., Yu, L., Song, S. H., Park, K. M., Kwak, H. H., et al. (2020). Decellularized Extracellular Matrix-rich Hydrogel-Silver Nanoparticle Mixture as a Potential Treatment for Acute Liver Failure Model. *J. Biomed. Mater. Res.* 108 (12), 2351–2367. doi:10.1002/jbm.a.36988

Alfaifi, M., Eom, Y. W., Newsome, P. N., and Baik, S. K. (2018). Mesenchymal Stromal Cell Therapy for Liver Diseases. *J. Hepatol.* 68 (6), 1272–1285. doi:10.1016/j.jhep.2018.01.030

Anderson, B. D., Nelson, E. D., Joo, D., Amiot, B. P., Katane, A. A., Mendenhall, A., et al. (2021). Functional Characterization of a Bioengineered Liver after Heterotopic Implantation in Pigs. *Commun. Biol.* 4 (1), 1157. doi:10.1038/s42003-021-02665-2

Ben-David, U., and Benvenisty, N. (2011). The Tumorigenicity of Human Embryonic and Induced Pluripotent Stem Cells. *Nat. Rev. Cancer* 11 (4), 268–277. doi:10.1038/nrc3034

Brown, B. N., Freund, J. M., Han, L., Rubin, J. P., Reing, J. E., Jeffries, E. M., et al. (2011). Comparison of Three Methods for the Derivation of a Biologic Scaffold Composed of Adipose Tissue Extracellular Matrix. *Tissue Eng. C: Methods* 17 (4), 411–421. doi:10.1089/ten.TEC.2010.0342

Bruinsma Bg, K. Y., Berendsen, T. A., Ozer, S., Yarmush, M. L., and Uygun, B. E. (2015). Layer-by-layer Heparinization of Decellularized Liver Matrices to Reduce Thrombogenicity of Recellularized Liver Grafts. *JCTRes* 1, 48–56. doi:10.18053/jctres.201501.004

Bühler, N. E. M., Schulze-Osthoff, K., Königsrainer, A., and Schenk, M. (2015). Controlled Processing of a Full-Sized Porcine Liver to a Decellularized Matrix in 24 H. *J. Biosci. Bioeng.* 119 (5), 609–613. doi:10.1016/j.jbiosc.2014.10.019

Butter, A., Aliyev, K., Hillebrandt, K. H., Raschzok, N., Kluge, M., Seiffert, N., et al. (2017). Evolution of Graft Morphology and Function after Recellularization of Decellularized Rat Livers. *J. Tissue Eng. Regen. Med.* 12 (2), e807–e816. doi:10.1002/term.2383

Caires-Júnior, L. C., Goulart, E., Telles-Silva, K. A., Araujo, B. H. S., Musso, C. M., Kobayashi, G., et al. (2021). Pre-coating Decellularized Liver with HepG2-Conditioned Medium Improves Hepatic Recellularization. *Mater. Sci. Eng. C* 121, 111862. doi:10.1016/j.msec.2020.111862

Chakraborty, J., Roy, S., and Ghosh, S. (2020). Regulation of Decellularized Matrix Mediated Immune Response. *Biomater. Sci.* 8 (5), 1194–1215. doi:10.1039/c9bm01780a

Changchen, W., Hongquan, W., Bo, Z., Leilei, X., Haiyue, J., and Bo, P. (2021). The Characterization, Cytotoxicity, Macrophage Response and Tissue Regeneration of Decellularized Cartilage in Costal Cartilage Defects. *Acta Biomater.* 136, 147–158. doi:10.1016/j.actbio.2021.09.031

Cheemerla, S., and Balakrishnan, M. (2021). Global Epidemiology of Chronic Liver Disease. *Clin. Liver Dis.* 17 (5), 365–370. doi:10.1002/cld.1061

Chen, Y., Devalliere, J., Bulutoglu, B., Yarmush, M. L., and Uygun, B. E. (2019). Repopulation of Intrahepatic Bile Ducts in Engineered Rat Liver Grafts. *Technology* 07 (1-2), 46–55. doi:10.1142/s2339547819500043

Cheng, J., Wang, C., and Gu, Y. (2019). Combination of Freeze-Thaw with Detergents: A Promising Approach to the Decellularization of Porcine Carotid Arteries. *Bme* 30 (2), 191–205. doi:10.3233/BME-191044

Chiarugi, P., and Giannoni, E. (2008). Anoikis: a Necessary Death Program for anchorage-dependent Cells. *Biochem. Pharmacol.* 76 (11), 1352–1364. doi:10.1016/j.bcp.2008.07.023

Choudhury, D., Yee, M., Sheng, Z. L. J., Amirul, A., and Naing, M. W. (2020). Decellularization Systems and Devices: State-Of-The-Art. *Acta Biomater.* 115, 51–59. doi:10.1016/j.actbio.2020.07.060

Cooper, D. K. C. (2021). Genetically Engineered Pig Kidney Transplantation in a Brain-dead Human Subject. *Xenotransplantation* 28 (6), e12718. doi:10.1111/xen.12718

Coronado, R. E., Somaraki-Cormier, M., Natesan, S., Christy, R. J., Ong, J. L., and Halff, G. A. (2017). Decellularization and Solubilization of Porcine Liver for Use as a Substrate for Porcine Hepatocyte Culture. *Cel Transpl.* 26 (12), 1840–1854. doi:10.1177/0963689717742157

Damdimopoulou, P., Rodin, S., Stenfelt, S., Antonsson, L., Tryggvason, K., and Hovatta, O. (2016). Human Embryonic Stem Cells. *Best Pract. Res. Clin. Obstet. Gynaecol.* 31, 2–12. doi:10.1016/j.bpobgyn.2015.08.010

Dang, L. H., Tseng, Y., Tseng, H., and Hung, S.-H. (2021). Partial Decellularization for Segmental Tracheal Scaffold Tissue Engineering: A Preliminary Study in Rabbits. *Biomolecules* 11 (6), 866. doi:10.3390/biom11060866

Debnath, T., Mallarpu, C. S., and Chelluri, L. K. (2020). Development of Bioengineered Organ Using Biological Acellular Rat Liver Scaffold and Hepatocytes. *Organogenesis* 16 (2), 61–72. doi:10.1080/15476278.2020.1742534

Devalliere, J., Chen, Y., Dooley, K., Yarmush, M. L., and Uygun, B. E. (2018). Improving Functional Re-endothelialization of Acellular Liver Scaffold Using REDV Cell-Binding Domain. *Acta Biomater.* 78, 151–164. doi:10.1016/j.actbio.2018.07.046

Dianat, N., Dubois-Pot-Schneider, H., Steichen, C., Desterke, C., Leclerc, P., Raveux, A., et al. (2014). Generation of Functional Cholangiocyte-like Cells from Human Pluripotent Stem Cells and HepaRG Cells. *Hepatology* 60 (2), 700–714. doi:10.1002/hep.27165

Everwien, H., Ariza de Schellenberger, A., Haep, N., Tzschätzsch, H., Pratschke, J., Sauer, I. M., et al. (2020a). Magnetic Resonance Elastography Quantification of the Solid-To-Fluid Transition of Liver Tissue Due to Decellularization. *J. Mech. Behav. Biomed. Mater.* 104, 103640. doi:10.1016/j.jmbbm.2020.103640

Everwien, H., Keshi, E., Hillebrandt, K. H., Ludwig, B., Weinhart, M., Tang, P., et al. (2020b). Engineering an Endothelialized, Endocrine Neo-Pancreas: Evaluation of Islet Functionality in an *Ex Vivo* Model. *Acta Biomater.* 117, 213–225. doi:10.1016/j.actbio.2020.09.022

Faccioli, L. A. P., Dias, G. S., Hoff, V., Dias, M. L., Pimentel, C. F., Hochman-Mendez, C., et al. (2020). Optimizing the Decellularized Porcine Liver Scaffold Protocol. *Cells Tissues Organs* 211, 1–10. doi:10.1159/000510297

Felgendreff, P., Schindler, C., Mussbach, F., Xie, C., Gremse, F., Settmacher, U., et al. (2021). Identification of Tissue Sections from Decellularized Liver Scaffolds for Repopulation Experiments. *Heliyon* 7 (2), e06129. doi:10.1016/j.heliyon.2021.e06129

Flynn, L. E. (2010). The Use of Decellularized Adipose Tissue to Provide an Inductive Microenvironment for the Adipogenic Differentiation of Human Adipose-Derived Stem Cells. *Biomaterials* 31 (17), 4715–4724. doi:10.1016/j.biomaterials.2010.02.046

Fuchs, T. A., Brill, A., Duerschmied, D., Schatzberg, D., Monestier, M., Myers, D. D., Jr., et al. (2010). Extracellular DNA Traps Promote Thrombosis. *Proc. Natl. Acad. Sci.* 107 (36), 15880–15885. doi:10.1073/pnas.1005743107

Gao, M., Wang, Y., He, Y., Li, Y., Wu, Q., Yang, G., et al. (2019). Comparative Evaluation of Decellularized Porcine Liver Matrices Crosslinked with Different Chemical and Natural Crosslinking Agents. *Xenotransplantation* 26 (1), e12470. doi:10.1111/xen.12470

Gao, Y., Li, Z., Hong, Y., Li, T., Hu, X., Sun, L., et al. (2020). Decellularized Liver as a Translucent *Ex Vivo* Model for Vascular Embolization Evaluation. *Biomaterials* 240, 119855. doi:10.1016/j.biomaterials.2020.119855

Geerts, S., Ozer, S., Jaramillo, M., Yarmush, M. L., and Uygun, B. E. (2016). Nondestructive Methods for Monitoring Cell Removal during Rat Liver Decellularization. *Tissue Eng. Part C: Methods* 22 (7), 671–678. doi:10.1089/ten.TEC.2015.0571

Gordillo, M., Evans, T., and Gouon-Evans, V. (2015). Orchestrating Liver Development. *Development* 142 (12), 2094–2108. doi:10.1242/dev.114215

Gracia-Sancho, J., Caparrós, E., Fernández-Iglesias, A., and Francés, R. (2021). Role of Liver Sinusoidal Endothelial Cells in Liver Diseases. *Nat. Rev. Gastroenterol. Hepatol.* 18 (6), 411–431. doi:10.1038/s41575-020-00411-3

Gridelli, B., Vizzini, G., Pietrosi, G., Luca, A., Spada, M., Gruttadauria, S., et al. (2012). Efficient Human Fetal Liver Cell Isolation Protocol Based on Vascular Perfusion for Liver Cell-Based Therapy and Case Report on Cell Transplantation. *Liver Transpl.* 18 (2), 226–237. doi:10.1002/lt.22322

Guimaraes, A. B., Correia, A. T., Alves, B. P., Da Silva, R. S., Martins, J. K., Pêgo-Fernandes, P. M., et al. (2019). Evaluation of a Physical-Chemical Protocol for Porcine Tracheal Decellularization. *Transplant. Proc.* 51 (5), 1611–1613. doi:10.1016/j.transproceed.2019.01.042

Hülsmann, J., Aubin, H., Bandesha, S. T., Kranz, A., Stoldt, V. R., Lichtenberg, A., et al. (2015). Rheology of Perfusates and Fluid Dynamical Effects during Whole Organ Decellularization: a Perspective to Individualize Decellularization Protocols for Single Organs. *Biofabrication* 7 (3), 035008. doi:10.1088/1758-5090/7/3/035008

Hussein, K. H., Park, K.-M., Yu, L., Kwak, H.-H., and Woo, H.-M. (2020). Decellularized Hepatic Extracellular Matrix Hydrogel Attenuates Hepatic Stellate Cell Activation and Liver Fibrosis. *Mater. Sci. Eng. C* 116, 111160. doi:10.1016/j.msec.2020.111160

Jeong, W., Kim, M. K., and Kang, H.-W. (2021). Effect of Detergent Type on the Performance of Liver Decellularized Extracellular Matrix-Based Bio-Inks. *J. Tissue Eng.* 12, 204173142199709. doi:10.1177/2041731421997091

Jiang, B., Suen, R., Wertheim, J. A., and Ameer, G. A. (2016). Targeting Heparin to Collagen within Extracellular Matrix Significantly Reduces Thrombogenicity and Improves Endothelialization of Decellularized Tissues. *Biomacromolecules* 17 (12), 3940–3948. doi:10.1021/acs.biomac.6b01330

Kakabadze, Z., Kakabadze, A., Chakhunashvili, D., Karalashvili, L., Berishvili, E., Sharma, Y., et al. (2018). Decellularized Human Placenta Supports Hepatic Tissue and Allows rescue in Acute Liver Failure. *Hepatology* 67 (5), 1956–1969. doi:10.1002/hep.29713

Kang, S. H., Kim, M. Y., Eom, Y. W., and Baik, S. K. (2020). Mesenchymal Stem Cells for the Treatment of Liver Disease: Present and Perspectives. *Gut and Liver* 14 (3), 306–315. doi:10.5009/gnl18412

Kim, D.-H., Ahn, J., Kang, H. K., Kim, M.-S., Kim, N.-G., Kook, M. G., et al. (2021). Development of Highly Functional Bioengineered Human Liver with Perfusable Vasculature. *Biomaterials* 265, 120417. doi:10.1016/j.biomaterials.2020.120417

Kim, J. K., Koh, Y.-D., Kim, J. O., and Seo, D. H. (2016). Development of a Decellularization Method to Produce Nerve Allografts Using Less Invasive Detergents and Hyper/hypotonic Solutions. *J. Plast. Reconstr. Aesthet. Surg.* 69 (12), 1690–1696. doi:10.1016/j.bjps.2016.08.016

Kobes, J. E., Georgiev, G. I., Louis, A. V., Calderon, I. A., Yoshimaru, E. S., Klemm, L. M., et al. (2018). A Comparison of Iron Oxide Particles and Silica Particles for Tracking Organ Recellularization. *Mol. Imaging* 17, 153601211878732. doi:10.1177/1536012118787322

Kojima, H., Yasuchika, K., Fukumitsu, K., Ishii, T., Ogiso, S., Miyauchi, Y., et al. (2018). Establishment of Practical Recellularized Liver Graft for Blood Perfusion Using Primary Rat Hepatocytes and Liver Sinusoidal Endothelial Cells. *Am. J. Transpl.* 18 (6), 1351–1359. doi:10.1111/ajt.14666

Lewis, P. L., Su, J., Yan, M., Meng, F., Glaser, S. S., Alpini, G. D., et al. (2018). Complex Bile Duct Network Formation within Liver Decellularized Extracellular Matrix Hydrogels. *Sci. Rep.* 8 (1), 12220. doi:10.1038/s41598-018-30433-6

Li, P., Zhou, J., Li, W., Wu, H., Hu, J., Ding, Q., et al. (2020). Characterizing Liver Sinusoidal Endothelial Cell Fenestrae on Soft Substrates upon AFM Imaging and Deep Learning. *Biochim. Biophys. Acta (Bba) - Gen. Subjects* 1864 (12), 129702. doi:10.1016/j.bbagen.2020.129702

Li, Y., Wu, Q., Wang, Y., Li, L., Chen, F., Shi, Y., et al. (2017). Construction of Bioengineered Hepatic Tissue Derived from Human Umbilical Cord Mesenchymal Stem Cells via Aggregation Culture in Porcine Decellularized Liver Scaffolds. *Xenotransplantation* 24 (1), e12285. doi:10.1111/xen.12285

Lin, C.-H., Hsia, K., Su, C.-K., Chen, C.-C., Yeh, C.-C., Ma, H., et al. (2021). Sonication-Assisted Method for Decellularization of Human Umbilical Artery for Small-Caliber Vascular Tissue Engineering. *Polymers* 13 (11), 1699. doi:10.3390/polym13111699

Liu, P., Tian, B., Yang, L., Zheng, X., Zhang, X., Li, J., et al. (2019). Hemocompatibility Improvement of Decellularized Spleen Matrix for Constructing Transplantable Bioartificial Liver. *Biomed. Mater.* 14 (2), 025003. doi:10.1088/1748-605X/aaf375

Liu, X., Li, N., Gong, D., Xia, C., and Xu, Z. (2018). Comparison of Detergent-Based Decellularization Protocols for the Removal of Antigenic Cellular Components in Porcine Aortic Valve. *Xenotransplantation* 25 (2), e12380. doi:10.1111/xen.12380

Lorvellec, M., Pellegata, A. F., Maestri, A., Turchetta, C., Alvarez Mediavilla, E., Shibuya, S., et al. (2020). An *In Vitro* Whole-Organ Liver Engineering for Testing of Genetic Therapies. *iScience* 23 (12), 101808. doi:10.1016/j.isci.2020.101808

Lorvellec, M., Scottoni, F., Crowley, C., Fiadeiro, R., Maghsoudlou, P., Pellegata, A. F., et al. (2017). Mouse Decellularised Liver Scaffold Improves Human Embryonic and Induced Pluripotent Stem Cells Differentiation into Hepatocyte-like Cells. *PLoS One* 12 (12), e0189586. doi:10.1371/journal.pone.0189586

Lu, S., Cuzzucoli, F., Jiang, J., Liang, L.-G., Wang, Y., Kong, M., et al. (2018). Development of a Biomimetic Liver Tumor-On-A-Chip Model Based on Decellularized Liver Matrix for Toxicity Testing. *Lab. Chip* 18 (22), 3379–3392. doi:10.1039/c8lc00852c

Lu, T., Yang, B., Wang, R., and Qin, C. (2019). Xenotransplantation: Current Status in Preclinical Research. *Front. Immunol.* 10, 3060. doi:10.3389/fimmu.2019.03060

Maghsoudlou, P., Georgiades, F., Smith, H., Milan, A., Shangaris, P., Urbani, L., et al. (2016). Optimization of Liver Decellularization Maintains Extracellular Matrix Micro-architecture and Composition Predisposing to Effective Cell Seeding. *PLoS One* 11 (5), e0155324. doi:10.1371/journal.pone.0155324

Magliaro, C., Tirella, A., Mattei, G., Pirone, A., and Ahluwalia, A. (2015). HisTOOLogy: an Open-Source Tool for Quantitative Analysis of Histological Sections. *J. Microsc.* 260 (3), 260–267. doi:10.1111/jmi.12292

Mak, K. M., and Mei, R. (2017). Basement Membrane Type IV Collagen and Laminin: An Overview of Their Biology and Value as Fibrosis Biomarkers of Liver Disease. *Anat. Rec.* 300 (8), 1371–1390. doi:10.1002/ar.23567

Maltepe, E., and Fisher, S. J. (2015). Placenta: the Forgotten Organ. *Annu. Rev. Cel Dev. Biol.* 31, 523–552. doi:10.1146/annurev-cellbio-100814-125620

Manalastas, T. M., Dugos, N., Ramos, G., and Mondragon, J. M. (2021). Effect of Decellularization Parameters on the Efficient Production of Kidney Bioscaffolds. *Appl. Biochem. Biotechnol.* 193 (5), 1239–1251. doi:10.1007/s12010-020-03338-2

Mattei, G., Di Patria, V., Tirella, A., Alaimo, A., Elia, G., Corti, A., et al. (2014). Mechanostructure and Composition of Highly Reproducible Decellularized Liver Matrices. *Acta Biomater.* 10 (2), 875–882. doi:10.1016/j.actbio.2013.10.023

Mattei, G., Magliaro, C., Pirone, A., and Ahluwalia, A. (2018). Bioinspired Liver Scaffold Design Criteria. *Organogenesis* 14 (3), 129–146. doi:10.1080/15476278.2018.1505137

Mattei, G., Magliaro, C., Pirone, A., and Ahluwalia, A. (2017). Decellularized Human Liver Is Too Heterogeneous for Designing a Generic Extracellular Matrix Mimic Hepatic Scaffold. *Artif. Organs* 41 (12), E347–E355. doi:10.1111/aor.12925

Mazza, G., Telese, A., Al-Akkad, W., Frenguelli, L., Levi, A., Marrali, M., et al. (2019). Cirrhotic Human Liver Extracellular Matrix 3D Scaffolds Promote Smad-dependent TGF-Β1 Epithelial Mesenchymal Transition. *Cells* 9 (1), 83. doi:10.3390/cells9010083

McCrary, M. W., Bousalis, D., Mobini, S., Song, Y. H., and Schmidt, C. E. (2020). Decellularized Tissues as Platforms for *In Vitro* Modeling of Healthy and Diseased Tissues. *Acta Biomater.* 111, 1–19. doi:10.1016/j.actbio.2020.05.031

McQuitty, C. E., Williams, R., Chokshi, S., and Urbani, L. (2020). Immunomodulatory Role of the Extracellular Matrix within the Liver Disease Microenvironment. *Front. Immunol.* 11, 574276. doi:10.3389/fimmu.2020.574276

Minami, T., Ishii, T., Yasuchika, K., Fukumitsu, K., Ogiso, S., Miyauchi, Y., et al. (2019). Novel Hybrid Three-Dimensional Artificial Liver Using Human Induced Pluripotent Stem Cells and a Rat Decellularized Liver Scaffold. *Regenerative Ther.* 10, 127–133. doi:10.1016/j.reth.2019.03.002

Mirmalek-Sani, S.-H., Sullivan, D. C., Zimmerman, C., Shupe, T. D., and Petersen, B. E. (2013). Immunogenicity of Decellularized Porcine Liver for Bioengineered Hepatic Tissue. *Am. J. Pathol.* 183 (2), 558–565. doi:10.1016/j.ajpath.2013.05.002

Miyauchi, Y., Yasuchika, K., Fukumitsu, K., Ishii, T., Ogiso, S., Minami, T., et al. (2017). A Novel Three-Dimensional Culture System Maintaining the Physiological Extracellular Matrix of Fibrotic Model Livers Accelerates Progression of Hepatocellular Carcinoma Cells. *Sci. Rep.* 7 (1), 9827. doi:10.1038/s41598-017-09391-y

Moulisová, V., Jiřík, M., Schindler, C., Červenková, L., Pálek, R., Rosendorf, J., et al. (2020). Novel Morphological Multi-Scale Evaluation System for Quality Assessment of Decellularized Liver Scaffolds. *J. Tissue Eng.* 11, 204173142092112. doi:10.1177/2041731420921121

Müller, P. C., Kabacam, G., Vibert, E., Germani, G., and Petrowsky, H. (2020). Current Status of Liver Transplantation in Europe. *Int. J. Surg.* 82, 22–29. doi:10.1016/j.ijsu.2020.05.062

Narciso, M., Otero, J., Navajas, D., Farré, R., Almendros, I., and Gavara, N. (2021). Image-Based Method to Quantify Decellularization of Tissue Sections. *Ijms* 22 (16), 8399. doi:10.3390/ijms22168399

Nishiguchi, A., and Taguchi, T. (2021). A pH-Driven Genipin Gelator to Engineer Decellularized Extracellular Matrix-Based Tissue Adhesives. *Acta Biomater.* 131, 211–221. doi:10.1016/j.actbio.2021.06.033

O'Neill, J. D., Anfang, R., Anandappa, A., Costa, J., Javidfar, J., Wobma, H. M., et al. (2013). Decellularization of Human and Porcine Lung Tissues for Pulmonary Tissue Engineering. *Ann. Thorac. Surg.* 96 (3), 1046–1056. doi:10.1016/j.athoracsur.2013.04.022

Ogiso, S., Yasuchika, K., Fukumitsu, K., Ishii, T., Kojima, H., Miyauchi, Y., et al. (2016). Efficient Recellularisation of Decellularised Whole-Liver Grafts Using Biliary Tree and Foetal Hepatocytes. *Sci. Rep.* 6, 35887. doi:10.1038/srep35887

Panahi, M., Rahimi, B., Rahimi, G., Yew Low, T., Saraygord-Afshari, N., and Alizadeh, E. (2020). Cytoprotective Effects of Antioxidant Supplementation on Mesenchymal Stem Cell Therapy. *J. Cel Physiol* 235 (10), 6462–6495. doi:10.1002/jcp.29660

Park, J., Kim, B., Han, J., Oh, J., Park, S., Ryu, S., et al. (2015). Graphene Oxide Flakes as a Cellular Adhesive: Prevention of Reactive Oxygen Species Mediated Death of Implanted Cells for Cardiac Repair. *ACS Nano* 9 (5), 4987–4999. doi:10.1021/nn507149w

Poisson, J., Lemoinne, S., Boulanger, C., Durand, F., Moreau, R., Valla, D., et al. (2017). Liver Sinusoidal Endothelial Cells: Physiology and Role in Liver Diseases. *J. Hepatol.* 66 (1), 212–227. doi:10.1016/j.jhep.2016.07.009

Prasertsung, I., Kanokpanont, S., Bunaprasert, T., Thanakit, V., and Damrongsakkul, S. (2008). Development of Acellular Dermis from Porcine Skin Using Periodic Pressurized Technique. *J. Biomed. Mater. Res.* 85B (1), 210–219. doi:10.1002/jbm.b.30938

PulverShevtsov, A., Leybovich, B., Artyuhov, I., Maleev, Y., and Peregudov, A. (2014). Production of Organ Extracellular Matrix Using a Freeze-Thaw Cycle Employing Extracellular Cryoprotectants. *Cryo Lett.* 35 (5), 400–406.

Reing, J. E., Brown, B. N., Daly, K. A., Freund, J. M., Gilbert, T. W., Hsiong, S. X., et al. (2010). The Effects of Processing Methods upon Mechanical and Biologic Properties of Porcine Dermal Extracellular Matrix Scaffolds. *Biomaterials* 31 (33), 8626–8633. doi:10.1016/j.biomaterials.2010.07.083

Rodin, S., Antonsson, L., Niaudet, C., Simonson, O. E., Salmela, E., Hansson, E. M., et al. (2014). Clonal Culturing of Human Embryonic Stem Cells on Laminin-521/e-Cadherin Matrix in Defined and Xeno-free Environment. *Nat. Commun.* 5, 3195. doi:10.1038/ncomms4195

Sassi, L., Ajayi, O., Campinoti, S., Natarajan, D., McQuitty, C., Siena, R. R., et al. (2021). A Perfusion Bioreactor for Longitudinal Monitoring of Bioengineered Liver Constructs. *Nanomaterials* 11 (2), 275. doi:10.3390/nano11020275

Say, S., Dugos, N. P., Roces, S. A., and Mondragon, J. M. (2019). Sonication-assisted Perfusion Decellularization of Whole Porcine Kidney. *Int. J. Biol. Biomed. Eng.* 13, 78–81.

Sengyoku, H., Tsuchiya, T., Obata, T., Doi, R., Hashimoto, Y., Ishii, M., et al. (2018). Sodium Hydroxide Based Non-detergent Decellularizing Solution for Rat Lung. *Organogenesis* 14 (2), 94–106. doi:10.1080/15476278.2018.1462432

Shaheen, M. F., Joo, D. J., Ross, J. J., Anderson, B. D., Chen, H. S., Huebert, R. C., et al. (2020). Sustained Perfusion of Revascularized Bioengineered Livers Heterotopically Transplanted into Immunosuppressed Pigs. *Nat. Biomed. Eng.* 4 (4), 437–445. doi:10.1038/s41551-019-0460-x

Shen, W., Berning, K., Tang, S. W., and Lam, Y. W. (2020). Rapid and Detergent-free Decellularization of Cartilage. *Tissue Eng. Part C: Methods* 26 (4), 201–206. doi:10.1089/ten.TEC.2020.0008

Shetty, S., Lalor, P. F., and Adams, D. H. (2018). Liver Sinusoidal Endothelial Cells - Gatekeepers of Hepatic Immunity. *Nat. Rev. Gastroenterol. Hepatol.* 15 (9), 555–567. doi:10.1038/s41575-018-0020-y

Shi, C., Yang, L., Braun, A., and Anders, H.-J. (2020). Extracellular DNA-A Danger Signal Triggering Immunothrombosis. *Front. Immunol.* 11, 568513. doi:10.3389/fimmu.2020.568513

Shimoda, H., Yagi, H., Higashi, H., Tajima, K., Kuroda, K., Abe, Y., et al. (2019). Decellularized Liver Scaffolds Promote Liver Regeneration after Partial Hepatectomy. *Sci. Rep.* 9 (1), 12543. doi:10.1038/s41598-019-48948-x

Song, A. T. W., Avelino-Silva, V. I., Pecora, R. A., Pugliese, V., D'Albuquerque, L. A., and Abdala, E. (2014). Liver Transplantation: Fifty Years of Experience. *Wjg* 20 (18), 5363–5374. doi:10.3748/wjg.v20.i18.5363

Soto-Gutierrez, A., Zhang, L., Medberry, C., Fukumitsu, K., Faulk, D., Jiang, H., et al. (2011). A Whole-Organ Regenerative Medicine Approach for Liver Replacement. *Tissue Eng. Part C: Methods* 17 (6), 677–686. doi:10.1089/ten.tec.2010.0698

Stahl, E. C., Bonvillain, R. W., Skillen, C. D., Burger, B. L., Hara, H., Lee, W., et al. (2018). Evaluation of the Host Immune Response to Decellularized Lung Scaffolds Derived from α-Gal Knockout Pigs in a Non-human Primate Model. *Biomaterials* 187, 93–104. doi:10.1016/j.biomaterials.2018.09.038

Stamataki, Z., and Swadling, L. (2020). The Liver as an Immunological Barrier Redefined by Single-cell Analysis. *Immunology* 160 (2), 157–170. doi:10.1111/imm.13193

Struecker, B., Butter, A., Hillebrandt, K., Polenz, D., Reutzel-Selke, A., Tang, P., et al. (2017). Improved Rat Liver Decellularization by Arterial Perfusion under Oscillating Pressure Conditions. *J. Tissue Eng. Regen. Med.* 11 (2), 531–541. doi:10.1002/term.1948

Suss, P. H., Ribeiro, V. S. T., Motooka, C. E., de Melo, L. C., and Tuon, F. F. (2021). Comparative Study of Decellularization Techniques to Obtain Natural Extracellular Matrix Scaffolds of Human Peripheral-Nerve Allografts. *Cell Tissue Bank.* Online ahead of print. doi:10.1007/s10561-021-09977-x

Syed, O., Walters, N. J., Day, R. M., Kim, H.-W., and Knowles, J. C. (2014). Evaluation of Decellularization Protocols for Production of Tubular Small Intestine Submucosa Scaffolds for Use in Oesophageal Tissue Engineering. *Acta Biomater.* 10 (12), 5043–5054. doi:10.1016/j.actbio.2014.08.024

Tajima, K., Yagi, H., and Kitagawa, Y. (2018). Human-Scale Liver Harvest and Decellularization for Preclinical Research. *Methods Mol. Biol.* 1577, 327–335. doi:10.1007/7651_2018_195

Takeishi, K., Collin de l'Hortet, A., Wang, Y., Handa, K., Guzman-Lepe, J., Matsubara, K., et al. (2020). Assembly and Function of a Bioengineered Human Liver for Transplantation Generated Solely from Induced Pluripotent Stem Cells. *Cel Rep.* 31 (9), 107711. doi:10.1016/j.celrep.2020.107711

Tang, J., Cui, X., Caranasos, T. G., Hensley, M. T., Vandergriff, A. C., Hartanto, Y., et al. (2017). Heart Repair Using Nanogel-Encapsulated Human Cardiac Stem Cells in Mice and Pigs with Myocardial Infarction. *ACS Nano* 11 (10), 9738–9749. doi:10.1021/acsnano.7b01008

Tao, M., Liang, F., He, J., Ye, W., Javed, R., Wang, W., et al. (2021). Decellularized Tendon Matrix Membranes Prevent post-surgical Tendon Adhesion and Promote Functional Repair. *Acta Biomater.* 134, 160–176. doi:10.1016/j.actbio.2021.07.038

Thanapirom, K., Caon, E., Papatheodoridi, M., Frenguelli, L., Al-Akkad, W., Zhenzhen, Z., et al. (2021). Optimization and Validation of a Novel Three-Dimensional Co-culture System in Decellularized Human Liver Scaffold for the Study of Liver Fibrosis and Cancer. *Cancers* 13 (19), 4936. doi:10.3390/cancers13194936

Touboul, T., Hannan, N. R. F., Corbineau, S., Martinez, A., Martinet, C., Branchereau, S., et al. (2010). Generation of Functional Hepatocytes from Human Embryonic Stem Cells under Chemically Defined Conditions that Recapitulate Liver Development. *Hepatology* 51 (5), 1754–1765. doi:10.1002/hep.23506

Trefts, E., Gannon, M., and Wasserman, D. H. (2017). The Liver. *Curr. Biol.* 27 (21), R1147–R1151. doi:10.1016/j.cub.2017.09.019

van Steenberghe, M., Schubert, T., Guiot, Y., Bouzin, C., Bollen, X., and Gianello, P. (2017). Enhanced Vascular Biocompatibility of Decellularized Xeno-/allogeneic Matrices in a Rodent Model. *Cell Tissue Bank* 18 (2), 249–262. doi:10.1007/s10561-017-9610-0

van Steenberghe, M., Schubert, T., Xhema, D., Bouzin, C., Guiot, Y., Duisit, J., et al. (2018). Enhanced Vascular Regeneration with Chemically/physically Treated Bovine/human Pericardium in Rodents. *J. Surg. Res.* 222, 167–179. doi:10.1016/j.jss.2017.09.043

Vasylovska, S., Schuster, J., Brboric, A., Carlsson, P.-O., Dahl, N., and Lau, J. (2021). Generation of Human Induced Pluripotent Stem Cell (iPSC) Lines (UUMCBi001-A, UUMCBi002-A) from Two Healthy Donors. *Stem Cel Res.* 50, 102114. doi:10.1016/j.scr.2020.102114

Verstegen, M. M. A., Willemse, J., van den Hoek, S., Kremers, G.-J., Luider, T. M., van Huizen, N. A., et al. (2017). Decellularization of Whole Human Liver Grafts Using Controlled Perfusion for Transplantable Organ Bioscaffolds. *Stem Cell Develop.* 26 (18), 1304–1315. doi:10.1089/scd.2017.0095

Vishwakarma, S. K., Bardia, A., Lakkireddy, C., Raju, N., Paspala, S. A. B., Habeeb, M. A., et al. (2019). Intraperitoneal Transplantation of Bioengineered Humanized Liver Grafts Supports Failing Liver in Acute Condition. *Mater. Sci. Eng. C* 98, 861–873. doi:10.1016/j.msec.2019.01.045

Visscher, D. O., Lee, H., van Zuijlen, P. P. M., Helder, M. N., Atala, A., Yoo, J. J., et al. (2021). A Photo-Crosslinkable Cartilage-Derived Extracellular Matrix Bioink for Auricular Cartilage Tissue Engineering. *Acta Biomater.* 121, 193–203. doi:10.1016/j.actbio.2020.11.029

Wang, Y., Bao, J., Wu, X., Wu, Q., Li, Y., Zhou, Y., et al. (2016). Genipin Crosslinking Reduced the Immunogenicity of Xenogeneic Decellularized Porcine Whole-Liver Matrices through Regulation of Immune Cell Proliferation and Polarization. *Sci. Rep.* 6, 24779. doi:10.1038/srep24779

Watanabe, M., Yano, K., Okawa, K., Yamashita, T., Tajima, K., Sawada, K., et al. (2019). Construction of Sinusoid-Scale Microvessels in Perfusion Culture of a Decellularized Liver. *Acta Biomater.* 95, 307–318. doi:10.1016/j.actbio.2018.12.042

Weng, J., Chen, B., Xie, M., Wan, X., Wang, P., Zhou, X., et al. (2021). Rabbit Thyroid Extracellular Matrix as a 3D Bioscaffold for Thyroid Bioengineering: a Preliminary *In Vitro* Study. *Biomed. Eng. Online* 20 (1), 18. doi:10.1186/s12938-021-00856-w

Willemse, J., Verstegen, M. M. A., Vermeulen, A., Schurink, I. J., Roest, H. P., van der Laan, L. J. W., et al. (2020). Fast, Robust and Effective Decellularization of Whole Human Livers Using Mild Detergents and Pressure Controlled Perfusion. *Mater. Sci. Eng. C* 108, 110200. doi:10.1016/j.msec.2019.110200

Wu, G., Wu, D., Lo, J., Wang, Y., Wu, J., Lu, S., et al. (2020). A Bioartificial Liver Support System Integrated with a DLM/GelMA-based Bioengineered Whole Liver for Prevention of Hepatic Encephalopathy via Enhanced Ammonia Reduction. *Biomater. Sci.* 8 (10), 2814–2824. doi:10.1039/c9bm01879d

Wu, Q., Li, Y., Yang, Z., Li, L., Yang, J., Zhu, X., et al. (2022). Ectopic Expansion and Vascularization of Engineered Hepatic Tissue Based on Heparinized Acellular Liver Matrix and Mesenchymal Stromal Cell Spheroids. *Acta Biomater.* 137, 79–91. doi:10.1016/j.actbio.2021.10.017

Xiang, J.-X., Zheng, X.-L., Gao, R., Wu, W.-Q., Zhu, X.-L., Li, J.-H., et al. (2015). Liver Regeneration Using Decellularized Splenic Scaffold: a Novel Approach in Tissue Engineering. *Hepatobiliary Pancreat. Dis. Int.* 14 (5), 502–508. doi:10.1016/s1499-3872(15)60423-4

Xiang, J., Zheng, X., Liu, P., Yang, L., Dong, D., Wu, W., et al. (2016). Decellularized Spleen Matrix for Reengineering Functional Hepatic-like Tissue Based on Bone Marrow Mesenchymal Stem Cells. *Organogenesis* 12 (3), 128–142. doi:10.1080/15476278.2016.1185584

Yagi, S., Singhal, A., Jung, D.-H., and Hashimoto, K. (2020). Living-donor Liver Transplantation: Right versus Left. *Int. J. Surg.* 82, 128–133. doi:10.1016/j.ijsu.2020.06.022

Yang, W., Chen, Q., Xia, R., Zhang, Y., Shuai, L., Lai, J., et al. (2018). A Novel Bioscaffold with Naturally-Occurring Extracellular Matrix Promotes Hepatocyte Survival and Vessel Patency in Mouse Models of Heterologous Transplantation. *Biomaterials* 177, 52–66. doi:10.1016/j.biomaterials.2018.05.026

You, J., Park, S.-A., Shin, D.-S., Patel, D., Raghunathan, V. K., Kim, M., et al. (2013). Characterizing the Effects of Heparin Gel Stiffness on Function of Primary Hepatocytes. *Tissue Eng. A* 19 (23-24), 2655–2663. doi:10.1089/ten.TEA.2012.0681

Yusof, F., Sha'ban, M., and Azhim, A. (2019). Development of Decellularized Meniscus Using Closed Sonication Treatment System: Potential Scaffolds for Orthopedics Tissue Engineering Applications. *Ijn* Vol. 14, 5491–5502. doi:10.2147/ijn.S207270

Zhang, H., Siegel, C. T., Li, J., Lai, J., Shuai, L., Lai, X., et al. (2018). Functional Liver Tissue Engineering by an Adult Mouse Liver-Derived Neuro-Glia Antigen 2-

expressing Stem/progenitor Population. *J. Tissue Eng. Regen. Med.* 12 (1), e190–e202. doi:10.1002/term.2311

Zhao, C., Li, Y., Peng, G., Lei, X., Zhang, G., and Gao, Y. (2020). Decellularized Liver Matrix-Modified Chitosan Fibrous Scaffold as a Substrate for C3A Hepatocyte Culture. *J. Biomater. Sci. Polym. Edition* 31 (8), 1041–1056. doi:10.1080/09205063.2020.1738690

Zhao, H., Li, M., Ouyang, Q., Lin, G., and Hu, L. (2020). VEGF Promotes Endothelial Cell Differentiation from Human Embryonic Stem Cells Mainly through PKC-ɛ/η Pathway. *Stem Cell Develop.* 29 (2), 90–99. doi:10.1089/scd.2019.0172

Conflict of Interest: The authors declare that the research was conducted in the absence of any commercial or financial relationships that could be construed as a potential conflict of interest.

frontiers
in Bioengineering and Biotechnology

ORIGINAL RESEARCH
published: 08 March 2022
doi: 10.3389/fbioe.2022.844119

Basal-Like Cell-Conditioned Medium Exerts Anti-Fibrotic Effects *In Vitro* and *In Vivo*

Petra Khan [1], ***Kleanthis Fytianos*** [2], ***Sabrina Blumer*** [1], ***Julien Roux*** [1,3], ***Amiq Gazdhar*** [2], ***Spasenija Savic*** [4], ***Lars Knudsen*** [5,6], ***Danny Jonigk*** [6,7], ***Mark P. Kuehnel*** [6,7], ***Sofia Mykoniati*** [8], ***Michael Tamm*** [1], ***Thomas Geiser*** [2] ***and Katrin E. Hostettler*** [1]*

[1]Department of Biomedicine and Clinics of Respiratory Medicine, University Hospital Basel, University of Basel, Basel, Switzerland, [2]Department of Pulmonary Medicine, University Hospital Bern, and Department of Biomedical Research, University of Bern, Bern, Switzerland, [3]Swiss Institute of Bioinformatics, Basel, Switzerland, [4]Institute of Medical Genetics and Pathology, University Hospital Basel, University of Basel, Basel, Switzerland, [5]Institute of Functional and Applied Anatomy, Hannover Medical School, Hannover, Germany, [6]Biomedical Research in Endstage and Obstructive Lung Disease Hannover (BREATH), Member of the German Center for Lung Research (DZL), Hannover, Germany, [7]Institute of Pathology, Hannover Medical School, Hannover, Germany, [8]Department of Internal Medicine, Jura Cantonal Hospital, Delemont, Switzerland

Edited by:
George Alexander Truskey,
Duke University, United States

Reviewed by:
David Warburton,
Children's Hospital Los Angeles,
United States
Olga Pershina,
Research Institute of Pharmacology and Regenerative Medicine named ED Goldberg (RAS), Russia

Correspondence:
Katrin E. Hostettler
Katrin.Hostettler@usb.ch

Specialty section:
This article was submitted to Tissue Engineering and Regenerative Medicine,
a section of the journal Frontiers in Bioengineering and Biotechnology

Received: *27 December 2021*
Accepted: *04 February 2022*
Published: *08 March 2022*

Citation:
Khan P, Fytianos K, Blumer S, Roux J, Gazdhar A, Savic S, Knudsen L, Jonigk D, Kuehnel MP, Mykoniati S, Tamm M, Geiser T and Hostettler KE (2022) Basal-Like Cell-Conditioned Medium Exerts Anti-Fibrotic Effects In Vitro and In Vivo.
Front. Bioeng. Biotechnol. 10:844119.
doi: 10.3389/fbioe.2022.844119

In idiopathic pulmonary fibrosis (IPF), basal-like cells are atypically present in the alveolar region, where they may affect adjacent stromal cells by paracrine mechanisms. We here aimed to confirm the presence of basal-like cells in peripheral IPF lung tissue *in vivo*, to culture and characterize the cells *in vitro,* and to investigate their paracrine effects on IPF fibroblasts *in vitro* and in bleomycin-injured rats *in vivo*. Basal-like cells are mainly localized in areas of pathological bronchiolization or honeycomb cysts in peripheral IPF lung tissue. Single-cell RNA sequencing (scRNA-seq) demonstrated an overall homogeneity, the expression of the basal cell markers cytokeratin KRT5 and KRT17, and close transcriptomic similarities to basal cells in the majority of cells cultured *in vitro*. Basal-like cells secreted significant levels of prostaglandin E2 (PGE2), and their conditioned medium (CM) inhibited alpha-smooth muscle actin (α-SMA) and collagen 1A1 (Col1A1) and upregulated matrix metalloproteinase-1 (MMP-1) and hepatocyte growth factor (HGF) by IPF fibroblasts *in vitro*. The instillation of CM in bleomycin-injured rat lungs resulted in reduced collagen content, improved lung architecture, and reduced α-SMA-positive cells. Our data suggested that basal-like cells may limit aberrant fibroblast activation and differentiation in IPF through paracrine mechanisms.

Keywords: basal cells, idiopathic pulmonary fibrosis, conditioned medium, PGE2, lung fibroblasts, aberrant basaloid cells

INTRODUCTION

Idiopathic pulmonary fibrosis (IPF) is a chronic and irreversible interstitial lung disease characterized by a progressive destruction of the lung parenchyma and the respective loss of lung function (Raghu et al., 2011). The initial events leading to the development and progression of IPF are still not elucidated; however, evidence suggests that repeated injury to the alveolar epithelial cells plays a central role (Selman et al., 2001). Typically, alveolar regeneration involves the self-renewal of alveolar epithelial-type (AT2) cells and their differentiation into (AT1) cells (Barkauskas et al., 2013). During normal lung homeostasis, there is no overlap of epithelial cell types of the alveolar and the conducting regions. However, after severe lung injury in mice and humans, an expansion of airway basal-like cells within the alveolar region was observed (Kumar et al., 2011; Vaughan et al., 2015; Zuo et al., 2015; Ray et al., 2016; Xi et al., 2017; Taylor et al., 2018; Yang et al., 2018; Fernanda de Mello Costa et al., 2020). In line with these findings, a decline in alveolar epithelial cells, corresponding to an expansion of cells expressing airway epithelial markers in IPF versus control lung tissue, was demonstrated (Xu et al., 2017; Adams et al., 2020; Habermann et al., 2020). Furthermore, the disease-enriched presence of basal-like cells (Chilosi et al., 2002; Smirnova et al., 2016; Xu et al., 2017; Prasse et al., 2019) and a novel KRT5-/KRT17+ aberrant basaloid cell population (Adams et al., 2020; Habermann et al., 2020) within the alveolar compartment and in bronchoalveolar lavage (BAL) fluid of IPF patients was described. In mice, where basal cells are restricted to the trachea and mainstem bronchi, these alveolar basal-like cells arise from a distinct intrapulmonary p63+ stem/progenitor cell population (Xi et al., 2017; Yang et al., 2018). In humans, the origin of alveolar basal-like cells is less clear: in contrast to mice, basal cells are present throughout the airways in humans (Rock et al., 2010). Therefore, migration of distal airway basal cells into the alveolar region after lung injury in humans is likely (Fernanda de Mello Costa et al., 2020).

While the occurrence of basal-like cells within the alveolar region in injured lungs is a widely accepted phenomenon, their role and function remains largely unknown. It was suggested that basal-like cells may help to regenerate the injured alveolar epithelium by differentiation into AT2 cells in rodent lungs (Kumar et al., 2011; Vaughan et al., 2015; Zuo et al., 2015). On the contrary, the cells' disease-enriched presence and a report of a correlation between increased mortality and the appearance of basal-like cells in BAL fluid of IPF patients (Prasse et al., 2019) would rather point to a non-beneficial role of these cells in lung fibrosis. In addition to their capacity to differentiate into specialized cells, different types of stem/progenitor cells have been shown to exert their effects through their secretome by paracrine mechanisms (Xia et al., 2019). In this study, we cultured KRT5+/KRT17+ basal-like cells from peripheral fibrotic lung tissue and investigated the effects of their conditioned medium (CM) on cultured primary human IPF fibroblasts and in a rat model of pulmonary fibrosis.

MATERIALS AND METHODS

Cell Culture

Basal-like cells or fibroblasts were cultured from peripheral fibrotic lung tissue of IPF or other interstitial lung disease patients. Tissue was cut into small pieces and placed into 12-well culture plates (one tissue piece/well) containing growth medium (DMEM with 10% FCS, 25 mM HEPES, 1× (vol/vol) sodium pyruvate, 1× (vol/vol) MEM vitamin-mix, and 1× (vol/vol) antibiotic-antimycotic). Tissue pieces, which showed outgrowth of basal-like cells within 2–5 days, proved large numbers of KRT17+/KRT5+ basal-like cells in subsequent IF-staining (**Supplementary Figure S1A**). Contrariwise, in tissue pieces without outgrowth of basal-like cells but with sprouting of fibroblasts after approximately 7 days, KRT17+/KRT5+ basal-like cells were absent or present in low numbers in subsequent IF-staining (**Supplementary Figure 1B**).

Both cell types could clearly be differentiated by their different morphologies (**Supplementary Figures 2A,B**). CM was collected of pure basal-like cell cultures after 5 days. For experiments, fibroblasts were kept in starving medium (DMEM with 0.1% FCS, 25 mM HEPES, 1× (vol/vol) sodium pyruvate, 1× (vol/vol) MEM vitamin-mix, and 1× (vol/vol) antibiotic-antimycotic) for 24 h prior to treatment with the control medium (DMEM with 10% FCS, 25 mM HEPES, 1× (vol/vol) sodium pyruvate, 1× (vol/vol) MEM vitamin-mix, and 1× (vol/vol) antibiotic-antimycotic), basal-like cell-CM, fibroblast (F)-CM, or several different recombinant factors (IL-17A, osteopontin, ENA-78, GM-CSF, HGF, GDF-15, GROα, IL-6, PGE2, or IL-8) ± chemical inhibitors AH6809 (20 μM), PF04418948 (1–10 μM), or indomethacin (1–10 μM). IPF was diagnosed based on ATS/ERS guidelines (Raghu et al., 2011; Raghu et al., 2018). The local ethical committee of the University Hospital, Basel, Switzerland (EKBB05/06), and of the Medical University of Hannover, Germany (2699–2015), approved the culture of human primary lung cells. All materials and instruments used in this study are listed in **Supplementary Tables 1, 2**.

Human Lung Tissue Staining

Peripheral human lung tissue was fixed in paraformaldehyde and embedded in paraffin. The paraffin blocks were cut, and routine hematoxylin and eosin (H&E) and immunofluorescence (IF) stainings were performed as described in **Supplementary Material**.

TaqMan RT-PCR, Immunoblotting, Immunofluorescence, ELISA, and Cytokine Array

TaqMan® PCR, immunoblotting, and IF stainings were performed as previously described (Hostettler et al., 2017; Seidel et al., 2009; Seidel et al., 2011). Details of primer and antibodies are listed in **Supplementary Table S1**. Mediators were measured in supernatants by using the DuoSet ELISA development systems, Prostaglandin E2 Parameter Assay Kit, or a Proteome Profiler™ Human XL Cytokine Array kit according to the manufacturers' instructions. Col1A1 deposition was analyzed by a cell-based ELISA as previously described (Lambers et al., 2014).

RNA Sequencing

scRNA-seq datasets were generated at the Genomics Facility Basel of the ETH Zurich, Basel, and data were analyzed by the Bioinformatics Core Facility, Department of Biomedicine, University of Basel. The processed scRNA-seq data can be obtained from the Gene Expression Omnibus (GEO) database under accession no. GSE145439. A detailed description of the analysis methods used for these datasets can be found in **Supplementary Material**.

Animals

Male Fisher F344 rats (220–240 g) were obtained from Charles River Laboratories GmbH, Sulzfeld, Germany. Experiments were performed in accordance with the standards of the European Convention of Animal Care. The study protocol was approved by the University of Bern Animal Study Committee (BE 135/16).

Instillation of Bleomycin

On day one of the protocol, F344 rats (220–240 g) were anesthetized by inhalation of 4% isoflurane in a glass chamber, intubated with a 14 GA i.v catheter, and instilled intratracheally with bleomycin (1.28 U/rat) to both lungs.

Instillation of Conditioned Media

Seven days after the instillation of bleomycin, rats were anesthetized as described above and divided into five groups with n = 5 in each group (A, B, C, D, and E). Group A received intratracheal administration of control media (DMEM without FBS), group B received fibroblast conditioned media (F-CM), and group C received basal-like cell-CM. Additional groups studied were group D receiving basal-like cell-CM pretreated with prostaglandin (PGE2) neutralizing antibody and group E receiving isotype control antibody (IgG) (n = 3). A volume of 500 µl was administered intratracheally to both the lungs in each group.

Assessment

On day 7 after basal-like cell-CM and control media instillation, the animals were anesthetized as described above. Thiopental (50 mg/kg body weight) was administered intraperitoneally. The heart–lung block was explanted, and tissue was collected for further analysis. Routine H&E staining, Sirus red staining, immunohistochemistry, and hydroxyproline assay were performed as described in **Supplementary Material**.

Rat Lung Tissue Homogenization for Single-Cell Isolation and Flow Cytometry

The entire right lung was minced in a 10 cm Petri dish in a sterile solution of RPMI 1640 containing 0.1% collagenase I and 0.25% collagenase II as described previously (Tamo et al., 2018). Cell suspensions were washed, stained, and analyzed as described in detail in **Supplementary Material**.

Data Analysis

All experiments were performed in primary human lung fibroblasts derived from at least three different patients, of which each fibroblast cell line was treated with basal-like cell-CM or F-CM from up to seven different patients. Where applicable, data were expressed as mean ± standard error of the mean (SEM), and Student`s *t*-test was used for statistical comparisons. p values ≤ 0.05 were considered as significant.

RESULTS

Basal-Like Cells Derived From Peripheral Fibrotic Lung Tissue

KRT5 and KRT17 positive basal-like cells were detected in peripheral lung tissue of five different IPF patients where they were mainly localized within the areas of pathological bronchiolization and honeycomb cysts (**Figures 1A,B**).

After quality control and filtering, a total of 8,953 basal-like cells derived from three different IPF patients were analyzed by scRNA-seq. scRNA-seq. data demonstrated homogeneity of the cell population with the majority of cells expressing the basal cell markers KRT5 (75%) and KRT17 (96%) (**Figure 2A**). Annotation of cultured cells using as reference an scRNA-seq atlas of cell types in the human lung (Travaglini et al., 2020) revealed the closest transcriptomic similarity to basal cells (basal, differentiating basal, and proliferating basal) of the majority of cells (79.9%) (**Figure 2B**). From the remaining cells, a small percentage of cells matched best to mesenchymal (fibroblasts/myofibroblasts/smooth muscle) (2.0%), AT cell type 1 (5.7%), immune (2.2%), ciliated (0.4%), or secretory (club/mucous/goblet) (10%) epithelial cells (**Figure 2B**). High expression of KRT5 and KRT17 was confirmed in 5–11 additional patients by TaqMan PCR (**Figure 2C**) and on the protein level by IF in cells derived from four different patients (**Figure 2D**).

Anti-Fibrotic Effects of Basal-Like Cell-CM in Cultured IPF Fibroblasts

The α-SMA RNA expression of IPF fibroblasts (n = 3) in the control medium was significantly downregulated after incubation with basal-like cell-CM and upregulated in fibroblasts incubated with F-CM (**Figure 3A**). α-SMA protein expression in IPF fibroblasts (n = 3) was reduced by basal-like cell-CM derived from six different patients (1–6; **Figure 3B**). α-Tubulin served as a control for equal protein loading.

Col1A1 RNA expression in IPF fibroblasts (n = 7) was significantly inhibited in basal-like cell-CM treated cells when compared to those in the control medium (**Figure 3C**). Similarly, collagen I deposition in IPF fibroblasts (n = 5) was significantly reduced by 15% ± 2.38 after treatment with basal-like cell-CM (**Figure 3D**). In contrast, when fibroblasts (n = 3) were treated with F-CM, Col1A1 RNA expression was upregulated in F-CM-treated cells when compared to the medium control (**Figure 3C**).

MMP-1 RNA expression in IPF fibroblasts (n = 6) was significantly increased by treatment with basal-like cell-CM and reduced by treating the cells with F-CM (**Figure 3E**). MMP-1 secretion was increased from 42.98 ± 16.99 ng/ml in the control medium to 90.74 ± 9.81 ng/ml in basal-like cell-CM-treated fibroblasts (**Figure 3F**). Basal-like cell-CM or F-CM had no significant effect on TIMP-1 RNA expression or protein secretion (**Figures 3G,H**). Basal-like cell-CM medium upregulated the secretion of anti-fibrotic HGF by IPF fibroblasts (**Figure 3I**): IPF fibroblasts (n = 12) in the control medium secreted HGF at a concentration of 13,125 ± 1,679 pg/ml, which was significantly increased to 25,205 ± 2,302 pg/ml HGF after the addition of basal-like cell-CM for 24 h. Basal-like cell-CM only (before addition to fibroblasts) contained 946.7 ± 114 pg/ml HGF (**Figure 3I**).

Mediators Secreted by Basal-Like Cells and Their Effects on IPF Fibroblasts

Cytokine arrays were incubated with basal-like cell-CM (n = 3, **Figure 4**). Several cytokines were detected, of which eight

[**Figure 4**, framed in the cytokine array (B) and highlighted in the table (A)] were selected to test their effects on Col1A1, MMP-1, TIMP-1, or HGF by fibroblasts. In addition, PGE2 was measured by ELISA: In basal-like cell-CM of 36 different patients, an average concentration of 3,034 ± 228.4 pg/ml PGE2 was detected.

IPF fibroblasts were treated with eight human recombinant cytokines (all at 10 ng/ml), IL-17A, osteopontin, ENA-78, GM-CSF, GDF-15, GRO-α, IL-6, and IL-8, or with PGE2 (1–1,000 nM). None of the eight tested cytokines upregulated the secretion of HGF by IPF fibroblasts (**Figure 5A**). GM-CSF weakly but significantly inhibited HGF secretion when compared to the medium control (**Figure 5A**). Only PGE2 increased HGF secretion by IPF fibroblasts in a dose-dependent manner between 10–1,000 nM PGE2 (**Figure 5B**). Col1A1 expression was significantly reduced by all tested cytokines (**Figure 5C**) and by PGE2 (**Figure 5D**). MMP-1 was significantly increased by osteopontin, IL-6, or IL-8 (**Figure 5E**), whereas PGE2 significantly downregulated MMP-1 expression (**Figure 5F**). TIMP-1 expression was significantly downregulated by ENA-78, IL-8, GDF-15, GM-CSF (**Figure 5G**), or PGE2 at 10–100 nM (**Figure 5H**).

Basal-Like Cell-CM Up-Regulates HGF *via* PGE2 in IPF Fibroblasts

Our data indicate that basal-like cell-CM-induced HGF secretion by fibroblasts is mainly regulated by PGE2. When fibroblasts (n = 6) were incubated with either the control medium or basal-like cell-CM, PGE2 levels in the control medium were below the detection limit (**Figure 6A**). PGE2 levels in basal-like cell-CM before (basal-like cell-CM only) and after addition to fibroblasts (basal-like cell-CM on fibroblasts) were not significantly different (**Figure 6A**), indicating that PGE2 is produced by basal-like cells, but not fibroblasts under the cell culture conditions described here.

When indomethacin (1 or 10 μM) was added to basal-like cells, PGE2 secretion was completely abolished (**Figure 6B**) and basal-like cell−/+indomethacin-CM failed to upregulate HGF secretion in IPF fibroblasts (n = 4) (**Figure 6C**).

The PGE2 receptor antagonists, AH6809 and PF04418948, were used to inhibit the action of PGE2 on IPF fibroblasts (n = 4). PF04418948 alone (1 or 10 μM) had no significant effects on HGF secretion when compared to fibroblasts incubated with the control medium (**Figure 6D**). Basal-like cell-CM significantly upregulated HGF secretion, which was dose-dependently reversed by PF04418948 at 1 and 10 μM (**Figure 6D**). Similarly, AH6809 alone (20 μM) had no effect on HGF secretion when compared to the medium control, but significantly reversed basal-like cell-CM-induced HGF secretion by IPF fibroblasts (**Figure 6E**).

Basal-Like Cell-CM Improves Lung Fibrosis *In Vivo* by a PGE2-Dependent Mechanism

The lung architecture was improved in the basal-like cell-CM-treated animals (group C), compared to the control groups (group A and B) as shown by H&E staining at day 7 (**Figure 7**). When a PGE2 antibody was added to basal-like cell-CM (group D), basal-like cell-CM did not improve lung architecture, whereas the addition of the isotype control (group E) did not alter the effect of basal-like cell-CM on lung architecture as shown by H&E staining (**Figure 7**). Pico Sirius staining further showed dense red-stained areas in the interstitium of the bleomycin control lung (group A) or in the lung of animals treated with F-CM (group B) (**Figure 7**). The group of animals treated with basal-like cell-CM (group C) did not show dense red collagen areas (**Figure 7**). However, blocking of PGE2 led to increased dense red collagen areas (group D), whereas the isotype control (group E) had no effect (**Figure 7**). Immunohistochemistry revealed dense areas of α-SMA positivity in control groups (group A and B, **Figure 7**). However, α-SMA-positive cells in the interstitial space in the group treated with basal-like cell-CM (group C) were not observed. Blocking of PGE2 in the basal-like cell-CM led to an increase in α-SMA-positive areas (group D), whereas the isotype control (group E) had no effect on α-SMA expression (**Figure 7**).

The Ashcroft score in fibrotic lungs treated with basal-like cell-CM (group C) was significantly reduced compared to the animals treated with the control medium (group A, **Figure 8A**). Application of F-CM (group B) to bleomycin-treated rats had no significant effect on the Ashcroft score (**Figure 8A**), when compared to group A. In presence of a PGE2 antibody in basal-like cell-CM (group D), its inhibitory effect was significantly reversed, whereas the addition of isotype control (group E) had no effect on the Ashcroft score (**Figure 8A**).

Collagen level of the lung in the animals treated with basal-like cell-CM (group C, 148.2 ± 14.36 μg/mg) was significantly reduced as measured by hydroxyproline assay compared to group A (332.4 ± 65.93 μg/mg) and group B (229.1 ± 31.88 μg/mg) (**Figure 8B**). The addition of F-CM (group B) did not significantly reduce collagen level when compared to animals treated with a control medium (group A, **Figure 8B**). The addition of a PGE2 antibody to basal-like cell-CM (group D) significantly reversed the inhibitory effect of basal-like cell-CM (group C) on collagen level, whereas the addition of isotype control (group E; 183.8 ± 13.33 μg/mg) had no effect (**Figure 8B**).

Flow cytometry measurements reveal that bleomycin-treated rats that received basal-like cell-CM (group C) have significantly lower numbers of myofibroblasts (22,232 ± 2,260 cells) compared to 31,741 ± 3,451 cells in control group A and 53,475.63 ± 2054 cells in group B. Furthermore, after PGE2 inhibition, the number of myofibroblasts increased (55,993 ± 975 cells) (group D). The cell number in group E was 6,163 ± 1,089 cells (**Figure 8C**).

Similarly, collagen-1a-expressing α-SMA cells in animals treated with basal-like cell-CM (group C) were reduced to 20,605 ± 1,846 cells compared to animals that received F-CM (group B) (52,643 ± 1,955 cells) and control animals (group A) (27,237 ± 942 cells). Furthermore, after PGE2 inhibition, the number of cells increased, 52,913 ± 955 (group D). The cell number in group E was 15,640 ± 444 cells (**Figure 8D**).

DISCUSSION

In this study, we confirmed the presence of KRT5+/KRT17+ basal-like cells in the peripheral lung of IPF patients, localized mainly within areas of pathological tissue remodeling with

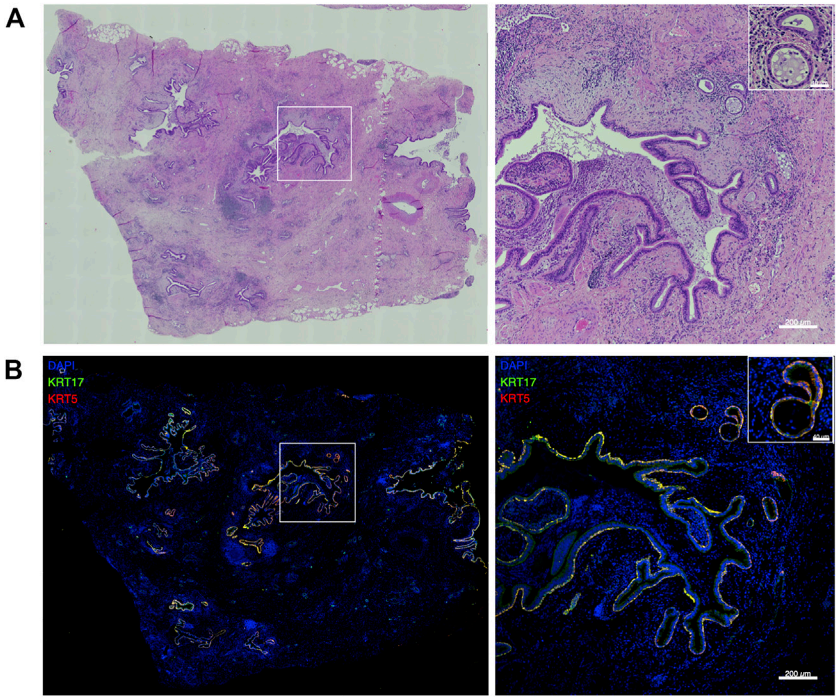

FIGURE 1 | Basal-like cells in peripheral IPF lung tissue. Representative large image composed of stitched ×20 images and the indicated region (white square) at higher magnification showing hematoxylin and eosin (H&E) stainings **(A)** and merged images of KRT5 (red) and KRT17 (green) stainings of peripheral lung tissue of IPF patients (n = 5) **(B)**.

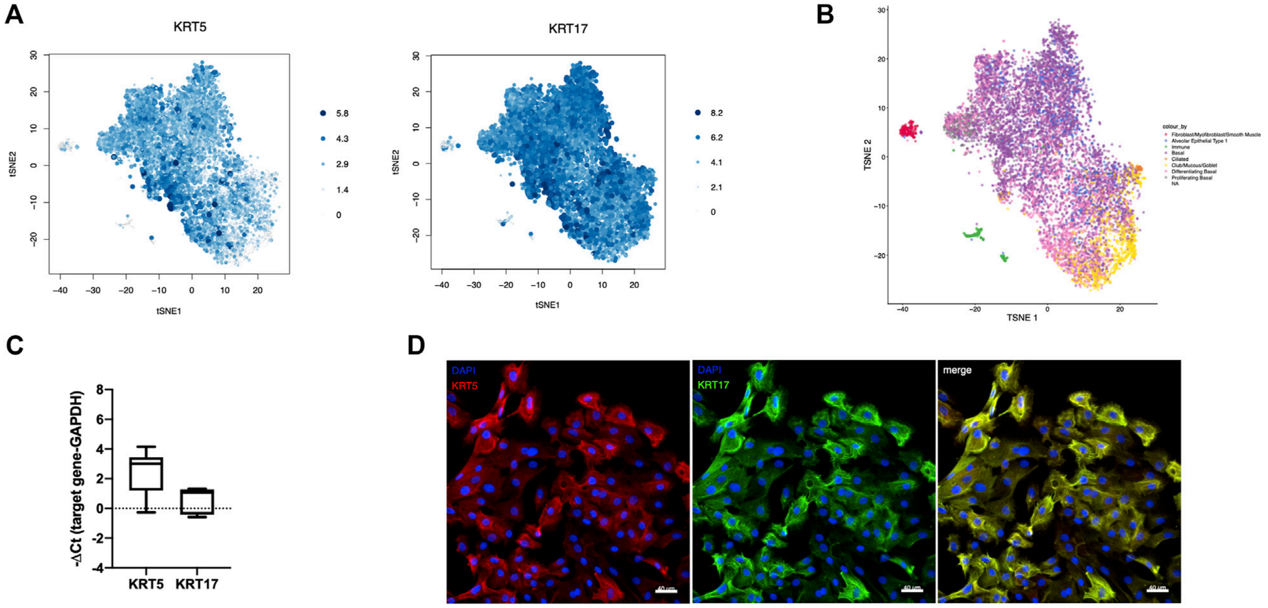

FIGURE 2 | Characteristics of cultured basal-like cells. scRNA-seq was performed in basal-like cells derived from three different IPF patients, and the expression levels of the basal cell markers KRT5 and KRT17, proportional to the size and color intensity of the dots, are shown on a t-SNE plot **(A)**. t-SNE shows the best matching cell type for each cell after annotation of cultured cells using as reference an scRNA-seq atlas of cell types in the human lung **(B)**. KRT5 (n = 11) and KRT17 (n = 5) RNA expression was confirmed by TaqMan PCR **(C)**. Representative images showing staining for KRT5 (red), left, and KRT17 (green), middle, and their merged image, right in cultured basal-like cells of four different IPF patients **(D)**.

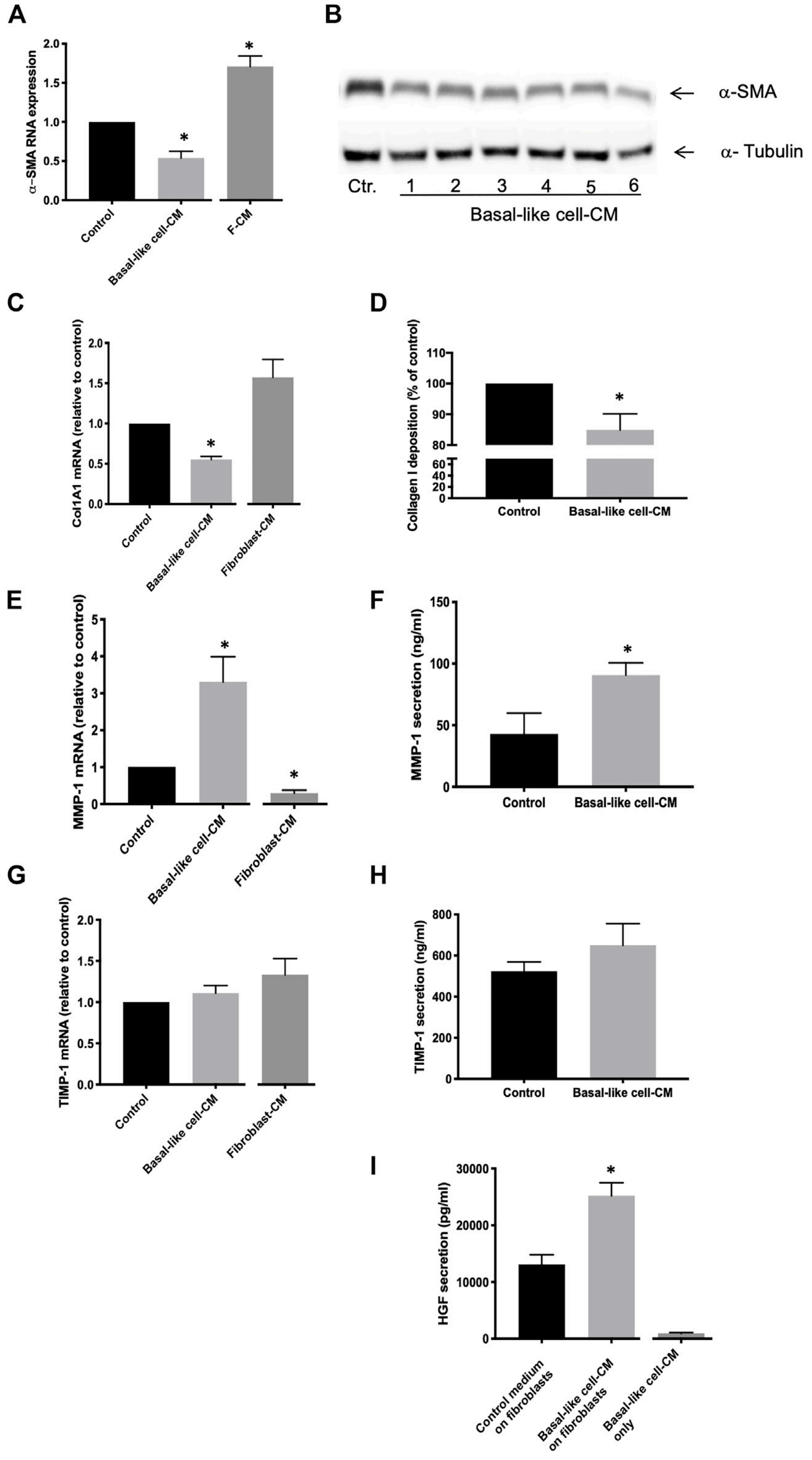

FIGURE 3 | Anti-fibrotic effects of basal-like cell-CM on fibroblasts *in vitro*. Fibroblasts were treated with the control medium, basal-like cell-conditioned medium (CM), or fibroblasts-CM (F-CM). α-SMA RNA expression was measured by TaqMan RT-PCR (n = 3) **(A)**, and changes in α-SMA protein in fibroblasts (n = 3) treated with basal-like cell-CM of six different patients (1–6) were determined by immunoblotting **(B)**. Col1A1 RNA expression was determined after 24 h (n = 7) **(C)** and Col1A1 deposition after 48 h (n = 5) **(D)**. MMP-1 or TIMP-1 RNA expression **(E,G)** or protein secretion **(F,H)** was measured after 24 h. Data are expressed as fold change or as a percentage of fibroblasts treated with control medium (RNA) or in ng/ml (protein). HGF in supernatants of fibroblasts (n = 12) treated with basal-like cell-CM, control medium, or in basal-like cell-CM before the addition to fibroblasts (basal-like cell-CM only) **(I)**.*$p < 0.05$.

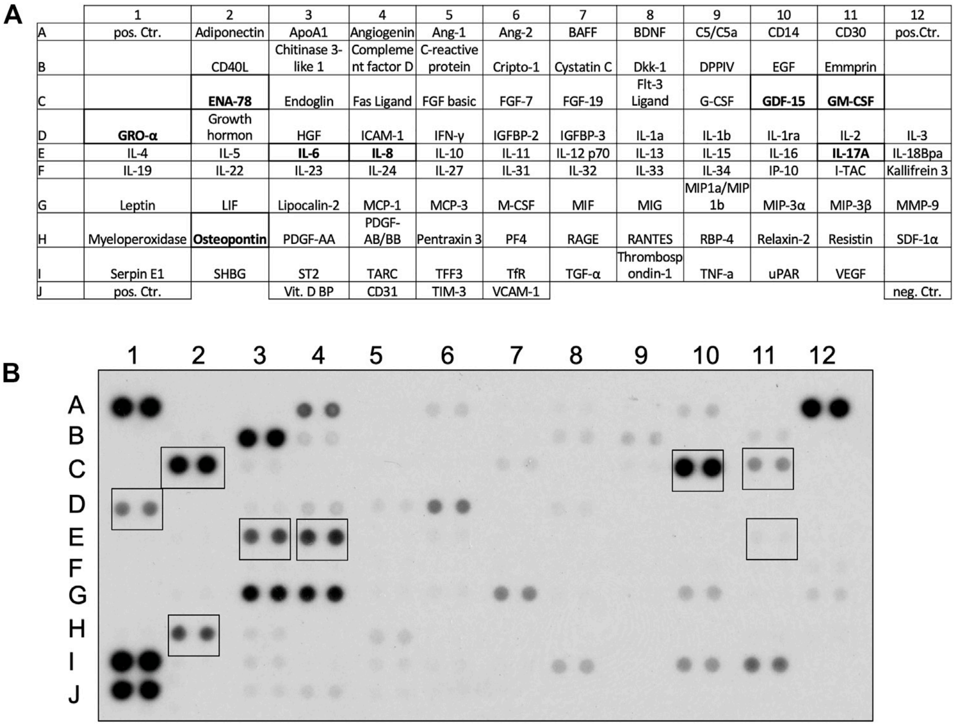

A

	1	2	3	4	5	6	7	8	9	10	11	12
A	pos. Ctr.	Adiponectin	ApoA1	Angiogenin	Ang-1	Ang-2	BAFF	BDNF	C5/C5a	CD14	CD30	pos.Ctr.
B		CD40L	Chitinase 3-like 1	Complement factor D	C-reactive protein	Cripto-1	Cystatin C	Dkk-1	DPPIV	EGF	Emmprin	
C		**ENA-78**	Endoglin	Fas Ligand	FGF basic	FGF-7	FGF-19	Flt-3 Ligand	G-CSF	**GDF-15**	**GM-CSF**	
D	**GRO-α**	Growth hormon	HGF	ICAM-1	IFN-γ	IGFBP-2	IGFBP-3	IL-1a	IL-1b	IL-1ra	IL-2	IL-3
E	IL-4	IL-5	**IL-6**	**IL-8**	IL-10	IL-11	IL-12 p70	IL-13	IL-15	IL-16	**IL-17A**	IL-18Bpa
F	IL-19	IL-22	IL-23	IL-24	IL-27	IL-31	IL-32	IL-33	IL-34	IP-10	I-TAC	Kallifrein 3
G	Leptin	LIF	Lipocalin-2	MCP-1	MCP-3	M-CSF	MIF	MIG	MIP1a/MIP1b	MIP-3α	MIP-3β	MMP-9
H	Myeloperoxidase	**Osteopontin**	PDGF-AA	PDGF-AB/BB	Pentraxin 3	PF4	RAGE	RANTES	RBP-4	Relaxin-2	Resistin	SDF-1α
I	Serpin E1	SHBG	ST2	TARC	TFF3	TfR	TGF-α	Thrombospondin-1	TNF-a	uPAR	VEGF	
J	pos. Ctr.		Vit. D BP	CD31	TIM-3	VCAM-1						neg. Ctr.

FIGURE 4 | Cytokines detected in the basal-like cell-CM. Proteome Profiler™ Human XL Cytokine Arrays were incubated with basal-like cell-CM derived from three different patients. Detectable cytokines and their location on the array **(A)**. Cytokines highlighted in **(A)** and framed in a representative cytokine array **(B)** were selected for further experiments.

bronchiolization and honeycomb cysts. We cultured these basal-like cells *in vitro* and investigated the effects of their conditioned medium (CM) on IPF fibroblasts *in vitro* and in a rat model of pulmonary fibrosis *in vivo*. We showed that basal-like cell-CM inhibits the expression and deposition of Col1A1 and upregulates MMP-1 RNA and protein expression, without having effects on TIMP-1 in IPF fibroblasts. The secretion of anti-fibrotic HGF was enhanced, and α-SMA expression was reduced in IPF fibroblasts by basal-like cell-CM. In a rat model of bleomycin-induced lung fibrosis, intratracheal instillation of basal-like cell-CM significantly reduced collagen level and α-SMA expression and improved lung structure, thus supporting the *in vitro* findings. Furthermore, PGE2 was identified as a crucial factor mediating the effects of lung-resident basal-like cell-CM. Our data suggest that basal-like cells secrete factors that limit aberrant fibroblast activation and their differentiation into myofibroblasts.

In line with our findings, a number of previous studies showed the disease-enriched presence of airway basal-like cells within the peripheral lung (Chilosi et al., 2002; Smirnova et al., 2016; Prasse et al., 2019; Fernanda de Mello Costa et al., 2020). Furthermore, a small population of aberrant basaloid cells, expressing some, but not all, canonical basal cell markers (KRT5-/KRT17+) was recently identified in peripheral lung tissue of IPF patients (Adams et al., 2020; Habermann et al., 2020) The role and function of these cells in IPF pathogenesis remains, however, largely unknown. The presence of basal-like cells in bronchoalveolar lavage (BAL) fluid or in the alveolar region of lung tissue derived from the IPF patients was associated with increased mortality (Prasse et al., 2019), pathological bronchiolization, and honeycomb formation (Chilosi et al., 2002; Prasse et al., 2019). On the contrary, findings from studies in mice suggested that basal-like cells regenerate the alveolar epithelium by their differentiation into AT2 cells (Kumar et al., 2011; Vaughan et al., 2015; Zuo et al., 2015; Yuan et al., 2019). However, there is growing evidence that the cells' capacity to regenerate AT2 cells is limited (Fernanda de Mello Costa et al., 2020).

The cross-talk between alveolar epithelial cells and adjacent fibroblasts seems crucial for maintaining normal lung homeostasis, and a loss of AT2 cell-secreted anti-fibrotic mediators may result in uncontrolled fibroblast differentiation and collagen secretion (Bagnato and Harari 2015; Knudsen et al., 2017). Since basal-like cells are present in the alveolar space of the fibrotic lung, we here determined the effects of their conditioned medium on IPF lung fibroblasts and in bleomycin-challenged rats. Surprisingly, we observed a number of anti-fibrotic effects mediated by basal-like cell-CM in our *in vitro* and *in vivo* models.

Prostaglandin E2 (PGE2), a bioactive eicosanoid that regulates many biologically important processes (Bozyk and Moore 2011), was identified as a crucial secretory factor mediating the effects in basal-like cell-CM. Similar to the basal-like cell-CM, recombinant PGE2 dose-dependently reduced Col1A1 and increased HGF in IPF fibroblasts. Furthermore, blocking PGE2 in basal-like cell-CM reversed HGF upregulation in IPF fibroblasts *in vitro* and

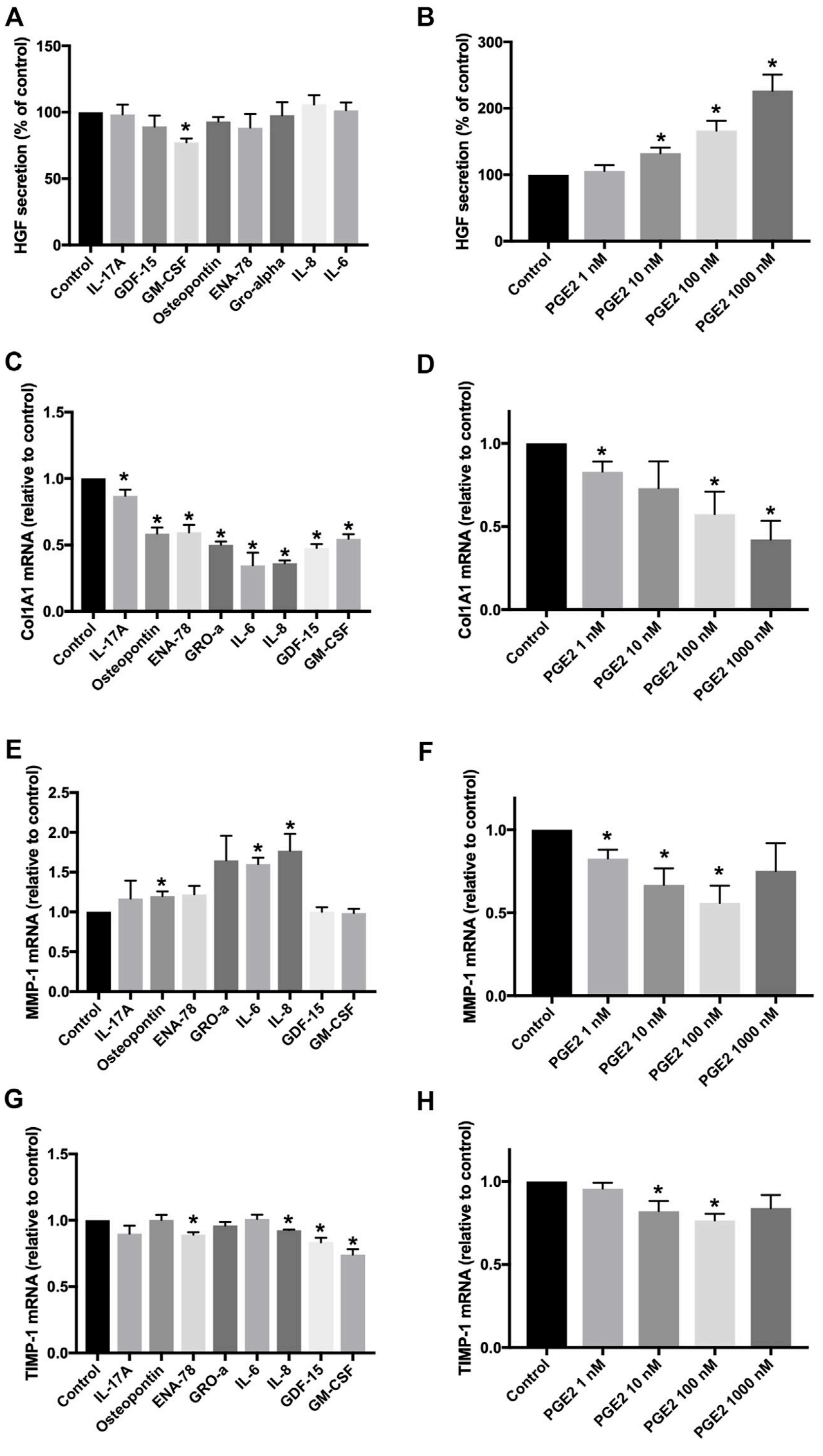

FIGURE 5 | Effects of different recombinant cytokines and PGE2 on fibroblasts *in vitro*. Fibroblasts were treated with eight different recombinant human cytokines (all at 10 ng/ml) or with PGE2 (1–1,000 nM) for 24 h. HGF secretion was measured in cell supernatants, and data were expressed as a percentage of fibroblasts treated with the control medium **(A,B)**. Col1A1 **(C,D)**, MMP-1 **(E,F),** and TIMP-1 **(G,H)** RNA expression was determined by TaqMan RT-PCR, and values were expressed as fold change of fibroblasts treated with the control medium. **p* < 0.05.

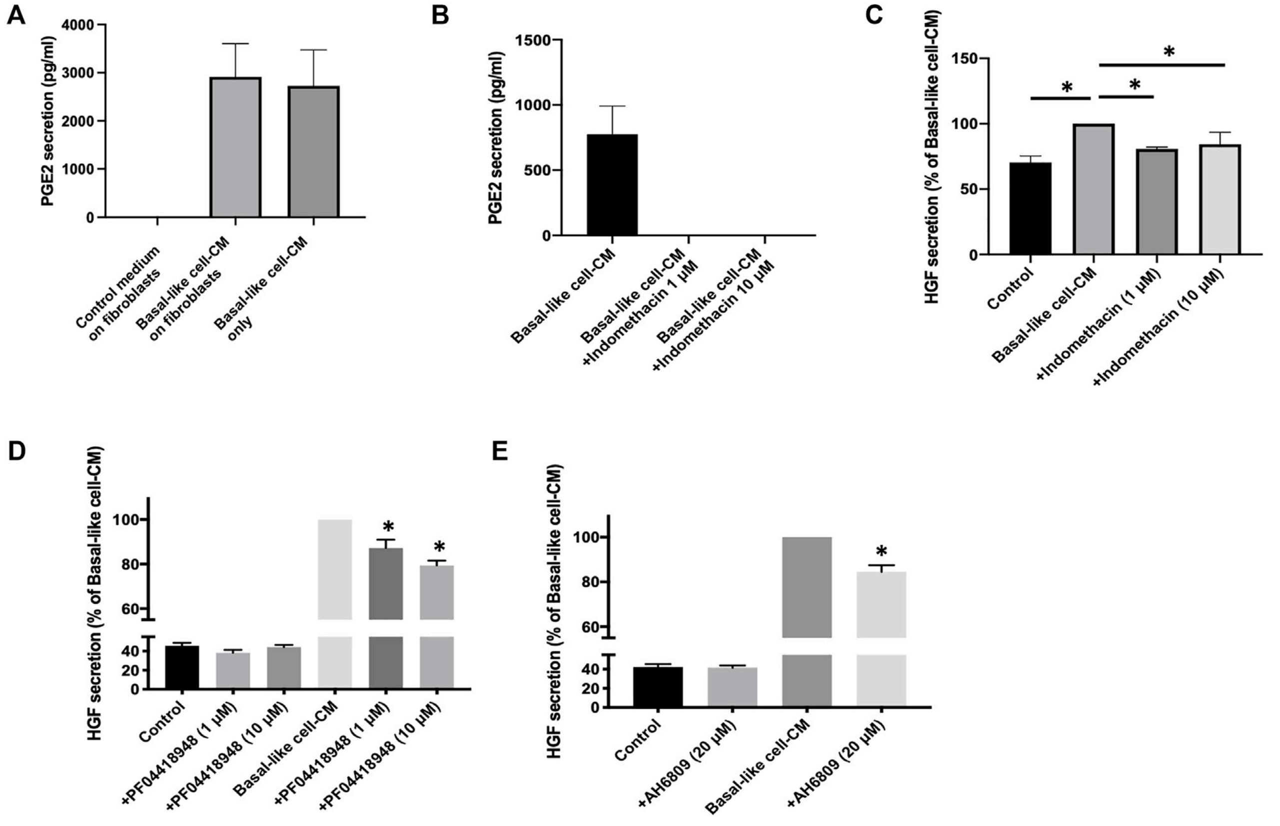

FIGURE 6 | PGE2 mediates basal-like cell-CM-induced HGF in IPF fibroblasts. PGE2 in supernatants of fibroblasts (n = 6) treated with basal-like cell-CM, control medium, or basal-like cell-CM before the addition to fibroblasts **(A)**. PGE2 secretion from basal-like cells with and without COX inhibitor indomethacin (1 and 10 μM) **(B)**. Data are expressed as pg/ml. IPF fibroblasts (n = 4) were incubated with the control medium or basal-like cell-CM collected from basal-like cells treated with or without indomethacin (1 and 10 μM). After 24 h, HGF secretion was measured in the cell supernatants, and data were expressed as a percentage of fibroblast HGF secretion treated with basal-like cell-CM alone **(C)**. IPF fibroblasts (n = 4) were treated with the control medium or basal-like cell-CM with or without PGE2 receptor antagonists PF04418948 [**(D)**, 1 and 10 μM] or AH6809 [**(E)**, 20 μM]. HGF secretion was measured, and values are expressed as a percentage of fibroblast HGF secretion treated with basal-like cell-CM **(D, E)**. $^*p < 0.05$.

total collagen and α-SMA-expressing cells in bleomycin-injured rat lung. In line with our data, other studies showed that PGE_2 mediates antifibrotic effects, primarily by inhibiting fibroblast proliferation, migration, collagen synthesis, and moreover, limiting lung myofibroblast differentiation (Bozyk and Moore 2011; Epa et al., 2015; Mukherjee et al., 2019). However, in a mixture of different mediators as in a conditioned medium, it seems difficult to appoint all effects to a single mediator, which is supported by our data showing that recombinant PGE2 failed to upregulate MMP-1. Furthermore, Col1A1 expression was reduced not only by recombinant PGE2 but also by several other recombinant cytokines.

In contrast to our findings, a recent pre-print reported enhanced collagen and α-SMA in lung fibroblasts treated with airway basal cell-derived CM (Jaeger et al., 2020). However, these putative contrasting findings likely arise from the use of different sampling locations. Basal cells reported in the pre-print were obtained by bronchial brushings, while we cultured the cells from peripheral lung tissue. Importantly, this may indicate that basal cells display differential characteristics and functional properties depending on their location within the lung.

It is important to mention that basal cells in the human lung represent a heterogenous cell population including multipotent, proliferating, or differentiating basal cells (Carraro et al., 2020; Travaglini et al., 2020), as well as the recently described fibrosis-enriched KRT5-/KRT17 + basaloid cells (Adams et al., 2020; Habermann et al., 2020). Cultured basal-like cells used in our experiments unlikely represent the newly described aberrant basaloid cells as they, in contrast to aberrant basaloid cells (Adams et al., 2020; Habermann et al., 2020), express high levels of KRT5. Furthermore, due to the low number of aberrant basaloid cells within fibrotic tissue and their specific location on the surface of fibroblastic foci (Adams et al., 2020; Habermann et al., 2020), the culture method described here seems insufficient to culture such a rare cell population. scRNA-seq. analysis demonstrated the presence of basal, differentiating basal, and proliferating basal cells within the cultured cell population. Furthermore, some of the cells showed transcriptional similarities to secretory or ciliated epithelial cells, suggesting spontaneous cell differentiation under the culture conditions described here. We cannot exclude that the secretome of the different basal cell subsets may differ and they, therefore, may contribute distinctly to the CM effects reported here. The use of an

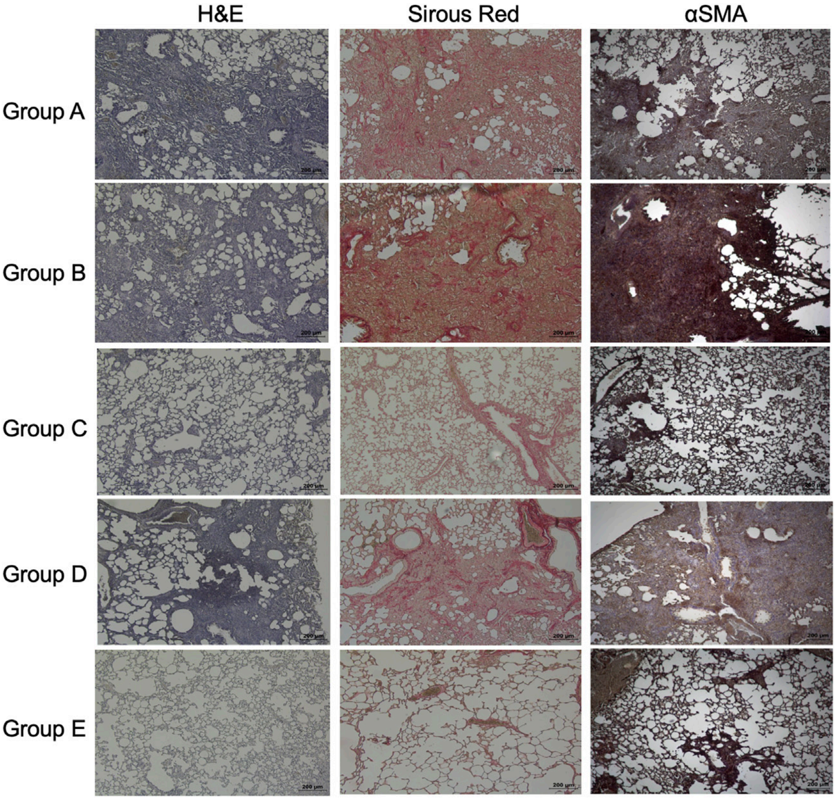

FIGURE 7 | Effects of basal-like cell-CM on lung structure, collagen, or α-SMA in the bleomycin-injured rat lung. H&E staining, Sirus red staining to visualize collagen, or immunohistochemistry of α-SMA in the bleomycin-injured rat lung in group (A–E). All images were taken at day 14 (scale bar 200 μm) (A). Group legends: A, control medium; B, fibroblast-CM; C, basal-like cell-CM; D, basal-like cell-CM + PGE2 inhibitor; and E, basal-like cell-CM+PGE2 isotype control (n = 5; error bars: mean ± SEM; *p = 0.05, and ***p = 0.001).

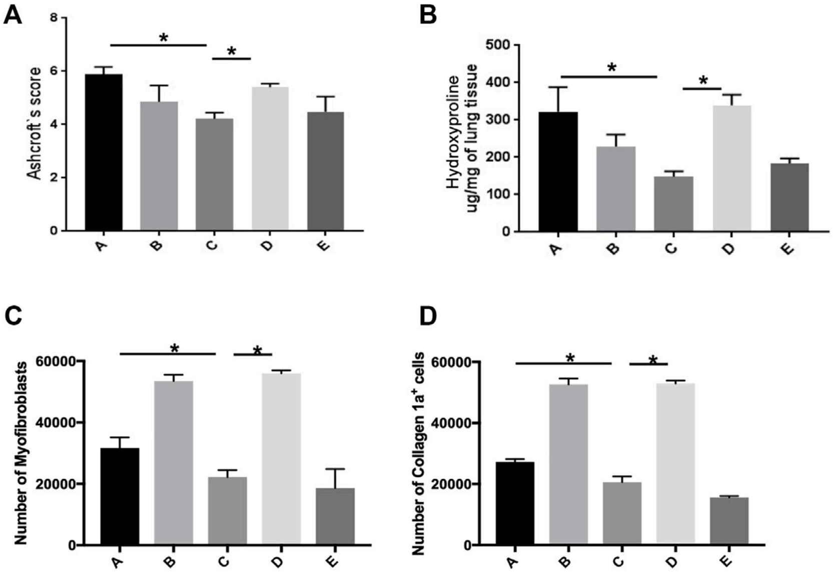

FIGURE 8 | Basal-like cell-CM reduces the Ashcroft score, collagen level, and number of myofibroblasts in bleomycin-injured rat lung. Assessment of lung fibrosis using the Ashcroft scores for grading pulmonary fibrosis 14 days after bleomycin instillation **(A)**. Collagen level as measured by hydroxyproline assay at day 14. ($^*p < 0.05$) **(B)**. Number of myofibroblasts (α-SMA$^+$/vimentin$^+$/desmin$^-$). Stopping gate was set at 30,000 recorded live events at the single cell gate. Dead and doublet cells were excluded from the analysis **(C)**. Number of α-SMA-positive cells producing collagen-1a **(D)**. A total of six groups were used (five rats per group). Group legends: A, control medium; B, fibroblast-CM; C, basal-like cell-CM; D, basal-like cell-CM + PGE2 inhibitor; and E, basal-like cell-CM + PGE2 isotype control (n = 5; error bars: mean ± SEM; *p = 0.05, and ***p = 0.001).

epithelial cell-specific culture medium would likely inhibit spontaneous cell differentiation, but would also limit the use of basal-like conditioned medium on cultured fibroblasts as these cells cannot be cultured in an epithelial cell-specific medium. It is also to consider that the *in vitro* culture of the cells may alter the composition of their secretome and, therefore, not fully reflect the cells' secretome and its effects *in vivo;* importantly, the cells' interaction with their microenvironment is not represented in our *in vitro* model. Furthermore, apart from their paracrine effects, other functional properties such as the cells' differentiation capacity may contribute to their pro- or anti-fibrotic properties. Further studies are, therefore, needed in order to get a full understanding of the cells' functional role in IPF. Furthermore, a seemingly missing validation cohort of basal-like cells grown from non-fibrotic tissue might be a point of criticism. However, we earlier showed that, under standardized cell culture conditions, basal-like cells readily grew from peripheral fibrotic, but only rarely from non-fibrotic tissue (Hostettler et al., 2017), making it difficult to provide a validation cohort of cultured non-fibrotic basal-like cells. Moreover, as a proof-of-concept study, we have used the bleomycin animal model. Although it is the most commonly used preclinical model, it has limitations of not being able to fully represent the human pathology.

Taken together, basal-like cells seem to re-epithelialize the damaged alveolar epithelium to maintain barrier function after severe lung injury. We here show that basal-like cells secrete factors that limit aberrant fibroblast activation. However, despite these beneficial effects, previous data indicate a potential harmful role of basal cells in the pathogenesis of lung fibrosis (Prasse et al., 2019). This discrepancy might be explained by the cells' limited capacity to differentiate into functional AT2 cells, which might hinder normal regeneration of the alveolar epithelium in the long term. Therefore, studying the capacity of basal-like cells to differentiate into functional AT2 cells and how this may be influenced by their specific microenvironment is of utmost interest.

DATA AVAILABILITY STATEMENT

The datasets presented in this study can be found in online repositories. The names of the repository/repositories and accession number(s) can be found in the following: https://www.ncbi.nlm.nih.gov/geo/, GSE145439.

ETHICS STATEMENT

The studies involving human participants were reviewed and approved by the local ethical committee of the University Hospital, Basel, Switzerland (EKBB05/06), and of the Medical University of Hannover, Germany (2699-2015). The patients/participants provided their written informed consent to participate in this study. The animal study was reviewed and approved by the University of Bern Animal Study Committee (BE 135/16).

AUTHOR CONTRIBUTIONS

PK: conception and design of the study, cell culture of human primary lung cells, PCR, ELISA, immunoblotting, data analysis and interpretation, and writing the manuscript; KF: bleomycin-rat model, hydroxyproline assay, FACS, data analysis and interpretation, and revision and editing of the manuscript for important intellectual content; SB: immunofluorescence in cultured cells and IPF tissue slides and revision and editing of the manuscript; JR: data analysis and interpretation of scRNA-seq data and revision and editing of the manuscript for important intellectual content; AG: conception and design of the study, bleomycin-rat model, hydroxyproline assay, histology, data analysis and interpretation, and revision and editing of the manuscript for important intellectual content; SS: paraffin embedding of IPF lung tissue, interpretation of stainings performed on IPF tissue slides, and revision and editing of the manuscript for important intellectual content; LK: provided samples of IPF lung explants and revision and editing of the manuscript; DJ: provided samples of IPF lung explants and revision and editing of the manuscript; MK: provided samples of IPF lung explants and revision and editing of the manuscript; SM: acquisition of the Ashcroft score and data analysis and interpretation; MT: conception and design of the study and revision of the manuscript for important intellectual content; TG: conception and design of the study, data analysis and interpretation, and revision and editing of the manuscript for important intellectual content; and KH: conception and design of the study, cell culture of human primary lung cells, data analysis and interpretation, writing the manuscript, and revision and editing of the manuscript for important intellectual content.

FUNDING

This study was supported by Sinergia (CRSII3.160704) and the project grant (310030_192536) by the Swiss National Research Foundation and a grant from the Swiss Lung Association, as well as a European Research Council Consolidator Grant (XHale, ref. no. 771883 to DJ).

ACKNOWLEDGMENTS

Single-cell RNA-sequencing was performed at the Genomics Facility Basel, ETH Zürich. Calculations were performed at the sciCORE (http://scicore.unibas.ch/) scientific computing center at the University of Basel.

SUPPLEMENTARY MATERIAL

The Supplementary Material for this article can be found online at: https://www.frontiersin.org/articles/10.3389/fbioe.2022.844119/full#supplementary-material.

REFERENCES

Adams, T. S., Schupp, J. C., Poli, S., Ayaub, E. A., Neumark, N., Ahangari, F., et al. (2020). Single-cell RNA-Seq Reveals Ectopic and Aberrant Lung-Resident Cell Populations in Idiopathic Pulmonary Fibrosis. *Sci. Adv.* 6, eaba1983. doi:10.1126/sciadv.aba1983

Bagnato, G., and Harari, S. (2015). Cellular Interactions in the Pathogenesis of Interstitial Lung Diseases. *Eur. Respir. Rev.* 24, 102–114. doi:10.1183/09059180.00003214

Barkauskas, C. E., Cronce, M. J., Rackley, C. R., Bowie, E. J., Keene, D. R., Stripp, B. R., et al. (2013). Type 2 Alveolar Cells Are Stem Cells in Adult Lung. *J. Clin. Invest.* 123, 3025–3036. doi:10.1172/jci68782

Bozyk, P. D., and Moore, B. B. (2011). Prostaglandin E2and the Pathogenesis of Pulmonary Fibrosis. *Am. J. Respir. Cel Mol Biol* 45, 445–452. doi:10.1165/rcmb.2011-0025rt

Carraro, G., Mulay, A., Yao, C., Mizuno, T., Konda, B., Petrov, M., et al. (2020). Single-Cell Reconstruction of Human Basal Cell Diversity in Normal and Idiopathic Pulmonary Fibrosis Lungs. *Am. J. Respir. Crit. Care Med.* 202, 1540–1550. doi:10.1164/rccm.201904-0792oc

Chilosi, M., Poletti, V., Murer, B., Lestani, M., Cancellieri, A., Montagna, L., et al. (2002). Abnormal Re-epithelialization and Lung Remodeling in Idiopathic Pulmonary Fibrosis: The Role of ΔN-p63. *Lab. Invest.* 82, 1335–1345. doi:10.1097/01.lab.0000032380.82232.67

Epa, A. P., Thatcher, T. H., Pollock, S. J., Wahl, L. A., Lyda, E., Kottmann, R. M., et al. (2015). Normal Human Lung Epithelial Cells Inhibit Transforming Growth Factor-β Induced Myofibroblast Differentiation via Prostaglandin E2. *PLoS One* 10, e0135266. doi:10.1371/journal.pone.0135266

Fernanda de Mello Costa, M., Weiner, A. I., and Vaughan, A. E. (2020). Basal-like Progenitor Cells: A Review of Dysplastic Alveolar Regeneration and Remodeling in Lung Repair. *Stem Cel Rep.* 15, 1015–1025. doi:10.1016/j.stemcr.2020.09.006

Habermann, A. C., Gutierrez, A. J., Bui, L. T., Yahn, S. L., Winters, N. I., Calvi, C. L., et al. (2020). Single-cell RNA Sequencing Reveals Profibrotic Roles of Distinct Epithelial and Mesenchymal Lineages in Pulmonary Fibrosis. *Sci. Adv.* 6, eaba1972. doi:10.1126/sciadv.aba1972

Hostettler, K. E., Gazdhar, A., Khan, P., Savic, S., Tamo, L., Lardinois, D., et al. (2017). Multipotent Mesenchymal Stem Cells in Lung Fibrosis. *PLoS One* 12, e0181946. doi:10.1371/journal.pone.0181946

Jaeger, B., Schupp, J. C., Plappert, L., Terwolbeck, O., Kayser, G., Engelhard, P., et al. (2020). Airway Basal Cells Show a Dedifferentiated KRT17^{high}Phenotype and Promote Fibrosis in Idiopathic Pulmonary Fibrosis. *bioRxiv.* doi:10.1101/2020.09.04.283408

Knudsen, L., Ruppert, C., and Ochs, M. (2017). Tissue Remodelling in Pulmonary Fibrosis. *Cell Tissue Res* 367, 607–626. doi:10.1007/s00441-016-2543-2

Kumar, P. A., Hu, Y., Yamamoto, Y., Hoe, N. B., Wei, T. S., Mu, D., et al. (2011). Distal Airway Stem Cells Yield Alveoli *In Vitro* and during Lung Regeneration Following H1N1 Influenza Infection. *Cell* 147, 525–538. doi:10.1016/j.cell.2011.10.001

Lambers, C., Qi, Y., Eleni, P., Costa, L., Zhong, J., Tamm, M., et al. (2014). Extracellular Matrix Composition Is Modified by β2-agonists through cAMP in COPD. *Biochem. Pharmacol.* 91, 400–408. doi:10.1016/j.bcp.2014.07.026

Mukherjee, S., Sheng, W., Michkov, A., Sriarm, K., Sun, R., Dvorkin-Gheva, A., et al. (2019). Prostaglandin E2 Inhibits Profibrotic Function of Human Pulmonary Fibroblasts by Disrupting Ca2+ Signaling. *Am. J. Physiology-Lung Cell Mol. Physiol.* 316, L810–l821. doi:10.1152/ajplung.00403.2018

Prasse, A., Binder, H., Schupp, J. C., Kayser, G., Bargagli, E., Jaeger, B., et al. (2019). BAL Cell Gene Expression Is Indicative of Outcome and Airway Basal Cell Involvement in Idiopathic Pulmonary Fibrosis. *Am. J. Respir. Crit. Care Med.* 199, 622–630. doi:10.1164/rccm.201712-2551oc

Raghu, G., Collard, H. R., Egan, J. J., Martinez, F. J., Behr, J., Brown, K. K., et al. (2011). An Official ATS/ERS/JRS/ALAT Statement: Idiopathic Pulmonary Fibrosis: Evidence-Based Guidelines for Diagnosis and Management. *Am. J. Respir. Crit. Care Med.* 183, 788–824. doi:10.1164/rccm.2009-040gl

Raghu, G., Remy-Jardin, M., Myers, J. L., Richeldi, L., Ryerson, C. J., Lederer, D. J., et al. (2018). Diagnosis of Idiopathic Pulmonary Fibrosis. An Official ATS/ERS/JRS/ALAT Clinical Practice Guideline. *Am. J. Respir. Crit. Care Med.* 198, e44–e68. doi:10.1164/rccm.201807-1255st

Ray, S., Chiba, N., Yao, C., Guan, X., McConnell, A. M., Brockway, B., et al. (2016). Rare SOX2 + Airway Progenitor Cells Generate KRT5 + Cells that Repopulate Damaged Alveolar Parenchyma Following Influenza Virus Infection. *Stem Cel Rep.* 7, 817–825. doi:10.1016/j.stemcr.2016.09.010

Rock, J. R., Randell, S. H., and Hogan, B. L. M. (2010). Airway Basal Stem Cells: a Perspective on Their Roles in Epithelial Homeostasis and Remodeling. *Dis. Models Mech.* 3, 545–556. doi:10.1242/dmm.006031

Seidel, P., Merfort, I., Hughes, J. M., Oliver, B. G. G., Tamm, M., and Roth, M. (2009). Dimethylfumarate Inhibits NF-Kb Function at Multiple Levels to Limit Airway Smooth Muscle Cell Cytokine Secretion. *Am. J. Physiology-Lung Cell Mol. Physiol.* 297, L326–L339. doi:10.1152/ajplung.90624.2008

Seidel, P., Roth, M., Ge, Q., Merfort, I., S'ng, C. T., and Ammit, A. J. (2011). I B Glutathionylation and Reduced Histone H3 Phosphorylation Inhibit Eotaxin and RANTES. *Eur. Respir. J.* 38, 1444–1452. doi:10.1183/09031936.00129610

Selman, M., King, T. E., and Pardo, A. (2001). Idiopathic Pulmonary Fibrosis: Prevailing and Evolving Hypotheses about its Pathogenesis and Implications for Therapy. *Ann. Intern. Med.* 134, 136–151. doi:10.7326/0003-4819-134-2-200101160-00015

Smirnova, N. F., Schamberger, A. C., Nayakanti, S., Hatz, R., Behr, J., and Eickelberg, O. (2016). Detection and Quantification of Epithelial Progenitor Cell Populations in Human Healthy and IPF Lungs. *Respir. Res.* 17, 83. doi:10.1186/s12931-016-0404-x

Tamò, L., Simillion, C., Hibaoui, Y., Feki, A., Gugger, M., Prasse, A., et al. (2018). Gene Network Analysis of Interstitial Macrophages after Treatment with Induced Pluripotent Stem Cells Secretome (iPSC-Cm) in the Bleomycin Injured Rat Lung. *Stem Cel Rev Rep* 14, 412–424. doi:10.1007/s12015-017-9790-9

Taylor, M. S., Chivukula, R. R., Myers, L. C., Jeck, W. R., Waghray, A., Tata, P. R., et al. (2018). A Conserved Distal Lung Regenerative Pathway in Acute Lung Injury. *Am. J. Pathol.* 188, 1149–1160. doi:10.1016/j.ajpath.2018.01.021

Travaglini, K. J., Nabhan, A. N., Penland, L., Sinha, R., Gillich, A., Sit, R. V., et al. (2020). A Molecular Cell Atlas of the Human Lung from Single-Cell RNA Sequencing. *Nature* 587, 619–625. doi:10.1038/s41586-020-2922-4

Vaughan, A. E., Brumwell, A. N., Xi, Y., Gotts, J. E., Brownfield, D. G., Treutlein, B., et al. (2015). Lineage-negative Progenitors Mobilize to Regenerate Lung Epithelium after Major Injury. *Nature* 517, 621–625. doi:10.1038/nature14112

Xi, Y., Kim, T., Brumwell, A. N., Driver, I. H., Wei, Y., Tan, V., et al. (2017). Local Lung Hypoxia Determines Epithelial Fate Decisions during Alveolar Regeneration. *Nat. Cel Biol* 19, 904–914. doi:10.1038/ncb3580

Xia, J., Minamino, S., Kuwabara, K., and Arai, S. (2019). Stem Cell Secretome as a New Booster for Regenerative Medicine. *Bst* 13, 299–307. doi:10.5582/bst.2019.01226

Xu, Y., Mizuno, T., Sridharan, A., Du, Y., Guo, M., Tang, J., et al. (2017). Single-cell RNA Sequencing Identifies Diverse Roles of Epithelial Cells in Idiopathic Pulmonary Fibrosis. *JCI Insight* 1, e90558. doi:10.1172/jci.insight.90558

Yang, Y., Riccio, P., Schotsaert, M., Mori, M., Lu, J., Lee, D.-K., et al. (2018). Spatial-Temporal Lineage Restrictions of Embryonic P63+ Progenitors Establish Distinct Stem Cell Pools in Adult Airways. *Dev. Cel* 44, 752–761. doi:10.1016/j.devcel.2018.03.001

Yuan, T., Volckaert, T., Redente, E. F., Hopkins, S., Klinkhammer, K., Wasnick, R., et al. (2019). FGF10-FGFR2B Signaling Generates Basal Cells and Drives Alveolar Epithelial Regeneration by Bronchial Epithelial Stem Cells after Lung Injury. *Stem Cel Rep.* 12, 1041–1055. doi:10.1016/j.stemcr.2019.04.003

Zuo, W., Zhang, T., Wu, D. Z. A., Guan, S. P., Liew, A.-A., Yamamoto, Y., et al. (2015). p63+Krt5+ Distal Airway Stem Cells Are Essential for Lung Regeneration. *Nature* 517, 616–620. doi:10.1038/nature13903

Conflict of Interest: The authors declare that the research was conducted in the absence of any commercial or financial relationships that could be construed as a potential conflict of interest.

frontiers
in Bioengineering and Biotechnology

ORIGINAL RESEARCH
published: 09 March 2022
doi: 10.3389/fbioe.2022.834267

GMP-Compliant Production of Autologous Adipose-Derived Stromal Cells in the NANT 001 Closed Automated Bioreactor

*Joan C. Fitzgerald[1†], Niamh Duffy[1†], Giacomo Cattaruzzi[2], Francesco Vitrani[2], Alice Paulitti[2], Flavia Mazzarol[2], Prisca Mauro[2], Antonio Sfiligoj[2], Francesco Curcio[3], Deirdre M. Jones[4], Veronica McInerney[5], Janusz Krawczyk[6], Jack Kelly[7], Andrew Finnerty[8], Katya McDonagh[8], Una McCabe[8], Matthew Duggan[8], Lauren Connolly[8], Georgina Shaw[1], Mary Murphy[1] and Frank Barry[1]**

[1]Regenerative Medicine Institute (REMEDI), National University of Ireland Galway, Galway, Ireland, [2]VivaBioCell S.p.A., Udine, Italy, [3]Dipartimento di Area Medica (DAME), University of Udine, Udine, Italy, [4]Department of Plastic and Reconstructive Surgery, Roscommon University Hospital, Galway, Ireland, [5]HRB Clinical Research Facility, National University of Ireland Galway, Galway, Ireland, [6]Department of Haematology, Galway University Hospital, Galway, Ireland, [7]Department of Plastic and Reconstructive Surgery, Galway University Hospital, Galway, Ireland, [8]Centre for Cell Manufacturing Ireland, National University of Ireland Galway, Galway, Ireland

Edited by:
Anna Lange-Consiglio,
University of Milan, Italy

Reviewed by:
Xinli Zhang,
University of California, Los Angeles, United States
Philippe Bourin,
Independent Researcher, Toulouse, France

***Correspondence:**
Frank Barry
frank.barry@nuigalway.ie

†These authors have contributed equally to this work and share first authorship

Specialty section:
This article was submitted to Tissue Engineering and Regenerative Medicine, a section of the journal Frontiers in Bioengineering and Biotechnology

Received: 13 December 2021
Accepted: 14 February 2022
Published: 09 March 2022

Citation:
Fitzgerald JC, Duffy N, Cattaruzzi G, Vitrani F, Paulitti A, Mazzarol F, Mauro P, Sfiligoj A, Curcio F, Jones DM, McInerney V, Krawczyk J, Kelly J, Finnerty A, McDonagh K, McCabe U, Duggan M, Connolly L, Shaw G, Murphy M and Barry F (2022) GMP-Compliant Production of Autologous Adipose-Derived Stromal Cells in the NANT 001 Closed Automated Bioreactor. Front. Bioeng. Biotechnol. 10:834267. doi: 10.3389/fbioe.2022.834267

In recent years mesenchymal stromal cells (MSCs) have received a great deal of interest for the treatment of major diseases, but clinical translation and market authorization have been slow. This has been due in part to a lack of standardization in cell manufacturing protocols, as well as a lack of biologically meaningful cell characterization tools and release assays. Cell production strategies to date have involved complex manual processing in an open environment which is costly, inefficient and poses risks of contamination. The NANT 001 bioreactor has been developed for the automated production of small to medium cell batches for autologous use. This is a closed, benchtop system which automatically performs several processes including cell seeding, media change, real-time monitoring of temperature, pH, cell confluence and cell detachment. Here we describe a validation of the bioreactor in an environment compliant with current good manufacturing practice (cGMP) to confirm its utility in replacing standardized manual processing. Stromal vascular fraction (SVF) was isolated from lipoaspirate material obtained from healthy donors. SVF cells were seeded in the bioreactor. Cell processing was performed automatically and cell harvesting was triggered by computerized analysis of images captured by a travelling microscope positioned beneath the cell culture flask. For comparison, the same protocol was performed in parallel using manual methods. Critical quality attributes (CQA) assessed for cells from each process included cell yield, viability, surface immunophenotype, differentiation propensity, microbial sterility and endotoxin contamination. Cell yields from the bioreactor cultures were comparable in the manual and automated cultures and viability was >90% for both. Expression of surface markers were consistent with standards for adipose-derived stromal cell (ASC) phenotype. ASCs expanded in both automated and manual processes were capable of adipogenic and osteogenic differentiation. Supernatants from all cultures tested negative for microbial and endotoxin contamination. Analysis of labor commitment indicated considerable economic advantage in the automated system in terms of operator, quality control, product release and management personnel. These data demonstrate that the NANT 001 bioreactor represents an effective option for small to medium scale, automated, closed expansion of ASCs from SVF and produces cell products with CQA equivalent to manual processes.

Keywords: mesenchymal stromal cells, automation, GMP—good manufacturing practice, autologous, bioreactor

INTRODUCTION

Mesenchymal stromal cells (MSCs) have attracted a great deal of interest in recent years because of their therapeutic potential in addressing a number of major diseases. The MSC as a cellular entity was first described almost 5 decades ago by Friedenstein and others, who isolated the cells from rat bone marrow and showed that they were capable of supporting haematopoiesis. The MSC as a therapeutic entity was proposed by Caplan et al. some 3 decades ago (Wakitani et al., 1994), and the first MSC investigative treatment of patients was reported in 1995 (Lazarus et al., 1995).

Despite the long history of investigation and large numbers of clinical trials either underway or completed, the number of market authorizations is still low. Although many early phase clinical trials are listed in registries, only a tiny fraction of these proceed to later stage testing and then fewer still receive approval. There are many reasons for this lack of progression of a successful pipeline and foremost amongst these is the challenge associated with standardized and consistent manufacturing as well as the lack of biologically meaningful cell characterization tools and standard release assays. It goes without saying that highly controlled manufacturing processes are essential to ensure that variability between batches is minimal. This has been one of the extraordinary flaws in the MSC field—cell expansion protocols have generally relied on manual processing in an open environment with a great deal of intrinsic variability including cell source, initial isolation, expansion media, use of supplements etc. (Kirouac and Zandstra, 2008). Although MSCs are widely used as an allogeneic product, there is strong interest in autologous application and many trials of autologous MSCs are listed in NIH clinical trials registry. These include applications in cardiac failure (Noiseux et al., 2016; Hare et al., 2017; Barry, 2019), renal transplantation (US National Library of Medicine, 2021a), ALS (US National Library of Medicine, 2021b) as well as a number of trials currently underway to test the effectiveness of autologous MSC treatment in acute respiratory distress associated with SARS-CoV-2.

In the production of MSCs for autologous use, the impact of processing variables is more acute than in allogeneic use. It is imperative that standardized, highly controlled and automated processing solutions are employed. Here we provide one solution to address the manufacturing bottleneck, namely the use of the highly automated NANT 001 bioreactor, developed for automated production of small to medium scale cell batches. It is a benchtop-sized, closed system which automatically performs several processes including cell seeding, media changes, real-time monitoring of temperature, pH, imaging and estimating cell confluency. Our interest was in providing a validation of the NANT 001 bioreactor in a fully GMP environment to confirm its utility in replacing standardized manual processing. For this purpose, a manual GMP-compliant process was converted to an automated protocol for the expansion of ASCs using the NANT 001 bioreactor. Our intention was to provide a comparison between the two processes to justify adoption of the bioreactor manufacturing system in clinical production.

The result of this study indicated that 1) the NANT 001 bioreactor was fully adaptable for use in regulated GMP-compliant manufacturing, 2) the cell product was comparable to that obtained using conventional methods, 3) the bioreactor provided significant advantages in terms of labor commitment and 4) it significantly reduced the cost of manufacture. Based on these observations we conclude that automated cell expansion using the bioreactor represents a highly significant advantage over conventional manual methods.

MATERIALS AND METHODS

Bioreactor Design

The NANT 001 bioreactor system uses a sterile, single-use cartridge consisting of a 636 cm^2 cell-culture chamber connected in a closed system to a series of bags containing complete culture medium (CCM), wash buffer, detaching agent, cell suspension for seeding, a waste bag and a harvesting bottle. Pinch-tube valves and a peristaltic pump control speed and volume of liquid import and export. The tilt and shake mechanisms of the cell culture chamber ensure homogenous distribution of reagents inside the culture chamber, allow complete emptying of culture medium and promote cell detachment. Continuous monitoring of temperature, pH and cell confluency is performed throughout culture. A web application allows remote monitoring of these critical parameters. For confluency estimation, an integrated, self-operating and auto-focusing microscope acquires images at given intervals. Images are automatically processed by an integrated software for the cell confluency estimation. This can be used to prompt media replenishment at a user-specified confluency or to identify the optimal time for cell harvesting. Automated cell detachment, harvesting and exporting to a collection bottle for preparation of the final formulation is also performed. At the end of the process, a detailed cell culture report file is generated which details all critical parameters and

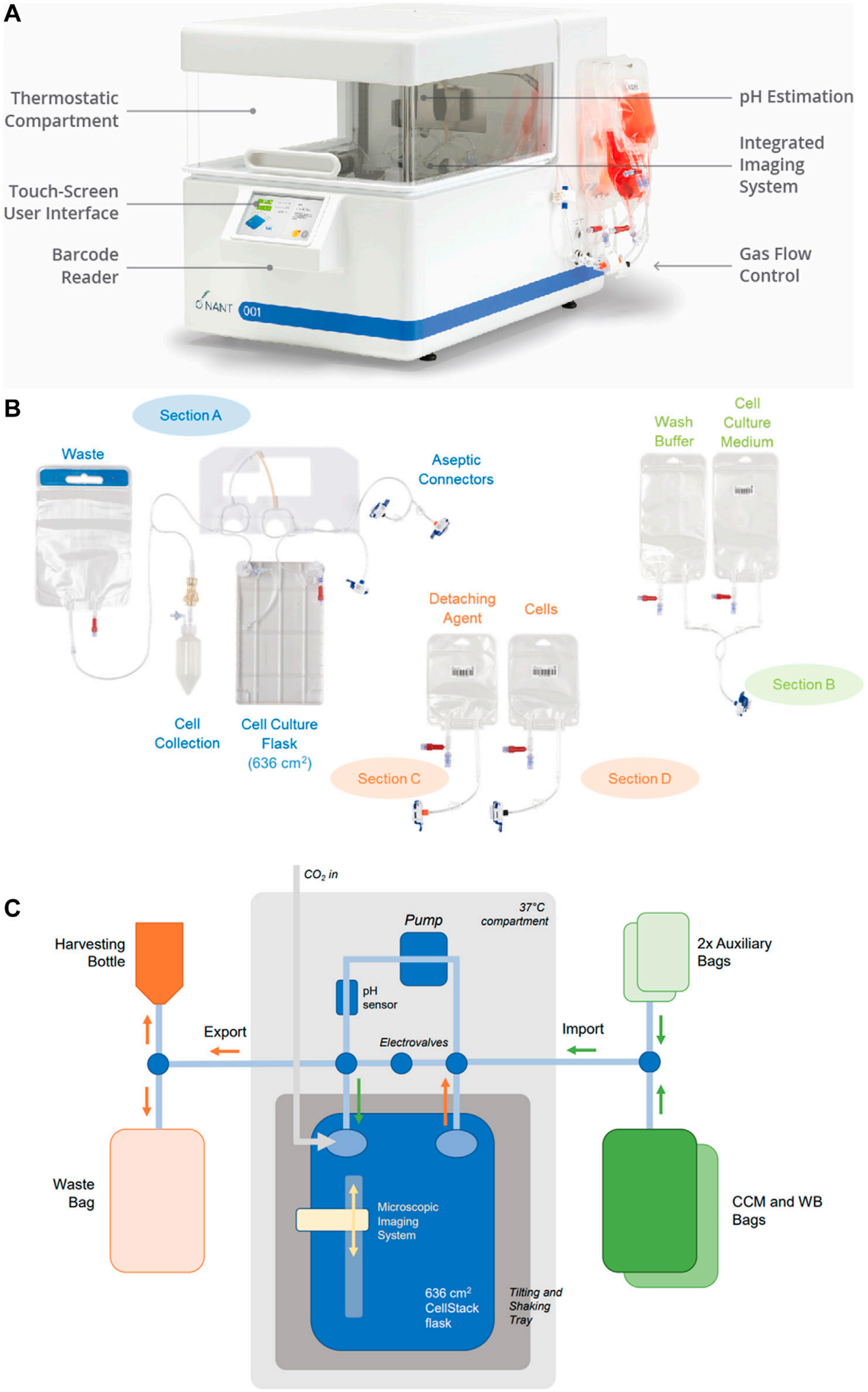

FIGURE 1 | Bioreactor design. **(A)** The closed, automated NANT 001 bioreactor with thermostatically controlled compartment, touch screen interface, barcode reader and with single use fluid reservoirs attached. **(B)** Configuration of the single use components of the bioreactor, comprising of a cell culture flask, reservoirs for storage of media, wash buffer, cells prepared for seeding, detaching agent (typically an enzyme preparation), bag for waste fluids and receptable for collection of the expanded cell population. **(C)** Fluidics design of the NANT 001 bioreactor system incorporating a sterile, single-use cell-culture chamber with a tilt and shake mechanism connected in a closed system to a series of bags containing complete culture medium, wash buffer (WB), detaching agent, cell suspension for seeding, a waste bag and a harvesting bottle. Continuous monitoring of temperature and pH is achieved by the inclusion of sensors. Cell morphology and confluence are monitored using an integrated, self-operating and auto-focusing microscope.

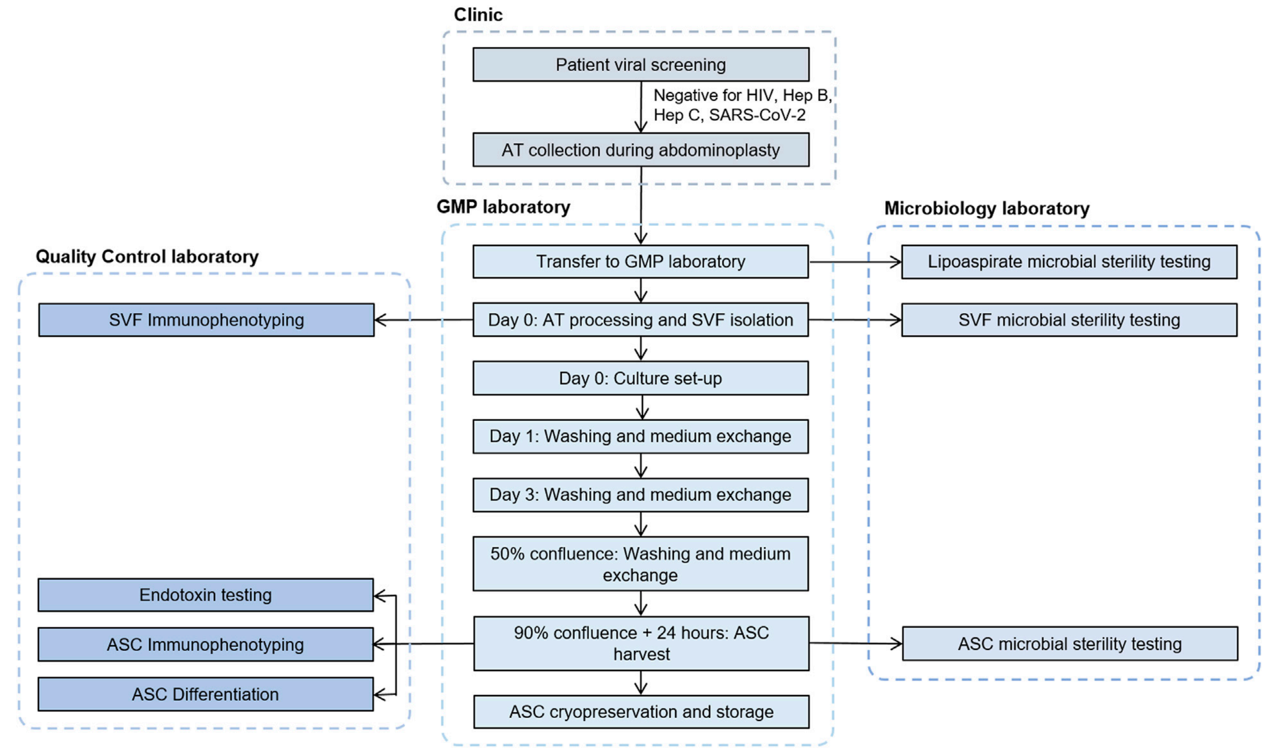

FIGURE 2 | Flowchart describing the process steps and testing involved from donor qualification to cryopreservation of ASCs. ASC, adipose-derived mesenchymal stromal cells; AT, adipose tissue; GMP, good manufacturing practices; SVF, stromal vascular fraction.

operator interactions ensuring complete traceability of the process and any deviations.

The essential design features of the bioreactor are shown in **Figure 1**.

The system design incorporates several features which align with EU guidelines for GMP-compliant advanced therapy medicinal products (ATMP) manufacturing. A description of these features and the relevant sections of “Guidelines on Good Manufacturing Practice specific to Advanced Therapy Medicinal Products”, issued by the European Commission (European Commission, 2017) are given in **Table 1**.

Process

The complete process from patient viral screening and donor selection to ASC cryopreservation and storage is described in detail in **Figure 2**.

Materials

All reagents and materials used for isolation, expansion and cryopreservation of cells were GMP-grade certified. A complete list is provided in **Supplementary Table S1**.

Donor Eligibility Criteria

Waste lipoaspirate tissues were obtained from three healthy donors (two male, one female) aged between 25 and 48, undergoing abdominoplasties at Roscommon University Hospital. The procurement of human tissues was carried out with the approval of the National University of Ireland Research Ethics Committee and the Galway University Hospital Ethics Board. In all cases the donors gave written consent. Before sample processing was initiated the donors were confirmed negative for human immunodeficiency virus (HIV) 1 and 2, hepatitis B, hepatitis C and SARS-CoV-2.

Lipoaspirate Procurement and Isolation of SVF

Liposuction of subcutaneous abdominal adipose tissue was performed under local anaesthesia using the body-jet® system (Human Med AG) to obtain a minimum of 60 ml lipoaspirate from each donor. Aspirates were transported to the manufacturing facility using an insulated transport box (Freetech) at a controlled temperature of between 2 and 8°C and stored at this temperature until processing (<24 h from the time of aspiration). Lipoaspirate was washed with Dulbecco’s phosphate-buffered saline (DPBS) and centrifuged at 340 g for 4 min following which the upper and lower phases were aseptically removed. Adipose tissue was digested by incubation with 0.4 PZ U/ml collagenase NB6 (Nordmark) in Alpha-MEM (Macopharma) at 37°C for 45 min with constant agitation. Enzymatic digestion was stopped by addition of CCM consisting of Alpha-MEM, 5% human platelet lysate (Macopharma) and 1 U/ml heparin (Wockhardt). After homogenization, the digested suspension was passed through 100 µm sterile filters, centrifuged at 600 g for 10 min, resuspended

TABLE 1 | Design features of the NANT 001 bioreactor which align to relevant sections of "Guidelines on Good Manufacturing Practice specific to Advanced Therapy Medicinal Products", issued by the European Commission" (European Commission, 2017).

Section	Content	NANT 001 design feature
9.35	Measures to prevent cross-contamination including: (iii) Use of "closed systems" for processing and material/product transfer between equipment (v) Use of single use disposable technologies	The NANT 001 bioreactor system operates without ever coming into direct contact with cells and reagents using a sterile, single-use, closed-system disposable unit (NANT cartridge)
5.13, 9.44	Connections that are to be made in aseptic conditions should be performed in a critical clean area of grade A with a background clean area of grade B, unless the connection is made by means of a validated sterile system When materials are added/withdrawn from the closed system without an aseptic connection the system can no longer be considered closed	Validated aseptic connectors are used to connect different sections to the cartridge when required, ensuring a closed system is maintained
9.29	Gases taken into the aseptic workplace or that come into contact with the product should be passed through sterilising filters	The NANT Cartridges include a sterile, single-use, disposable 0.22 μm filter for air/CO_2 to be imported to the cell culture container or into the thermostatic compartment
9.41, 17.24	Production in a closed system, in an isolator, or positive pressure isolators: a background clean area of Grade D is acceptable	Expansion of cells within the NANT 001 system occurs in a closed system enabling operation in a Grade D area
4.41	The presence of containers and/or materials liable to generate particles should be minimised in the clean areas	The NANT 001 bioreactor does not include parts that generate particles, nor parts that may spread particles
4.19 (a)	The use of more than one closed isolator (or other closed systems) in the same room at the same time is acceptable, provided that appropriate mitigation measures are taken to avoid cross-contamination or mix-ups of materials, including separated expulsion of the exhausted air from the isolators	The NANT 001 system can be operated exclusively with one NANT Cartridge per run Parallel cultures with two different NANT systems are totally independent
9.70	Critical quality parameters should be monitored at appropriate intervals. When technically possible, continuous monitoring of key process parameters is expected	During automated runs, key parameters pH and temperature are continuously monitored and recorded. Cell confluency is monitored and recorded at user specified intervals At the end of each run, a Cell Culture Report file featuring a summary of critical parameters and operator interactions can be downloaded and archived
	Any deviations should be recorded and investigated, and the measures taken should also be documented	A log file, containing all detailed parameters recorded by the system, can also be downloaded and archived Deviations can be manually traced

in CCM and a mononuclear cell count was obtained using a haemocytometer.

Cell Seeding, Expansion and Harvest

Automated and manual processes were performed in parallel as follows. For the manual process, cells from the SVF were seeded in one 636 cm^2 CellSTACK® culture chamber (Corning) at a density of 4,000 cells/cm^2 in 150 ml CCM and cultured at 37°C in an atmosphere saturated with moisture and 5% CO_2. Washing of the cell monolayer with 150 ml DPBS and complete replacement of CCM was performed at day 1, day 3 and at 50% confluence. ASCs were harvested 24 h after the culture reached 90% confluence according to the following protocol: after aspiration of the medium and washing with DPBS, 50 ml of recombinant TrypLE solution (Gibco) was added for 5 min and incubated at 37°C. TrypLE activity was inhibited by the addition of 150 ml CCM and the cell suspension was collected.

For the automated process, the appropriate bags were filled with DPBS, CCM, TrypLE and SVF cell suspension respectively and connected to the bioreactor system via sterile connectors. The same SVF seeding density and volumes of CCM, DPBS and TrypLE as the manual process were used. Import of the CCM and SVF cells were performed by the bioreactor as well as monitoring of temperature, estimated pH and confluency. The bioreactor automatically performed all washes and media changes as described above during the expansion process. Intervention was required on the harvesting day (24 h after the system had automatically assessed the culture to have reached 90% confluency) to prompt the initiation of cell detachment and harvesting. The system performed cell detachment as described above and exported the suspended cell product to the harvesting bottle.

Samples of cell suspension from each process were taken for cell counting using a haemocytometer and assessment of viability using Trypan blue exclusion. Following counting, cell yields from each process were cryopreserved in aliquots of 2×10^6/ml in 5% human albumin (Octopharma) containing 10% Cryosure-DMSO (Wak-Chemie). Samples of spent media were taken for endotoxin and microbial sterility testing.

Cell Viability and Immunophenotype Using Flow Cytometry

Cell viability was evaluated using the Trypan Blue exclusion method and cells were manually counted under a microscope using a haemocytometer. Flow cytometry was performed to confirm cell identity in accordance with Chapter 2.7.24 of the

European Pharmacopeia. ASCs at passage 0 (P0) were first washed with FACS stain buffer, passed through a 40 μm cell strainer and blocked using BD Human Fc Block™ for 10 min before incubation for 30 min at 4°C with the following fluorochrome-conjugated antibodies: anti-CD45-FITC, anti-CD90-PE, anti-CD73-APC, anti-CD14-FITC, anti-CD105-PE, anti-CD13-APC, anti-CD36-FITC, anti-CD34-PE, anti-CD31-APC. Following staining, cells were washed with stain buffer and re-suspended in 300 μl buffer for acquisition using the CytoFLEX flow cytometer. For viability assessment, cells were also incubated with 7-AAD and the data were analysed with FlowJo software.

Differentiation Assays

The osteogenic and adipogenic propensity of ASCs cultured using automated and manual processes were assessed. For both assays, thawed P0 ASCs were seeded at 2×10^4 cells/cm^2 in 24 well plates and allowed to expand until confluent in ASC culture medium (MEM-alpha, 10% FBS). Osteogenesis was induced via incubation of ASCs in monolayer for 10–17 days in osteogenic medium (Dulbecco's modified Eagle's medium low-glucose [DMEM-LG], 10% FBS, 100 nM dexamethasone, 10 mM β-glycerophosphate, 100 μM ascorbic acid-2-phosphate), while control cultures were maintained in ASC culture medium. The level of osteogenesis was assessed by staining deposited calcium with alizarin red and quantification of calcium using the Stanbio Calcium (CPC) LiquiColor® Test. Adipogenesis was performed by incubation of ASCs in monolayer for 3 days with adipogenic induction medium (Dulbecco's modified Eagle's medium high-glucose [DMEM-HG], 10% FBS, 1 μM dexamethasone, 500 μM methyl-isobutylxanthine, 10 μg/ml insulin and 200 μM indomethacin), followed by a 1 day incubation in adipogenic maintenance medium (DMEM-HG, 10% FBS and 10 μg/ml insulin). ASCs were subjected to three rounds of this cycle, with the final maintenance cycle lasting 5–7 days. Control cultures were maintained in ASC culture medium. The level of adipogenesis was assessed by staining lipid deposits with Oil Red O. The stain was then extracted via incubation with isopropanol and measured spectrophotometrically at 520 nm for quantification.

Bacterial and Endotoxin Contamination Testing

Bacterial contamination was assessed using the Bactec FX40 system in accordance with methodology recommendations of Chapter 2.6.27 of the European Pharmacopeia (Ph. Eur.). Cell supernatants were collected and 3 ml of each were inoculated in aerobic and anaerobic culture bottles for up to 7 days. The absence of bacterial growth was considered a negative result. The presence of endotoxin was analysed from the supernatant of cell cultures following harvest using the limulus amoebocyte lysate (LAL) test. Measurements were performed in accordance with the instructions of Chapter 2.6.14 of the European Pharmacopeia. Values of ≤1 EU/ml were considered negative for endotoxin contamination.

Media Fill

As part of the process validation, three aseptic processing 'media fill' runs were also performed. All solutions and reagents used in the manufacturing process were replaced by Tryptic Soy Broth (TSB) and all aseptic manipulations including filling of the bags, cell seeding, washes, media changes and harvesting were simulated with the incubation time reduced to 1 day. Sampling activities were carried out as performed for normal routine production (representative samples taken to simulate endotoxin and microbial sampling) with the additional inclusion of the waste bag which was sealed off using a heat sealer and the cell suspension bottle.

ASC Specifications

Stringent in-process controls were set up to control the critical steps of cell expansion from receipt of lipoaspirate tissue to the final end product (P0 ASCs harvested from the bioreactor). This set of specifications was established to ensure GMP compliance and to determine if ASCs produced by the bioreactor were equivalent to those produced during traditional manual processing. Prior to tissue procurement, serological testing was performed on donors to ensure absence of hepatitis B, C and HIV. Maintenance of the lipoaspirate between +2°C and +8°C during transport was required. A minimum weight of 60 g of harvested adipose tissue was specified with processing taking place within 24 h of harvest. A minimum weight of 20 g of processed adipose tissue was required following centrifugation in order to proceed with tissue digestion. Following isolation of SVF, specifications included a cell count of $\geq 15 \times 10^6$ cells and a surface immunophenotype as follows: CD45 and CD14 <80% and CD34 ≥5%, while expression levels of CD31, CD90 and CD73 were not specified. Release criteria of the final product were defined as a yield of $\geq 20 \times 10^6$ cells from the bioreactor, with a cellular viability ≥80%. The specified percentage of cells positive for mesenchymal markers (CD90, CD73, CD105) was ≥90% and for hematopoietic markers (CD45 and CD14) ≤5%. There was no specification for expression levels of CD13, CD31, CD34 and CD36. Supernatants of the cell culture had to return a negative result in tests for microbial contamination and have an endotoxin level of ≤1 EU/ml. Finally, cells had to demonstrate the capacity to differentiate to both adipogenic and osteogenic lineages. These specifications are summarized in **Table 2**.

Labor Commitment and Cost-Effectiveness Analysis

A cost-effectiveness analysis was performed to compare the cost of an open manual manufacturing process with an automated process using the NANT 001 system for the production of an autologous MSC-based therapy. The analysis was based on the following assumptions: 300 working days per year, a production team consisting of two manufacturing technicians, one quality control technician and one Qualified Person (all FTE), one Class A/B cleanroom facility available and a production process of 8 ± 1 days resulting in the production of 130 batches per year. Upstream, downstream and all manual expansion processes were performed in a Grade A/B cleanroom with the bioreactors operating in a Grade D area. All relevant

TABLE 2 | Specifications and in process controls for starting material, SVF and final cell product.

Process steps	Test parameters	Analytical method	Specifications	Eur. Ph. Reference
Donor validation	Donor serological testing	PCR	Negative for Hepatitis B, C, HIV, SARS-CoV-2	n/a
Receipt of adipose tissue at the manufacturing site	Weight of adipose tissue	Weight	>60 g	n/a
	Temperature during transport	Temperature tracker	Between +2°C and +8°C	n/a
	Duration of time between harvest and processing of tissue	Monitor time	<24 h	n/a
	Weight of pure adipose tissue (following centrifugation)	Weight	>20 g	n/a
Isolation of SVF	Cell count	Haemocytometer	$\geq 15 \times 10^6$ cells	Eur. Ph. 2.7.29
	$CD34^+$	Flow cytometry	≥5%	Eur. Ph. 2.7.24
	$CD45^+$	Flow cytometry	<80%	Eur. Ph. 2.7.24
	$CD14^+$	Flow cytometry	<80%	Eur. Ph. 2.7.24
	$CD31^+$	Flow cytometry	Not specified	Eur. Ph. 2.7.24
	$CD73^+$	Flow cytometry	Not specified	Eur. Ph. 2.7.24
	$CD90^+$	Flow cytometry	Not specified	Eur. Ph. 2.7.24
Final product (P0 ASCs)	Cell count	Haemocytometer + trypan blue	$\geq 20 \times 10^6$ cells	Eur. Ph. 2.7.29
	Viability	Trypan blue, 7AAD	≥80%	n/a
	$CD90^+$	Flow cytometry	≥90%	Eur. Ph. 2.7.24
	$CD73^+$	Flow cytometry	≥90%	Eur. Ph. 2.7.24
	CD105+	Flow cytometry	≥90%	Eur. Ph. 2.7.24
	$CD45^+$	Flow cytometry	≤5%	Eur. Ph. 2.7.24
	$CD14^+$	Flow cytometry	≤5%	Eur. Ph. 2.7.24
	$CD13^+$	Flow cytometry	Not specified	Eur. Ph. 2.7.24
	$CD31^+$	Flow cytometry	Not specified	Eur. Ph. 2.7.24
	$CD34^+$	Flow cytometry	Not specified	Eur. Ph. 2.7.24
	$CD36^+$	Flow cytometry	Not specified	Eur. Ph. 2.7.24
	Microbial testing	Bactec	Negative	Eur. Ph. 2.6.27
	Endotoxin testing	LAL Test	≤1 EU/ml	Eur. Ph. 2.6.14

Abbreviations: Eur. Ph. (European Pharmacopoeia); PCR (polymerase chain reaction); HIV (human immunodeficiency virus); SVF (stromal vascular fraction); ASCs (adipose-derived mesenchymal stromal cells); 7AAD (7-Aminoactinomycin D); qPCR (quantitative polymerase chain reaction); LAL (limulus amoebocyte lysate).

manufacturing costs including the expansion phase and all upstream and downstream processes were calculated and compared. Costs analyzed included fixed costs, both direct (facility, Capex, maintenance and inspection) and indirect (running costs, administration overheads, insurance etc.) and direct variable costs including labour (manufacturing, QC and QA/QP), consumables, reagents, cleaning and QC tests.

Based on the same assumptions, an analysis of the labor commitment required to support the automated production of a patient batch using the NANT 001 system compared to an equivalent manual production process was performed. Working hours for manufacturing technicians, quality control technician and Qualified Person were calculated per batch for both automated and manual processes.

RESULTS

Research Validation

Prior to execution of the validation runs in the GMP facility, a series of expansion runs were first carried out in a process development/research laboratory to permit training of validation scientists and the generation of batch manufacturing records and standard operating procedures. These runs were conducted using the same protocol as those carried out under GMP conditions, except cells were harvested at 90% confluency. Three research validation runs were performed using pre-expanded ASCs at passage 1. Following harvest, cell viability, sterility, differentiation capacity and surface immunophenotype were assessed. In brief, cells cultured using both automated and manual processes demonstrated the characteristic fibroblast-like morphology of ASCs and cell yields were comparable from both cultures. Viability was not affected by the bioreactor process with >96% cell viability recorded from all three runs. Supernatants from all cultures tested negative for microbial contamination. Expression of surface markers in all cases was consistent with standards published by the International Federation for Adipose Therapeutics and Science (IFATS) and the International Society for Cellular Therapy (ISCT) for ASC characterization (Bourin et al., 2013). There were no significant differences in the adipogenic and osteogenic differentiation propensity of the cells regardless of the expansion process (data not shown).

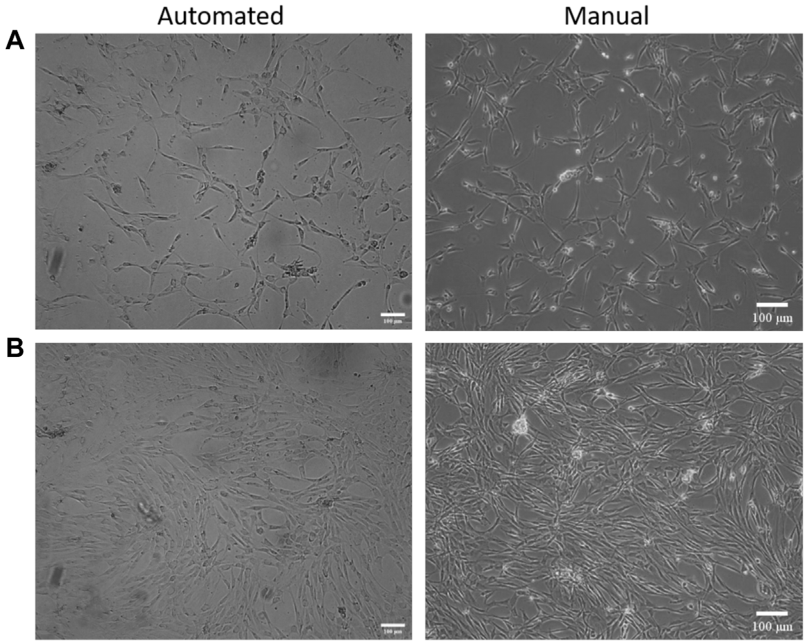

Validation Run	Process	Days in culture	Viable cell count (total no.)	Cell viability (%)
1	Automated	7	25.8 x 10^6	90.7
	Manual	6	15.8 x 10^6	97.5
2	Automated	9	29.3 x 10^6	96.5
	Manual	8	30.0 x 10^6	96.6
3	Automated	7	20.8 x 10^6	94.5
	Manual	6	28.4 x 10^6	91.1

FIGURE 3 | Expansion characteristics of ASCs. Representative phase contrast images of cell morphology at **(A)** 50% and **(B)** 90% confluency respectively for automated and manual processes. **(C)** Expansion characteristics of cells from automated and manual processes for each validation run. Scale bar = 100 μm.

GMP Validation

Expansion of ASCs From Automated and Manual Processes

ASCs cultured in both automated and manual processes displayed the typical fibroblastic morphology associated with ASCs (**Figures 3A,B**). The number of days in culture ranged from 7–9 days for the automated process and 6–8 days for the manual process. This is likely due to loading the SVF suspension into the NANT 001 bag, where some loss of SVF suspension in residual space of the tubing occurs. Cell yields from the automated processes (average $2.5 \times 10^7 \pm 7.8 \times 10^6$) were comparable to those from the manual process ($2.5 \times 10^7 \pm 4.3 \times 10^6$) and cell viability was >90% for all cultures (**Figure 3C**).

Immunophenotype of ASCs From Automated and Manual Processes

ASC immunophenotypes were consistent with the IFATS and ISCT standard. Surface marker expression profiles were almost identical between expansion processes (**Figure 4A**). More than 90% of ASCs from both processes were positive for CD73, CD90, CD105 and CD13. Expression of CD36 varied between donors but was consistent between processes, approximately 20–60% of cells expressed CD36. Expression of the standard negative markers CD31, CD45 and CD14 was less than 1% in all cases.

Sterility Tests

Microbial tests for aerobic and anaerobic bacteria from automated and manual cultures were all negative. Endotoxin concentration was assessed for automated cultures only and was <1 EU/ml for all cell preparations (**Figure 4B**).

Differentiation Potential of ASCs

ASCs expanded using both automated and manual processes were tested for their osteogenic and adipogenic differentiation propensity. ASCs from all three validation runs were capable of osteogenic and adipogenic differentiation (**Figures 4C,D**).

Labor Commitment and Cost-Effectiveness Analysis

Cost-effectiveness analysis of the automated process demonstrated an overall cost reduction of 50% compared to equivalent manual processing, based on the production of 130 batches per year (**Figure 5**). Reductions in variable, fixed and personnel costs were 32, 67 and 55% respectively. A detailed breakdown of the cost analysis is given in **Supplementary Table S2**.

Analysis of the labor commitment indicates considerable savings with automated processing in terms of hours of labor per batch, with an overall reduction of 43% over an equivalent manual process (**Figure 6**). Automated feeding reduces the labor burden on production operators by 48%, while the associated reduction in QC testing reduces QC labor by 16%. The reporting performed by the bioreactor decreases the labor required by the Qualified Person by 60%.

DISCUSSION

The production of expanded MSCs from post-natal sources for therapeutic use is a complex process, requiring stringent control of the aseptic environment. In traditional manual processes, that are essentially open, cells and other materials are exposed to the environment. This requires a dedicated and fully GMP-compliant facility with physical infrastructure elements including air exchange, air filtration, barriers and controlled access. In addition, an aseptic processing facility represents a sub-optimal work environment with a risk to operators of fatigue and exposure to repetitive manipulation. It also involves a measurable risk of operator-associated or environmental

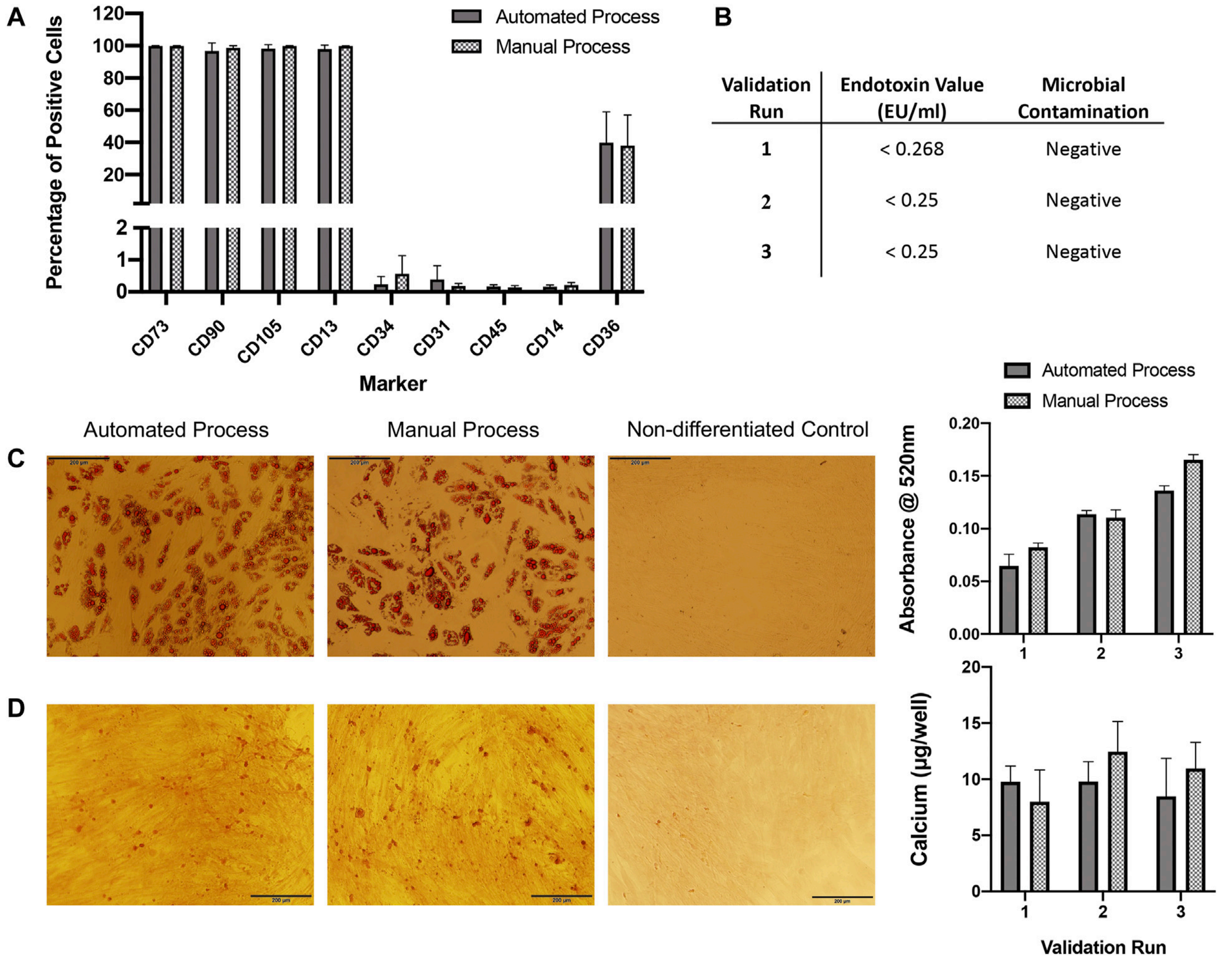

Validation Run	Endotoxin Value (EU/ml)	Microbial Contamination
1	< 0.268	Negative
2	< 0.25	Negative
3	< 0.25	Negative

FIGURE 4 | QC analysis. **(A)** Flow cytometry immunophenotyping of ASCs expanded in automated or manual processes over three validation runs (*n* = 3). Expression is shown as percentage positive cells. Results are expressed as mean ± SEM. **(B)** ASCs expanded in both automated and manual cultures tested negative for microbial contamination. Endotoxin concentration was assessed in automated cultures only and was <1 EU/ml for all. **(C)** ASCs expanded using the automated and manual processes were capable of undergoing adipogenic differentiation for all three validation runs, representative images of oil red O staining in automated and manual process test samples and a control (non-differentiated) sample are shown. Semi-quantification of oil red O staining by measurement of absorbance at 520 nm was performed, results are expressed as mean ± SEM. Magnification = ×10, scale bar = 200 μm. **(D)** ASCs expanded using the automated and manual processes were capable of undergoing osteogenic differentiation for all three validation runs, a representative image of alizarin red staining in automated and manual process test samples and a control sample are shown. Calcium quantification was performed for each validation run, results are expressed as mean ± SEM. Magnification = ×10, scale bar = 200 μm. Calcium deposition was not detected in control wells (data not shown).

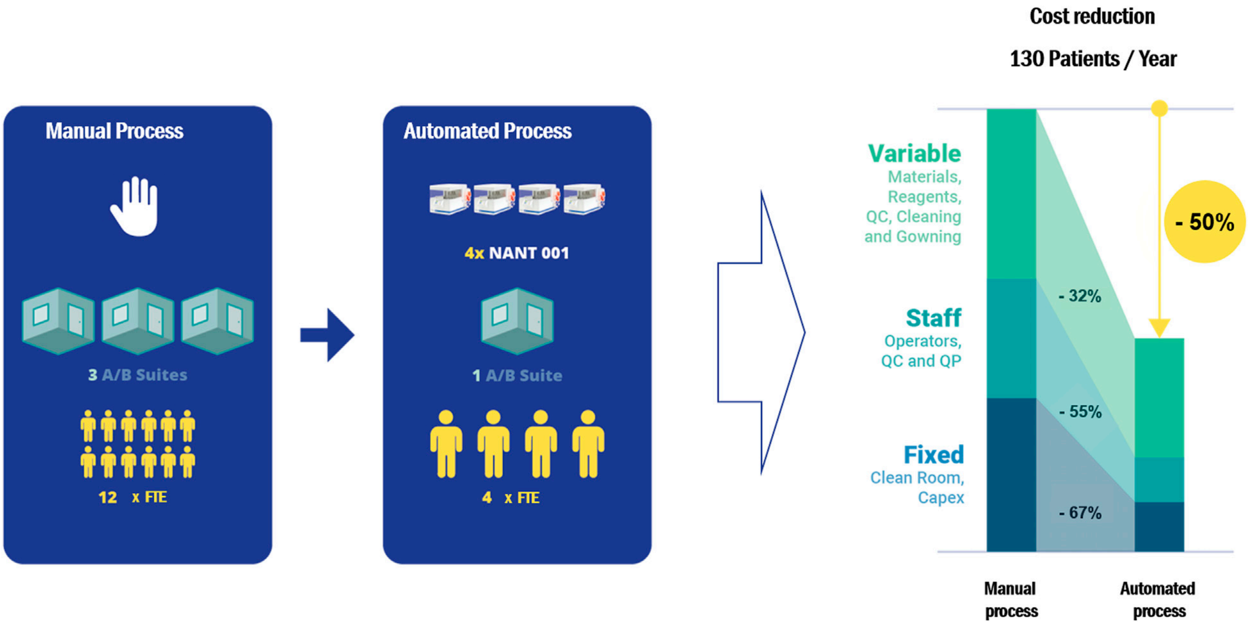

FIGURE 5 | A cost-effectiveness analysis comparing the cost of a manual expansion process with an automated process using the NANT 001 system to produce 130 batches of an autologous ASC therapy per year. The following assumptions were applied: personnel consists of a production team of two manufacturing technicians, one QC technician and one Qualified Person (all FTE), one Class A/B cleanroom facility available and a production process of 7 ± 1 days. Upstream, downstream and all manual expansion processes would be performed in a Grade A/B cleanroom with the bioreactors operating in a Grade D area. All relevant manufacturing costs including direct and indirect fixed costs and direct variable costs for the expansion phase and all upstream and downstream processes were calculated and compared.

contamination. As the manufacture of cell therapy products increases dramatically, these considerations become critically important. In this context, the advantage of a fully closed expansion system is self-evident in terms of product safety and operational convenience.

Several automated systems have been developed and marketed in recent years for MSC expansion, incorporating a wide array of bioreactor configurations. These include the Quantum Cell Expansion System, a closed automated hollow-fibre bioreactor developed by Terumo which has been widely used for the large-scale expansion of MSCs (Rojewski et al., 2013; Russell et al., 2018). This system provides advantages in terms of process scalability and is adaptable to a range of different cell types, viral vectors and exosomes. For adherent cells however, an attachment factor is required, the selection of which can greatly affect the cell yield (Frank et al., 2019), while harvesting of expanded adherent cells from the hollow fibre material may be quite challenging. Furthermore, the scale of this system precludes its use in autologous manufacturing.

The CliniMACS Prodigy® developed by Miltenyi Biotec consists of a closed system of interlinked bioreactors and bioprocessors designed for large-scale end-to-end production (Zhu et al., 2018). They offer two platform configurations, the T-Cell Transduction Process for the automated generation of engineered T cells, primarily chimeric antigen receptor (CAR)-T cells (Miltenyi Biotec, 2020a). The Adherent Cell Culture System, is an all-in-one solution which can perform isolation of MSCs from bone marrow by density gradient centrifugation, cell expansion, subculture and harvesting (Miltenyi Biotec, 2020b). However, for small-scale ASC manufacturing, this may represent an overly complex and expensive manufacturing solution given the high cost of associated consumables (Dai et al., 2019).

The Cocoon system presented by Lonza provides a more compact solution for end-to-end production in a manner which, similar to the NANT 001, accommodates scale out with application at the point of care (Byrne, 2020). The platform is customizable, with multiple functional modules including isolation, cell selection, activation, transduction and expansion (Lonza, 2021b). Lonza have recently reported the treatment of four patients with B-cell malignancies using CD19 autologous CAR-T cells expanded using the Cocoon platform (Lonza, 2021a). This is potentially a very useful solution for the expansion of MSCs but its wide adoption at this time is unclear.

Another bioreactor option that is widely used is the Xuri Cell Expansion System W25 from Cytiva, a closed, automated system based on WAVE™ rocking technology (Cytiva, 2021). It has been primarily used for the large-scale production of suspension cells such as T cells, CAR-T cells and natural killer cells (Smith, 2020) but has also been tested for the expansion of adherent cell types including MSCs on microcarriers or in aggregates (Tsai et al., 2017; Davis et al., 2018).

The NANT 001 solution is ideally scaled for autologous use making it suitable for use in a distributed manufacturing model. It has been designed to perfectly reproduce manual cell culture

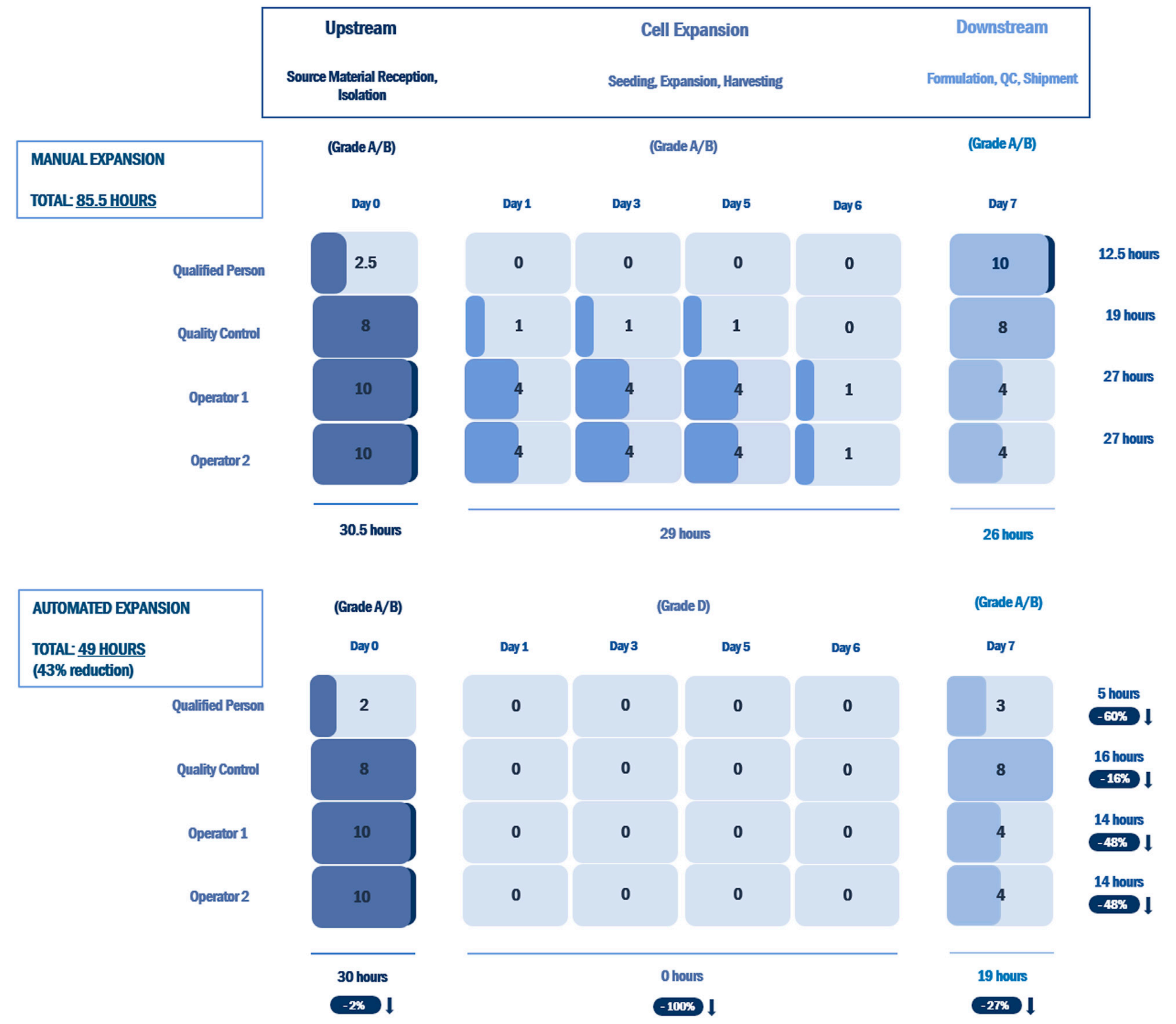

	Upstream	Cell Expansion				Downstream	
	Source Material Reception, Isolation	Seeding, Expansion, Harvesting				Formulation, QC, Shipment	
MANUAL EXPANSION TOTAL: 85.5 HOURS	(Grade A/B)	(Grade A/B)				(Grade A/B)	
	Day 0	Day 1	Day 3	Day 5	Day 6	Day 7	
Qualified Person	2.5	0	0	0	0	10	12.5 hours
Quality Control	8	1	1	1	0	8	19 hours
Operator 1	10	4	4	4	1	4	27 hours
Operator 2	10	4	4	4	1	4	27 hours
	30.5 hours	29 hours				26 hours	

AUTOMATED EXPANSION TOTAL: 49 HOURS (43% reduction)	(Grade A/B)	(Grade D)				(Grade A/B)	
	Day 0	Day 1	Day 3	Day 5	Day 6	Day 7	
Qualified Person	2	0	0	0	0	3	5 hours - 60% ↓
Quality Control	8	0	0	0	0	8	16 hours - 16% ↓
Operator 1	10	0	0	0	0	4	14 hours - 48% ↓
Operator 2	10	0	0	0	0	4	14 hours - 48% ↓
	30 hours - 2% ↓	0 hours - 100% ↓				19 hours - 27% ↓	

FIGURE 6 | Labor commitment analysis comparing an open, manual expansion process with an automated expansion process using the NANT 001 system for an autologous therapy with a production process of 7 ± 1 days. Results are presented as hours of labor required per batch by a production team consisting of two manufacturing technicians, one QC technician and one Qualified Person for all upstream, downstream and expansion processes. The percentage reductions in hours of labor for the automated expansion process vs. the manual process are indicated.

processes (Paulitti et al., 2020), is compatible with all standard culture reagents and does not require the use of attachment factors for MSCs, enabling an easy translation of manual processes to an automated expansion process incorporating the system. The imaging system is a unique feature which provides visual feedback to the operator and constant monitoring of the culture. At the end of the process, complete traceability of all operations and events is guaranteed through the generation of a detailed cell culture report.

The results of this study provide several interesting findings: 1) the NANT 001 bioreactor is capable of producing ASCs with identical phenotype and yield compared to standard manual processing; 2) the bioreactor is fully compatible with a GMP environment; 3) it eliminates a large number of manual processing steps, greatly reducing the labor burden per patient batch and the risk of contamination; 4) it provides valuable real time analytical information on cell health, growth and morphology; 5) it contributes to a significant reduction of cost of goods.

A number of critical quality parameters have been suggested for cell therapy products, including product identity, purity and safety (Robb et al., 2019). The cells isolated and produced by the NANT 001 bioreactor in this study were in accordance with these critical quality attributes in that cell viability was >90%, surface marker expression profiles were consistent with IFATS standards (Bourin et al., 2013), cells were free from microbial and endotoxin contamination and were capable of differentiating towards the adipogenic and osteogenic lineages.

Finally, being a completely automated and closed system, the NANT 001 can be effortlessly operated in a Grade D environment, and utilised in a multiplex configuration, with several instruments operating in parallel increasing the efficiency of the facility and process workflow, and ultimately resulting in a reduction of cell therapy manufacturing costs. All these results confirm the ability of the NANT 001 System in conducting automated ASC expansions, meeting all the GMP requirements in terms of safety, traceability and reproducibility in a cost-effective manner.

DATA AVAILABILITY STATEMENT

The original contributions presented in the study are included in the article/**Supplementary Material**, further inquiries can be directed to the corresponding author.

AUTHOR CONTRIBUTIONS

JF and ND performed isolation and expansion of ASCs from lipoaspirate samples, ASC characterization and manuscript writing. VM facilitated lipoaspirate procurement and DJ, JKr, and JKe provided the lipoaspirate material. AF, KM, LC, MD, and UM provided GMP support and ASC quality control analysis. GS and MM provided cell manufacturing support. AP, GC, FV, PM, AS, and FC contributed to protocol optimization and set-up, provided technical support for use of the NANT 001 bioreactor and reviewed the manuscript. FB provided production management and wrote the manuscript. All authors approved the publication of this work.

FUNDING

The study was financially supported by Science Foundation Ireland (Grant Number 16/RI/3759). Funding was received from the European Union’s Horizon 2020 research and innovation program under grant agreement numbers 874671 (AutoCRAT), 667932 (ADIPOA2) and 761214-2 (Starstem). The work was also supported by a grant from VivaBioCell S.p.A. under the ARTE Project of the European Union’s Interreg V-A Italy Slovenia (2014–2020).

SUPPLEMENTARY MATERIAL

The Supplementary Material for this article can be found online at: https://www.frontiersin.org/articles/10.3389/fbioe.2022.834267/full#supplementary-material

REFERENCES

Barry, F. (2019). MSC Therapy for Osteoarthritis: An Unfinished Story. *J. Orthop. Res.* 37 (6), 1229–1235. doi:10.1002/jor.24343

Bourin, P., Bunnell, B. A., Casteilla, L., Dominici, M., Katz, A. J., March, K. L., et al. (2013). Stromal Cells from the Adipose Tissue-Derived Stromal Vascular Fraction and Culture Expanded Adipose Tissue-Derived Stromal/stem Cells: a Joint Statement of the International Federation for Adipose Therapeutics and Science (IFATS) and the International Society for Cellular Therapy (ISCT). *Cytotherapy* 15 (6), 641–648. doi:10.1016/j.jcyt.2013.02.006

Byrne, J. (2020). *Lonza Hails ‘significant Milestone’ as First Lymphoma Patient Treated with Cocoon CAR-T System*. [Online]. Available: https://www.biopharma-reporter.com/Article/2020/09/09/Lonza-hails-significant-milestone-as-first-lymphoma-patient-treated-with-Cocoon-CAR-T-system?utm_source=copyright&utm_medium=OnSite&utm_campaign=copyright (Accessed October 26, 2021).

Cytiva (2021). *Xuri Cell Expansion System W25*. [Online]. Available: https://www.cytivalifesciences.com/en/us/shop/cell-therapy/systems/xuri-cell-expansion-system-w25-p-06192 (Accessed November 4, 2021).

Dai, X., Mei, Y., Cai, D., and Han, W. (2019). Standardizing CAR-T Therapy: Getting it Scaled up. *Biotechnol. Adv.* 37 (1), 239–245. doi:10.1016/j.biotechadv.2018.12.002

Davis, B. M., Loghin, E. R., Conway, K. R., and Zhang, X. (2018). Automated Closed-System Expansion of Pluripotent Stem Cell Aggregates in a Rocking-Motion Bioreactor. *SLAS TECHNOLOGY: Translating Life Sci. Innovation* 23 (4), 364–373. doi:10.1177/2472630318760745

European Commission (2017). *EudraLex the Rules Governing Medicinal Products in the European Union Volume 4 Good Manufacturing Practice Guidelines on Good Manufacturing Practice Specific to Advanced Therapy Medicinal Products*. [Online]. Available: https://ec.europa.eu/health/sites/default/files/files/eudralex/vol-4/2017_11_22_guidelines_gmp_for_atmps.pdf (Accessed October 26, 2021).

Frank, N. D., Jones, M. E., Vang, B., and Coeshott, C. (2019). Evaluation of Reagents Used to Coat the Hollow-Fiber Bioreactor Membrane of the Quantum Cell Expansion System for the Culture of Human Mesenchymal Stem Cells. *Mater. Sci. Eng. C* 96, 77–85. doi:10.1016/j.msec.2018.10.081

Hare, J. M., DiFede, D. L., Rieger, A. C., Florea, V., Landin, A. M., El-Khorazaty, J., et al. (2017). Randomized Comparison of Allogeneic versus Autologous Mesenchymal Stem Cells for Nonischemic Dilated Cardiomyopathy. *J. Am. Coll. Cardiol.* 69 (5), 526–537. doi:10.1016/j.jacc.2016.11.009

Kirouac, D. C., and Zandstra, P. W. (2008). The Systematic Production of Cells for Cell Therapies. *Cell Stem Cell* 3 (4), 369–381. doi:10.1016/j.stem.2008.09.001

Lazarus, H. M., Haynesworth, S. E., Gerson, S. L., Rosenthal, N. S., and Caplan, A. I. (1995). *Ex Vivo* expansion and Subsequent Infusion of Human Bone Marrow-Derived Stromal Progenitor Cells (Mesenchymal Progenitor Cells): Implications for Therapeutic Use. *Bone Marrow Transpl.* 16 (4), 557–564.

Lonza (2021a). *Lonza and Sheba Medical Center Use Cocoon® Platform and Show Successful Clinical Outcomes in Patients Treated with CAR-T Cell Immunotherapy*. [Online]. Available: https://www.lonza.com/news/2021-08-12-15-00 (Accessed November 4, 2021).

Lonza (2021b). *The Next Level in Patient-specific Cell Therapy Manufacturing*. [Online]. Available: https://pharma.lonza.com/technologies-products/cocoon-platform (Accessed November 4, 2021).

Miltenyi Biotec (2020a). *CliniMACS Prodigy® T Cell Transduction Process*. [Online]. Available: https://www.miltenyibiotec.com/_Resources/Persistent/3af55fb5695605fcf01ea988980144b47a3edc24/CliniMACS_Prodigy_T%20Cell_Transduction_flyer.pdf (Accessed November 6, 2021).

Miltenyi Biotec (2020b). *GMP-compliant Human Mesenchymal Stem Cell Expansion Process*. [Online]. Available: https://www.miltenyibiotec.com/_Resources/Persistent/6e5ce7aa3ebb80eae83cca42bd972894413a8428/CliniMACS_Prodigy_ACC_MSC_expansion_Appsheet.pdf (Accessed November 6, 2021).

Noiseux, N., Mansour, S., Weisel, R., Stevens, L.-M., Der Sarkissian, S., Tsang, K., et al. (2016). The IMPACT-CABG Trial: A Multicenter, Randomized Clinical Trial of CD133+ Stem Cell Therapy during Coronary Artery Bypass Grafting for Ischemic Cardiomyopathy. *J. Thorac. Cardiovasc. Surg.* 152 (6), 1582–1588. e1582. doi:10.1016/j.jtcvs.2016.07.067

Paulitti, A., Barchiesi, A., Moretti, M., and Cattaruzzi, G. (2020). *Automated Expansion of Adipose-Derived Mesenchymal Stem Cells (AD-MSCs) with NANT 001 System*. [Online]. Available: https://www.vivabiocell.it/nant001/WHITE-PAPER_Automated-Expansion-of-AD-MSCs-with-NANT-001-System.pdf (Accessed October 26, 2021).

Robb, K. P., Fitzgerald, J. C., Barry, F., and Viswanathan, S. (2019). Mesenchymal Stromal Cell Therapy: Progress in Manufacturing and Assessments of Potency. *Cytotherapy* 21 (3), 289–306. doi:10.1016/j.jcyt.2018.10.014

Rojewski, M. T., Fekete, N., Baila, S., Nguyen, K., Fürst, D., Antwiler, D., et al. (2013). GMP-compliant Isolation and Expansion of Bone Marrow-Derived MSCs in the Closed, Automated Device Quantum Cell Expansion System. *Cel Transpl.* 22 (11), 1981–2000. doi:10.3727/096368912X657990

Russell, A. L., Lefavor, R. C., and Zubair, A. C. (2018). Characterization and Cost-Benefit Analysis of Automated Bioreactor-Expanded Mesenchymal Stem Cells for Clinical Applications. *Transfusion* 58 (10), 2374–2382. doi:10.1111/trf.14805

Smith, T. A. (2020). "CAR-T Cell Expansion in a Xuri Cell Expansion System W25," in *Chimeric Antigen Receptor T Cells: Development and Production*. Editors K. Swiech, K. C. R. Malmegrim, and V. Picanço-Castro. (New York, NY: Springer US), 151–163. doi:10.1007/978-1-0716-0146-4_11:

Tsai, A.-C., Liu, Y., Yuan, X., Chella, R., and Ma, T. (2017). Aggregation Kinetics of Human Mesenchymal Stem Cells under Wave Motion. *Biotechnol. J.* 12, 1600448. doi:10.1002/biot.201600448

US National Library of Medicine (2021a). *ClinicalTrials.gov NCT00658073*. [Online]. Available: https://clinicaltrials.gov/ct2/show/NCT00658073 (Accessed October 26, 2021).

US National Library of Medicine (2021b). *ClinicalTrials.gov NCT02017912*. [Online]. Available: https://clinicaltrials.gov/ct2/show/NCT02017912 (Accessed October 26, 2021).

Wakitani, S., Goto, T., Pineda, S. J., Young, R. G., Mansour, J. M., Caplan, A. I., et al. (1994). Mesenchymal Cell-Based Repair of Large, Full-Thickness Defects of Articular Cartilage. *J. Bone Jt. Surg.* 76 (4), 579–592. doi:10.2106/00004623-199404000-00013

Zhu, F., Shah, N., Xu, H., Schneider, D., Orentas, R., Dropulic, B., et al. (2018). Closed-system Manufacturing of CD19 and Dual-Targeted CD20/19 Chimeric Antigen Receptor T Cells Using the CliniMACS Prodigy Device at an Academic Medical center. *Cytotherapy* 20 (3), 394–406. doi:10.1016/j.jcyt.2017.09.005

Conflict of Interest: GC, FV, AP, FM, PM, and AS were employed by VivaBioCell S.p.A.

The remaining authors declare that the research was conducted in the absence of any commercial or financial relationships that could be construed as a potential conflict of interest.

frontiers | Frontiers in Bioengineering and Biotechnology

ORIGINAL RESEARCH
published: 27 April 2022
doi: 10.3389/fbioe.2022.895998

CD73-Positive Small Extracellular Vesicles Derived From Umbilical Cord Mesenchymal Stem Cells Promote the Proliferation and Migration of Pediatric Urethral Smooth Muscle Cells Through Adenosine Pathway

Shilin Zhang*, Jierong Li, Chunjing Li, Xumin Xie, Jun He, Fengsheng Ling, Bowei Li, Huayan Wu, Zhilin Li and Jianwei Zheng

Department of Urology, Affiliated Foshan Maternity and Child Healthcare Hospital, Southern Medical University, Foshan, China

Edited by:
Anna Lange-Consiglio,
University of Milan, Italy

Reviewed by:
Wei Seong Toh,
National University of Singapore, Singapore
Jafar Rezaie,
Urmia University of Medical Sciences, Iran

****Correspondence:***
Shilin Zhang
zhang_40_1@163.com

Specialty section:
This article was submitted to Tissue Engineering and Regenerative Medicine,
a section of the journal Frontiers in Bioengineering and Biotechnology

Received: *14 March 2022*
Accepted: *11 April 2022*
Published: *27 April 2022*

Citation:
Zhang S, Li J, Li C, Xie X, He J, Ling F, Li B, Wu H, Li Z and Zheng J (2022) CD73-Positive Small Extracellular Vesicles Derived From Umbilical Cord Mesenchymal Stem Cells Promote the Proliferation and Migration of Pediatric Urethral Smooth Muscle Cells Through Adenosine Pathway.
Front. Bioeng. Biotechnol. 10:895998.
doi: 10.3389/fbioe.2022.895998

Smooth muscle cells (SMCs) are the main functional component of urethral tissue, but are difficult to proliferate *in vitro*. Mesenchymal stem cells (MSCs) and mesenchymal stem cell-derived small extracellular vesicles (MSC-sEV) have been shown to promote tissue repair by regulating the proliferation and migration of different types of cells. In this study, we investigated the effect of umbilical cord mesenchymal stem cell-derived sEV (UCMSC-sEV) on the proliferation and migration of pediatric urethral smooth muscle cells (PUSMCs) and the mechanism by which sEV regulates the function of PUSMCs. We observed that UCMSC-sEV can significantly promote the proliferation and migration of PUSMCs *in vitro*. UCMSC-sEV exerted proliferation and migration promotion effects by carrying the CD73 to PUSMCs and catalyzing the production of adenosine. Conversely, the effect of UCMSC-sEV on the proliferation and migration of PUSMCs were no longer observed with addition of the PSB12379 as a CD73 inhibitor. It was found that the phosphatidylinositol 3-kinase (PI3K)/protein kinase B (AKT) signaling pathway in PUSMCs was activated by adenosine or UCMSC-sEV intervention. In summary, UCMSC-sEV promoted proliferation and migration of PUSMCs *in vitro* by activating CD73/adenosine signaling axis and downstream PI3K/AKT pathway. Thus, we concluded that UCMSC-sEV may be suggested as a new solution strategy for the urethral tissue repair.

Keywords: mesenchymal stem cells, small extracellular vesicles, smooth muscle cells, hypospadias, CD73, proliferation, migration

INTRODUCTION

Hypospadias is one of the most common developmental malformation of reproductive organs in male children (Chan et al., 2020) and surgery remains the only treatment in clinical. However, the surgery is associated with postoperative complications such as urinary fistula and penile curvature, mainly due to the lack of protection by smooth muscle cells (SMCs) in the formed urethra (Arenas et al., 2014; Abbas et al., 2017). Smooth muscle is the main functional component of the urethra, and SMCs are terminally differentiated cells. Once damaged, smooth muscle is difficult to regenerate

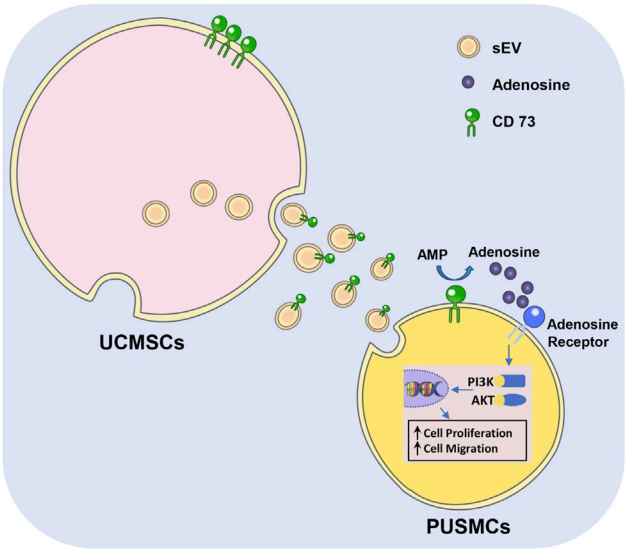

GRAPHICAL ABSTRACT | Graphical diagram of CD73/Adenosine/PI3K/AKT axis in facilitating cell proliferation and migration of PUSMCs *in vitro*.

(Sergeant et al., 2019). Some researchers have attempted to obtain primary SMCs and then proliferate the cells *in vitro* (Ning et al., 2010). However, the *in vitro* proliferation capacity of SMCs is limited, hindering their application in the field of tissue engineering (Li et al., 2016).

Mesenchymal stem cells (MSCs) are a type of adult stem cells, which were first discovered in the bone marrow, and subsequently found in many kinds of tissues during the occurrence and development of the human body. They can differentiate not only into mesoderm, but can also differentiate into endoderm and neuroectoderm-derived cells, and can be targeted to differentiate into various terminal functional cells, such as muscle cells, osteocyte, vascular cells, endothelial cells, and nerve cells, under specific conditions (Galipeau and Sensebe, 2018). MSCs have obtained increasing attention as seed cells for tissue engineering (Gao et al., 2021; Rajasingh et al., 2021). In addition, MSCs can also promote the repair of various tissue injuries through direct intercellular contact and paracrine factors such as cytokines, growth factors, and small extracellular vesicles (sEV) (Keshtkar et al., 2018; Xia et al., 2019).

Umbilical cord mesenchymal stem cells (UCMSCs) are easy to collect, have strong proliferative ability and low immunogenicity, and that secreted sEV are often used in regenerative medicine and the treatment of various diseases (Ding et al., 2015; Can et al., 2017). UCMSC-derived sEV (UCMSC-sEV) are tiny vesicles with a diameter of 30–150 nm secreted by UCMSCs. As a carrier of intercellular communication cargo, UCMSC-sEV enter target cells and regulate a variety of physiological processes including cell proliferation, differentiation, migration and apoptosis (Fu et al., 2019; Keshtkar et al., 2018; Wu et al., 2018; Yaghoubi et al., 2019). However, whether UCMSC-sEV can promote the proliferation and migration of pediatric urethral smooth muscle cells (PUMSCs) and the related molecular mechanisms are still unclear. This study explored the potential molecular mechanisms that affect the functions of PUMSCs.

METHODS

Isolation and Culture of PUSMCs

This experiment was approved by the Ethics Committee of the Maternal and Child Health Hospital of Foshan, and informed consent was obtained from the donors. Pediatric urethral tissues were collected from patients with hypospadias. The urethral tissues were cut into small pieces using surgical scissors and transferred to centrifuge tubes. A five-fold volume of 1 mg/ml type II collagenase (Sigma) was added into the tubes, and the tissue was digested at 37°C for 4 h. After filtration through a 70-mesh cell sieve (NEST, China), the cells were cultured in SMC complete medium (ScienCell, United States). When the cells were cultured to 80% confluency, they were digested with 0.25% trypsin (Gibco, United States) and seeded into a new culture dish. After the cells adhered to the dishes for 0.5–1 h, the supernatant was then transferred to a new culture dish, and the above process was repeated. Multiple passages of purified PUSMCs were obtained through this procedure.

Human UCMSC Culture

UCMSCs were purchased from Cyagen Biosciences Inc. (Guangzhou, China) and were cultured in the complete MSC medium (Cyagen, China) supplemented with 10% fetal bovine serum (FBS). Cells were passaged at a ratio of 1:2.

Cell Identification

The third and sixth passages of PUSMCs were seeded into 96-well plates. Six wells were stained with cell counting kit-8 (CCK-8) at the same time every day and then analyzed on a microplate reader (MK3, Thermo). The results were recorded, and a growth curve was plotted. After the sixth passage, the PUSMCs were washed, permeabilized and blocked with goat serum, and fluorescein isothiocyanate (FITC)-labeled α-smooth muscle actin (α-SMA) monoclonal antibody (Bioss, China) was added; the cells were incubated overnight in a 4°C refrigerator in the dark. Then, the cells were counterstained with 4′,6-diamidino-2-phenylindole (DAPI). The expression of SMA-α, a marker for SMCs, was observed under an inverted fluorescence microscope.

Surface markers of UCMSCs were detected by a flow cytometry assay. UCMSCs were incubated with fluorescently labeled CD29, CD44, CD45, CD73, CD90, and human leucocyte antigen DR (HLA-DR) monoclonal antibodies (Biolegend, United States) for half an hour, and the results were analyzed using a CytoFLEX flow cytometer (Beckman Coulter, United States).

Extraction, Purification and Identification of sEV

The FBS used for cell culture was spun at 100,000 g overnight to remove the existing serum EVs. UCMSCs at passages four to eight were cultured in sEV-free medium for 48 h, and the cell supernatant was collected. sEV were isolated using ultracentrifugation and purified using a sEV purification reagent and concentration system (Exojuice, WeinaBio, China). Cell conditioned medium was collected and centrifuged at 300 g for 20 min to remove cells and centrifuged at 10,000 g for 20 min to remove cell debris. Supernatants were transferred into ultracentrifugation tubes and centrifuged at 100, 000 g for 70 min in order to obtain a pellet enriched in sEV. The precipitates were suspended in PBS and purified by Exojuice Kit at 100,000 g for 70 min in accordance with the protocol provided by the manufacturer. The resultant sEV was stored at −80°C.

sEV characterization was performed following the International Society for Extracellular Vesicles guidelines (Thery et al., 2018; Witwer et al., 2019). Briefly, the morphology of isolated sEV samples were visualized using transmission electron microscopy (TEM), and the particle size and concentration of sEV were analyzed by NanoFCM analysis. The sEV specific proteins, including CD9, CD63, CD81 and tumor susceptibility 101 (TSG101), were analyzed by Western blot.

CCK-8 Assay

PUSMCs were seeded in 96-well plates at a density of 5,000 cells/well/100 μL. After 12 h of culture, medium containing UCMSC-sEV with or without PSB12379 (a CD73 inhibitor) was added to cells. After 24 and 48 h of culture, 10 μL of CCK-8 reagent was added, and the cells were incubated at 37°C for 1.5 h. Then a microplate reader (Thermo MK3, United States) was used to measure the absorbance at 450 nm.

EdU Incorporation Assay

PUSMCs were seeded in 6-well plates at a density of 5×10^5 cells/well. After 12 h of culture, medium containing UCMSC-sEV was added, and the culture was continued for 12 h. Then, the cells were treated with 5-ethynyl-2′-deoxyuridine (EdU) solution (Beyotime, China) for 2 h and then incubated in click reaction solution at 37°C for 30 min in the dark. The cells were stained following the instructions provided with the EdU solution and then imaged under a fluorescence microscope to calculate the percentage of EdU-positive cells.

Scratch Wound Assay

A culture insert (Ibidi, Martinsried, Germany) was placed in the middle of a 24-well culture plate. Subsequently, PUSMCs were seeded at a density of 5×10^5/ml per well (70 μL volume). After 24 h, the culture insert was carefully removed, and UCMSC-sEV were added to the PUSMCs for 12 h. Cell migration was imaged using an inverted microscope (Olympus IX 71, 100 × magnification, Olympus, Japan) and analyzed using ImageJ software v1.8 (National Institutes of Health, United States).

Transwell Assay

PUSMCs were resuspended in serum-free medium and then were seeded in the upper chamber of a Transwell at a density of 5×10^5 cells/ml (100 μL volume), and culture medium containing UCMSC-sEV with or without PSB12379 was added to the lower chamber of the Transwell. After 24 h of culture, the cells that had migrated to the lower chamber were counted after fixation and crystal violet staining.

TABLE 1 | Primers used for real-time quantitative reverse transcription-polymerase chain reaction.

Gene	Strand	5–3′ Sequence
β-actin	Sense	GGCATCCACGAAACTACATTCAATTCC
	Anti-sense	GTACCACCAGACAGCACTGTGTTG
CD 73	Sense	TGGGAGCTTACGATTTTGCACACC
	Anti-sense	CGGATCTGCTGAACCTTGGTGAAG

qRT–PCR Assay

Total RNA was extracted using TRIzol reagent (Thermo, United States), and cDNA was synthesized using HiScript® III RT SuperMix for qPCR (+gDNA wiper) (Novvia, China). Quantitative PCR was performed using ChamQ universal SYBR qPCR Master Mix (Novenza, China) to detect the mRNA level of CD73. All gene sequences were obtained through GenBank, and primers were designed using Primer Premier five and synthesized by Sangong Biotech (Shanghai, China). The primer sequences are provided in **Table 1**.

Western Blotting

The protein concentration was determined using a bicinchoninic acid (BCA) reagent kit. Total protein (30 mg) was separated by 10% sodium dodecyl-sulfate polyacrylamide gel electrophoresis (SDS-PAGE) and transferred to a polyvinylidene difluoride (PVDF) membrane (Millipore, United States). The membrane was blocked with 5% skim milk for 2 h and then incubated with a primary antibody (dilution ratio of 1:1,000) at 4°C overnight. After washing with 0.1% Tween® 20 (TBST) 3 times, the corresponding horseradish peroxidase-labeled secondary antibody (dilution ratio of 1:5,000) was added, and the membrane was incubated for 1 h. After washing with TBST 3 times, a chemiluminescence reagent (Tanon, China) was added dropwise to the membrane. Finally, the protein expression was observed using a chemiluminescent imaging system (Tanon, China). The monoclonal antibodies for CD9 and CD81 were from Affinity Biosciences (Affinity, United States). The monoclonal antibodies for TSG101 and CD63 were from Santa Cruz Biotechnology (Santa Cruz, United States). The monoclonal antibodies for CD73 were from Abcam (United Kingdom). The monoclonal antibodies for phospho-AKT, phospho-PI3K and glyceraldehyde-3-phosphate dehydrogenase (GAPDH) were from Bioss Biotechnology (Bioss, China).

Immunofluorescence Staining

The extracted UCMSC-sEV were dissolved in phosphate buffered saline (PBS) containing 2% bovine serum albumin (BSA), followed by incubation with CD73 antibody to obtain

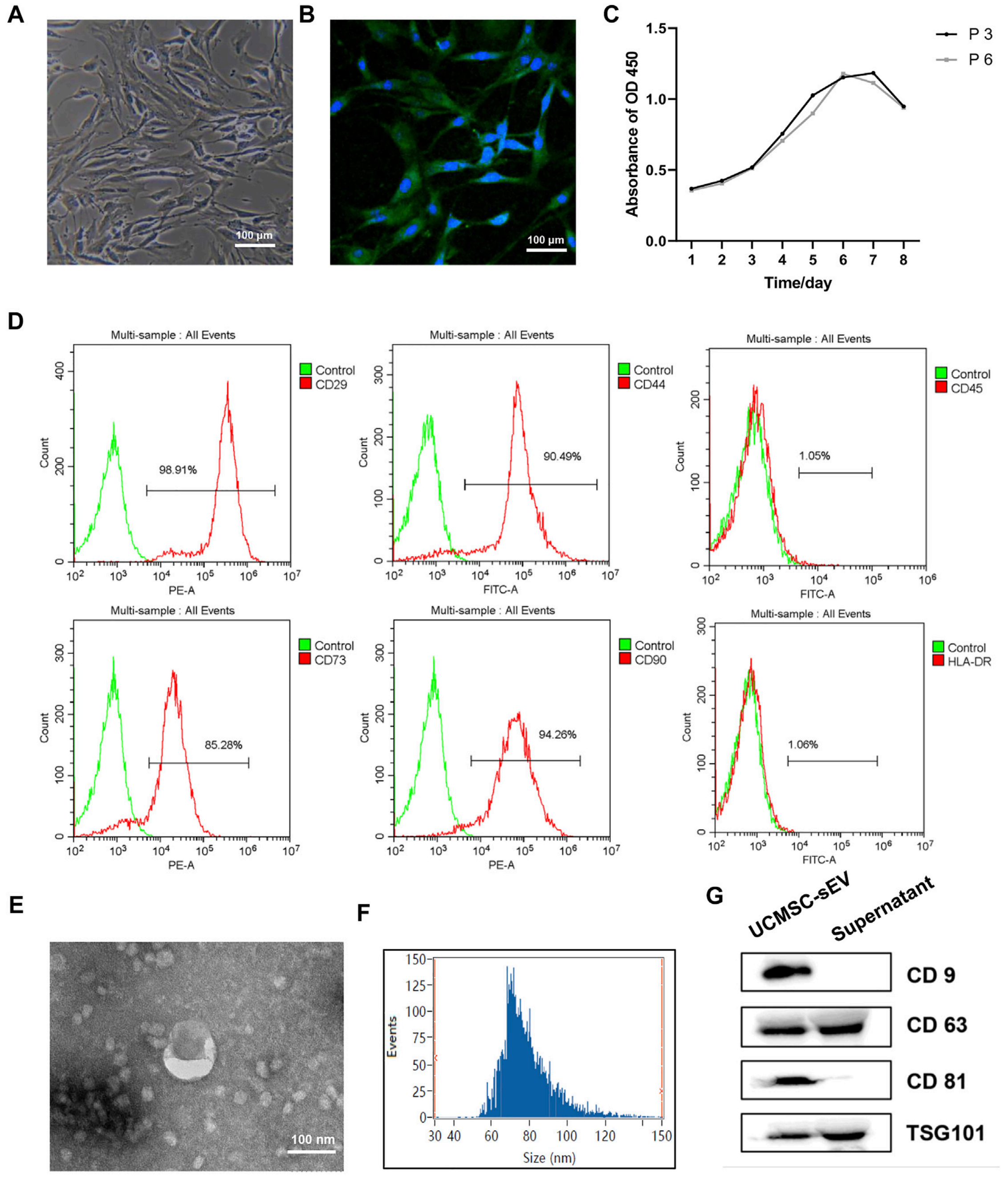

FIGURE 1 | Identification of PUMSCs, UCMSCs and UCMSC-sEV. **(A)** Morphology of PUMSCs. **(B)** Immunofluorescence staining results show that the isolated PUMSCs express α-SMA, a smooth muscle cell surface marker. **(C)** Growth curve of PUMSCs. **(D)** Flow cytometric analysis of MSC surface markers shows that UCMSCs express high levels = of CD29, CD44, CD73, and CD90 but do not express CD45 and HLA-DR. **(E)** Transmission electron microscopy shows that the UCMSC-sEV are cup-shaped vesicles. Scale bar = 100 nm. **(F)** NanoFCM analysis of the particle size of UCMSC-sEV. **(G)** Western blotting was used to detect the expression of the sEV marker proteins CD9, CD63, CD81, and TSG101.

phycoerythrin (PE)-conjugated CD73 sEV. Subsequently, the PE-conjugated CD73 sEV were incubated with PUSMCs at 37°C for 3 h, after which the cells were fixed in 4% paraformaldehyde for 15 min. The cytoskeleton was stained with FITC-phalloidin for 45 min, and the nuclei were stained with DAPI. Fluorescence microscopy was used to detect fluorescence signals in the cells.

Adenosine Assay

PUSMCs were seeded at a density of 50,000 cells/well and cultured in medium with or without 5′AMP (Sigma) and UCMSC-sEV for 4 h. Then, the supernatant was collected and quickly frozen at −80°C. Adenosine concentrations were analyzed using an Adenosine Assay Kit (BioVision) in

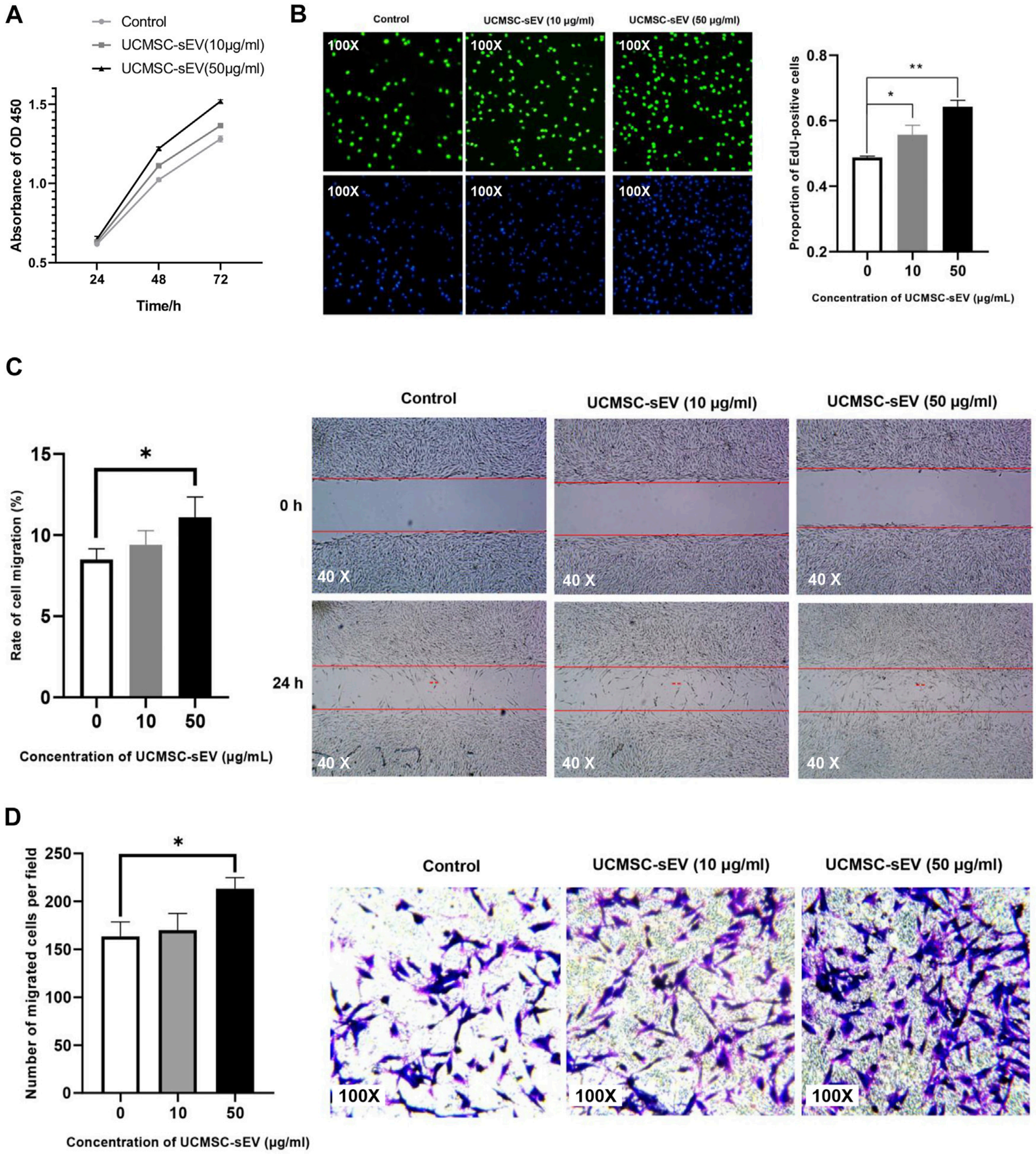

FIGURE 2 | UCMSC-sEV promote the proliferation and migration of PUMSCs. **(A)** A CCK-8 assay was used to detect the proliferation of PUMSCs treated with 10 μg/ml and 50 μg/ml UCMSC-sEV for 24, 48 and 72 h **(B)** The EdU incorporation assay results show that UCMSC-sEV (10 μg/ml and 50 μg/ml) significantly promote the proliferation of PUMSCs. The scratch wound assay results **(C)** and Transwell assay results **(D)** are consistent. Low concentrations of UCMSC-sEV (10 μmol/L) have no effect on the migration of PUSMCs, and high concentrations of UCMSC-sEV (50 μmol/L) significantly promote the migration of PUSMCs.

accordance with the protocol provided by the manufacturer. The fluorescent intensity was measured at Ex/Em 535/587 by Thermo Scientific Varioskan Flash Multimode Reader (Thermo, United States).

Statistical Analysis

Shapiro-Wilk normality tests were performed for each set of data, in the case of normal distribution, the data are presented as mean ± SD. The data were assessed using the SPSS 11.0 program for Windows (SPSS Co., United States). Significance was evaluated at *p*-value of 0.05 and 0.01 using *t* test.

RESULTS

Cell Identification

After passaging, the PUSMCs grew in bundles and exhibited a cascade arrangement and a "peak-to-valley" phenomenon

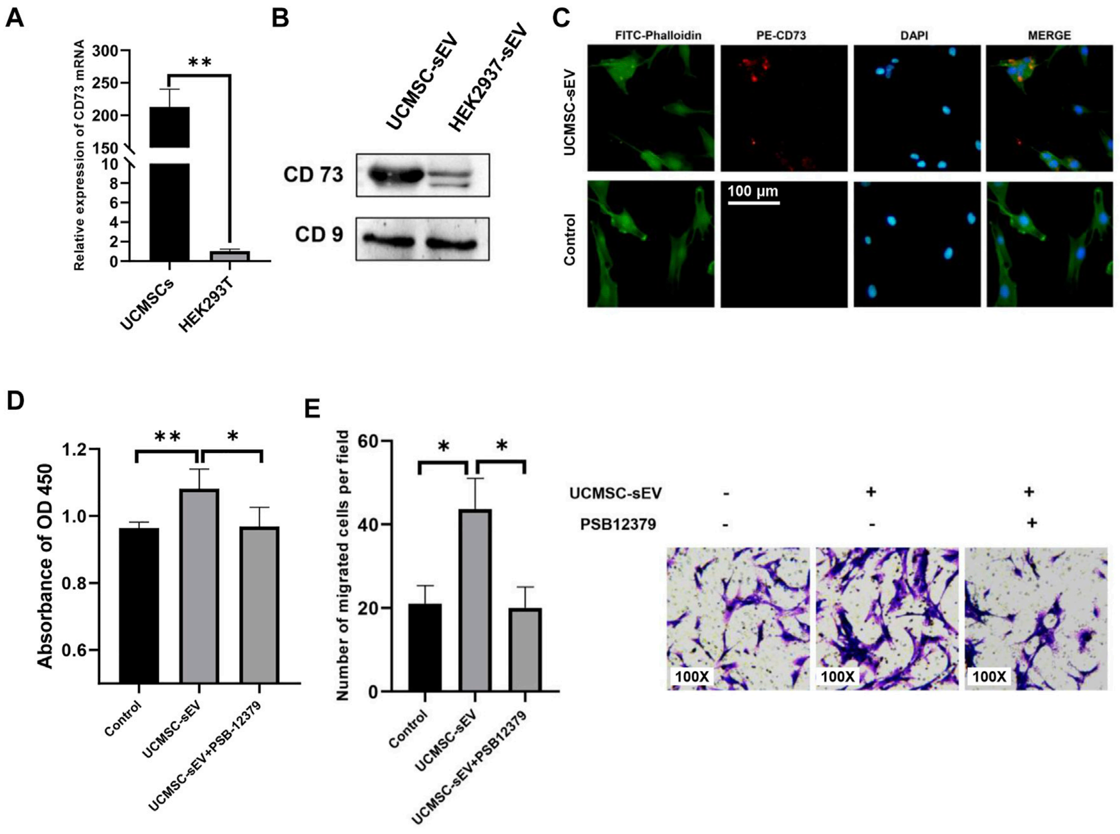

FIGURE 3 | UCMSC-sEV promote proliferation and migration through CD73 molecules. **(A)** Detection of the mRNA expression level of CD73 in UCMSCs using real-time PCR (HEK293T was used as the control group). **(B)** Western blotting was used to detect the protein expression level of CD73 in UCMSC-sEV (HEK293T-sEV were used as the control group). **(C)** Immunofluorescence staining shows that PE-CD73-labeled sEV are internalized by PUMSCs. **(D)** CCK-8 and Transwell assay results **(E)** show that the inhibition of the sEV CD73 molecular activity by PSB12379 blocks the proliferation- and migration-promoting effects of UCMSC-sEV.

(**Figure 1A**). The immunofluorescence assay results showed that the cultured cells expressed α-SMA, a smooth muscle surface marker (**Figure 1B**). The proliferation of PUSMCs was vigorous, and the growth curve (**Figure 1C**) trend was S-shaped, with lag, logarithmic and plateau phases.

Flow cytometry analysis of the surface markers of MSCs indicated that UCMSCs expressed high levels of the CD29, CD44, CD73, and CD90 but were negative for the CD45 and HLA-DR (**Figure 1D**), findings that are consistent with the general characteristics of MSCs.

Identification of the sEV

Transmission electron microscopy revealed that the UCMSC-sEV were cup-shaped vesicles (**Figure 1E**). NanoFCM analysis indicated that the average diameter of the sEV was 78.91 nm and that the concentration was 2.53E+10 particles/mL (**Figure 1F**). Western blot results showed that the extracted sEV expressed CD81, CD63, CD9 and TSG101 (**Figure 1G**).

UCMSC-sEV Promoted PUSMC Proliferation and Migration

Results of CCK-8 assays (**Figure 2A**) and EdU assays (**Figure 2B**) indicated that UCMSC-sEV promoted the proliferation of PUSMCs in a dose- and time-dependent manner.

As shown in **Figures 2C,D**, both scratch wound assay and Transwell assay results indicated that low concentrations of UCMSC-sEV (10 μmol/L) had no effect on the migration of PUSMCs, and high concentrations of UCMSC-sEV (50 μmol/L) significantly promoted the migration of PUSMCs.

UCMSC-sEV Highly Expressed CD73 Molecules That Were Endocytosed by PUSMCs

CD73, also known as ecto-5′-nucleotidase, is a cell surface enzyme that is highly expressed on the surface of UCMSCs (**Figure 1D**). To verify whether UCMSC-sEV also expressed CD73, qRT-PCR and Western blotting were used to assess the mRNA and protein levels of CD73 in UCMSCs and UCMSC-sEV, respectively. The results showed that compared with HEK293T cell-derived sEV (HEK293T-sEV), UCMSCs and UCMSC-sEV highly expressed CD73 mRNA and protein (**Figure 3A** and **Figure 3B**).

To confirm internalization of CD73-positive UCMSC-sEV by PUSMCs, a PE-conjugated anti-CD73 monoclonal

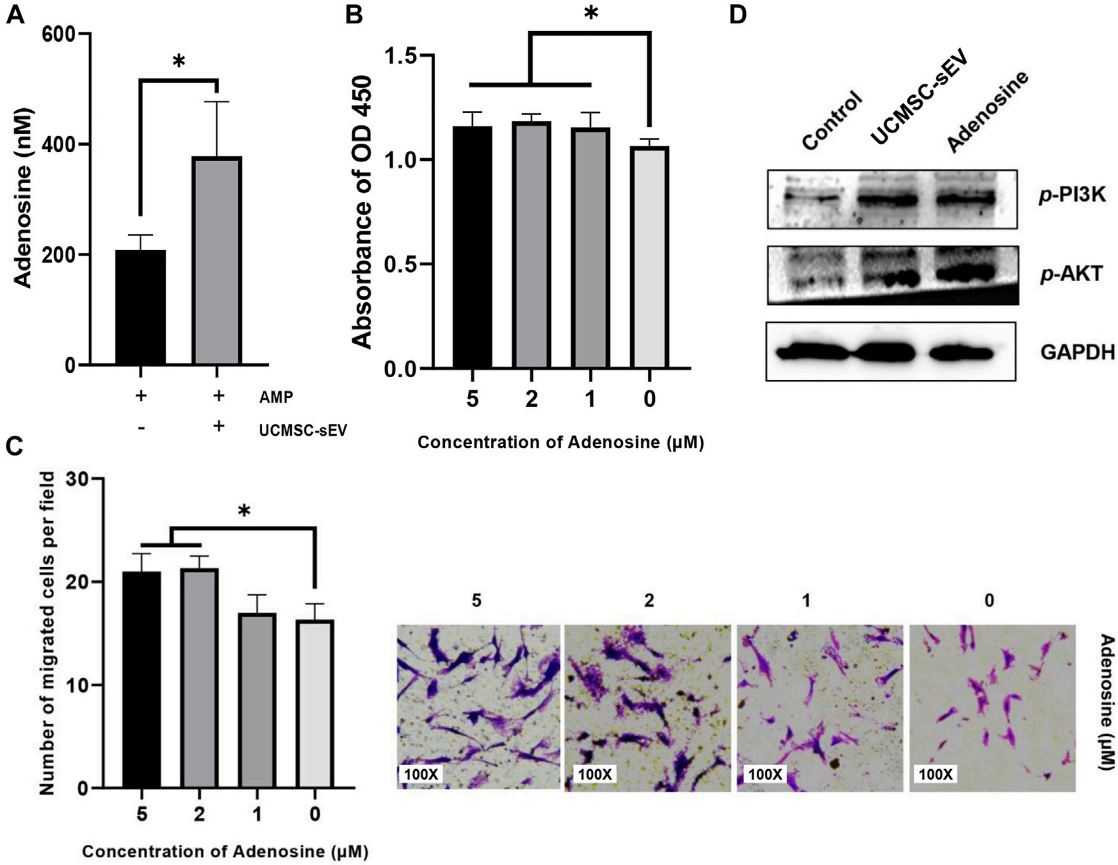

FIGURE 4 | The sEV CD73 catalyzes the production of adenosine and activates the PI3K/AKT pathway to promote proliferation and migration. **(A)** UCMSC-sEV use exogenous 5′AMP to produce adenosine through surface CD73. **(B)** CCK-8 and Transwell assay results **(C)** show that the addition of exogenous adenosine significantly promotes the proliferation and migration of PUSMCs *in vitro*. **(D)** Western blot detection of the expression levels of PI3K/AKT in PUSMCs.

antibody was used to label UCMSC-sEV. The labeled sEV were cocultured with PUSMCs for 3 h, and the internalization of UCMSC-sEV was observed under a fluorescence microscope. The red fluorescence of CD73 on the surface of UCMSC-sEV was localized to PUSMCs, indicating that CD73-positive UCMSC-sEV were endocytosed by PUSMCs (**Figure 3C**).

Inhibition of CD73 Molecular Activity Blocked the Proliferation- and Migration-Promoting Effects of UCMSC-sEV

To further investigate whether the proliferation- and migration-promoting effects of UCMSC-sEV were related to the transmission of CD73 molecules, we added a CD73 inhibitor (PSB12379, MCE) to the medium contained with UCMSC-sEV. The results indicated that the addition of PSB12379 inhibited CD73 activity and blocked the proliferation- and migration-promoting effects of UCMSC-sEV on PUSMCs (**Figures 3D,E**).

The CD73 Metabolite Adenosine Promotes the Proliferation and Migration of PUSMCs

The expression of adenosine was detected in the cell culture supernatant containing 5′AMP (Sigma) and UCMSC-sEV (**Figure 4A**), indicating that CD73 on the surface of UCMSC-sEV used exogenous 5′AMP to produce adenosine. Moreover, the addition of exogenous adenosine to the culture medium of PUSMCs significantly promoted the proliferation and migration of PUSMCs (**Figures 4B,C**). These results demonstrate that the proliferation- and migration-promoting effects of UCMSC-sEV were related to the CD73/adenosine signaling axis.

Activation of the PI3K/AKT Signaling Pathway

The PI3K/AKT signaling pathway is an important pathway for cell proliferation and survival and is closely related to adenosine metabolism. Therefore, we investigated the downstream PI3K/AKT signaling pathway by which CD73 affects the cellular functions of PUSMCs through Western blotting analysis. The protein expression levels of phospho-AKT and phospho-PI3K in PUSMCs increased after treated with adenosine or UCMSC-sEV (**Figure 4D**), indicating that UCMSC-sEV activated the PI3K/AKT signaling pathway in PUSMCs.

DISCUSSION

This study explored whether UCMSC-sEV could affect the proliferation and migration of PUSMCs and preliminarily researched the related molecular mechanism. The results showed that UCMSC-sEV significantly promoted the proliferation and migration of PUSMCs *in vitro* and this process may be related to the CD73/adenosine signaling axis and the PI3K/AKT pathway.

sEV are secreted and released by cells. As a carrier of intercellular communication, sEV has recently been confirmed as a new mechanism of cell-to-cell communication (Meldolesi, 2018; Kalluri and LeBleu, 2020; Rezaie et al., 2021). sEV are nanoscale lipid inclusion structures that contain substances such as proteins, mRNAs, and microRNAs and can accelerate the repair of damaged tissues by transferring RNA to adjacent target cells (Zhang et al., 2015; Kilchert et al., 2016; Hassanpour et al., 2020). Activated proteins can also be transferred to target cells by sEV and produce corresponding biological effects (Li et al., 2017; Toh et al., 2018). In this study, we first isolated UCMSC-sEV by the ultracentrifugation method and then characterized UCMSC-sEV by transmission electron microscopy, nanoflow cytometry, and the detection of the expression of the sEV marker molecules such as CD9, CD63, CD81, and TSG101, respectively.

In recent years, mesenchymal stem cell-derived sEV have been found to promote the proliferation and migration of many different types of cells *in vitro*, such as chondrocytes (Wen et al., 2022), vascular endothelial cells (Zhang et al., 2021), neuronal cells (Wei et al., 2020), keratinocytes (Kim et al., 2018), and fibroblasts (Shabbir et al., 2015). In view of the key role of sEV in boosting the regeneration and repair of different tissues, we speculate that UCMSC-sEV may also affect the repair of urethral tissue injury by affecting the biological behaviors of PUSMCs (such as proliferation and migration). In this study, in the presence of UCMSC-sEV, the *in vitro* migration and proliferation rates of PUSMCs were significantly higher than those of PUSMCs in the negative control group. These results demonstrate that UCMSC-sEV can indeed increase the proliferation and migration of PUSMCs *in vitro*, the finding that is consistent with the report by Wei (Huo et al., 2020) that bone marrow mesenchymal stem cell-derived sEV carrying miR-21-5p promote the proliferation of corpus cavernosum SMCs and inhibit their apoptosis *in vitro*.

As a surface marker of MSCs, CD73 can catalyze the hydrolysis of adenosine 5-phosphate to adenosine and exert a series of biological functions through the interaction of adenosine and adenosine receptors (Adamiak et al., 2019). Studies have shown that CD73 $^{+}$ MSCs are the dominant subpopulation involved in myocardial repair (Li et al., 2021). CD73 is over-expressed in tumor tissues and can increase tumor cell proliferation (Xie et al., 2017). During tumorigenesis and development, CD73 promotes the formation of new blood vessels by endothelial cells (Wang et al., 2013). This study found that UCMSCs highly expressed CD73 and could carry CD73 molecules to PUSMCs through the communication function of sEV to generate adenosine, thereby affecting cell proliferation and migration. When using PSB12379 to inhibit the CD73 enzymatic activity of UCMSC-sEV, the proliferation- and migration-promoting activities of UCMSC-sEV were no longer observed. To determine the signaling pathways through which the proliferation- and migration-promoting effects of UCMSC-sEV are mediated, we hypothesized that PI3K/AKT is a possible candidate pathway because the PI3K/AKT pathway is closely related to cell proliferation and migration and exosomal CD73 catalyzes adenosine production, and after binding to adenosine receptors, downstream signaling pathways, such as AKT and ERK, can be activated (Chew et al., 2019; Ma et al., 2019). In this study, we demonstrated that UCMSC-sEV and adenosine-mediated cell proliferation and migration of PUSMCs could indeed cause the phosphorylation of PI3K and AKT.

In summary, this study demonstrated that UCMSC-sEV can significantly promote PUSMC proliferation and migration *in vitro*. Moreover, we also found that UCMSC-sEV increased the proliferation and migration of PUSMCs *in vitro* through the activation of the CD73/adenosine signaling axis and the PI3K/AKT pathway.

DATA AVAILABILITY STATEMENT

The original contributions presented in the study are included in the article/supplementary materials, further inquiries can be directed to the corresponding author.

ETHICS STATEMENT

All procedures in the present study were approved by the Animal Ethics Committee of Foshan Maternity and Child Health care Hospital (decision number: FSFY-MEC-2016-009). Written informed consent was obtained from all donors.

AUTHOR CONTRIBUTIONS

SZ: Experiment, Writing- Original draft preparation, and manuscript revision. JL, CL, XX, and JH: Experiment, Original draft preparation. FL and BL: Data curation and Writing-Reviewing. HW and ZL: Supervision and language polishment. JZ: Conceptualization and manuscript revision.

FUNDING

This study was supported by the Medical Science Project of Foshan Science and Technology Bureau (2020001005636) and Innovation Project of Women and Children medical research center affiliated to Foshan Institute of Fetal Medicine (FEYJZX-2020-007).

ACKNOWLEDGMENTS

We thank Dongsheng Li at Weina Biomedicine, Foshan, China, for his help and guidance on our project.

REFERENCES

Abbas, T. O., Mahdi, E., Hasan, A., AlAnsari, A., and Pennisi, C. P. (2017). Current Status of Tissue Engineering in the Management of Severe Hypospadias. *Front. Pediatr.* 5, 283. doi:10.3389/fped.2017.00283

Adamiak, M., Bujko, K., Brzezniakiewicz-Janus, K., Kucia, M., Ratajczak, J., and Ratajczak, M. Z. (2019). The Inhibition of CD39 and CD73 Cell Surface Ectonucleotidases by Small Molecular Inhibitors Enhances the Mobilization of Bone Marrow Residing Stem Cells by Decreasing the Extracellular Level of Adenosine. *Stem Cel Rev Rep* 15 (6), 892–899. doi:10.1007/s12015-019-09918-y

Arenas da Silva, L. F., Micol, L., Tiemessen, D., van Kuppevelt, T. H., Frey, P., Oosterwijk, E., et al. (2014). Is There a Need for Smooth Muscle Cell Transplantation in Urethral Reconstruction? *Tissue Eng. A* 20 (9-10), 1542–1549. doi:10.1089/ten.TEA.2013.0185

Can, A., Celikkan, F. T., and Cinar, O. (2017). Umbilical Cord Mesenchymal Stromal Cell Transplantations: A Systemic Analysis of Clinical Trials. *Cytotherapy* 19 (12), 1351–1382. doi:10.1016/j.jcyt.2017.08.004

Chan, Y. Y., Bury, M. I., Yura, E. M., Hofer, M. D., Cheng, E. Y., and Sharma, A. K. (2020). The Current State of Tissue Engineering in the Management of Hypospadias. *Nat. Rev. Urol.* 17 (3), 162–175. doi:10.1038/s41585-020-0281-4

Chew, J. R. J., Chuah, S. J., Teo, K. Y. W., Zhang, S., Lai, R. C., Fu, J. H., et al. (2019). Mesenchymal Stem Cell Exosomes Enhance Periodontal Ligament Cell Functions and Promote Periodontal Regeneration. *Acta Biomater.* 89, 252–264. doi:10.1016/j.actbio.2019.03.021

Ding, D.-C., Chang, Y.-H., Shyu, W.-C., and Lin, S.-Z. (2015). Human Umbilical Cord Mesenchymal Stem Cells: A new era for Stem Cell Therapy. *Cel Transpl.* 24 (3), 339–347. doi:10.3727/096368915X686841

Fu, X., Liu, G., Halim, A., Ju, Y., Luo, Q., and Song, A. G. (2019). Mesenchymal Stem Cell Migration and Tissue Repair. *Cells* 8 (8), 784. doi:10.3390/cells8080784

Galipeau, J., and Sensébé, L. (2018). Mesenchymal Stromal Cells: Clinical Challenges and Therapeutic Opportunities. *Cell Stem Cell* 22 (6), 824–833. doi:10.1016/j.stem.2018.05.004

Gao, G., Fan, C., Li, W., Liang, R., Wei, C., Chen, X., et al. (2021). Mesenchymal Stem Cells: Ideal Seeds for Treating Diseases. *Hum. Cel* 34 (6), 1585–1600. doi:10.1007/s13577-021-00578-0

Hassanpour, M., Rezabakhsh, A., Rezaie, J., Nouri, M., and Rahbarghazi, R. (2020). Exosomal Cargos Modulate Autophagy in Recipient Cells via Different Signaling Pathways. *Cell Biosci* 10, 92. doi:10.1186/s13578-020-00455-7

Huo, W., Li, Y., Zhang, Y., and Li, H. (2020). Mesenchymal Stem Cells-derived Exosomal microRNA-21-5p Downregulates PDCD4 and Ameliorates Erectile Dysfunction in a Rat Model of Diabetes Mellitus. *FASEB j.* 34 (10), 13345–13360. doi:10.1096/fj.202000102RR

Kalluri, R., and LeBleu, V. S. (2020). The Biology , Function , and Biomedical Applications of Exosomes. *Science* 367 (6478), eaau6977. doi:10.1126/science.aau6977

Keshtkar, S., Azarpira, N., and Ghahremani, M. H. (2018). Mesenchymal Stem Cell-Derived Extracellular Vesicles: Novel Frontiers in Regenerative Medicine. *Stem Cel Res. Ther.* 9 (1), 63. doi:10.1186/s13287-018-0791-7

Kilchert, C., Wittmann, S., and Vasiljeva, L. (2016). The Regulation and Functions of the Nuclear RNA Exosome Complex. *Nat. Rev. Mol. Cel Biol* 17 (4), 227–239. doi:10.1038/nrm.2015.15

Kim, S., Lee, S., Kim, H., and Kim, T. (2018). Exosomes Secreted from Induced Pluripotent Stem Cell-Derived Mesenchymal Stem Cells Accelerate Skin Cell Proliferation. *Ijms* 19 (10), 3119. doi:10.3390/ijms19103119

Li, Q., Hou, H., Li, M., Yu, X., Zuo, H., Gao, J., et al. (2021). CD73+ Mesenchymal Stem Cells Ameliorate Myocardial Infarction by Promoting Angiogenesis. *Front. Cel Dev. Biol.* 9, 637239. doi:10.3389/fcell.2021.637239

Li, W., Li, C., Zhou, T., Liu, X., Liu, X., Li, X., et al. (2017). Role of Exosomal Proteins in Cancer Diagnosis. *Mol. Cancer* 16 (1), 145. doi:10.1186/s12943-017-0706-8

Li, Y., Wen, Y., Wang, Z., Wei, Y., Wani, P., Green, M., et al. (2016). Smooth Muscle Progenitor Cells Derived from Human Pluripotent Stem Cells Induce Histologic Changes in Injured Urethral Sphincter. *Stem Cell Transl Med* 5 (12), 1719–1729. doi:10.5966/sctm.2016-0035

Ma, X.-L., Shen, M.-N., Hu, B., Wang, B.-L., Yang, W.-J., Lv, L.-H., et al. (2019). CD73 Promotes Hepatocellular Carcinoma Progression and Metastasis via Activating PI3K/AKT Signaling by Inducing Rap1-Mediated Membrane Localization of P110β and Predicts Poor Prognosis. *J. Hematol. Oncol.* 12 (1), 37. doi:10.1186/s13045-019-0724-7

Meldolesi, J. (2018). Exosomes and Ectosomes in Intercellular Communication. *Curr. Biol.* 28 (8), R435–R444. doi:10.1016/j.cub.2018.01.059

Ning, N., Lin, G., Lue, T. F., and Lin, C.-S. (2010). Effects of Estrogen, Raloxifene, and Levormeloxifene on the Expression of Rho-Kinase Signaling Molecules in Urethral Smooth Muscle Cells. *Urology* 76 (6), e6–1517. doi:10.1016/j.urology.2010.07.470

Rajasingh, S., Sigamani, V., Selvam, V., Gurusamy, N., Kirankumar, S., Vasanthan, J., et al. (2021). Comparative Analysis of Human Induced Pluripotent Stem Cell-Derived Mesenchymal Stem Cells and Umbilical Cord Mesenchymal Stem Cells. *J. Cel. Mol. Med.* 25 (18), 8904–8919. doi:10.1111/jcmm.16851

Rezaie, J., Aslan, C., Ahmadi, M., Zolbanin, N. M., Kashanchi, F., and Jafari, R. (2021). The Versatile Role of Exosomes in Human Retroviral Infections: From Immunopathogenesis to Clinical Application. [Journal Article; Review]. *Cel Biosci* 11 (1), 19. doi:10.1186/s13578-021-00537-0

Sergeant, G. P., Hollywood, M. A., and Thornbury, K. D. (2019). Spontaneous Activity in Urethral Smooth Muscle. *Adv. Exp. Med. Biol.* 1124, 149–167. doi:10.1007/978-981-13-5895-1_6

Shabbir, A., Cox, A., Rodriguez-Menocal, L., Salgado, M., and Van Badiavas, E. (2015). Mesenchymal Stem Cell Exosomes Induce Proliferation and Migration of normal and Chronic Wound Fibroblasts, and Enhance Angiogenesis *In Vitro*. *Stem Cell Dev* 24 (14), 1635–1647. doi:10.1089/scd.2014.0316

Thery, C., Witwer, K. W., Aikawa, E., Alcaraz, M. J., Anderson, J. D., Andriantsitohaina, R., et al. (2018). Minimal Information for Studies of Extracellular Vesicles 2018 (MISEV2018): A Position Statement of the International Society for Extracellular Vesicles and Update of the MISEV2014 Guidelines. [Journal Article]. *J. Extracell Vesicles* 7 (1), 1535750. doi:10.1080/20013078.2018.1535750

Toh, W. S., Lai, R. C., Zhang, B., and Lim, S. K. (2018). MSC Exosome Works through a Protein-Based Mechanism of Action. *Biochem. Soc. Trans.* 46 (4), 843–853. doi:10.1042/BST20180079

Wang, L., Tang, S., Wang, Y., Xu, S., Yu, J., Zhi, X., et al. (2013). Ecto-5'-nucleotidase (CD73) Promotes Tumor Angiogenesis. *Clin. Exp. Metastasis* 30 (5), 671–680. doi:10.1007/s10585-013-9571-z

Wei, H., Xu, Y., Chen, Q., Chen, H., Zhu, X., and Li, Y. (2020). Mesenchymal Stem Cell-Derived Exosomal miR-223 Regulates Neuronal Cell Apoptosis. *Cell Death Dis* 11 (4), 290. doi:10.1038/s41419-020-2490-4

Wen, C., Lin, L., Zou, R., Lin, F., and Liu, Y. (2022). Mesenchymal Stem Cell-Derived Exosome Mediated Long Non-coding RNA KLF3-AS1 Represses Autophagy and Apoptosis of Chondrocytes in Osteoarthritis. *Cell Cycle* 21 (3), 289–303. doi:10.1080/15384101.2021.2019411

Witwer, K. W., Van Balkom, B., Bruno, S., Choo, A., Dominici, M., Gimona, M., et al. (2019). Defining Mesenchymal Stromal Cell (MSC)-derived Small Extracellular Vesicles for Therapeutic Applications. [Journal Article]. *J. Extracell Vesicles* 8 (1), 1609206. doi:10.1080/20013078.2019.1609206

Wu, P., Zhang, B., Shi, H., Qian, H., and Xu, W. (2018). MSC-exosome: A Novel Cell-free Therapy for Cutaneous Regeneration. *Cytotherapy* 20 (3), 291–301. doi:10.1016/j.jcyt.2017.11.002

Xia, J., Minamino, S., Kuwabara, K., and Arai, S. (2019). Stem Cell Secretome as a New Booster for Regenerative Medicine. *Biosci. Trends.* 13 (4), 299–307. doi:10.5582/bst.2019.01226

Xie, M., Qin, H., Luo, Q., Huang, Q., He, X., Yang, Z., et al. (2017). MicroRNA-30a Regulates Cell Proliferation and Tumor Growth of Colorectal Cancer by Targeting CD73. *BMC Cancer* 17 (1), 305. doi:10.1186/s12885-017-3291-8

Yaghoubi, Y., Movassaghpour, A., Zamani, M., Talebi, M., Mehdizadeh, A., and Yousefi, M. (2019). Human Umbilical Cord Mesenchymal Stem Cells Derived-

Exosomes in Diseases Treatment. *Life Sci.* 233, 116733. doi:10.1016/j.lfs.2019.116733

Zhang, J., Li, S., Li, L., Li, M., Guo, C., Yao, J., et al. (2015). Exosome and Exosomal microRNA: Trafficking, Sorting, and Function. *Genomics Proteomics Bioinformatics* 13 (1), 17–24. doi:10.1016/j.gpb.2015.02.001

Zhang, Y., Xie, Y., Hao, Z., Zhou, P., Wang, P., Fang, S., et al. (2021). Umbilical Mesenchymal Stem Cell-Derived Exosome-Encapsulated Hydrogels Accelerate Bone Repair by Enhancing Angiogenesis. *ACS Appl. Mater. Inter.* 13 (16), 18472–18487. doi:10.1021/acsami.0c22671

Conflict of Interest: The authors declare that the research was conducted in the absence of any commercial or financial relationships that could be construed as a potential conflict of interest.

frontiers | Frontiers in Bioengineering and Biotechnology

ORIGINAL RESEARCH
published: 12 May 2022
doi: 10.3389/fbioe.2022.870324

Inflammatory Microenvironment Accelerates Bone Marrow Mesenchymal Stem Cell Aging

Xin Peng[1,2,3†], *Xin Zhou*[1,2,3†], *Ying Yin, Beibei Luo, Yang Liu*[1,2,3]* *and Cheng Yang*[1,2,3]*

[1]*Department of Stomatology, Union Hospital, Tongji Medical College, Huazhong University of Science and Technology, Wuhan, China,* [2]*School of Stomatology, Tongji Medical College, Huazhong University of Science and Technology, Wuhan, China,* [3]*Hubei Province Key Laboratory of Oral and Maxillofacial Development and Regeneration, Wuhan, China*

MSC senescence is considered a contributing factor in aging-related diseases. We investigated the influence of the inflammatory microenvironment on bone marrow mesenchymal stem cells (BMSCs) under aging conditions and the underlying mechanism to provide new ideas for stem cell therapy for age-related osteoporosis. The BMSCs were cultured until passage 3 (P3) (young group) and passage 10 (P10) (aging group) *in vitro*. The supernatant was collected as the conditioned medium (CM). The young BMSCs were cultured in the CM of P3 or P10 cells. The effects of CM from different groups on the aging and stemness of the young BMSCs were examined. A Quantibody® mouse inflammation array on serum extracts from young (aged 8 weeks) and old (aged 78 weeks) mice was performed, and differentially expressed factors were screened out. We discovered that the CM from senescent MSCs changed the physiology of young BMSCs. Systemic inflammatory microenvironments changed with age in the mice. In particular, the pro-inflammatory cytokine IL-6 increased, and the anti-inflammatory cytokine IL-10 decreased. The underlying mechanism was investigated by GO and KEGG analyses, and there was a change in the JAK-STAT signaling pathway, which is closely related to IL-6 and IL-10. Collectively, our results demonstrated that the age-related inflammatory microenvironment has a significant effect on the biological functions of BMSCs. Targeted reversal of this inflammatory environment may provide a new strategy for stem cell therapy to treat aging-related skeletal diseases.

Keywords: aging-related skeletal diseases, stem cell therapy, inflammatory microenvironment, bone marrow mesenchymal stem cell, aging

OPEN ACCESS

Edited by:
Charlotte Riviere,
Université Claude Bernard Lyon 1,
France

Reviewed by:
Nicola Alessio,
Università della Campania Luigi
Vanvitelli, Italy
Antonio Casado Díaz,
Centro de Investigación Biomédica en
Red sobre Fragilidad y Envejecimiento
Saludable (CIBERFES), Spain

****Correspondence:***
Cheng Yang
ycheng715@163.com
Yang Liu
liuyang_46@163.com

[†]*These authors have contributed equally to this work and share first authorship*

Specialty section:
This article was submitted to
Tissue Engineering and Regenerative
Medicine,
a section of the journal
Frontiers in Bioengineering and
Biotechnology

Received: *06 February 2022*
Accepted: *11 April 2022*
Published: *12 May 2022*

Citation:
Peng X, Zhou X, Yin Y, Luo B, Liu Y and Yang C (2022) Inflammatory Microenvironment Accelerates Bone Marrow Mesenchymal Stem Cell Aging.
Front. Bioeng. Biotechnol. 10:870324.
doi: 10.3389/fbioe.2022.870324

INTRODUCTION

Osteoporosis is a common aging-related disease. Currently, the clinical treatment of osteoporosis is mainly medical therapy, including bisphosphonates, calcitonin, and SERM (Khosla and Hofbauer, 2017). However, these drugs often bring about side effects, such as atypical femoral fractures and osteonecrosis of the jaw (Khosla and Hofbauer, 2017), and their long-term efficacy is not fully confirmed. Studies have shown that cell therapy based on bone marrow mesenchymal stem cells is suitable for the treatment of osteoporosis (Aghebati-Maleki et al., 2019).

As osteoporosis is related to a decline in the number and function of osteoblasts, substantial evidence indicates that the transplantation of stem cells with osteogenic differentiation ability has the ability to reverse bone demineralization (Paspaliaris and Kolios, 2019). Microenvironment regulation is one of the main mechanisms of stem cell–mediated anti-aging and the treatment of aging diseases (Paspaliaris and Kolios, 2019). Stem cells can secrete various biologically active proteins, including growth factors and cytokines, and act on different cells in tissues and organs through an intercellular signal transduction system (Galkowski et al., 2017).

Increasing evidence indicates that chronic inflammation in elderly individuals (inflammaging) is intensively associated with many aging-related diseases, such as Alzheimer's disease, atherosclerosis, heart disease, type II diabetes, and cancer. Inflammatory factors affect bone remodeling under physiological conditions, such as fracture repair. Inflammation is closely associated with osteoclast differentiation and bone loss; however, it has become clear that there is an important relationship between inflammation and bone formation (Adamopoulos, 2018). However, whether we can adjust this inflammatory microenvironment to improve the function of bone marrow mesenchymal stem cells to provide new strategies for stem cell therapy to treat aging-related skeletal diseases remains to be shown.

This study aimed to evaluate the effects of the inflammatory microenvironment on BMSC proliferation, differentiation, and stemness. We also used the inflammation array to examine the serum of mice in different age groups to explore changes in the related signaling pathways. After being treated with P10 MSC CM, BMSCs' stemness was reduced compared with that of the BMSCs treated with P3 MSC CM. A Quantibody® mouse inflammation array was used to examine the serum of mice in different age groups to explore changes in the related signaling pathways. With increasing age, an inflammatory microenvironment occurred, and IL-6 and IL-10 had the most significant changes; IL-6 increased and IL-10 decreased. The immunohistochemical analysis showed that the local environment in the bone marrow had the same change. Furthermore, ELISA was used to verify that IL-6 was increased and IL-10 was decreased in P10 MSC CM. The mechanism was evaluated through the GO and KEGG analyses, and the JAK-STAT signaling pathway was changed. Therefore, our findings suggested that the increase in IL-6 and the decrease in IL-10 in the microenvironment reduced BMSCs' stemness through the JAK-STAT signaling pathway, leading to decreased osteogenic differentiation. Additionally, these results suggested that inflammaging was a major contributor to the decline in the regenerative capacity of the skeleton, suggesting a potential therapeutic strategy for preventing bone loss in osteoporosis. Perhaps targeting specific inflammatory mediators to control age-related inflammation could have beneficial therapeutic effects in treating age-related diseases (Lasry and Ben-Neriah, 2015).

MATERIALS AND METHODS

Ethics

All animal care and experimental protocols were approved by the Institutional Animal Care and Use Committee of Tongji Medical College, Huazhong University of Science and Technology (Wuhan, China, S780), which were according to the National Institutes of Health Guidelines for the Care and Use of Laboratory Animals.

Animals

All male C57BL/6J mice (aged 8 weeks or 78 weeks) were purchased from Beijing Vital River Laboratory Animal Technology Co., Ltd. All these mice were raised in the specific pathogen-free (SPF) animal center of Tongji Medical College, Huazhong University of Science and Technology (Wuhan, China). The mice were maintained at a room temperature of 23 ± 1°C and 55 ± 5% humidity under a 12 h light/dark cycle and supplied with sterilized food and water. The irradiated corncob bedding was changed every week.

Isolation and Cultivation of Rat BMSCs

Sprague–Dawley rats (aged 3 weeks, male, weighing approximately 60–80 g) were used for collecting and culturing the BMSCs for the experiments *in vitro*.

The bone marrow of femurs and tibias was drawn out by flushing with a complete medium. The bone marrow cells of each rat were seeded in two 25-cm^2 tissue culture flasks containing DMEM/F-12 medium (HyClone, Logan, UT, United States), 10% fetal bovine serum (FBS) (Gibco, United States), and 1% penicillin-streptomycin solution (Beyotime, Shanghai, China). The BMSCs were maintained at 37°C in a 5% CO_2 humidified incubator. By changing the medium every 2 days, non-adherent cells were removed and adherent cells were cultured until confluent to 80%.

Cell Proliferation and Apoptosis Assay

CCK8 Assay

At a density of 1 × 103 cells/well, the BMSCs were seeded in 96-well plates. Cell counting kit-8 (Dojindo, Kumamoto, Japan) was used to measure cell proliferation. As described previously, 10 μl of CCK-8 solution per 100 μl medium was added to every well, and the plates were incubated for 1 h after being mixed. The OD value was recorded by using a microplate reader (EnSpire, PerkinElmer, United States) at 450 nm. We performed this assay on day 1, day 3, day 5, and day 7.

EdU Assay

The cells were cultured on the slides (round, thickness: 0.2 mm, and diameter: 15 mm). Cell proliferation was analyzed using the BeyoClick™ EdU Cell Proliferation Kit (Beyotime, Shanghai, China) with Alexa Fluor 488, according to the protocol. Every well was treated with 500 μl of medium containing 10 μM EdU. After incubation at 37°C, with 5% CO_2 for 2 h, the cells were fixed with 4% paraformaldehyde at room temperature for 15 min and incubated with 0.3% Triton X-100 in PBS for 10–15 min. The cell nuclei were stained with Hoechst 33342. Images of three randomly selected areas of each group were taken using a laser scanning confocal microscope (A1si+/A1Rsi+, Nikon, Japan). The percentage of proliferative cells was calculated by the number of EdU-positive cells compared with all cells in different fields as already shot.

TUNEL Assay

Cell apoptosis was evaluated by using the One-Step TUNEL Apoptosis Assay Kit (Beyotime, Shanghai, China). The apoptotic cells were detected using a fluorescence microscope (Olympus, Japan). Images of three randomly selected areas of each group were taken.

Senescence Assay

The senescence β-galactosidase staining kit was used to test the activity of senescence-associated β-galactosidase (SA-β-Gal) (Beyotime, Shanghai, China). According to the protocol, the senescent cells will be stained.

Osteogenic and Adipogenic Differentiation Assay

To induce osteogenic differentiation, the BMSCs were cultured in a commercially available osteogenic medium (Cyagen, Soochow, China) for 14 days. Thereafter, the cells were washed twice with phosphate-buffered saline (PBS), fixed in 4% paraformaldehyde for 15 min at room temperature, and stained with alizarin red (Servicebio, Wuhan, China) for 30 min. After rinsing the cells 2–3 times with PBS, the calcified nodules were visualized under an inverted microscope (Olympus, Tokyo, Japan). Similarly, the BMSCs were cultured in a commercially available adipogenic medium (Cyagen, Soochow, China) for 2 weeks. Subsequently, the cells were washed twice with PBS, fixed in 4% paraformaldehyde for 15 min at room temperature, then washed with PBS, and stained with 2% oil red O (Servicebio, Wuhan, China) for 1 h at room temperature. The BMSCs were washed again with PBS. The intracellular lipid droplets were visualized under a microscope (Olympus, Tokyo, Japan).

RNA Extraction and Real-Time RT-PCR of mRNA

Total RNA was extracted from cells using the RNA isolater Total RNA Extraction Reagent (Vazyme, Jiangsu, China), following the manufacturer's protocol. Complementary DNA was generated using the HiScript® II Q RT SuperMix for qPCR (+ gDNA wiper) (Vazyme, Jiangsu, China). The qRT-PCR was performed in a 96-well plate with ChamQ SYBR qPCR Master Mix (Vazyme, Jiangsu, China), and it was performed on an ABI StepOnePlus real-time PCR instrument (Applied Biosystems). The mRNA levels of the target genes were normalized against that of GAPDH, which served as an internal control.

Western Blot Analysis

The cells were lysed by RIPA buffer supplemented with a protease inhibitor cocktail. An equal amount of proteins (containing 30 mg protein lysate) were loaded into 12% polyacrylamide gel for SDS-PAGE electrophoresis and transferred to 0.45 μm or 0.22 μm polyvinylidene fluoride membranes, which were subsequently incubated with 5% skim milk for 1 h and then probed with rabbit antibodies against Perilipin 1 (1:2000, ab3526, Abcam), FABP4 (1:500, 15872-1-AP, Proteintech), SOX2 (1:500, A0561, ABclonal), and GAPDH (1:10000, 10494-1-AP, Proteintech). The enhanced chemiluminescence substrate reagent (Millipore, Billerica, MA, United States) was used to detect immunoreactive protein bands. The gray values of the blots were analyzed by ImageJ software. The value of each blot was normalized to the value of GAPDH.

Quantibody® Mouse Inflammation Array 1

The RayBiotech Quantibody® Array, multiplexed sandwich ELISA-based quantitative array platform, enables us to accurately measure the concentration of multiple cytokines simultaneously. In detail, the serum samples and standards were incubated on the array overnight at 4°C. The slides were washed with a proprietary buffer and then incubated with a detection antibody at room temperature for 2 h. The slides were then washed and incubated with the streptavidin-conjugated Cy3 equivalent dye at room temperature for 1 h. Thereafter, the slides were washed a final time and then dried thoroughly before scanning with a laser scanner using the Cy3 excitation profile. Then, we calculated and analyzed the cytokine concentration.

Enzyme-Linked Immunosorbent Assay

Supernatants were collected from the BMSCs. The concentrations of IL-6 and IL-10 in the supernatant were determined by using commercial ELISA kits (NEOBIOSCIENCE, China), according to the manufacturer's instructions. The absorbance was measured by using a microplate reader at 450 nm.

Histological Procedure and Immunohistochemical Staining

The femur specimens were fixed in 4% paraformaldehyde for 24 h, decalcified with 10% EDTA in PBS for 3 weeks, embedded in paraffin, and sectioned to a 5-μm thick specimen. Sections were stained by hematoxylin and eosin (H&E) staining. For immunohistochemical staining, the sections were placed in sodium citrate buffer for 20 min at 90o̲C for antigen retrieval and incubated with monoclonal anti-mouse IL-6 and IL-10 antibodies overnight at 4°C.

Statistical Analysis

All the data were displayed as mean ± standard deviation (SD). ImageJ software was used for quantitative protein analysis. Data were evaluated by GraphPad Prism 7.00 software using Student's *t*-test or one-way ANOVA followed by Tukey's *post hoc* test. A *p*-value < 0.05 was considered significant.

RESULTS

With Increasing Age, the Probability of Age-Related Osteoporosis Increases.

Clinically, older patients have a higher incidence of fractures than younger patients. Hematoxylin–eosin (HE) staining of femur slices was used to assess the bone mass and fat content in young (8-week-old) mice and aged (78-week-old) mice. The bone mass in the aged group was significantly lower than that

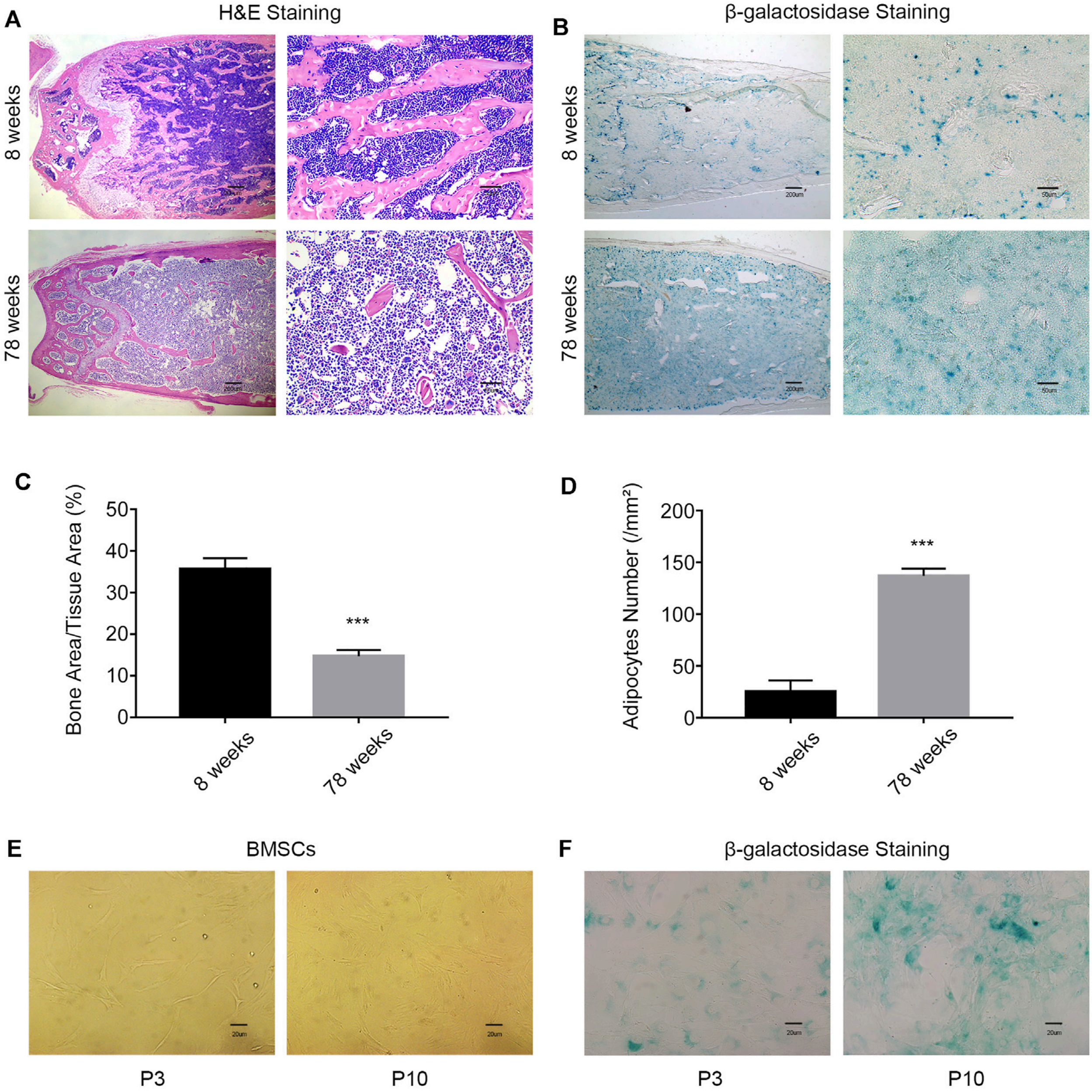

FIGURE 1 | With increasing age, the probability of age-related osteoporosis increases. **(A)** Representative images of H&E staining of the femurs of 8-week-old and 78-week-old WT mice. Scale bars, 200 and 50 μm. **(B)** β-Galactosidase staining of femur sections from 8-week-old and 78-week-old WT mice. Scale bars, 200 and 50 μm. **(C)** Percentage of the bone mass in femur sections from 8-week old and 78-week-old WT mice ($n = 3$ and $^{***}p < 0.001$). **(D)** Enumeration of bone adipocytes in the femurs of 8-week-old and 78-week-old WT mice ($n = 3$ and $^{***}p < 0.001$). **(E)** Morphology of MSCs was observed under an inverted microscope. Scale bar, 20 μm. **(F)** β-gal staining (blue: senescent cells) of MSCs was observed under an inverted microscope. Scale bar, 20 μm. P3, early passage; P10, late passage.

in the young group. Conversely, the fat content in the aged group was higher than that in the young group (**Figures 1A,C,D**). The activity of β-galactosidase was enhanced in the bone marrow cavity in the aged group, which indicated an increased percentage of the senescent cells in aged mice (**Figure 1B**). After long-term passage *in vitro*, the BMSCs in the aging group (P10) showed changes in morphology, including larger and flatter cell features (**Figure 1E**), and enhanced β-galactosidase activity (**Figure 1F**). These results indicated that the number of senescent cells increases with aging.

CM From Senescent MSCs Changes the Physiology of Young BMSCs

Stem cell senescence is caused by a combination of intrinsic and irreversible changes through circulating effectors or

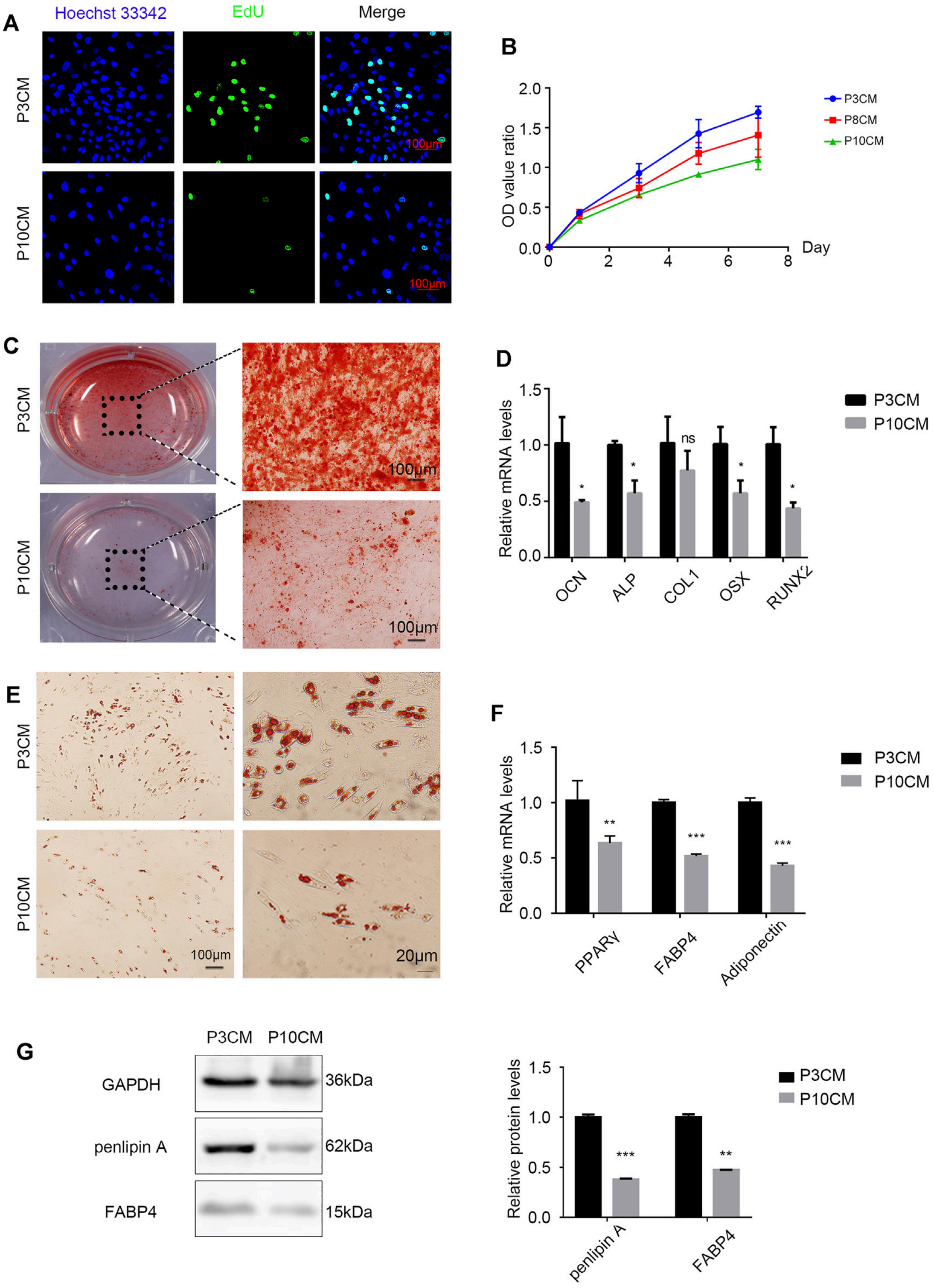

FIGURE 2 | CM from the senescent MSCs changes the physiology of young BMSCs. **(A)** EdU staining of the BMSCs cultured with P3 CM or P10 CM (scale bar: 100 μm). **(B)** Growth curves of the BMSCs cultured with P3 CM or P10 CM. **(C)** Alizarin red staining shows the osteogenic induction of the young BMSCs cultured with P3 CM or P10 CM ($n = 3$, magnification: × 100, and scale: 100 μm). **(D)** Real-time PCR showing the expressions of OCN, ALP, COL1, OSX, and RUNX2 ($n = 3$, $^{*}p < 0.05$, ns., and $p > 0.05$). **(E)** Oil red O staining of the young BMSCs cultured with P3 CM or P10 CM. **(F)** Real-time PCR showing the expressions of PPARγ, FABP4, and adiponectin ($n = 3$, $^{**}p < 0.01$, and $^{***}p < 0.001$). **(G)** Western blot analysis of lipid-related indicators such as FABP4 and perilipin A ($n = 3$, $^{**}p < 0.01$, and $^{***}p < 0.001$).

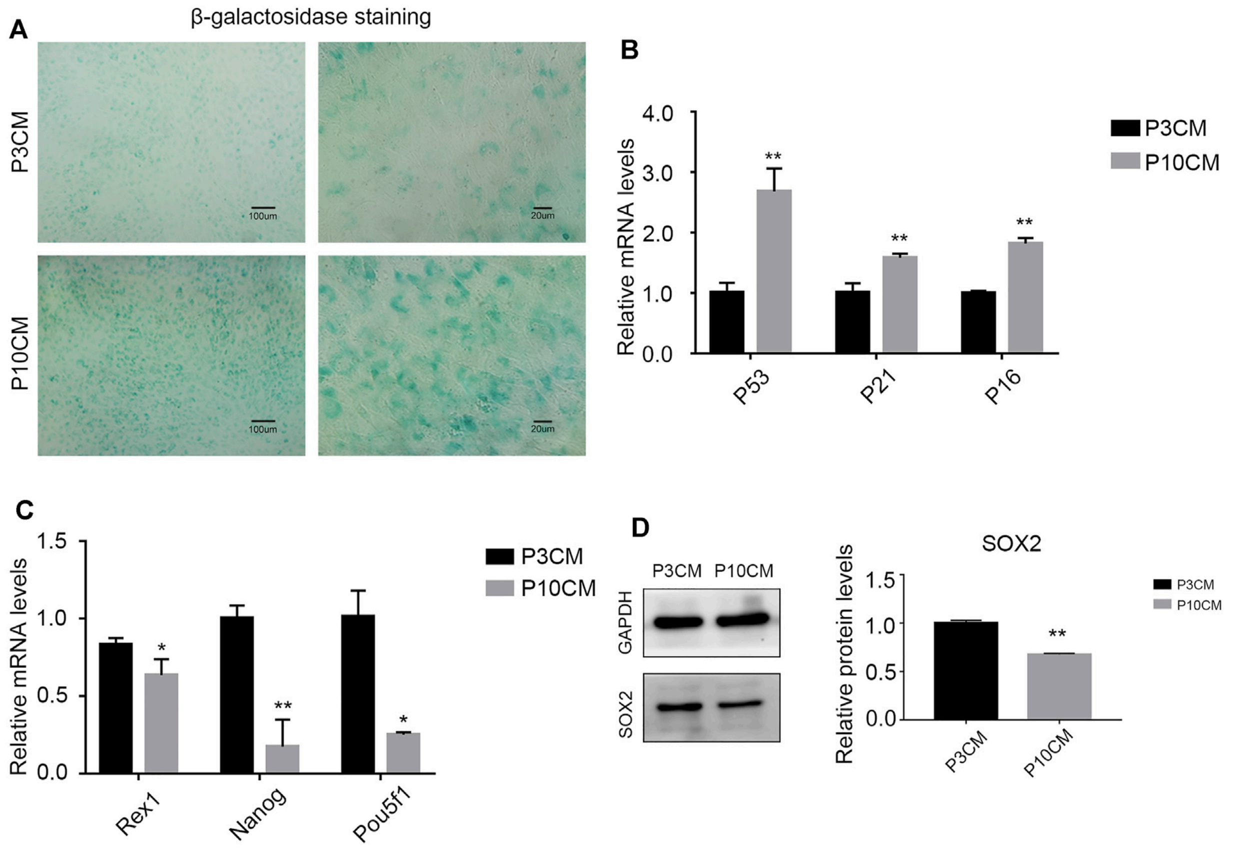

FIGURE 3 | CM from the senescent MSCs decreases stemness and triggers senescence in young BMSCs. **(A)** β-galactosidase staining of the BMSCs cultured with P3 CM or P10 CM. (Magnification: × 100, scale bar: 100 μm; magnification: × 400, scale bar: 20 μm). **(B)** Real-time PCR results showing the expressions of P53, P21, and P16 and other aging-related indicators ($n = 3$, **, and $p < 0.01$). **(C)** Real-time PCR results showing the expression of the stemness-related indicators Rex1, Nanog, and Pou5f1 ($n = 3$, *$p < 0.05$, and **, $p < 0.01$). **(D)** Western blot analysis verified the protein expression level of SOX2, a stemness-related indicator ($n = 3$ and **$p < 0.01$).

factors secreted by local stem cell niches (Severino et al., 2013). To determine whether extracellular factors produced by the senescent cells can alter the physiological characteristics of stem cells, proliferation and the differentiation capacity of young MSCs cultured with conditioned medium (CM) from the P3 and P10 BMSCs were evaluated. When P3 and P10 BMSC cultures reached an 80% confluency, the serum-free base medium was added after discarding the original medium, and the supernatant (CM) was collected and stored at −80°C for 48 h. As expected, the positive rate of EdU staining in the CM-P10 cultured cells was lower than that in the CM-P3 cultured cells ($n = 3$ and $p < 0.01$) (**Figure 2A**). The proliferation rate of BMSCs was gradually decreased when the cells were cultured in CM-P10 compared with those cultured in CM-P3 (**Figure 2B**). Alizarin red staining revealed that there was an evident decrease in osteoblast differentiation in the mBMSCs cultured in CM-P10 compared with those cultured in CM-P3 (**Figure 2C**, **Supplementary Figure S1**). Furthermore, the RT–PCR analysis indicated that the expressions of osteogenic markers, such as OCN, ALP, Runx2, and OSX, were decreased when the cells were cultured in CM-P10 ($n = 3$ and $p < 0.05$) (**Figure 2D**). Oil red O staining indicated that the number of lipid droplets in the CM-P10 group was significantly reduced compared to that in the CM-P3 group (**Figure 2E**, **Supplementary Figure S1**). Moreover, the expressions of PPARγ, Fabp4, adiponectin, and perilipin A, which are adipogenic markers, were decreased in the CM-P10 group (**Figures 2F**,G). The adipogenic capacity was decreased in the CM-P10 group. Taken together, these data indicate that the proliferation and differentiation capacity of BMSCs is significantly decreased by treatment with a conditioned medium of senescent cells.

With aging, the external microenvironment has a greater impact on the proliferation capacity of the BMSCs. However, the TUNEL assay showed that the external environment in aging had no obvious effect on BMSC apoptosis (**Supplementary Figure S2**). This result shows that the external environment in aging mainly reduces the number of BMSCs by reducing the proliferation of the BMSCs rather than inducing apoptosis.

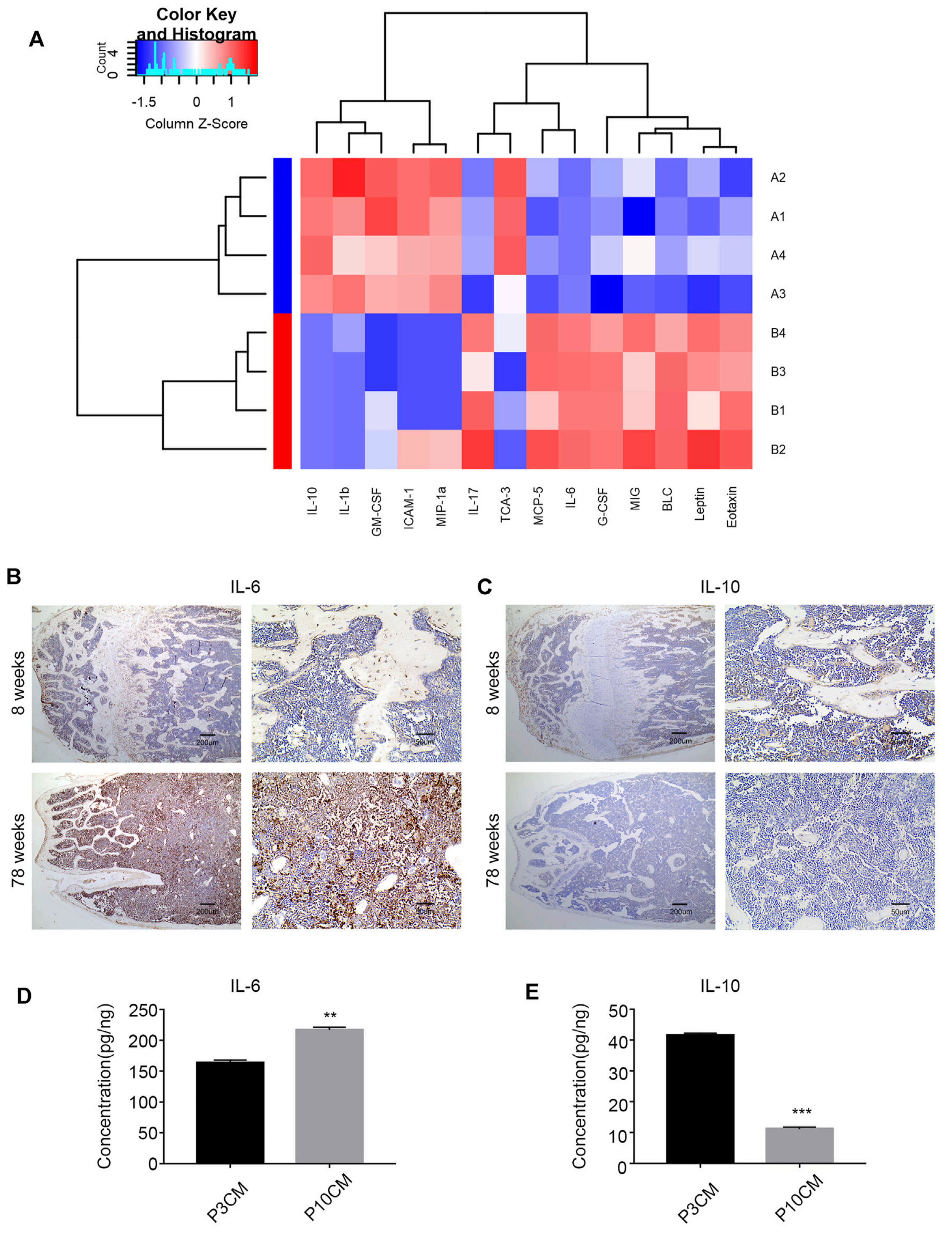

FIGURE 4 | Increased inflammation in the microenvironment with age. **(A)** Heatmap analysis of inflammatory factors in the serum of young mice (8 weeks old) and old mice (78 weeks old). (Group A: young group, Group B: aged group, *n* = 4). **(B)** Immunohistochemical analysis of the IL-6 expression in the bone marrow cavities of mice in different age groups. **(C)** Immunohistochemical analysis of the IL-10 expression in the bone marrow cavities of mice in different age groups. **(D)** ELISA was used to verify the level of IL-6 in the cell supernatant of the young group (P3 CM) and senescent group (P10 CM) (*n* =3, $^{**}p < 0.01$). **(E)** ELISA was used to verify the level of IL-10 in the cell supernatant of the young group (P3 CM) and senescent group (P10 CM) (*n* = 4 and $^{***}p < 0.001$).

CM From Senescent MSCs Decreases Stemness and Triggers Senescence in Young BMSCs

We cultured the BMSCs with CM-P3 and CM-P10 *in vitro*. The activity of β-galactosidase in the CM-P10 group was enhanced (**Figure 3A**). RT–PCR showed that the transcription level of the aging-related indicators P53, P21, and P16 was increased (**Figure 3B**). We know that the external microenvironment in aging can accelerate aging in young BMSCs. In addition, we measured the expression levels of Rex1, Nanog, and Pou5f1, which are related to cell stemness, and found that the external microenvironment in aging could reduce the stemness of BMSCs (**Figure 3C**). Western blot analysis verified that the protein expression level of SOX2, a dryness-related indicator, decreased after cells were cultured with CM-P10 (**Figure 3D**). These results demonstrated that the external environment in aging decreased the proliferation and stemness of the BMSCs and promoted BMSC senescence.

Increased Inflammation in the Microenvironment With Age

Chronic inflammation is associated with many diseases, and inflammatory factors play a key role. Studies have shown that elderly individuals are in a chronic, low-level subclinical pro-inflammatory state (Chung et al., 2011; Cevenini et al., 2013; Lin et al., 2017). To explore the relationship between the age-related inflammatory microenvironment and osteoporosis, we performed a Quantibody® mouse inflammation array on serum extracts from young (aged 8 weeks) and old (aged 78 weeks) mice. The expressions of pro-inflammatory cytokines and chemokines were increased in the serum of old mice, and 14 cytokines reached statistical significance (**Figure 4A**). The cytokines with significant differences are shown in **Supplementary Table S1**. Among them, the pro-inflammatory factor IL-6 was increased, and the anti-inflammatory factor IL-10 was decreased most obviously, suggesting a trend of increased inflammation.

To evaluate the changes in IL-6 and IL-10 in the bone marrow microenvironment during aging, we studied femur sections from young (8-week-old) and aged (78-week-old) male C57BL/6 mice. We analyzed the levels of IL-6 and IL-10 in the bone marrow in different age groups by immunohistochemistry. The results showed an increase in IL-6 and a decrease in IL-10 in the aged group (**Figures 4B,C**). We confirmed this trend in CM by ELISA, and the results revealed increases in the pro-inflammatory cytokine IL-6 and decreases in the anti-inflammatory cytokine IL-10 in CM-P10 (,**Figures 4D,E**). In summary, we demonstrated that the age-associated shift in the inflammatory microenvironment is associated with an increase in the pro-inflammatory cytokine IL-6 and a decrease in the anti-inflammatory cytokine IL-10.

GO and KEGG Analyses Predicted Age-Related Signaling

The age-related inflammatory microenvironment is characterized by an imbalance in inflammatory and anti-inflammatory pathways and is the basic mechanism of aging (Fougère et al., 2017; Franceschi et al., 2007). The GO and KEGG analyses (**Figures 5A,B**) were used to predict the potential mechanism. We hypothesized that these differentially expressed signaling pathways were the potential mechanism by which the BMSC functional changes were caused by the inflammatory microenvironment.

DISCUSSION

Chronic inflammation in the elderly population (inflammaging) is closely associated with many aging-related diseases, and an increasing number of studies have shown that stem cell therapy is a promising treatment for senile degenerative diseases (Kiernan et al., 2017; Samsonraj et al., 2017; Ding et al., 2019). Our study indicated that with increasing age, the bone mass decreased, and the number of aging cells increased. *In vitro* experiments proved that the aging microenvironment reduced the proliferation and differentiation of the BMSCs, resulting in enhanced aging characteristics in stem cells and decreased cell dryness. The inflammatory microenvironment affects many cellular physiological processes, one of which is cell senescence (Bottazzi et al., 2018). The senescent cells cannot function normally and secrete inflammatory cytokines and degradation proteins, which are called senescence-related secretory phenotype (SASP) factors (Wu et al., 2020). The SASP induces further aging and inflammation, leading to stem cell dysfunction, an aging phenotype, and chronic diseases (Kirkland and Tchkonia, 2017). The SASP is increasingly recognized as a promising therapeutic target for the prevention of age-related degenerative diseases, including osteoporosis (Farr et al., 2016). The inflammation-related factors with the most significant differences were the pro-inflammatory factor IL-6 and the anti-inflammatory factor IL-10, as screened by the protein chip technology. The changes in inflammation-related factors in the microenvironment of aging cells *in vitro* were consistent with the trend *in vivo*. The GO and KEGG analyses can lay the foundation for further mechanistic research and provide a theoretical basis and treatment strategy for stem cell therapy of age-related osteoporosis.

Many studies have shown that this age-related stem cell senescence is largely due to metabolic changes, abnormal mitochondrial activity, and impaired protein homeostasis (García-Prat et al., 2017). However, the importance of the aging pro-inflammatory environment for stem cell senescence is often neglected. A study suggested that age-related inflammation triggers skeletal stem/progenitor cell dysfunction (Josephson et al., 2019). Therefore, exploring this age-related pro-inflammatory state is of great clinical importance for the prevention and treatment of age-related osteoporosis. Our research explored the effect of the inflammatory microenvironment on the bone marrow mesenchymal stem cells *in vitro* and *in vivo*. *In vitro*, the bone marrow mesenchymal stem cells with aging characteristics were obtained through the long-term passage, and these cells were characterized by morphological changes and enhanced β-galactosidase activity (Biran et al., 2017). We found that the

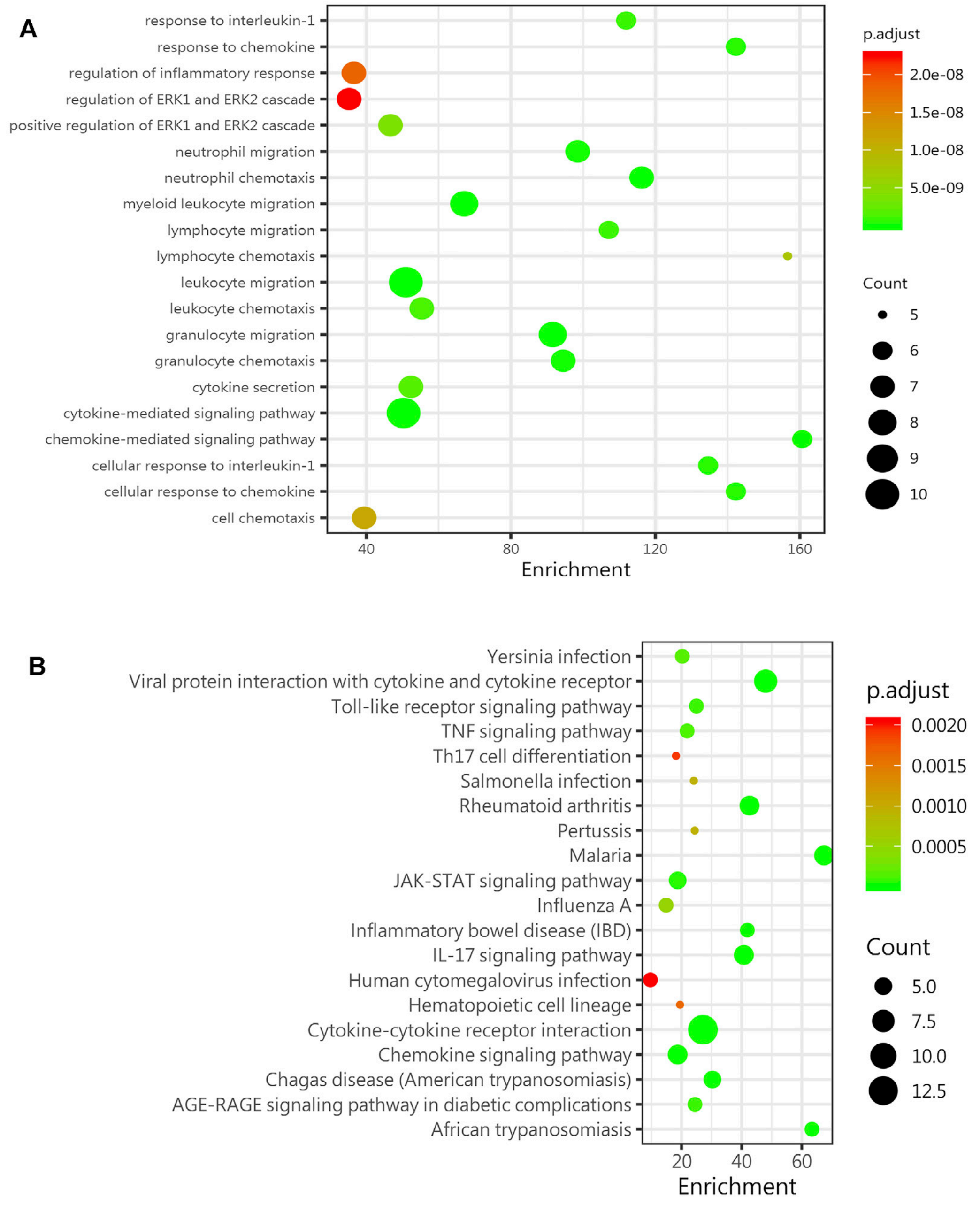

FIGURE 5 | GO and KEGG analyses predict age-related signaling pathways. **(A)** Representative GO_BP (biological process) analysis of inflammatory factors in the sera of mice in the young group (8-week-old mice) and the old group (78-week-old mice) (*n* = 4). **(B)** KEGG enrichment analysis of DEGs among inflammatory factors in the sera of mice in the young group (8-week-old mice) and the old group (78-week-old mice) (*n* = 4). Abbreviations: DEGs, differentially expressed genes.

proliferation of cells cultured in CM-P10 was weaker than that of the cells cultured in CM-P3. From this, we observed that this age-related external environment can reduce cell proliferation and accelerate cell aging. Furthermore, we induced osteogenesis and adipogenesis in the bone marrow mesenchymal stem cells and found that the ability of the P10CM-induced stem cells to undergo osteogenesis and adipogenesis was weaker than that of P3CM-induced stem cells. It is well known that the lineage of the bone marrow cells changes with age and is characterized by an obvious reduction in osteogenesis and an increase in adipogenesis (Li et al., 2017; Infante and Rodríguez, 2018). However, other studies pointed out that the ability of the mesenchymal stem cells to undergo osteogenesis and adipogenesis was generally decreased (Bonab et al., 2006). BMSCs have different aging mechanisms *in vitro* and *in vivo*. *In vivo*, the differentiation of the bone marrow mesenchymal stem cells is strictly controlled by the local environment, which maintains a balance between osteogenesis and adipogenesis. Aging itself may provide a favorable adipogenic environment, resulting in fat accumulation in the aged bone due to the cellular resistance to oxidative stress and apoptosis. (Kim et al., 2012; Chen et al., 2016; Li et al., 2016; Ganguly et al., 2017). According to Chen et al. (2016), the *in vitro* culture environment lacks complex molecular fate control mechanisms, including transforming growth factor-β (TGF-β)/ bone morphogenetic protein (BMP), Wnt and Hedgehog signals, and specific transcription factors, such as runt-related transcription factor 2 (Runx2) and peroxisome proliferator-activated receptor γ (PPARγ); thus, the balance between osteogenic and adipogenic differentiation is not maintained. According to our experimental results, we hypothesized that the aging-related inflammatory environment reduces the stemness of BMSCs, leading to the loss of differentiation ability. By examining stemness-related factors such as Nanog and OCT4, it was confirmed that the age-related inflammatory environment reduced the stemness of BMSCs.

To explore this aging inflammatory state in detail, we selected mice in different age groups and tested their sera with Quantibody®Mouse Infection Array 1. We found that 14 inflammatory factors and chemokines were significantly changed in the aged group compared with the young group, and most of these factors were upregulated. The two inflammation-related factors with the greatest changes were the pro-inflammatory factor IL-6 and the anti-inflammatory factors IL-10, IL-6, and IL-10 in the bone marrow, which showed the same trend. A study showed that an imbalance in IL-6 cytokine signaling contributes to the onset and maintenance of several diseases, including rheumatoid arthritis and osteoporosis. IL-6-type cytokines can lead to the activation of JAK/STAT (Janus kinase/signal transduction and transcription activator) and MAPK (mitogen activation) (Heinrich et al., 2003). Laren Becker et al. (Sui et al., 2016) showed that an increase in inflammatory factors such as IL-6, IL-1β, and IL-18 was observed in the enteric nervous system with age. Interleukin-10 (IL-10) is an anti-inflammatory cytokine with an important immunoregulatory role (Farr et al., 2017). IL-10 can block the NF-κB activity and participate in the regulation of the JAK-STAT signaling pathway. The increase in chemokines such as BLC (CXCL13), MCP-5 (CCL2), and eotaxin (CCL11) also indicates a disorder of the extracellular microenvironment. Through the GO and KEGG analyses, the JAK-STAT signaling pathway was shown to be significantly changed, laying the foundation for further research on relevant mechanisms.

Treatment strategies for osteoporosis include inhibiting stem cell senescence or eliminating the senescent cells (Jeon et al., 2017; Khosla et al., 2018). With increasing age, the number of senescent cells in the bone increases. These senescent cells produce pro-inflammatory factors, resulting in increased bone resorption and decreased bone formation (Lasry and Ben-Neriah, 2015; Sui et al., 2016). Targeting aging cells represents a novel therapeutic strategy that can prevent not only the bone loss but also a variety of age-related diseases (Lasry and Ben-Neriah, 2015; Sui et al., 2016). Studies have shown that small molecular compounds such as quercetin, rapamycin, resveratrol, and melatonin can inhibit stem cell senescence (Shuai et al., 2016; Yi et al., 2016; Li et al., 2018). Regeneration can be restored by regulating the inflammatory environment with pharmacological compounds (Hardeland, 2019). For example, JAK 1/2 inhibitors are used to inhibit the production of the pro-inflammatory SASP in aging cells (Xu et al., 2015a; Xu et al., 2015b; Wu et al., 2020). Another treatment strategy for osteoporosis is stem cell transplantation. Stem cells have a wide range of applications in basic research, and they have great potential in regenerative medicine. Stem cell therapy has been extensively studied in degenerative diseases and is a feasible treatment option (Drosos and Kolios, 2013; Holan et al., 2017). However, the limitation of stem cell transplantation is that a large number of young stem cells are needed. Understanding the inflammatory microenvironment is helpful in maintaining stem cell stemness. Some studies have shown the protective effect of melatonin on bone marrow mesenchymal stem cells during long-term passage *in vitro*. In addition to protecting stem cells and inhibiting aging, we can further explore whether the aging of stem cells can be reversed by changing the inflammatory environment to provide further support for stem cell therapy for age-related osteoporosis.

DATA AVAILABILITY STATEMENT

The original contributions presented in the study are included in the article/**Supplementary Material**; further inquiries can be directed to the corresponding authors.

ETHICS STATEMENT

The animal study was reviewed and approved by the Institutional Animal Care and Use Committee of Tongji Medical College, Huazhong University of Science and Technology (Wuhan, China, S780).

AUTHOR CONTRIBUTIONS

CY and YL designed the experiments and supervised the study. XP and XZ conducted the experiments and acquired the data. YY and BL analyzed the data. XP and XZ wrote the manuscript.

FUNDING

This work was funded by the National Natural Science Fund (82001026, to XZ) and the Hubei Province Key Research and Development (R&D) Program Project (2020BCA072, to CY).

SUPPLEMENTARY MATERIAL

The Supplementary Material for this article can be found online at: https://www.frontiersin.org/articles/10.3389/fbioe.2022.870324/full#supplementary-material

REFERENCES

Adamopoulos, I. E. (2018). Inflammation in Bone Physiology and Pathology. *Curr. Opin. Rheumatol.* 30, 59–64. doi:10.1097/bor.0000000000000449

Aghebati-Maleki, L., Dolati, S., Zandi, R., Fotouhi, A., Ahmadi, M., Aghebati, A., et al. (2019). Prospect of Mesenchymal Stem Cells in Therapy of Osteoporosis: A Review. *J. Cel Physiol* 234, 8570–8578. doi:10.1002/jcp.27833

Biran, A., Zada, L., Abou Karam, P., Vadai, E., Roitman, L., Ovadya, Y., et al. (2017). Quantitative Identification of Senescent Cells in Aging and Disease. *Aging Cell* 16, 661–671. doi:10.1111/acel.12592

Bonab, M. M., Alimoghaddam, K., Talebian, F., Ghaffari, S. H., Ghavamzadeh, A., and Nikbin, B. (2006). Aging of Mesenchymal Stem Cell *In Vitro*. *BMC Cel Biol* 7, 14. doi:10.1186/1471-2121-7-14

Bottazzi, B., Riboli, E., and Mantovani, A. (2018). Aging, Inflammation, and Cancer. *Semin. Immunol.* 40, 74–82. doi:10.1016/j.smim.2018.10.011

Cevenini, E., Monti, D., and Franceschi, C. (2013). Inflamm-ageing. *Curr. Opin. Clin. Nutr. Metab. Care* 16, 14–20. doi:10.1097/mco.0b013e32835ada13

Chen, Q., Shou, P., Zheng, C., Jiang, M., Cao, G., Yang, Q., et al. (2016). Fate Decision of Mesenchymal Stem Cells: Adipocytes or Osteoblasts? *Cell Death Differ* 23, 1128–1139. doi:10.1038/cdd.2015.168

Chung, H. Y., Lee, E. K., Choi, Y. J., Kim, J. M., Kim, D. H., Zou, Y., et al. (2011). Molecular Inflammation as an Underlying Mechanism of the Aging Process and Age-Related Diseases. *J. Dent Res.* 90, 830–840. doi:10.1177/0022034510387794

Ding, S. S. L., Subbiah, S. K., Khan, M. S. A., Farhana, A., and Mok, P. L. (2019). Empowering Mesenchymal Stem Cells for Ocular Degenerative Disorders. *Int. J. Mol. Sci.* 20. doi:10.3390/ijms20071784

Drosos, I., and Kolios, G. (2013). Stem Cells in Liver Regeneration and Their Potential Clinical Applications. *Stem Cel Rev Rep* 9, 668–684. doi:10.1007/s12015-013-9437-4

Farr, J. N., Fraser, D. G., Wang, H., Jaehn, K., Ogrodnik, M. B., Weivoda, M. M., et al. (2016). Identification of Senescent Cells in the Bone Microenvironment. *J. Bone Miner Res.* 31, 1920–1929. doi:10.1002/jbmr.2892

Farr, J. N., Xu, M., Weivoda, M. M., Monroe, D. G., Fraser, D. G., Onken, J. L., et al. (2017). Targeting Cellular Senescence Prevents Age-Related Bone Loss in Mice. *Nat. Med.* 23, 1072–1079. doi:10.1038/nm.4385

Fougère, B., Boulanger, E., Nourhash Mi, F., Guyonnet, S., and Cesari, M. (2017). Chronic Inflammation: Accelerator of Biological Aging. *J. Gerontol. A. Biol. Sci. Med. Sci.* 72, 1218–1225.

Franceschi, C., Capri, M., Monti, D., Giunta, S., Olivieri, F., Sevini, F., et al. (2007). Inflammaging and Anti-inflammaging: a Systemic Perspective on Aging and Longevity Emerged from Studies in Humans. *Mech. Ageing Develop.* 128, 92–105. doi:10.1016/j.mad.2006.11.016

Galkowski, D., Ratajczak, M. Z., Kocki, J., and Darzynkiewicz, Z. (2017). Of Cytometry, Stem Cells and Fountain of Youth. *Stem Cel Rev Rep* 13, 465–481. doi:10.1007/s12015-017-9733-5

Ganguly, P., El-Jawhari, J. J., Giannoudis, P. V., Burska, A. N., Ponchel, F., and Jones, E. A. (2017). Age-related Changes in Bone Marrow Mesenchymal Stromal Cells. *Cel Transpl.* 26, 1520–1529. doi:10.1177/0963689717721201

García-Prat, L., Sousa-Victor, P., and Mu Oz-C Noves, P. (2017). Proteostatic and Metabolic Control of Stemness. *Cell Stem Cell* 20, 593–608.

Hardeland, R. (2019). Aging, Melatonin, and the Pro- and Anti-inflammatory Networks. *Int. J. Mol. Sci.* 20. doi:10.3390/ijms20051223

Heinrich, P. C., Behrmann, I., Haan, S., Hermanns, H. M., Müller-newen, G., and Schaper, F. (2003). Principles of Interleukin (IL)-6-type Cytokine Signalling and its Regulation. *Biochem. J.* 374, 1–20. doi:10.1042/bj20030407

Holan, V., Hermankova, B., and Kossl, J. (2017). Perspectives of Stem Cell-Based Therapy for Age-Related Retinal Degenerative Diseases. *Cel Transpl.* 26, 1538–1541. doi:10.1177/0963689717721227

Infante, A., and Rodríguez, C. I. (2018). Osteogenesis and Aging: Lessons from Mesenchymal Stem Cells. *Stem Cel Res Ther* 9, 244. doi:10.1186/s13287-018-0995-x

Jeon, O. H., Kim, C., Laberge, R.-M., Demaria, M., Rathod, S., Vasserot, A. P., et al. (2017). Local Clearance of Senescent Cells Attenuates the Development of post-traumatic Osteoarthritis and Creates a Pro-regenerative Environment. *Nat. Med.* 23, 775–781. doi:10.1038/nm.4324

Josephson, A. M., Bradaschia-Correa, V., Lee, S., Leclerc, K., Patel, K. S., Muinos Lopez, E., et al. (2019). Age-related Inflammation Triggers Skeletal Stem/progenitor Cell Dysfunction. *Proc. Natl. Acad. Sci. U.S.A.* 116, 6995–7004. doi:10.1073/pnas.1810692116

Khosla, S., Farr, J. N., and Kirkland, J. L. (2018). Inhibiting Cellular Senescence: A New Therapeutic Paradigm for Age-Related Osteoporosis. *J. Clin. Endocrinol. Metab.* 103, 1282–1290. doi:10.1210/jc.2017-02694

Khosla, S., and Hofbauer, L. C. (2017). Osteoporosis Treatment: Recent Developments and Ongoing Challenges. *Lancet Diabetes Endocrinol.* 5, 898–907. doi:10.1016/s2213-8587(17)30188-2

Kiernan, J., Davies, J. E., and Stanford, W. L. (2017). Concise Review: Musculoskeletal Stem Cells to Treat Age-Related Osteoporosis. *Stem Cell Transl Med* 6, 1930–1939. doi:10.1002/sctm.17-0054

Kim, M., Kim, C., Choi, Y. S., Kim, M., Park, C., and Suh, Y. (2012). Age-related Alterations in Mesenchymal Stem Cells Related to Shift in Differentiation from Osteogenic to Adipogenic Potential: Implication to Age-Associated Bone Diseases and Defects. *Mech. Ageing Develop.* 133, 215–225. doi:10.1016/j.mad.2012.03.014

Kirkland, J. L., and Tchkonia, T. (2017). Cellular Senescence: A Translational Perspective. *EBioMedicine* 21, 21–28. doi:10.1016/j.ebiom.2017.04.013

Lasry, A., and Ben-Neriah, Y. (2015). Senescence-associated Inflammatory Responses: Aging and Cancer Perspectives. *Trends Immunol.* 36, 217–228. doi:10.1016/j.it.2015.02.009

Li, H., Liu, P., Xu, S., Li, Y., Dekker, J. D., Li, B., et al. (2017). FOXP1 Controls Mesenchymal Stem Cell Commitment and Senescence during Skeletal Aging. *J. Clin. Invest.* 127, 1241–1253. doi:10.1172/jci89511

Li, J., Liu, X., Zuo, B., and Zhang, L. (2016). The Role of Bone Marrow Microenvironment in Governing the Balance between Osteoblastogenesis and Adipogenesis. *Aging Dis.* 7, 514–525. doi:10.14336/ad.2015.1206

Li, Y.-R., Li, S., and Lin, C.-C. (2018). Effect of Resveratrol and Pterostilbene on Aging and Longevity. *Biofactors* 44, 69–82. doi:10.1002/biof.1400

Lin, H., Lunetta, K. L., Zhao, Q., Rong, J., Benjamin, E. J., Mendelson, M. M., et al. (2017). Transcriptome-wide Association Study of Inflammatory Biologic Age. *Aging* 9, 2288–2301. doi:10.18632/aging.101321

Paspaliaris, V., and Kolios, G. (2019). Stem Cells in Osteoporosis: From Biology to New Therapeutic Approaches. *Stem Cell Int* 2019, 1730978. doi:10.1155/2019/1730978

Samsonraj, R. M., Raghunath, M., Nurcombe, V., Hui, J. H., Van Wijnen, A. J., and Cool, S. M. (2017). Concise Review: Multifaceted Characterization of Human Mesenchymal Stem Cells for Use in Regenerative Medicine. *Stem Cell Transl Med* 6, 2173–2185. doi:10.1002/sctm.17-0129

Severino, V., Alessio, N., Farina, A., Sandomenico, A., Cipollaro, M., Peluso, G., et al. (2013). Insulin-like Growth Factor Binding Proteins 4 and 7 Released by Senescent Cells Promote Premature Senescence in Mesenchymal Stem Cells. *Cell Death Dis* 4, e911. doi:10.1038/cddis.2013.445

Shuai, Y., Liao, L., Su, X., Yu, Y., Shao, B., Jing, H., et al. (2016). Melatonin Treatment Improves Mesenchymal Stem Cells Therapy by Preserving Stemness during Long-Term *In Vitro* Expansion. *Theranostics* 6, 1899–1917. doi:10.7150/thno.15412

Sui, B. D., Hu, C. H., Zheng, C. X., and Jin, Y. (2016). Microenvironmental Views on Mesenchymal Stem Cell Differentiation in Aging. *J. Dent Res.* 95, 1333–1340. doi:10.1177/0022034516653589

Wu, W., Fu, J., Gu, Y., Wei, Y., Ma, P., and Wu, J. (2020). JAK2/STAT3 Regulates Estrogen-Related Senescence of Bone Marrow Stem Cells. *J. Endocrinol.* 245, 141–153. doi:10.1530/joe-19-0518

Xu, M., Palmer, A. K., Ding, H., Weivoda, M. M., Pirtskhalava, T., White, T. A., et al. (2015a). Targeting Senescent Cells Enhances Adipogenesis and Metabolic Function in Old Age. *Elife* 4, e12997. doi:10.7554/eLife.12997

Xu, M., Tchkonia, T., Ding, H., Ogrodnik, M., Lubbers, E. R., Pirtskhalava, T., et al. (2015b). JAK Inhibition Alleviates the Cellular Senescence-Associated Secretory Phenotype and Frailty in Old Age. *Proc. Natl. Acad. Sci. U S A.* 112, E6301–E6310. doi:10.1073/pnas.1515386112

Yi, J. S., Huang, Y., Kwaczala, A. T., Kuo, I. Y., Ehrlich, B. E., Campbell, S. G., et al. (2016). Low-dose Dasatinib Rescues Cardiac Function in Noonan Syndrome. *JCI Insight* 1, e90220. doi:10.1172/jci.insight.90220

Conflict of Interest: The authors declare that the research was conducted in the absence of any commercial or financial relationships that could be construed as a potential conflict of interest.

frontiers | Frontiers in Bioengineering and Biotechnology

TYPE Original Research
PUBLISHED 15 August 2022
DOI 10.3389/fbioe.2022.905194

OPEN ACCESS

EDITED BY
V. Prasad Shastri,
University of Freiburg, Germany

REVIEWED BY
Shireesh Srivastava,
International Centre for Genetic Engineering and Biotechnology (India), India
Muhammad Nawaz,
University of Gothenburg, Sweden

*CORRESPONDENCE
Junrong Cai,
drjunrongcai@outlook.com
Yunjun Liao,
Yunjun1000@sina.com

[†]These authors contributed equally to this work and should be considered co-first authors.

[‡]These authors contributed equally to this work and should be considered co-corresponding authors.

SPECIALTY SECTION
This article was submitted to Preclinical Cell and Gene Therapy, a section of the journal Frontiers in Bioengineering and Biotechnology

RECEIVED 26 March 2022
ACCEPTED 21 July 2022
PUBLISHED 15 August 2022

CITATION
He Y, Liang Z, Wang J, Tang H, Li J, Cai J and Liao Y (2022), Ceiling culture of human mature white adipocytes with a browning agent: A novel approach to induce transdifferentiation into beige adipocytes.
Front. Bioeng. Biotechnol. 10:905194.
doi: 10.3389/fbioe.2022.905194

Ceiling culture of human mature white adipocytes with a browning agent: A novel approach to induce transdifferentiation into beige adipocytes

Yufei He[†], Zhuokai Liang[†], Jing Wang, Haojing Tang, Jian Li, Junrong Cai*[‡] and Yunjun Liao*[‡]

Department of Plastic and Cosmetic Surgery, Nanfang Hospital, Southern Medical University, Guangzhou, Guangdong, China

Excess and dysfunctional adipose tissue plays an important role in metabolic diseases, including obesity, atherosclerosis and type 2 diabetes mellitus. In mammals, adipose tissue is categorized into two types: white and brown. Adult brown tissue is mainly composed of beige adipocytes, which dispose of stored energy as heat and have become increasingly popular as a therapeutic target for obesity. However, there is still a paucity of cell models that allow transdifferentiation of mature white adipocytes into beige adipocytes, as seen *in vivo*. Here, we describe a novel, ceiling culture-based model of human mature white adipocytes, which transdifferentiate into beige adipocytes under the mechanical force and hypoxia of ceiling culture. We also show that the use of rosiglitazone and rapamycin can modulate transdifferentiation, up and down regulating expression of beige adipocyte-specific genes, respectively. Rosiglitazone additionally facilitated the upregulation of fatty acid lipolysis and oxidation genes. Finally, these beige adipocytes derived from dedifferentiated adipocytes exhibited a progenitor-specific phenotype, with higher expression of mature adipocyte-specific genes than adipocyte-derived stem cells. Overall, we report a novel approach to conveniently cultivate beige adipocytes from white adipocytes *in vitro*, suitable for mechanistic studies of adipose biology and development of cell and drug therapies in the future.

KEYWORDS

white adipocytes, beige adipocytes, ceiling culture, transdifferentiate, metabolic disease

Introduction

Obesity is an increasingly prevalent lifestyle disease defined by excess adipose tissue (Saxton et al., 2019). Adipose tissue is a highly plastic organ essential for energy homeostasis by storing and releasing fat (primarily triglyceride) in response to energy demands (Klöting and Bluher, 2014). The limited storage capacity of adipose tissue can lead to ectopic fat storage, a key element in the pathogenesis of insulin-resistant cardiometabolic diseases, which can result metabolic dysfunction and in an imbalance of lipid homeostasis (Lotta et al., 2017).

Inducing the browning of white adipose tissue (to create beige adipocytes) may become a way of treating obesity and its associated metabolic complications (Cheng et al., 2021). Beige adipocytes exhibit multilocular lipid droplets (LDs), similar to brown adipocytes *in vivo*, and possess the metabolic activity of thermogenic cells, such as uncoupled respiration and cAMP-induced lipolysis (Cannon and Nedergaard, 2004). Compared with white adipocytes, beige adipocytes promote glucose clearance and fatty acid oxidation, thereby increasing energy consumption *via* thermogenesis, and potentially protecting against obesity and metabolic dysfunction (Desjardins and steinberg, 2018; Yao et al., 2017). As a result, an attractive therapeutic strategy has been identified to transform mature unilocular white adipocytes into multilocular, brown-like adipocytes with high uncoupling protein 1 (UCP1) expression (Harms and Seale, 2013).

However, the origin of beige adipocytes is controversial: they may transdifferentiate from existing mature white adipocytes or differentiate directly from beige precursor cells (Kaisanlahti and Glumoff, 2019; Wang et al., 2013; Wu et al., 2012). The browning of white adipose tissue by drug-induced transdifferentiation has become an increasingly popular research focus, including *via* peroxisome proliferator-activated receptor (PPAR)γ agonists (Rosiglitazone), β3 adrenergic receptor agonists (Mirabegron), and cyclic guanosine monophosphate-dependent protein kinase I agonists (Sildenafil) (Cypess et al., 2015; Merlin et al., 2018; Mitschke et al., 2013). However, due to a lack of appropriate culture models of transdifferentiation *in vitro*, most cell models use beige adipose precursor cells induced to differentiate into beige adipocytes (Hammarstedt et al., 2018; Rui, 2017). Therefore, a cell model of transdifferentiation of mature white adipocytes into beige cells is required.

Models of mature white adipocytes *in vitro* are still poorly understood, potentially slowing the development of clinical treatments for type 2 diabetes mellitus and other metabolic diseases. A method that utilizes a permeable, porous membrane and allows culture of freshly isolated, mature adipocytes provides a more representative model of *in vitro* conditions (Harms et al., 2019); however, the effect of oxygen concentration is often not considered on the fragile white adipocytes separated from the body. Another widely used method uses the stromal vascular fraction (SVF) from isolated adipose tissue and a 3D biological scaffold to create an adipose depot *in vitro*, termed “fat-on-a-chip” (Bender et al., 2020). Although this model maintains the structural integrity and functional characteristics of adipose tissue, such as lipolysis and secretion, it still differs from mature adipocytes *in vivo*.

Due to these limitations, many researchers rely on adipocytes differentiated from various cell types, including mouse embryonic fibroblasts, SVF from adipose tissue and the 3T3-L1 fibroblast-like cell line. However, it is unclear how much these cells represent the adipogenesis process from precursor cells *in vivo* (Ghaben and Scherer, 2019). As a result of the shortcomings of current cell models, development of cell and drug therapies for obesity and its related diseases has been severely restricted.

One method to overcome the limitations of current models is the ceiling culture method. During the process of transdifferentiation of white adipocytes to beige adipocytes, an increase of mitochondria and formation of numerous small LDs occurs (Barbatelli et al., 2010; Himms-Hagen et al., 2000). During this process, physical mechanics can facilitate the reduction of LD volume *via* lipolysis and liposecretion, allowing fatty acids to consumed as an energy source. The ceiling culture method applies mechanical force on freshly isolated, mature adipocytes, which float on culture medium and attach to the top of a filled, inverted cell culture flask (the “ceiling”). A few days later, adhered cells rapidly transdifferentiate into fibroblast-like cells, which are named dedifferentiated adipocytes (DAs) (Sugihara et al., 1987, 1986). Previously, we found a higher retention rate of fat grafts by using beige adipocytes from ceiling culture than adipose-derived stem cells (ADSCs), suggesting cells cultured by this method are physiologically relevant model (Xia et al., 2021).

In present, there are a number of characteristic specific markers are investigated during the period of adipocyte differentiation and maturation. Peroxisome proliferator-activated receptorγ (*PPARγ*), a primary regulator in adipocyte differentiation and maintenance, governs the main gene expression of lipid and glucose metabolism such as adipogenesis and fatty acid transport (Hernandez-Quiles et al., 2021). Its expression was detected in most of the induction processes in present study, which revealed cell component changes after applied agents. Expression of glucose transporter type 4 (*GLUT4*) has been demonstrated increased insulin-stimulated glucose uptake after the adipocyte differentiation. In addition, as a significant role in energy and expenditure, the adipocyte hormone Leptin is referred in control of adipocyte differentiation and homeostasis (Hwang et al., 1997). Adipocyte lipid binding protein 2 (*AP2*, also known as *FABP4*) is recognized as an essential link between lipid metabolism and cellular functions in adipocytes, which promotes proteosomal degradation of *PPARγ* in the terminal stage of adipocyte differentiation (Yang and Smith, 2007). These lineage specific differentiation markers were better to assess triglyceride

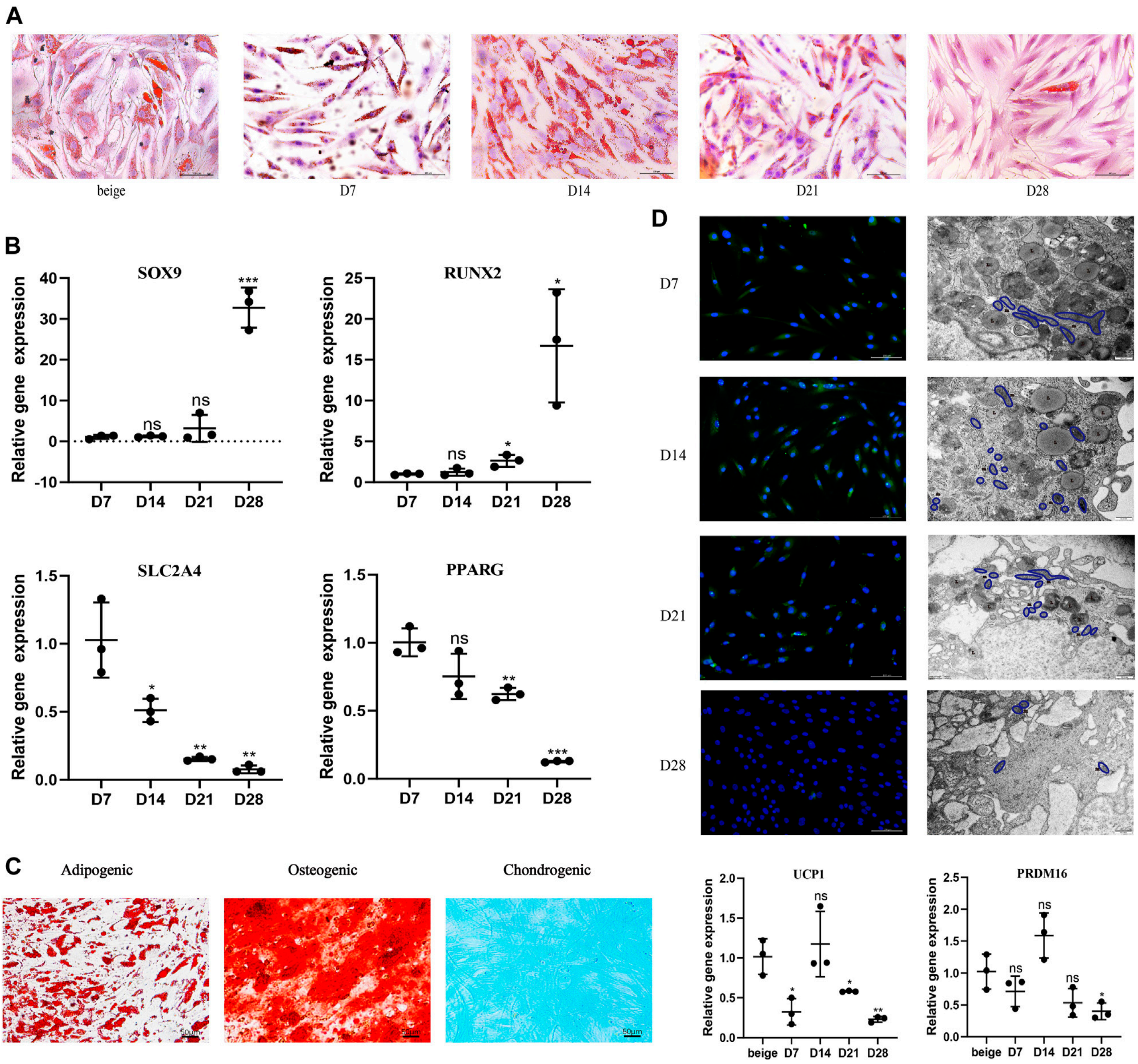

FIGURE 1
White adipocytes grown in ceiling culture display characteristics of beige adipocytes. **(A)** Intracellular lipid droplets were stained with Oil Red O and visualized by light microscopy at indicated timepoints (days) after the ceiling culture of mature white adipocytes. Scale bar 100 μm. **(B)** Relative gene expression levels of *SOX9*, *RUNX2*, *SLC2A4*, and *PPARG*, normalized to *GAPDH* as an endogenous control. **(C)** Human dedifferentiated adipocytes (DAs) were cultured for 3 weeks in adipogenic medium, osteogenic medium or chondrogenic medium. Cells were stained positively for lipid vacuoles with Oil Red O, for calcified extracellular matrix with Alizarin Red, and for chondrogenic differentiation Alcian Blue. Scale bar 50 μm. **(D)** Fluorescence microscopy visualized UCP1 expression stained with Alexa Fluor 488 (green) and nuclei stained with DAPI (blue). Scale bar 100 μm. Transmission electron microscopy showed condensed mitochondria and lipid droplet content at different stages of dedifferentiation. L, lipid; m, mitochondria. Scale bar 500 nm. Relative gene expression levels of *UCP1* and *PRDM16* compared to beige adipocytes, normalized to *GAPDH* as an endogenous control. Data are mean ± SEM ($n = 3$). ns, non-significant. $^{*}p < 0.05$, $^{**}p < 0.01$, $^{***}p < 0.001$.

accumulation per cell and adipocyte-specific gene expression during the process of transdifferentiation.

In this report, we describe a novel method for the ceiling culture of mature white adipocytes combined with a browning inducer (Rosiglitazone), which causes transdifferentiation into beige adipocytes. These adipocytes provide an *in vitro* model that simulates the phenotype and function of beige cells *in vivo*, which was superior to traditional culture methods. Importantly, we found evidence that mature white adipocytes can directly

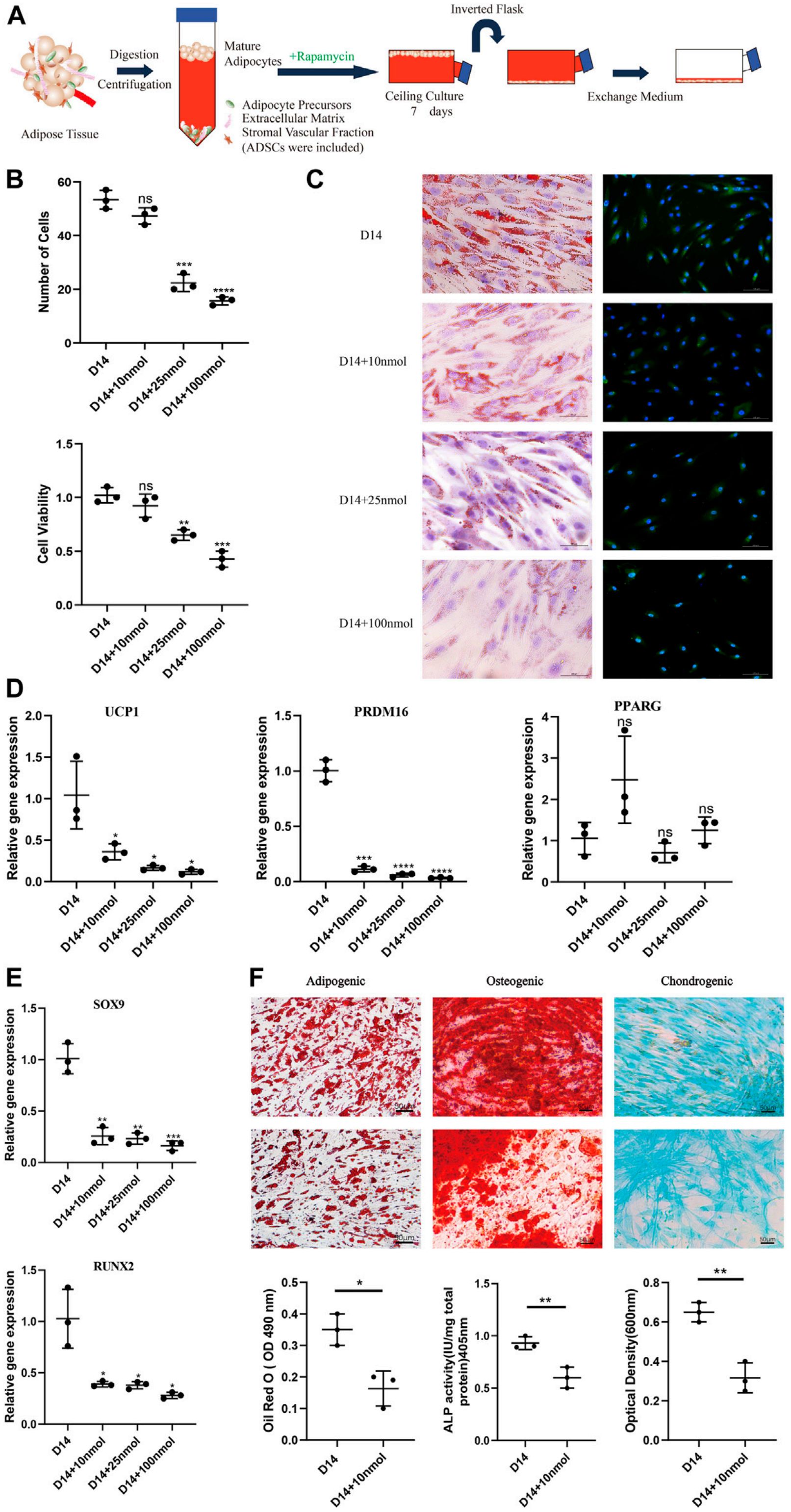

FIGURE 2

Effect of rapamycin on the dedifferentiation capacity of mature white adipocytes. **(A)** Model depicting the use of rapamycin to culture mature adipocytes. **(B)** MTT assay results confirmed that cell viability of dedifferentiated adipocyte (DA)-intermediate cells was inhibited by rapamycin, and the effect was concentration-dependent. **(C)** Intracellular lipid droplets were stained with Oil Red O and visualized by light microscopy. Fluorescence microscopy visualized UCP1 expression stained with Alexa Fluor 488 (green) and nuclei stained with DAPI (blue), in cells treated with 10, 25, and

(Continued)

FIGURE 2
100 nM rapamycin during ceiling culture of mature white adipocytes for 14 days. Scale bar 100 μm. **(D)** Relative gene expression levels of *UCP1*, *PRDM16*, and *PPARG*, normalized to *GAPDH* as an endogenous control. **(E)** Relative gene expression levels of *SOX9* and *RUNX2* normalized to *GAPDH* as an endogenous control, treated with 10, 25, and 100 nM rapamycin during ceiling culture of mature white adipocytes for 14 days. Data are mean ± SEM ($n = 3$). ns, non-significant. $*p < 0.05$, $**p < 0.01$, $***p < 0.001$. **(F)** Confluent human DA cells were cultured for 3 weeks and treated with 10 nM rapamycin in adipogenic medium, osteogenic medium and chondrogenic medium. Cells were stained positively for lipid vacuoles with Oil Red O, before Oil Red O extracted from cells with isopropanol and quantified at an optical absorbance of 510 nm. Calcified extracellular matrix was visualized with Alizarin Red and measured at an optical absorbance of 405 nm. Chondrogenic differentiation was visualized with Alcian Blue and the extract was measured at 600 nm. Scale bar 50 μm.

transdifferentiate into beige cells *in vitro* without the involvement of precursor cells.

Materials and methods

Human adipose

Adipose tissue was removed as abdominal lipoaspirates from three young, non obese females (mean BMI = 22.8 ± 0.26). Under general anesthesia, the abdominal wall was injected with saline solution containing 0.001% epinephrine and adipose tissue was suctioned using a multiport 3 mm cannula with sharp side holes 1 mm in diameter. Freshly obtained fat tissue was preserved at 4°C and prepared for downstream experiments.

Isolation and induction of beige adipocytes and ADSCs

Approximately 20 g of adipose tissue was incubated for 45 min at 37°C with 0.075% (w/v) collagenase solution (collagenase type I; Sigma, St. Louis, MO, United States); tissue was rotated two to three times at 15 min intervals. After 45 min, collagenase digestion was terminated by the addition of an equal volume of complete medium consisting of high-glucose (4.5 g/L) Dulbecco's Modified Eagle Medium (Gibco, Thermo Fisher Scientific, Inc., Waltham, MA, , United States), 10% (v/v) fetal bovine serum (Gibco), and 1% penicillin-streptomycin solution (Gibco); the cell suspensions were then centrifuged for 10 min at 200 rpm. Floating, unilocular adipocytes were harvested from the top layer and filtered with 100 μm strainer; ADSCs were harvested from the SVF in the bottom layer and filtered with 100 and 70 μm strainers (Xia et al., 2021). Harvested ADSCs was identified the surface antigens CD44 by flow cytometry and detected multi-differentiation potential (adipogenic, osteogenic, and chondrogenic characteristics). Adipocytes and ADSCs were respectively identified by qPCR to detect the expression of *FABP4*, *SLC2A4* and *CD44*, *THY1* markers (Wheeler et al., 2018) (Supplementary Material S1).

For ceiling culture of beige adipocytes, extracted mature adipocytes were seeded at a density of 0.5–1 × 106 cells per 25 cm^2 flask. Flasks were filled with complete culture medium and inverted, so that floating cells could attach to the top surface of the flask. Culture medium consisted of high-glucose (4.5 g/L) Dulbecco's Modified Eagle Medium, 10% (v/v) newborn calf serum, 4 mM L-glutamine, 50 U/ml penicillin, and 50 U/ml streptomycin; cells grown in this condition are referred to as ceiling-cultured cells. Where indicated, this was supplemented with 1 μM rosiglitazone (Merlin et al., 2018); cells grown in this condition are referred to as ceiling-cultured+roziglitazone cells. Cells were incubated at 37°C in 5% carbon dioxide; after 7 days, flasks were reinverted, and medium was changed every 3 days.

To culture and induce the ADSCs, cells from the SVF were seeded into a 25 cm^2 flask and cultured in Growth Medium for Human ADSCs (Cyagen Biosciences, Inc., Guangzhou, People's Republic of China) supplemented with 10% (v/v) fetal bovine serum, 2 mM L-glutamine, 50 U/ml penicillin, and 50 U/ml streptomycin and subcultured after reaching 70–80% confluence. After cells were passaged one to three times, confluent cultures were stimulated with a "browning cocktail" (growth media supplemented with 0.5 μg/ml insulin, 10 μM dexamethasone, 0.5 mM 3-Isobutyl-1-methylxanthine, 1 μM rosiglitazone, and 2 nM triiodothyronine) for 3 days. After this, cells were maintained in growth media supplemented with 0.5 μg/ml insulin for 1 day. The process of stimulated and maintained culture was continuously repeated three to four times (12–16 days). Cells were treated with CL316,243 (2 μM, Apexbio, Houston, United Kingdom), a highly selective β3-adrenoceptor agonist, 8–12 h before harvest.

Transmission electron microscopy

Beige adipocytes differentiated from ADSCs, ceiling culture-induced beige adipocytes, DA-induced beige adipocytes and DA-intermediate state (multilocular adipocytes formed in ceiling-cultured with a similar appearance to beige adipocytes) were washed with phosphate-buffered saline (PBS) and centrifuged at 3000 rpm for 5 min to form a pellet. The cell pellet was fixed with 2% glutaraldehyde in PBS for 2 h at 4°C, then postfixed by incubating with 1% osmium tetroxide in phosphate buffer 0.1 M (pH 7.4) for 15 min three times. Finally, the sample was dehydrated in ethanol and

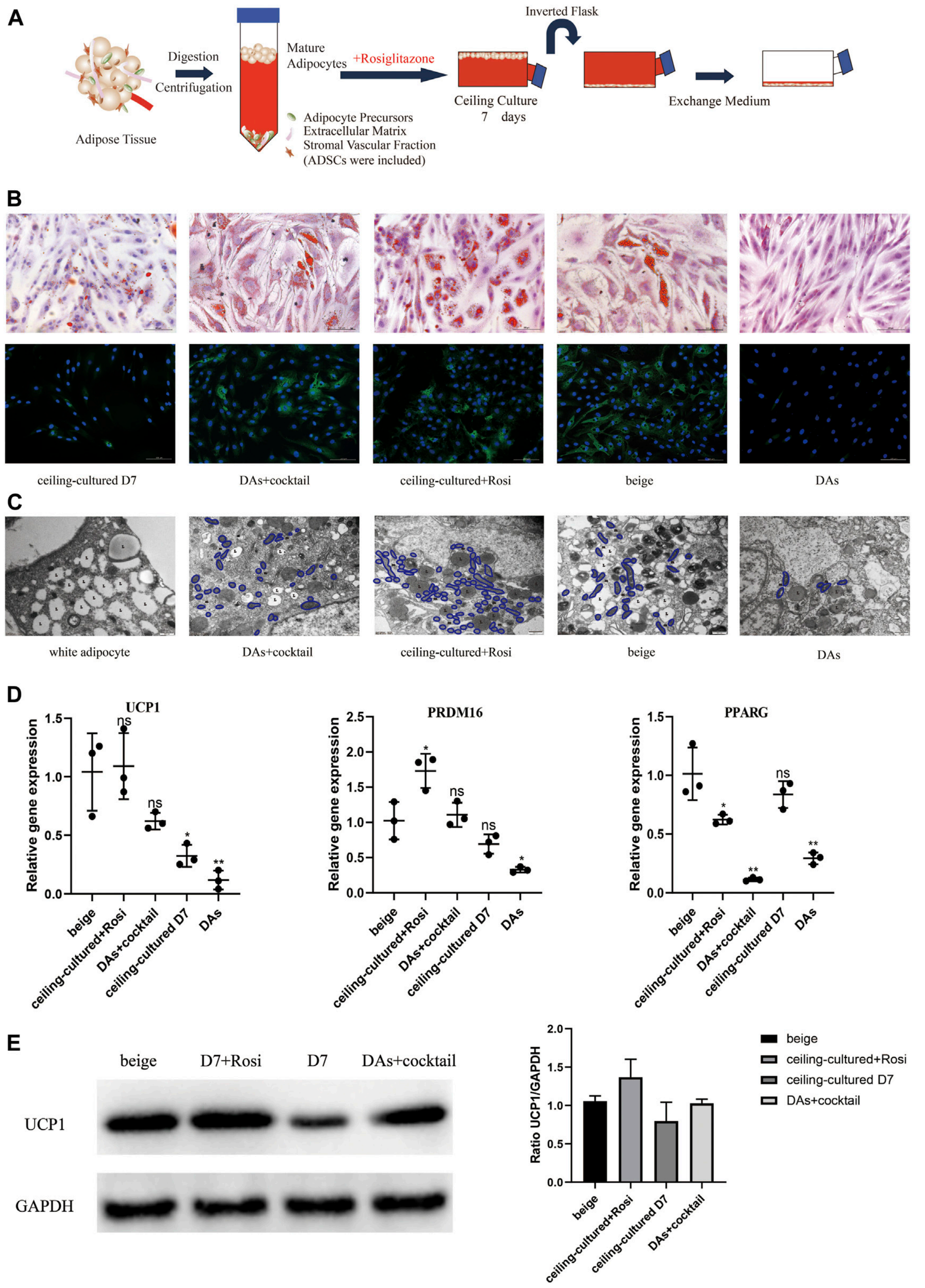

FIGURE 3
Ceiling-cultured adipocytes can transdifferentiate into beige adipocytes. **(A)** Model depicting the use of rosiglitazone to culture mature adipocytes. **(B)** Intracellular lipid droplets were stained with Oil Red O and visualized by light microscopy. Fluorescence microscopy visualized UCP1 expression stained with Alexa Fluor 488 (green) and nuclei stained with DAPI (blue). Scale bar 100 μm. **(C)** Transmission electron microscopy results showed that induced beige adipocytes and ceiling-cultured+Rosi cells exhibited condensed mitochondria compared with

(*Continued*)

FIGURE 3
dedifferentiated adipocytes (DAs) and white adipocytes. L, lipid; m, mitochondria. Scale bar 500 nm. **(D)** Relative gene expression levels of *UCP1*, *PRDM16*, and *PPARG*, normalized to *GAPDH* as an endogenous control. Data are mean ± SEM (n = 3). ns, non-significant. *$p < 0.05$, **$p < 0.01$, ***$p < 0.001$. **(E)** Representative protein bands of UCP1. Corresponding peak areas were normalized to GAPDH, and relative ratios compared to GAPDH are shown. Data are mean ± SEM (n = 3). *$p < 0.05$, **$p < 0.01$, ***$p < 0.001$.

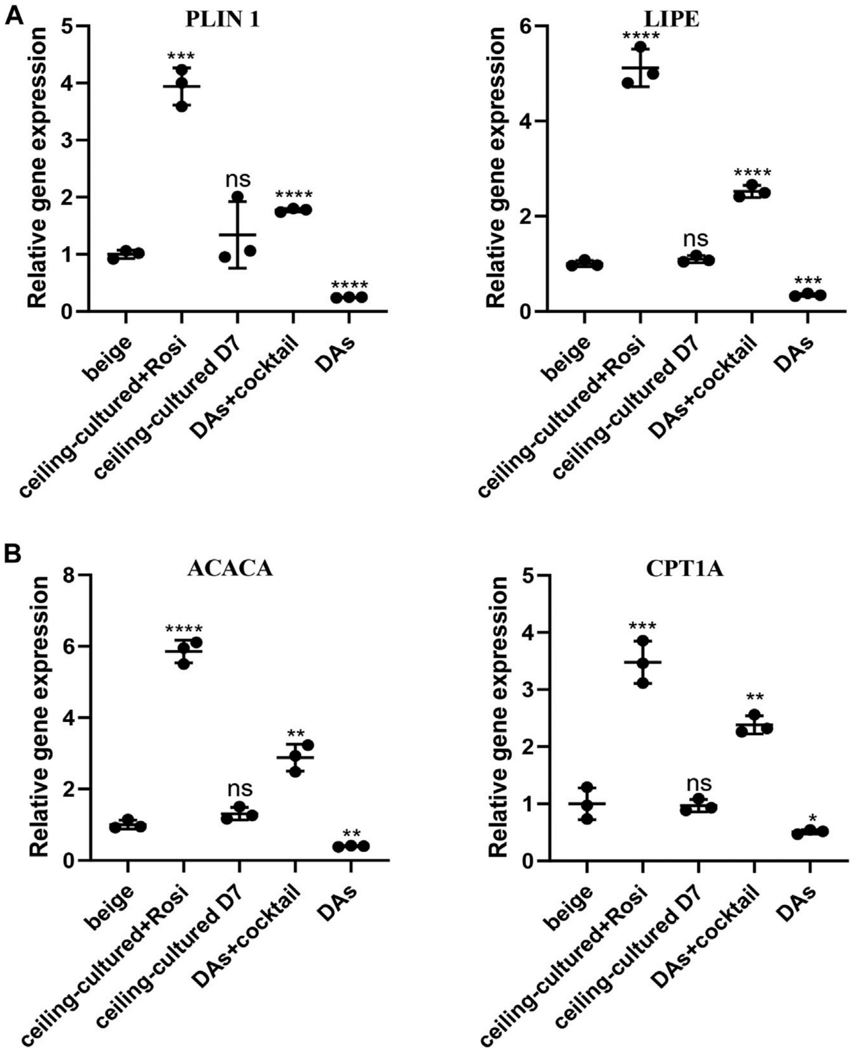

FIGURE 4
Fatty acid metabolism-related gene expression in beige adipocytes. **(A)** Relative gene expression levels of the lipolysis-related genes *PLIN1* and *LIPE*, normalized to *GAPDH* as an endogenous control. **(B)** Relative gene expression levels of the oxidative genes *ACACA* and *CPT1A*, normalized to *GAPDH* as endogenous control. Data are mean ± SEM (n = 3). ns, non-significant. *$p < 0.05$, **$p < 0.01$, ***$p < 0.001$.

embedded in an Epon-Araldite mixture. Thin sections were obtained with an EM UC7 Ultramicrotome (Leica, Wentzler, Germany), before staining with lead citrate, and examining with a transmission electron microscope (Tecnai G2 Spirit 120kV; ThermoFisher, NY, United States). For each condition, 100 cells were randomly picked and examined at a final magnification of 8750×. The cytoplasmic area was obtained with the aid of an image analysis system (Tecnai G2 Spirit 120kV; ThermoFisher, NY, United States). The investigators performing the transmission electron microscopy were blinded to the study and were asked to make an unbiased assessment.

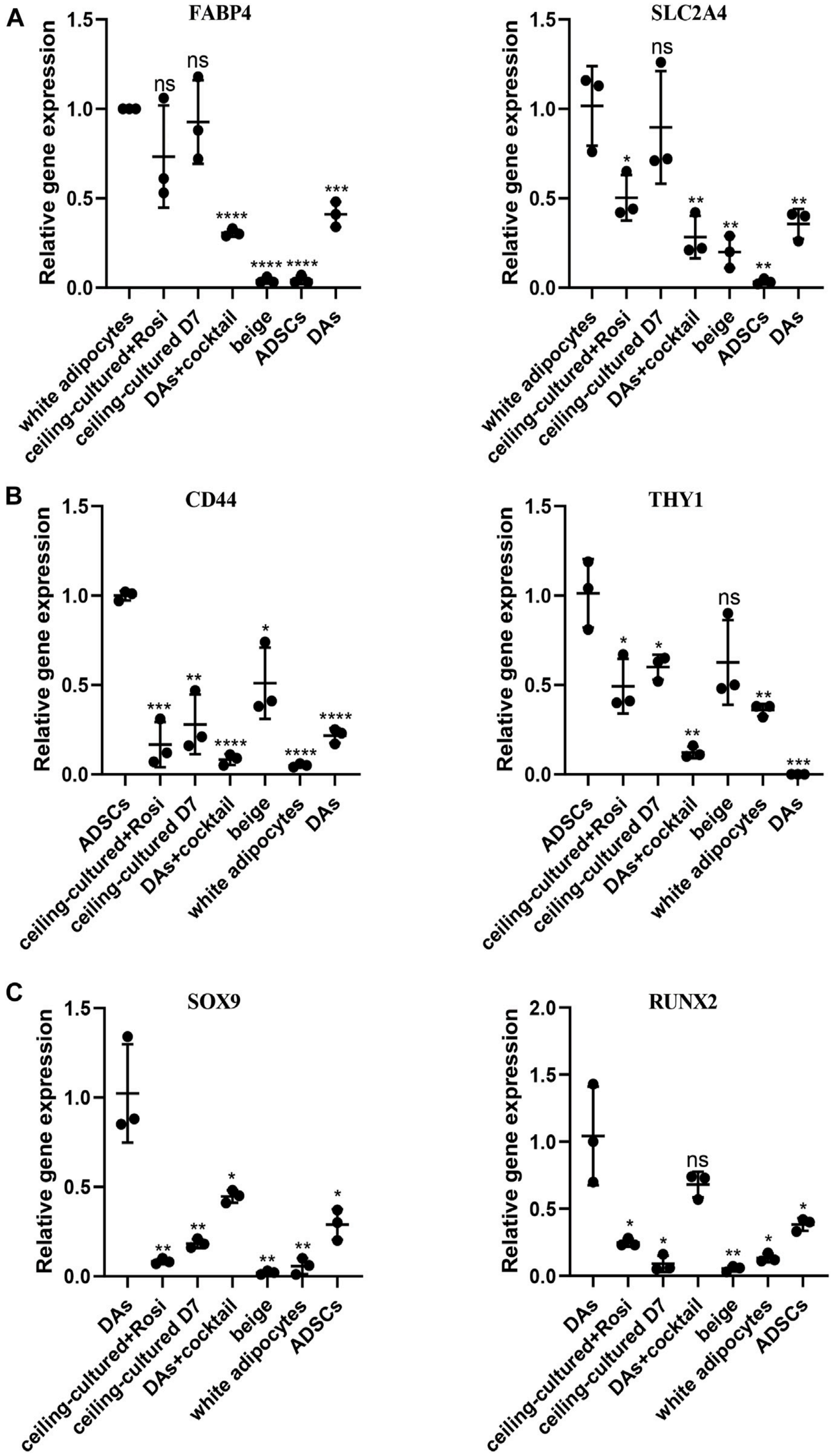

FIGURE 5
Beige adipocytes from different sources identified by gene expression of cell type-specific markers. **(A)** Relative gene expression levels of adipocyte-specific genes *FABP4* and *SLC2A4*, normalized to *GAPDH* as an endogenous control. **(B)** Relative gene express of the ADSC-specific markers *CD44* and *THY1*, normalized to *GAPDH* as an endogenous control. **(C)** Dedifferentiated adipocytes **(**DAs**)** gene expression of the mesenchymal lineage-committed markers *RUNX2* and *SOX9*, normalized to *GAPDH* as an endogenous control. Data are mean ± SEM ($n = 3$). ns, non-significant. $^{*}p < 0.05$, $^{**}p < 0.01$, $^{***}p < 0.001$.

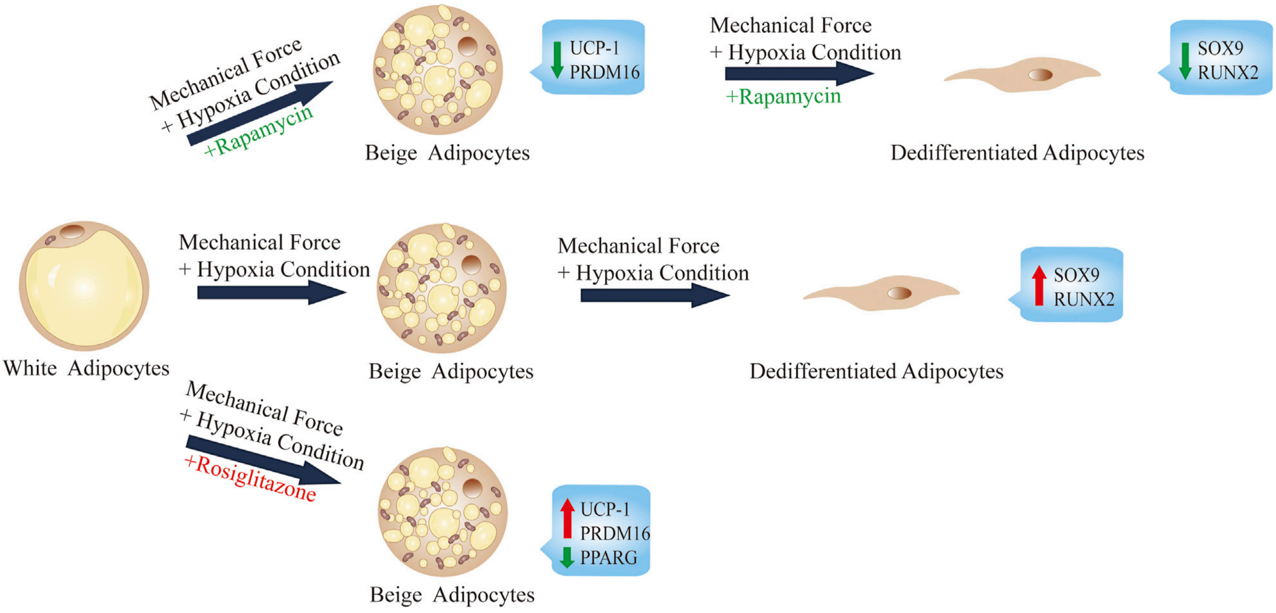

FIGURE 6
Summary and proposed model of ceiling culture of human mature white adipocytes with a browning agent.

MTT assay

Cell viability was determined by using the 3-(4,5-dimethylthiazol-2-yl)-2,5-diphenyltetrazolium bromide (MTT; Solarbio, Guangzhou, People's Republic of China) colorimetric assay. In short, cells were seeded into 96-well plates and treated for 72 h with different concentrations of rapamycin (0, 10, 25 and 100 nM). After treatment, cells were washed with PBS and incubated in MTT solution (Solarbio) for 4 h. Dimethyl sulfoxide was then added to each well, and absorbance was measured at 490 nm with a microplate reader (BioRad, CA, United States).

Oil Red O staining

Cells were fixed with 10% formalin and incubated for 30 min at 37°C with gentle shaking. Cells were then washed with 60% isopropanol and incubated in Oil Red O working solution. After 10 min, plates were rinsed with distilled water four times. Next, cells were stained in Mayer's hematoxylin for 30 s and washed thoroughly in distilled water three times. Oil Red O was quantified by measuring optical absorbance at 510 nm.

Alizarin Red staining

Cells were fixed in cold 10% formalin for 20 min at 4°C. Fixed cells were then stained with 400 μl Alizarin Red at pH 7.2 for 5–10 min. For calcium quantification, 300 μl 10% acetic acid was added to cells stained with Alizarin Red and incubated for 30 min at room temperature with agitation. Cells were scraped off and centrifuged for 30 min at 2000 rpm, before 200 μl of the supernatant was transferred to another microtube, and 22.5 μl of 10% ammonium hydroxide was added to neutralize the acid. Finally, optical absorbance was measured at 405 nm.

Alcian Blue staining

Cells were fixated in 10% formalin for 1 h and washed twice with PBS before incubation in 1% Alcian Blue prepared in 0.1 N HCl for 30 min. Cells were washed three times in 0.1 N HCl and distilled water was used to neutralize the pH. Quantification was performed by incubation in 6 M Guanidine-HCl solution overnight at 4°C. Staining was measured *via* absorbance at 600 nm.

Immunofluorescent staining

For immunofluorescent staining, cells were fixed with 4% paraformaldehyde and blocked with 5% BSA for 2 h at room temperature, and then incubated with the primary antibody rabbit anti-mouse UCP1 (dilution, 1:200; Proteintech, Chicago, United States). After washing, sections were incubated with the secondary antibody Alexa Fluor 488-

conjugated goat anti-rabbit immunoglobulin G (1:200; Thermo Fisher, Holtsville, NY, United States). Nuclei were stained with DAPI (Solarbio, Guangzhou, People's Republic of China).

Western blot analysis

Whole beige adipocyte lysates (25 μg) in RIPA buffer containing protease inhibitor cocktail and phenylmethylsulfonyl fluoride were prepared using 5× SDS-PAGE loading buffer [250 mM Tris-HCl (pH 6.8), 0.25% bromophenol blue, 50% glycerol, 10% SDS, 0.5 M DTT (Bioseang Inc., Seongnam, Korea)] for separation by SDS-PAGE. After electrophoretic separation, gels were transferred onto activated polyvinylidene difluoride membranes for 1 h at 0.4 A. Membranes were blocked with 5% BSA for 2 h at room temperature and incubated with the primary antibody, rabbit anti-mouse UCP1 (dilution, 1:500; Proteintech, Chicago, United States)., which was diluted in blocking solution, for a minimum of 12 h at 4°C. Membranes were then incubated with secondary horseradish peroxidase-conjugated antibodies, HRP-conjugated affinipure goat anti-mouse immunoglobulin G (1: 10,000; ZSGB-BIO, Inc., Beijing, People's Republic of China)) for 2 h at room temperature, before visualization using the Supernova ECL western blotting detection system and imaging with the ChemiDocTMTouch (BioRad, CA, United States). Band intensities were quantified using ImageJ software. Assays were performed with samples from at least three independent experiments.

Quantitative real-time polymerase chain reaction

Total RNA was extracted from cells using the RNeasy Lipid Tissue Mini Kit (Qiagen, Hilden, Germany), according to the manufacturer's instructions. cDNA was synthesized and amplified over 40 cycles using a QuantiTect Reverse Transcription Kit (Qiagen) and a Rotor-Gene 3000 Real-Time PCR Detection System (Corbett Research, Sydney, Australia). (quantity of total RNA(ng) and cDNA(ng) were listed in Supplementary Material S2).

The primer sequences were as follows: UCP1: forward 5′-AGGATCGGCCTCTACGACAC-3′ and reverse 5′-GCCCAATGAATACTGCCACTC-3′; PRDM16: forward 5′-CGAGGCCCCTGTCTACATTC-3′ and reverse 5′-GCTCCCATCCGAAGTCTGTC-3′; PPARG: forward 5′-GGGATCAGCTCCGTGGATCT-3′ and reverse 5′-TGCACTTTGGTACTCTTGAAGTT-3′; SOX9: forward: 5′-AGGTGCTCAAAGGCTACGAC-3′ and reverse 5′-GTAATCCGGGTGGTCCTTCT-3′; RUNX2: forward 5′-GGACGAGGCAAGAGTTTCAC-3′ and reverse 5′-TGCCTGCCTGGGGTCTGTAA-3′; LIPE: forward 5′-CTCCTCCTATTCCTAATCCTCC-3′ and reverse 5′-CACTTCCTCTTGGGTTTCACTC-3′; PLIN1: forward 5′-GCAAGAAGAGCTGAGCAGAC-3′ and reverse 5′-AATCTGCCCACGAGAAAGGA-3′; CPT1A: forward 5′-AGAACACTCATGGGCAGATGCT-3′ and reverse 5′-TACCTTTCACCTGGGCTACACG-3′; ACACA: forward 5′-GGACCACTGCATGGAATGTTAA-3′ and reverse 5′-TGAGTGACTGCCGAAACATCTC-3′ FABP4: forward 5′-GCTTTTGTAGGTACCTGGAAACTT-3′ and reverse 5′-ACACTGATGATCATGTTAGGTTTGG-3′ SLC2A4: forward 5′-TGGGCGGCATGATTTCCTC-3′ and reverse 5′-GCCAGGACATTGTTGACCAC-3′ CD44: forward 5′-CTGCAGGTATGGGTTCATAG-3′ and reverse 5′-ATATGTGTCATACTGGGAGGTG-3′ THY1: forward 5′-ATGAACCTGGCCATCAGCA-3′ and reverse 5′-GTGTGCTCAGGCACCCC-3′.

The expression of each gene was normalized relative to that of *GAPDH*, with expression levels calculated using the $2^{-\Delta\Delta Ct}$ method.

Statistical analysis

Statistical analyses were performed using SPSS version 25.0 (IBM, Inc., Armonk, NY, United States). Data are expressed as mean ± SD and were compared among groups using a one-way analysis of variance or the Kruskal-Wallis test. Comparisons between two groups were performed using the least significant difference method or the Mann-Whitney *U*-test. A value of $p < 0.05$ was considered statistically significant.

Results

Browning occurs during dedifferentiation of white adipocytes in ceiling culture

After seeding, mature unilocular white adipocytes extracted from abdominal fat tissue of nonobese females successfully adhered to the flask in ceiling culture. Filling the flask with media also simulated the hypoxia and pressure seen *in vivo* after fat grafting. ADSCs from the same participant were induced and differentiated into beige adipocytes using the browning cocktail. To explore dedifferentiation capacity and timing *in vitro*, the appearance and quantity of LDs were observed 7, 14, 21, and 28 days post-seeding in ceiling culture with Oil Red O (Figure 1A). Compared with the positive control (ADSC-derived beige adipocytes), by D7, some white, dedifferentiating adipocytes showed formation of small, multilocular LDs., By D14, LD number increased and size decreased in all dedifferentiating adipocytes. At D21, the majority of cells had no visible LDs and finally differentiated into fibroblast-like cells, or DAs, at D28.

Previous research suggests DAs have high proliferative activity and a cell surface antigen profile similar to ADSCs; in addition, they retain or gain the expression of mesenchymal lineage-committed marker genes such as *RUNX2* and *SOX9* (Matsumoto et al., 2008). Dedifferentiation would also be expected to downregulate proadipogenic markers, such as PPARγ, which subsequently downregulates downstream expression of early adipogenic markers (Cawthorn et al., 2012). To examine potential changes in gene expression during different stages of ceiling culture, real-time PCR was used to analyze the expression of several markers in DAs and mature adipocytes. Expression of *RUNX2* and *SOX9* was higher, whereas expression of *SLC2A4*, which encodes the GLUT4 protein and is downstream of PPARγ (Benchamana et al., 2019), was lower, as was PPARγ mRNA (*PPARG*) at D28 than at D7 (Figure 1B).

DAs can also differentiate into adipocytes, chondrocytes, and osteoblasts under appropriate culture conditions *in vitro* (Matsumoto et al., 2008). We cultured DA cells with adipogenic, osteogenic, and chondrogenic induction medium and found, consistent with other researchers, abundant accumulation of LDs after 3 weeks of adipogenic induction. Osteoblast and chondrocyte characteristics were observed by staining for Alizarin Red or Alcian Blue, respectively; both of which were positive (Figure 1C). These results indicate that DAs obtained after ceiling culture are able to gain the characteristics of adipogenic-, osteogenic-, and chondrogenic-lineage cells and lose expression of mature adipocyte-specific markers.

We found that multilocular LDs formed in ceiling-cultured adipocytes had a similar appearance to beige adipocytes; we termed these DA-intermediate state cells. Beside LD size, we measured UCP1 protein expression by immunofluorescence during different states of dedifferentiation: UCP1 expression was higher at first, then decreased, with the peak appearing at D14. Transmission electron microscopy results showed that mitochondria content followed the same tendency, along with the decrease of LDs. We measured gene expression of transcription factors mainly expressed in mature brown/beige adipocytes, rather than SVF, which contains preadipocytes and other cell types (Seale et al., 2007). The expression of browning-related genes in ceiling-cultured adipocytes also peaked at D14, in line with the immunofluorescence results. However, the level of *UCP1* and *PRDM16* expression in DA-intermediate cells was partly lower than in beige adipocytes differentiated from ADSCs (Figure 1D). Although, ceiling-cultured cells displayed comparable *PPARG* expression at D7 and D14 (Figure 1B), LD morphology began to change, with large LDs at D7 reducing in size by D14 into smaller, multilocular droplets, most likely as a result of downregulation of early adipogenic factors.

The dedifferentiation process is affected by browning of white adipocytes in ceiling culture

Previously, the mTOR pathway was identified as essential in the control of β3-adrenoceptor-stimulated glucose uptake in brown adipose depots (Olsen et al., 2014). However, rapamycin, the mammalian target of mTOR inhibitor, has been used as an alternative immuno-suppressive agent in clinical practice to minimize the side effect of some classical immuno-suppressive agents. The impact of rapamycin on insulin signaling, thermogenic gene expression, and mitochondrial respiration in brown/beige adipocytes has been well studied (García-Casarrubios et al., 2016). Thus, brown/beige adipocytes are established targets of rapamycin.

To study the impact of the browning process on dedifferentiation modulation, we ceiling-cultured white adipocytes with or without rapamycin (at 10, 25, and 100 nM), with medium changed every 3 days (Figure 2A). When treated with 10 nM rapamycin, cells displayed minimal signs of toxicity and cell death; however, at higher doses, rapamycin treatment reduced cell number and adversely affected cell morphology (Figure 2B). At D14, cell viability was significantly and dose-dependently lower in the 25 and 100 nM rapamycin-treated groups than in cells treated with 10 nM rapamycin ($p < 0.05$). Thus, 10 nM rapamycin caused relatively low toxicity in these cells.

In addition, the number of LDs decreased in all rapamycin-treated cells and were barely visible in cells treated with 100 nM rapamycin. Immunofluorescence analysis showed that UCP1 expression decreased throughout the ceiling culture process in all rapamycin-treated groups compared with the untreated DA-intermediate adipocytes (Figure 2C). Compared with non-treated cells, rapamycin-treated cells displayed more than a three-fold decrease in expression of key browning genes, such as *UCP1* and *PRDM16* at D14, with no significant changes in expression of the adipogenic marker *PPARG* (Figure 2D). We also analyzed the expression of several cell lineage-specific markers in DA cells such as *RUNX2* and *SOX9*, which are critical transcription factors for osteogenesis and chondrogenesis, respectively. Expression levels of both these genes dose-dependently decreased as rapamycin concentration increased (Figure 2E).

Next, we investigated the effect of rapamycin on the function of DAs to further identify the relationship between browning and dedifferentiation. We chose DA cells cultured under different induction media and additionally added 10 nM rapamycin in the experimental group. Three weeks after adipogenic induction, accumulation of LDs in cells was lower in rapamycin-treated cells that untreated cells. In addition, mineralized matrix aggregates were observed with Alizarin Red staining, with this osteoblast marker attenuated in rapamycin-treated cells. Alcian Blue staining indicated a gradual decrease of sulfated proteoglycans and dispersion of the cells with rapamycin treatment (Figure 2F). These results suggest that rapamycin downregulates DA lineage commitment, with impaired functional characteristics of adipogenic, osteogenic, and chondrogenic cells.

Ceiling-cultured human mature white adipocytes can transdifferentiate into beige adipocytes after browning induction

In recent years, attention has focused on the thermogenic action of brown/beige adipocytes in mammals in response to cold stimuli or β3-adrenergic agonists (Vitali et al., 2012). One study reported that beige adipocytes are highly inducible and display many similar characters compared to brown adipocytes, such as multilocular lipid droplets, dense mitochondria, and expression of UCP1.(Rui, 2017). There is evidence that under browning stimuli, some mature adipocytes can transdifferentiate into beige adipocytes (Jeremic et al., 2017; Jiang et al., 2017), although this is not conclusive.

We developed a novel model whereby ceiling culture of mature white adipocytes directly transdifferentiate into beige adipocytes with induction by browning factors. We selected white adipocytes that had been in ceiling culture for 7 days and treated them with 1 μM rosiglitazone to explore their transdifferentiation capacity and efficiency compared with untreated ceiling-cultured cells (Figure 3A). In addition, ADSCs and DAs from the same donor were induced into multilocular "brown-like" adipocytes by the browning cocktail for comparison.

Characteristics of beige adipocyte transdifferentiation at D7 or D12 across the five cell types is shown in Figure 3B. Smaller, multilocular LDs were found in beige adipocytes (ADSCs+cocktail), DAs+cocktail and ceiling-cultured+rosiglitazone groups, whereas untreated ceiling-cultured D7 cells and DAs showed fewer or no visible droplets, most likely due to a lack of browning factors. We also measured UCP1 expression *via* immunofluorescence to assess the level of browning. UCP1 expression was significantly lower in DAs whereas expression was not different between DAs+cocktail beige cells and ADSCs+cocktail beige adipocytes at D12. Surprisingly, we found that ceiling-cultured+rosiglitazone cells expressed high levels of UCP1, comparable to classic beige adipocytes (ADSCs+cocktail), compared with untreated ceiling-cultured D7 cells.

Transmission electron microscope results showed that the three types of beige adipocytes (ADSCs+cocktail, DAs+cocktail and ceiling-cultured+rosiglitazone) contained more condensed mitochondria than white adipocytes, a trend replicated by UCP1 expression, where expression was higher in induced beige cells than untreated cells (Figure 3C). To validate the efficiency of various browning induction methods and assess the effect of rosiglitazone on browning markers, we measured gene expression of transcription factors involved in browning-related transdifferentiation. Interestingly, the expression of the browning-related genes *UCP1* and *PRDM16* in the ceiling-cultured+rosiglitazone group was the same or higher than beige adipocytes induced from ADSCs. Untreated ceiling-cultured D7 cells and beige adipocytes induced from DAs had lower expression of *UCP1* and *PRDM16* than the two groups above. Furthermore, ceiling-cultured D7 cells showed higher expression of *PPARG* than ADSC beige adipocytes, most likely due to the differences in cell origin (Figure 3D). Corresponding UCP1 protein levels in cells treated with different induction methods showed the same tendency compared to gene expression (Figure 3E and Supplementary Material S3), suggesting improved browning efficiency. These observations indicate that ceiling culture combined with rosiglitazone induced transdifferentiation of beige adipocytes from white adipocytes, resulting in upregulated expression of browning-related genes.

Ceiling-cultured beige adipocytes display increased expression of fatty acid metabolism genes

We further investigated the role of ceiling culture and rosiglitazone on lipolysis and fat oxidation in mature white adipocytes by measuring the expression of genes involved in lipid metabolism, such as *LIPE* and *PLIN1,* and mitochondrial fat oxidation, including *ACACA* and *CPT1A* (Lone and Yun, 2016). Cells from the ceiling-cultured+rosiglitazone group displayed more LDs, suggestive of lipolysis and supported by elevated expression of lipolysis-related genes *LIPE* and *PLIN1* (Figure 4A). Moreover, expression of *ACACA* and *CPT1A* in ceiling-culture induced beige adipocytes was significantly upregulated upon rosiglitazone treatment, indicating an elevation of fat oxidation (Figure 4B). In addition, DAs+cocktail had higher expression of *LIPE, PLIN1, ACACA and CPT1A,* than classical ADSCs+cocktail beige adipocytes. These results suggest that the increased presence of LDs in ceiling-cultured+rosiglitazone-induced beige cells may be due to increased lipolysis and fatty acid oxidation.

Beige adipocytes from different sources can be identified by gene expression of cell type-specific markers

To distinguish between beige adipocytes from different progenitor cells, we quantified several cell markers of gene expression after browning stimulation. During differentiation of human cells, the expression of a progenitor cell's markers are significantly reduced over time (Lam et al., 2018; Xu et al., 2020).

Thus, we selected adipocyte-specific genes as mature white adipose tissue markers, including *FABP4* and *SLC2A4*. There was no significant difference in the expression between ceiling-cultured+rosiglitazone-induced beige adipocytes and untreated ceiling-cultured D7 cells, which are both derived from white adipocytes (Figure 5A). By contrast, high levels of mesenchymal-specific cell key markers CD44, CD90 are expressed on the surface of ADSCs (Najafipour et al., 2019). In line with this, browning cocktail-induced beige adipocytes still expressed higher levels of *CD44* and *THY1* (CD90) than non ADSC-derived cells (Figure 5B). Next, we observed DA-related expression of the mesenchymal lineage-committed marker genes *RUNX2* and *SOX9*. DAs induced by the browning cocktail maintained greater levels of *RUNX2* and *SOX9* expression than beige adipocytes from different progenitor cells (Figure 5C). Together, these results indicate that beige adipocytes cultured from various sources can be identified by gene expression of cell type-specific markers.

Discussion

Accumulation of excess white adipose tissue contributes to a wide range of diseases, such as obesity, insulin resistance and type 2 diabetes mellitus (Cotillard et al., 2014; Klöting et al., 2010). However, current methods of adipocyte culture *in vitro* are limited in their physiological relevance, which restrict the development of cell and drug therapies for obesity-related diseases. To investigate the pathogenic effects of excess adipose tissue (Skurk et al., 2007), researchers require more functional, responsive cell models. Specifically, a model where mature white adipocytes transdifferentiate into beige adipocytes would more closely simulate processes *in vivo* than differentiation of beige adipocytes from ADSCs.

In this study, we show that during the process of adipocyte dedifferentiation in ceiling culture, the continuous mechanical force and browning agent (rosiglitazone) causes adipocytes to accumulate multilocular LDs, similar to those seen in beige adipocytes (Figure 6). In addition, various genes involved in the transcriptional regulation of browning were induced in ceiling-cultured cells: the browning-related genes *UCP1* and *PRDM16* were upregulated, an effect that was suppressed by rapamycin treatment (an inhibitor of browning) in a dose-dependent manner. By contrast, the lipogenic gene *PPARG* was downregulated, and fewer and smaller LDs were present in cells 28 days after seeding in ceiling culture; again, these changes were downregulated in rapamycin-treated cells. Overall, our results suggest that browning may play an important role in the process of dedifferentiation by ceiling culture and that rapamycin appears to prevent this transformation.

Unlike beige adipocytes induced by the classical cocktail, ceiling-cultured beige cells originate directly from mature white adipocytes, which is consistent with the process seen *in vivo*. One challenge in researching browning mechanisms is the lack of models derived from mature white adipocytes, since almost all induction models rely on isolating precursors or stem cells from adipose tissue. After 7 days in ceiling culture, we found that, compared with cells from other sources, gene expression in ceiling-cultured cells was closer to that of mature adipocytes. By contrast, markers of the DAs and ADSCs, the other progenitor cells from which beige adipocytes were derived, maintained their unique, depot-specific gene expression patterns, which further indicates the importance of cell source in creating a physiological model.

The model of transdifferentiating ceiling-cultured white adipocytes into beige adipocytes can be quickly set up, with resulting morphology and gene and protein expression similar to beige cells derived from ADSCs using the classical cocktail induction media. The model has a number of potential applications. Firstly, since ceiling culture more accurately replicates the process of transdifferentiation, this model can be used to study the potential pathophysiological or therapeutic effects of this process *in vitro*. Secondly, we found that the efficiency of browning in ceiling culture was increased with rosiglitazone, but impaired by rapamycin, allowing the relationship between browning and dedifferentiation to be investigated. Thirdly, the environment better replicates the hypoxia and compression present in adipose tissue *in vivo*, especially after fat grafting, providing a suitable model or this procedure. Finally, ceiling culture is a viable model to investigate drug treatment: the presence of beige adipocytes derived from mature white adipocytes may contribute to the resolution of insulin resistance and obesity-associated metabolic diseases. However, exposure of mature white adipocytes under the ceiling culture with hypoxic condition will undergo other cellular responses. Research have reported that the white adipocytes, whether derived from murine or human, exhibit changes over 1300 genes expression in response to hypoxia, including some key adipokines such as leptin, vascular endothelial growth factor (VEGF) and adiponectin (Trayhurn, 2014). In addition, hypoxia also affects the uptake of glucose and increases the production of lactate, with the regulation of genes linked to oxidative metabolism and glycolysis (Trayhurn, 2013). These unavoidable pathways will affect the ultimate productivity of induced beige adipocytes and interfere target for the treatment while stimulating the expression of genes to some extent.

There were some limitations of the study. The role of rapamycin is still controversial. Due to the limitation of chemoresistance of mTOR inhibitor rapamycin, it is still unclear whether the restrain of dedifferentiation *via* inhibition of the mTOR pathway or increase the cytotoxic effects by reactive oxygen species (ROS), apoptosis and mitophagy reportedly(Shen et al., 2018). Therefore, it is less rigorous to restrain the browning by this kind of drugs. As a result, a more specific and effective substitution for rapamycin is required to explore the relationship between browning and dedifferentiation further. Secondly, like other methods, this ceiling culture technology has advantages and disadvantages. The operation is simple, and the culture cycle is short, which makes it a highly alternative culture method. However, there is still a long way to go to accurately control the mechanical pressure intensity and produce functional beige adipocytes in large quantities and high quality in the process of ceiling culture.

Overall, we show that transdifferentiation of white adipocytes to beige adipocytes in ceiling culture is a physiologically relevant model, which may allow the study of phenotypic changes of different adipocytes and provide a novel model for drug screening and the modulation of adipose tissue function.

Data availability statement

The original contributions presented in the study are included in the article/Supplementary Files, further inquiries can be directed to the corresponding authors.

Ethics statement

The studies involving human participants were reviewed and approved by Ethics Committee of Guangdong Nanfang Hospital, Southern Medical University. The patients/participants provided their written informed consent to participate in this study.

Author contributions

YH and ZL conducted the experiments under the guidance of JC and YL. JW provided technical support during tissue slice observation. HT and JL extracted and analyzed the data. All authors contributed to the article and approved the submitted version.

Funding

This study was supported by the National Natural Science Foundation of China (81971852, 81901976) and the Administrator Foundation of Nanfang Hospital (2018Z010).

Conflict of interest

The authors declare that the research was conducted in the absence of any commercial or financial relationships that could be construed as a potential conflict of interest.

Publisher's note

Supplementary material

The Supplementary Material for this article can be found online at: https://www.frontiersin.org/articles/10.3389/fbioe.2022.905194/full#supplementary-material

References

Barbatelli, G., Murano, I., Madsen, L., Hao, Q., Jimenez, M., Kristiansen, K., et al. (2010). The emergence of cold-induced Brown adipocytes in mouse white fat depots is determined predominantly by white to Brown adipocyte transdifferentiation. *Am. J. Physiology-Endocrinology Metabolism* 298 (6), E1244–E1253. doi:10.1152/ajpendo.00600.2009

Benchamana, A., Mori, H., MacDougald, O. A., and Soodvilai, S. (2019). Regulation of adipocyte differentiation and metabolism by lansoprazole. *Life Sci.* 239, 116897. doi:10.1016/j.lfs.2019.116897

Bender, R., McCarthy, M., Brown, T., Bukowska, J., Smith, S., Abbott, R. D., et al. (2020). Human adipose derived cells in two- and Three-Dimensional cultures: Functional validation of an in vitro fat construct. *Stem Cells Int.* 2020, 1–14. doi:10.1155/2020/4242130

Cannon, B., and Nedergaard, J. (2004). Brown adipose tissue: Function and physiological significance. *Physiol. Rev.* 84 (1), 277–359. doi:10.1152/physrev.00015.2003

Cawthorn, W. P., Scheller, E. L., and MacDougald, O. A. (2012). Adipose tissue stem cells meet preadipocyte commitment: Going back to the future. *J. Lipid Res.* 53 (2), 227–246. doi:10.1194/jlr.R021089

Cheng, L., Wang, J., Dai, H., Duan, Y., An, Y., Shi, L., et al. (2021). Brown and beige adipose tissue: A novel therapeutic strategy for obesity and type 2 diabetes mellitus. *Adipocyte* 10 (1), 48–65. doi:10.1080/21623945.2020.1870060

Cotillard, A., Poitou, C., Torcivia, A., Bouillot, J., Dietrich, A., Klöting, N., et al. (2014). Adipocyte size threshold matters: Link with risk of type 2 diabetes and improved insulin resistance after gastric bypass. *J. Clin. Endocrinol. Metab.* 99 (8), E1466–E1470. doi:10.1210/jc.2014-1074

Cypess, A. M., Weiner, L. S., Roberts-Toler, C., Franquet, E. E., Kessler, S. H., Kahn, P. A., et al. (2015). Activation of human Brown adipose tissue by a β3-adrenergic receptor agonist. *Cell Metab.* 21 (1), 33–38. doi:10.1016/j.cmet.2014.12.009

Desjardins, E. M., and Steinberg, G. R. (2018). Emerging role of AMPK in Brown and beige adipose tissue (BAT): Implications for obesity, insulin resistance, and type 2 diabetes. *Curr. Diab. Rep.* 18 (10), 80. doi:10.1007/s11892-018-1049-6

García-Casarrubios, E., de Moura, C., Arroba, A. I., Pescador, N., Calderon-Dominguez, M., Garcia, L., et al. (2016). Rapamycin negatively impacts insulin signaling, glucose uptake and uncoupling protein-1 in Brown adipocytes. *Biochimica Biophysica Acta (BBA) - Mol. Cell Biol. Lipids* 1861 (12), 1929–1941. doi:10.1016/j.bbalip.2016.09.016

Ghaben, A. L., and Scherer, P. E. (2019). Adipogenesis and metabolic health. *Nat. Rev. Mol. Cell Biol.* 20 (4), 242–258. doi:10.1038/s41580-018-0093-z

Hammarstedt, A., Gogg, S., Hedjazifar, S., Nerstedt, A., and Smith, U. (2018). Impaired adipogenesis and dysfunctional adipose tissue in human hypertrophic obesity. *Physiol. Rev.* 98 (4), 1911–1941. doi:10.1152/physrev.00034.2017

Harms, M. J., Li, Q., Lee, S., Zhang, C., Kull, B., Hallen, S., et al. (2019). Mature human white adipocytes cultured under membranes maintain identity, function, and can transdifferentiate into Brown-like adipocytes. *Cell Rep.* 27 (1), 213–225.e5. doi:10.1016/j.celrep.2019.03.026

Harms, M., and Seale, P. (2013). Brown and beige fat: Development, function and therapeutic potential. *Nat. Med.* 19 (10), 1252–1263. doi:10.1038/nm.3361

Hernandez-Quiles, M., Broekema, M. F., and Kalkhoven, E. (2021). PPARgamma in metabolism, immunity, and cancer: Unified and diverse mechanisms of action. *Front. Endocrinol.* 12, 624112. doi:10.3389/fendo.2021.624112

Himms-Hagen, J., Melnyk, A., Zingaretti, M. C., Ceresi, E., Barbatelli, G., and Cinti, S. (2000). Multilocular fat cells in WAT of CL-316243-treated rats derive directly from white adipocytes. *Am. J. Physiology-Cell Physiology* 279 (3), C670–C681. doi:10.1152/ajpcell.2000.279.3.C670

Hwang, C. S., Loftus, T. M., Mandrup, S., and Lane, M. D. (1997). Adipocyte differentiation and leptin expression. *Annu. Rev. Cell Dev. Biol.* 13, 231–259. doi:10.1146/annurev.cellbio.13.1.231

Jeremic, N., Chaturvedi, P., and Tyagi, S. C. (2017). Browning of white fat: Novel insight into factors, mechanisms, and therapeutics. *J. Cell. Physiol.* 232 (1), 61–68. doi:10.1002/jcp.25450

Jiang, Y., Berry, D. C., and Graff, J. M. (2017). Distinct cellular and molecular mechanisms for β3 adrenergic receptor-induced beige adipocyte formation. *eLife* 6, e30329. doi:10.7554/eLife.30329

Kaisanlahti, A., and Glumoff, T. (2019). Browning of white fat: Agents and implications for beige adipose tissue to type 2 diabetes. *J. Physiol. Biochem.* 75 (1), 1–10. doi:10.1007/s13105-018-0658-5

Klöting, N., and Blüher, M. (2014). Adipocyte dysfunction, inflammation and metabolic syndrome. *Rev. Endocr. Metab. Disord.* 15 (4), 277–287. doi:10.1007/s11154-014-9301-0

Klöting, N., Fasshauer, M., Dietrich, A., Kovacs, P., Schön, M. R., Kern, M., et al. (2010). Insulin-sensitive obesity. *Am. J. Physiology-Endocrinology Metabolism* 299 (3), E506–E515. doi:10.1152/ajpendo.00586.2009

Lam, J., Bellayr, I. H., Marklein, R. A., Bauer, S. R., Puri, R. K., and Sung, K. E. (2018). Functional profiling of chondrogenically induced multipotent stromal cell aggregates reveals transcriptomic and emergent morphological phenotypes predictive of differentiation capacity. *Stem Cells Transl. Med.* 7 (9), 664–675. doi:10.1002/sctm.18-0065

Lone, J., and Yun, J. W. (2016). Monoterpene limonene induces Brown fat-like phenotype in 3T3-L1 white adipocytes. *Life Sci.* 153, 198–206. doi:10.1016/j.lfs.2016.04.010

Lotta, L. A., Gulati, P., Day, F. R., Payne, F., Ongen, H., van de Bunt, M., et al. (2017). Integrative genomic analysis implicates limited peripheral adipose storage capacity in the pathogenesis of human insulin resistance. *Nat. Genet.* 49 (1), 17–26. doi:10.1038/ng.3714

Matsumoto, T., Kano, K., Kondo, D., Fukuda, N., Iribe, Y., Tanaka, N., et al. (2008). Mature adipocyte-derived dedifferentiated fat cells exhibit multilineage potential. *J. Cell. Physiol.* 215 (1), 210–222. doi:10.1002/jcp.21304

Merlin, J., Sato, M., Nowell, C., Pakzad, M., Fahey, R., Gao, J., et al. (2018). The PPARγ agonist rosiglitazone promotes the induction of brite adipocytes, increasing β-adrenoceptor-mediated mitochondrial function and glucose uptake. *Cell. Signal.* 42, 54–66. doi:10.1016/j.cellsig.2017.09.023

Mitschke, M. M., Hoffmann, L. S., Gnad, T., Scholz, D., Kruithoff, K., Mayer, P., et al. (2013). Increased cGMP promotes healthy expansion and browning of white adipose tissue. *FASEB J.* 27 (4), 1621–1630. doi:10.1096/fj.12-221580

Najafipour, H., Bagheri-Hosseinabadi, Z., Eslaminejad, T., and Mollaei, H. R. (2019). The effect of sodium valproate on differentiation of human adipose-derived stem cells into cardiomyocyte-like cells in two-dimensional culture and fibrin scaffold conditions. *Cell Tissue Res.* 378 (1), 127–141. doi:10.1007/s00441-019-03027-5

Olsen, J. M., Sato, M., Dallner, O. S., Sandström, A. L., Pisani, D. F., Chambard, J., et al. (2014). Glucose uptake in Brown fat cells is dependent on mTOR complex 2–promoted GLUT1 translocation. *J. Cell Biol.* 207 (3), 365–374. doi:10.1083/jcb.201403080

Rui, L. (2017). Brown and beige adipose tissues in health and disease. *Compr. Physiol.* 7 (4), 1281–1306. doi:10.1002/cphy.c170001

Saxton, S. N., Clark, B. J., Withers, S. B., Eringa, E. C., and Heagerty, A. M. (2019). Mechanistic links between obesity, diabetes, and blood pressure: Role of perivascular adipose tissue. *Physiol. Rev.* 99 (4), 1701–1763. doi:10.1152/physrev.00034.2018

Seale, P., Kajimura, S., Yang, W., Chin, S., Rohas, L. M., Uldry, M., et al. (2007). Transcriptional control of Brown fat determination by PRDM16. *Cell Metab.* 6 (1), 38–54. doi:10.1016/j.cmet.2007.06.001

Shen, Y., Guerra-Librero, A., Fernandez-Gil, B. I., Florido, J., García-López, S., Martinez-Ruiz, L., et al. (2018). Combination of melatonin and rapamycin for head and neck cancer therapy: Suppression of AKT/mTOR pathway activation, and activation of mitophagy and apoptosis via mitochondrial function regulation. *J. Pineal Res.* 64 (3), e12461. doi:10.1111/jpi.12461

Skurk, T., Alberti-Huber, C., Herder, C., and Hauner, H. (2007). Relationship between adipocyte size and adipokine expression and secretion. *J. Clin. Endocrinol. Metab.* 92 (3), 1023–1033. doi:10.1210/jc.2006-1055

Sugihara, H., Yonemitsu, N., Miyabara, S., and Toda, S. (1987). Proliferation of unilocular fat cells in the primary culture. *J. Lipid Res.* 28 (9), 1038–1045. doi:10.1016/s0022-2275(20)38619-3

Sugihara, H., Yonemitsu, N., Miyabara, S., and Yun, K. (1986). Primary cultures of unilocular fat cells: Characteristics of growth in vitro and changes in differentiation properties. *Differentiation* 31 (1), 42–49. doi:10.1111/j.1432-0436.1986.tb00381.x

Trayhurn, P. (2014). Hypoxia and adipocyte physiology: Implications for adipose tissue dysfunction in obesity. *Annu. Rev. Nutr.* 34, 207–236. doi:10.1146/annurev-nutr-071812-161156

Trayhurn, P. (2013). Hypoxia and adipose tissue function and dysfunction in obesity. *Physiol. Rev.* 93 (1), 1–21. doi:10.1152/physrev.00017.2012

Vitali, A., Murano, I., Zingaretti, M. C., Frontini, A., Ricquier, D., and Cinti, S. (2012). The adipose organ of obesity-prone C57BL/6J mice is composed of mixed white and Brown adipocytes. *J. Lipid Res.* 53 (4), 619–629. doi:10.1194/jlr.M018846

Wang, Q. A., Tao, C., Gupta, R. K., and Scherer, P. E. (2013). Tracking adipogenesis during white adipose tissue development, expansion and regeneration. *Nat. Med.* 19 (10), 1338–1344. doi:10.1038/nm.3324

Wheeler, K. C., Jena, M. K., Pradhan, B. S., Nayak, N., Das, S., Hsu, C. D., et al. (2018). VEGF may contribute to macrophage recruitment and M2 polarization in the decidua. *PLoS One* 13 (1), e0191040. doi:10.1371/journal.pone.0191040

Wu, J., Boström, P., Sparks, L. M., Ye, L., Choi, J. H., Giang, A. H., et al. (2012). Beige adipocytes are a distinct type of thermogenic fat cell in mouse and human. *Cell* 150 (2), 366–376. doi:10.1016/j.cell.2012.05.016

Xia, J., Zhu, H., Zhu, S., Ge, J., Wang, Z., Lu, F., et al. (2021). Induced beige adipocytes improved fat graft retention by promoting adipogenesis and angiogenesis. *Plastic Reconstr. Surg.* 148 (3), 549–558. doi:10.1097/PRS.0000000000008227

Xu, L., Hanamatsu, H., Homan, K., Onodera, T., Miyazaki, T., Furukawa, J., et al. (2020). Alterations of glycosphingolipid glycans and chondrogenic markers during differentiation of human induced pluripotent stem cells into chondrocytes. *Biomolecules* 10 (12), 1622. doi:10.3390/biom10121622

Yang, X., and Smith, U. (2007). Adipose tissue distribution and risk of metabolic disease: Does thiazolidinedione-induced adipose tissue redistribution provide a clue to the answer? *Diabetologia* 50 (6), 1127–1139. doi:10.1007/s00125-007-0640-1

Yao, L., Cui, X., Chen, Q., Yang, X., Fang, F., Zhang, J., et al. (2017). Cold-Inducible SIRT6 regulates thermogenesis of Brown and beige fat. *Cell Rep.* 20 (3), 641–654. doi:10.1016/j.celrep.2017.06.069

frontiers | Frontiers in Bioengineering and Biotechnology

TYPE Mini Review
PUBLISHED 16 August 2022
DOI 10.3389/fbioe.2022.942077

Magnetic bead-based adsorption strategy for exosome isolation

Sun Jiawei[1], Chen Zhi[2], Tian Kewei[1] and Li Xiaoping[1]*

[1]Shulan International Medical College, Zhejiang Shuren College, Hangzhou, China, [2]Zhejiang University School of Medicine, Hangzhou, China

OPEN ACCESS

EDITED BY
Charlotte Riviere,
Université Claude Bernard Lyon 1,
France

REVIEWED BY
Andrey Cherstvy,
University of Potsdam, Germany

*CORRESPONDENCE
Li Xiaoping,
li-xp@zjsru.edu.cn

SPECIALTY SECTION
This article was submitted to Tissue Engineering and Regenerative Medicine, a section of the journal Frontiers in Bioengineering and Biotechnology

RECEIVED 12 May 2022
ACCEPTED 30 June 2022
PUBLISHED 16 August 2022

CITATION
Jiawei S, Zhi C, Kewei T and Xiaoping L (2022), Magnetic bead-based adsorption strategy for exosome isolation.
Front. Bioeng. Biotechnol. 10:942077.
doi: 10.3389/fbioe.2022.942077

Exosomes, one type of extracellular vesicle (EV) secreted by cells, participate in intercellular communication and other biological processes as carriers of lipids, functional proteins, mRNAs, miRNAs, lncRNAs, and DNA fragments. Their presence in biofluids makes them attractive candidates as innovative clinical diagnostic tools. However, the conventional isolation and analysis of high-purity exosomes in clinical application is challenging, with traditional methods facing a number of shortcomings, including low yield or purity, long periods of processing, high cost, and difficulties in standardization. In this study, we provide an overview of commonly used exosome isolation approaches with a focus on magnetic bead-based capture, an ideal methodology with high purity and integrality of exosomes. The current challenges on exosome isolation methods are also described to highlight areas for future research and development.

KEYWORDS
exosomes, extracellular vesicles, exosome isolation, magnetic bead, ultracentrifugation

Introduction

Currently, molecular testing in biopsy samples has become a committed step in diagnosis, prognosis, and individualized therapy of disease in the era of precision medicine. At present, the tumor sample of a patient was obtained by surgery or puncture. However, tissue biopsy cannot always be performed because of the invasiveness of surgery and puncture. Moreover, results from a single biopsy might not provide sufficient real-time information to characterize the genetic heterogeneity of disease (Gerlinger et al., 2012; Swanton, 2012). Compared with the tissue biopsy, liquid biopsy (including circulating tumor cells (CTCs), circulating tumor DNA (ctDNA), and exosomes) is based on the non-invasive collection measure, convenient storage of samples, and fast acquisition of information at different stages of disease progression (Herrero et al., 2019).

Exosomes (Figure 1A), one type of extracellular vesicle (EV) secreted by cells, with size ranging from 30 to 150 nm in diameter (Raposo and Stoorvogel, 2013; Pegtel and Gould, 2019), participate in the intercellular communication and other biological processes as carriers of lipids, functional proteins, mRNAs, miRNAs, lncRNAs, and DNA fragments (Rani et al., 2011; Colombo et al., 2014; Wortzel et al., 2019). In various biological fluids including plasma, lymph, urine, saliva, ascites, saliva, and bronchoalveolar lavage fluid, exosomes can be found. At present, exosomes were widespread detected diagnostic

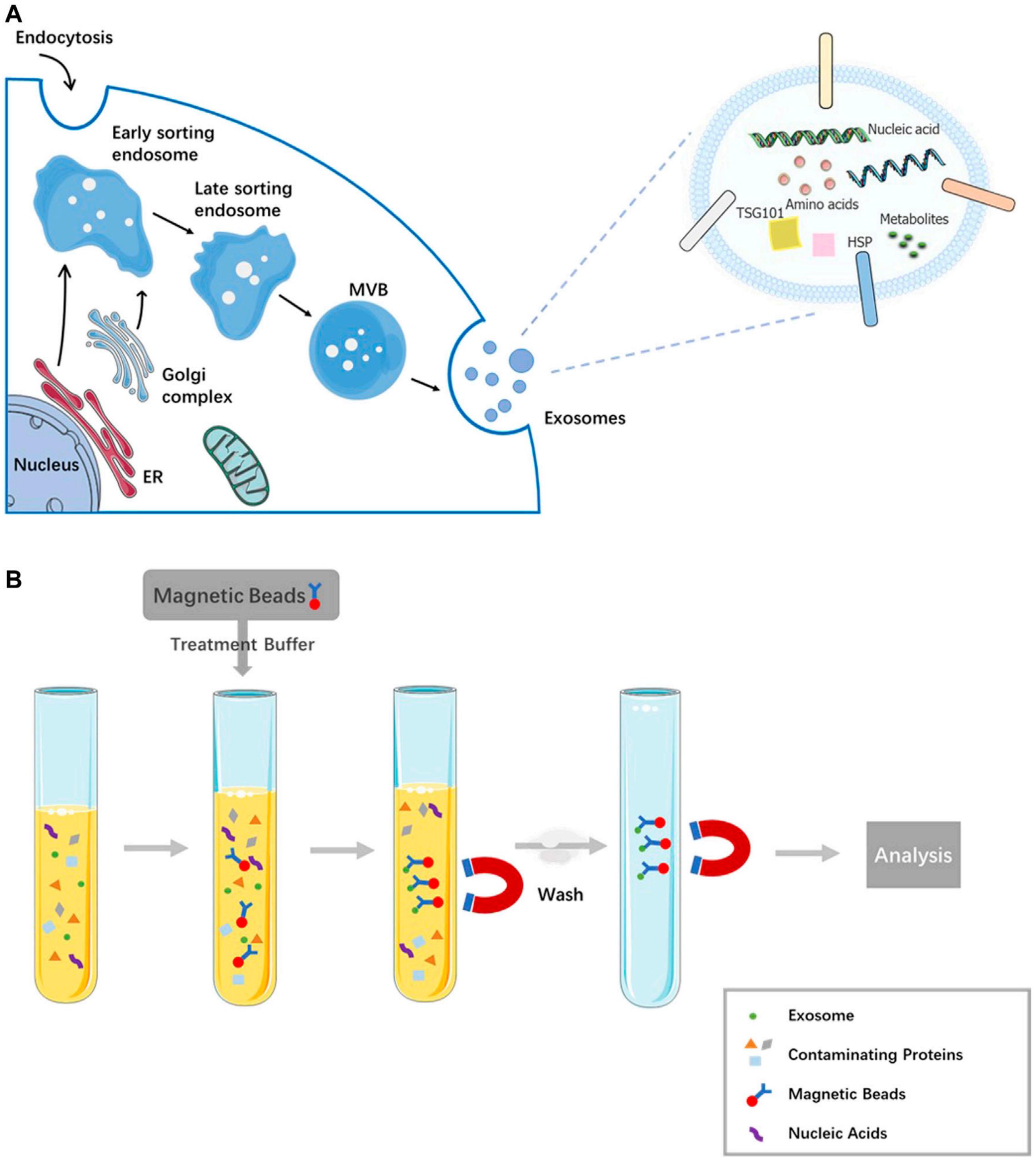

FIGURE 1
Biogenesis and its contents of exosome and magnetic bead affinity exosome isolation method. **(A)** The process production and overall composition of an exosome. **(B)** The scheme of magnetic bead affinity for exosome extraction.

biomarkers owing to their vital roles as monitor in different stages of disease progression (Zhang et al., 2015; Kalluri, 2016; Li et al., 2019).

Exosomes are detectable in various biofluids, but the detection and analysis of exosomes are interfered because a large numbers of biomacromolecules are present in these biofluids (Yang et al., 2020; Zhu et al., 2020). The complexity of biological samples and the heterogeneity of exosomes increased the difficulty of extraction and separation of exosomes, exploring the method of exosome isolation, and enrichment from complex biofluids for clinical detection is efficiently urgent. The main exosome isolation methods include ultracentrifugation, ultrafiltration, immunomagnetic isolation, and microfluidics (Yang et al., 2017; Sidhom et al.,

TABLE1 Comparison of the current exosome extraction methods.

Method	Principle	Advantages	Disadvantages	Yield	Purity	Time	Equipment/ material cost, $	Reference
Ultracentrifugation	Centrifugation and ultracentrifugation steps	Cost-effective Suitable for large volume preparation	Time consuming Large primary sample size Low accuracy Contamination with media proteins Time consuming	Low	High	2–20h	~3000/10	Johnstone et al. (1989); Cvjetkovic et al. (2014); Gudbergsson et al. (2016); Helwa et al. (2017)
Ultrafiltration	Centrifugation and filtration	Large primary sample size	Low portability Sensitive to centrifugation time	Low	High	~20h	1000/20	Cheruvanky et al. (2007); Lobb et al. (2015); Konoshenko et al. (2018)
Immunoaffinity enrichment	Nano-magnetic bead	Low primary sample volume High accuracy	Costly	High	High	~1h	0/650	Tauro et al. (2012); Greening et al. (2015)
Microfluidics	Microfluidic devices	Low primary sample volume Easily automated and integrated with diagnosis	High-price	High	High	<2h	4217/1400	Chen et al. (2010); Zhang et al. (2016)

2020). Among them, the most widely used approach is ultracentrifugation (UC), but it has deficiencies such as poor effectiveness for viscous liquids, requirement for expensive equipment, time-consuming, and ineffectiveness of distinguishing between exosome subsets or other particles of similar size and density. The mechanism of immunomagnetic isolation protocols is using magnetic beads coated with anti-marker antibodies to capture exosomes by recognizing the specific signature receptors on their surface. This method has advantages such as low primary sample volume, high accuracy, and no chemical contamination. The aim of the review is to summarize the roles of magnetic beads in exosome isolation.

Exosomes isolation techniques

In recent years, the separation and enrichment technology of exosomes in body fluid samples has developed rapidly, and various innovative technologies and new platforms are emerging, which play a key role in further exploring exosomes. At the same time, because the contents of biological samples are complex and changeable, it is still technically difficult to separate exosomes efficiently. Here we summarize the principle of different isolation methods and discuss their advantages and disadvantages (Table 1).

Ultracentrifugation, the gold standard exosome isolation method, is the most commonly used method to extract exosomes from cell biological fluid and culture supernatant (Gudbergsson et al., 2016; Helwa et al., 2017). Exosomes can be separated using size differences in the ultracentrifugation approach (Johnstone et al., 1989). Although ultracentrifugation is considered as the gold standard for exosome separation, it is tedious and time-consuming to separate exosomes by ultracentrifugation; in addition, high impurities including lipoprotein and protein, structure corruption of exosomes, and the high price of the device discourage the adoption of ultracentrifuge in the exosome separation. By this method, a number of factors, such as rotor type, ultracentrifugation time, and liquid viscosity influence the purity and yield of exosomes (Cvjetkovic et al., 2014).

In the protocol of ultrafiltration, a membrane with a specified pore size is used to separate a predetermined range of particles (Cheruvanky et al., 2007; Lobb et al., 2015; Konoshenko et al., 2018). This protocol can be used as a stand-alone isolation technique; meanwhile, it can also play the role as a complement to ultracentrifugation. After exosomes be separated from proteins *via* ultracentrifugation, membranes are used to sieve cells and large EVs. Ultrafiltration can cause the pores of the membrane to be blocked by vesicles, thus shortening the service life of the membrane and reducing the separation efficiency (Li et al., 2017). Some exosomes can also be attached to the membranes, which interfere downstream analysis, resulting in a decrease in yield and even false-positive or false-negative detection results.

The immunoaffinity capture technology has strong specificity to screen and separate exosomes selectively. Generally, the EVs with CD9, CD63, CD81, and other proteins on the membrane surface are considered as exosomes (Tauro et al., 2012). Because only a subset of exosomes expressing antibody recognition protein is captured, the yield is usually insufficient, but its purity is much higher than that of exosomes separated according to the physical properties of exosomes (Greening et al., 2015). With the progression of tumor, the specific antibodies may lose their recognition ability; in addition, the surface antigen may also be blocked or shielded, resulting in the antigen–antibody unable to combine normally, so the target exosomes cannot be obtained.

The microfluidic method, which can be applicable to exosome separation and downstream analysis, is a promising development direction of liquid biopsy in the future for its high efficiency and easy operability. Exosomes are targeted by the binding with specific antibodies immobilized on the inner capture surface of microfluidic devices (Chen et al., 2010; Zhang et al., 2016). However, the application of microfluidic technology in the exosome separation is still immature, and the yield and purity are insufficient (Contreras-Naranjo et al., 2017). Therefore, many people pay attention to synergistically apply other technologies including immunomagnetic beads with microfluidic technology for the exosome biopsy (Sharma et al., 2018).

Magnetic bead-based exosome isolation

Specific capture of exosomes, which is closely related to immunoaffinity, is suitable for isolating by targeting specific markers on the membrane of exosome. Antibody-coated beads can be used to enrich by targeting exosome membrane markers, such as CD9, CD63, ALIX, and the epithelial cell adhesion molecule (EpCAM) (Greening et al., 2015). Latex beads have been used in the passive absorption of purified exosomes. The protocol is cheap, easy to recover from the solution while involving numerous centrifugation steps, and is challenging in terms of reproducibility (Théry et al., 2001). An alternative to latex beads for exosome capture, magnetic bead-based technology (Figure 1B), is attributed to the differences in specific interactions between receptors and ligands and other physical characteristics of exosomes (Jara-Acevedo et al., 2019).

The isolation of exosomes by magnetic beads includes two steps generally. First, exosomes from biofluid or pre-enriched by ultracentrifugation are captured by magnetic beads utilizing immunoaffinity, and then intact exosomes can be released from beads in the buffer. To enrich EVs and EV-associated miRNA efficiently, a two-step magnetic bead-based (2MBB) method is proposed for the isolation of exosomes as well as associated miRNAs from samples. Exosome-associated miRNAs are extracted by a second set of magnetic beads coated with complementary oligonucleotides after the enrichment of EV using magnetic beads. The result of RT-PCR demonstrated high efficiency of 2MBB in the EV enrichment (74 ± 7%, $n = 4$) and miRNA isolation (91 ± 4%, $n = 4$) (Chen et al., 2020). Several studies found a sandwich-type immunocomplex can be constructed for specific isolation and accurate quantification of exosomes. After exosomes specifically being captured by immunomagnetic beads, different types of nanoprobes are fixed on the surface of exosomes by hydrophobic interactions between cholesterol and lipid membranes, thus forming a sandwich-type immunocomplex. The immunocomplex can be magnetically captured and produce enhanced detectable signals (He et al., 2017; He et al., 2018; Huang et al., 2018; Tian et al., 2018; Zeng et al., 2021).

Tumor-specific exosomes are small in number, isolating total of them is complex to achieve, while the immunoaffinity bead-based method has been confirmed to be able to capture several types of tumor-specific exosomes. A 10-uL aliquot of magnetic beads coated with an anti-CD34 antibody, which is a unique marker of acute myeloid leukemia (AML), can isolate all the AML-specific exosomes from 100 to 1,000 μl AML plasma (Hong et al., 2014). The anti-epithelial cell adhesion molecule (EpCAM) tagged bead scan can be used to obtain highly pure circulating tumor-derived exosomes of ovarian cancer and esophageal squamous cell carcinoma patients (Taylor and Gercel-Taylor, 2008; Zhao et al., 2019). A CSPG4-coated magnetic bead can capture CSPG4+ exosomes produced by melanoma cells. The efficiency of immune-based capture of melanoma-derived exosomes obtained from the plasma of melanoma patients is around 95% (Sharma et al., 2018). To obtain prostate cancer-related exosomes, immunomagnetic beads coated with an anti-prostate-specific membrane antigen (PSMA) antibody can be applied to isolate them from the plasma of prostate cancer patients (Mizutani et al., 2014).

The immunomagnetic method is executed by different antibodies coated on the magnetic beads to target the surface markers of exosomes. A direct exosome isolation strategy using anti-human CD81 antibody-coated magnetic beads is able to enrich exosomes from T lymphocyte cell culture without the pre-enrichment step (Pedersen et al., 2013). Tim4, a phosphatidylserine receptor, can recognize the phosphatidylserine on the surface of EVs. Wataru N. et al. (Nakai et al., 2016) developed a practical and effective method using magnetic beads bound with Tim4 to purify exosomes and adding Ca^{2+} chelators to release exosomes from Tim4 easily. Monoclonal anti-HLA DP, DQ, and DR antibodies can be coated on magnetic beads to target exosomes derived by antigen-presenting cells (Clayton et al., 2001).The CD63-1 aptamer/magnetic bead complex formed by incubating can isolate exosomes from the colon and breast cancer cell culture supernatant effectively (Song et al., 2020). Combining the traditional immunomagnetic bead-based protocol and the microfluidic method results in benefits from both the high purity of the former and the automated continuous superiority (Niu et al., 2020).

Furthermore, some scholars found strategies of isolating exosomes in a generic way using physical or other properties of exosomes by magnetic beads. We know that the EV surface contains phosphatidylserine with negative charge. ExoCAS-2, a magnetic bead-based ion exchange platform for isolating exosomes attempts to separate exosomes by polycationic polymer-coated magnetic beads from plasma. The yield provided by ExoCAS-2 is 6.6-fold higher than UC. High purity and batch-to-batch repeatability are also unique features of ExoCAS-2 (Kim and Shin, 2021). A biofunctionalized magnetic bead with high affinity Ti(IV) ions and the insertion of a phospholipid derivative, 1,2-distearoyl-sn-glycero-3-phosphoethanolamine, is shown to effectively isolate exosomes with low contamination, a high recovery rate (>80%), and a short separation time (<1h) from the urine of prostate cancer patient (Sun et al., 2021).

Multiple studies have compared immunomagnetic beads and other current exosome isolation methods in terms of yield, purity, and operation difficulty. Comparation of common exosome isolation strategies including ultracentrifugation, OptiPrep™ density-based separation, and immunoaffinity capture using anti-EpCAM-coated magnetic beads is performed by detecting exosome markers. Human colon cancer cell line LIM1863-derived exosomes based on the number of MS/MS spectra identified for exosome markers and proteins associated with their biogenesis, trafficking, and release; the researchers found IAC-Exos to be the most effective method to isolate exosomes. For example, Alix, TSG101, CD9, and CD81 were significantly higher (at least 2-fold) in anti-EpCAM-coated magnetic beads than the other two methods (Tauro et al., 2012). A comparative evaluation of ultra-centrifugation, polypeptide precipitation (ME Kit, NEP), and submicron size supermagnetic beads (SMB) with anti-CD9 confirmed SMB as a method of choice for plasma exosome enrichment; as the result of Western blot and FACS (fluorescence-activated cell sorter), the analysis verified multifold increase of exosome specific protein comparing to exosomes purified *via* other methods from plasma of the same volume. Moreover bead-based assays allow simple and rapid protocol in comparison to the plate-based ELISA (Zarovni et al., 2015). The magnetic bead-mediated selective adsorption strategy (MagExo), which tends to adsorb EVs on the surface of magnetic beads selectively, can separate EVs from plasma and cell culture media (CCM) with high purity, resulting in two times higher yield than EVs obtained by ultracentrifugation (Figure 1; Fang et al., 2021). However, in a comprehensive evaluation of differential centrifugation coupled with ultracentrifugation, epithelial cell adhesion molecule (EpCAM)-coupled microbead, and OptiPrepTM density gradient separation, the microbead shows inferior performance of purified exosomes. In Western blot analysis, less exosomal markers including HSP70, CD9, FLOT1, and CD63 are detected in exosomes purified by EpCAM-coupled microbeads. Microscopic analysis showed that the purified exosomes contain a large number of background proteins (Kalra et al., 2013).

Discussion

In practical experiments and clinical studies, the most suitable method for exosome isolation is usually chosen based on the objective factors such as sample type, downstream experiments, study target, and rigid experimental conditions. Compared with the traditional methods, the method of extracting exosomes by magnetic beads can obtain a considerable number of high active exosomes. The magnetic bead-based method has better repeatability than the latex bead-based method, and increased capture efficiency and sensitivity compared to the plate surface-based method due to the larger surface area. However, the magnetic bead-based method has its own limitations. Considering that the magnetic bead-based method has not been standardized, it is recommended to conduct necessary identification, characterization, and functional experiments on exosomes in order to rule out the possibility of other impurities. Now neither the magnetic bead-based method nor other methods can completely isolate exosomes from other EV subsets. Also, several factors such as incubation time, temperature, level of surface markers expression, concentration of target vesicles state, characteristics of the antibody–antigen interaction, sample type, concentration and ratio of beads, and target molecules will have influence on the efficiency of the magnetic bead-based separation (Sioud, 2015). Magnetic beads only capture exosomes with target proteins on membrane surfaces selectively, so the yield of exosome is limited (Zhu et al., 2020). More targets coated on magnetic bead, stabler separation device, and combination of different approaches will be the future direction to boost the yield of exosome isolation. The advance of emerging strategies for labeling and tracking of exosomes will also promote the progress of the magnetic bead affinity method (Betzer et al., 2020; Thapa et al., 2019), and the technical improvements of exosome extracting, labeling, and tracking are expected to greatly facilitate exosome-based medical applications.

To sum up, the magnetic bead affinity method is an ideal method to enrich EVs including exosomes. However, for clinical application, ultracentrifugation and ultrafiltration are still the best alternative methods; we still have a long way to go before the magnetic bead affinity method being used in clinical diagnosis.

Author contributions

SJ: data curation, writing—original draft, and writing—reviewing and editing. CZ: writing—reviewing and editing. TK: writing—original draft. LX: writing—original draft and writing—reviewing and editing.

Funding

The authors are grateful for the support of the Zhejiang Provincial Natural Science Foundation of China (LGF21H200007).

Conflict of interest

The authors declare that the research was conducted in the absence of any commercial or financial relationships that could be construed as a potential conflict of interest.

Publisher's Note

References

Chen, C., Skog, J., Hsu, C. H., Lessard, R. T., Balaj, L., Wurdinger, T., et al. (2010). Microfluidic isolation and transcriptome analysis of serum microvesicles. *Lab. Chip* 10, 505–511. doi:10.1039/b916199f

Chen, S., Shiesh, S. C., Lee, G. B., and Chen, C. (2020). Two-step magnetic bead-based (2MBB) techniques for immunocapture of extracellular vesicles and quantification of microRNAs for cardiovascular diseases: A pilot study. *PLoS One* 15, e0229610. doi:10.1371/journal.pone.0229610

Cheruvanky, A., Zhou, H., Pisitkun, T., Kopp, J. B., Knepper, M. A., Yuen, P. S., et al. (2007). Rapid isolation of urinary exosomal biomarkers using a nanomembrane ultrafiltration concentrator. *Am. J. Physiology-Renal Physiology* 292, F1657–F1661. doi:10.1152/ajprenal.00434.2006

Clayton, A., Court, J., Navabi, H., Adams, M., Mason, M. D., Hobot, J. A., et al. (2001). Analysis of antigen presenting cell derived exosomes, based on immuno-magnetic isolation and flow cytometry. *J. Immunol. Methods* 247, 163–174. doi:10.1016/s0022-1759(00)00321-5

Colombo, M., Raposo, G., and Théry, C. (2014). Biogenesis, secretion, and intercellular interactions of exosomes and other extracellular vesicles. *Annu. Rev. Cell Dev. Biol.* 30, 255–289. doi:10.1146/annurev-cellbio-101512-122326

Contreras-Naranjo, J. C., Wu, H. J., and Ugaz, V. M. (2017). Microfluidics for exosome isolation and analysis: Enabling liquid biopsy for personalized medicine. *Lab. Chip* 17, 3558–3577. doi:10.1039/c7lc00592j

Cvjetkovic, A., Lötvall, J., and Lässer, C. (2014). The influence of rotor type and centrifugation time on the yield and purity of extracellular vesicles. *J. Extracell. Vesicles* 3. doi:10.3402/jev.v3.23111

Fang, X., Chen, C., Liu, B., Ma, Z., Hu, F., Li, H., et al. (2021). A magnetic bead-mediated selective adsorption strategy for extracellular vesicle separation and purification. *Acta Biomater.* 453. doi:10.1016/j.actbio.2021.02.004

Gerlinger, M., Rowan, A. J., Horswell, S., Larkin, M., Endesfelder, J., Gronroos, D., et al. (2012). Intratumor heterogeneity and branched evolution revealed by multiregion sequencing. *N. Engl. J. Med.* 366, 883–892. doi:10.1056/nejmoa1113205

Greening, D. W., Xu, R., Ji, H., Tauro, B. J., and Simpson, R. J. (2015). A protocol for exosome isolation and characterization: Evaluation of ultracentrifugation, density-gradient separation, and immunoaffinity capture methods. *Methods Mol. Biol.* 1295, 179–209. doi:10.1007/978-1-4939-2550-6_15

Gudbergsson, J. M., Johnsen, K. B., Skov, M. N., and Duroux, M. (2016). Systematic review of factors influencing extracellular vesicle yield from cell cultures. *Cytotechnology* 68, 579–592. doi:10.1007/s10616-015-9913-6

He, F., Liu, H., Guo, X., Yin, B. C., and Ye, B. C. (2017). Direct exosome quantification via bivalent-cholesterol-labeled DNA anchor for signal amplification. *Anal. Chem.* 89, 12968–12975. doi:10.1021/acs.analchem.7b03919

He, F., Wang, J., Yin, B. C., and Ye, B. C. (2018). Quantification of exosome based on a copper-mediated signal amplification strategy. *Anal. Chem.* 90, 8072–8079. doi:10.1021/acs.analchem.8b01187

Helwa, I., Cai, J., Drewry, M. D., Zimmerman, A., Dinkins, M. B., Khaled, M. L., et al. (2017). A comparative study of serum exosome isolation using differential ultracentrifugation and three commercial reagents. *PLoS One* 12, e0170628. doi:10.1371/journal.pone.0170628

Herrero, C., De La Fuente, A., Casas-Arozamena, C., Sebastian, V., Prieto, M., Arruebo, M., et al. (2019). *Extracellular Vesicles-Based Biomarkers Represent a Promising Liquid Biopsy in Endometrial Cancer*, 11. doi:10.3390/cancers11122000*Cancers (Basel)*

Hong, C. S., Muller, L., Boyiadzis, M., and Whiteside, T. L. (2014). Isolation and characterization of CD34+ blast-derived exosomes in acute myeloid leukemia. *PLoS One* 9, e103310. doi:10.1371/journal.pone.0103310

Huang, L., Wang, D. B., Singh, N., Yang, F., Gu, N., and Zhang, X. E. (2018). A dual-signal amplification platform for sensitive fluorescence biosensing of leukemia-derived exosomes. *Nanoscale* 10, 20289–20295. doi:10.1039/c8nr07720g

Jara-Acevedo, R., Campos-Silva, C., Valés-Gómez, M., Yáñez-Mó, M., Suárez, H., and Fuentes, M. (2019). Exosome beads array for multiplexed phenotyping in cancer. *J. Proteomics* 198, 87–97. doi:10.1016/j.jprot.2018.12.023

Johnstone, R. M., Bianchini, A., and Teng, K. (1989). Reticulocyte maturation and exosome release: Transferrin receptor containing exosomes shows multiple plasma membrane functions. *Blood* 74, 1844–1851. doi:10.1182/blood.v74.5.1844.1844

Kalluri, R. (2016). The biology and function of exosomes in cancer. *J. Clin. Invest.* 126, 1208–1215. doi:10.1172/jci81135

Kalra, H., Adda, C. G., Liem, M., Ang, C. S., Mechler, A., Simpson, R. J., et al. (2013). Comparative proteomics evaluation of plasma exosome isolation techniques and assessment of the stability of exosomes in normal human blood plasma. *Proteomics* 13, 3354–3364. doi:10.1002/pmic.201300282

Kim, H., and Shin, S. (2021). ExoCAS-2: Rapid and pure isolation of exosomes by anionic exchange using magnetic beads. *Biomedicines* 9, 89–94. doi:10.3390/biomedicines9010028

Konoshenko, M. Y., Lekchnov, E. A., Vlassov, A. V., and Laktionov, P. P. (2018). Isolation of extracellular vesicles: General methodologies and latest trends. *Biomed. Res. Int.* 2018, 8545347. doi:10.1155/2018/8545347

Li, F. X., Liu, J. J., Xu, F., Lin, X., Zhong, J. Y., Wu, F., et al. (2019). Role of tumor-derived exosomes in bone metastasis. *Oncol. Lett.* 18, 3935–3945. doi:10.3892/ol.2019.10776

Li, P., Kaslan, M., Lee, S. H., Yao, J., and Gao, Z. (2017). Progress in exosome isolation techniques. *Theranostics* 7, 789–804. doi:10.7150/thno.18133

Lobb, R. J., Becker, M., Wen Wen, S. W., Wong, C. S., Wiegmans, A. P., Leimgruber, A., et al. (2015). Optimized exosome isolation protocol for cell culture supernatant and human plasma. *J. Extracell. Vesicles* 4, 27031. doi:10.3402/jev.v4.27031

Mizutani, K., Terazawa, R., Kameyama, K., Kato, T., Horie, K., Tsuchiya, T., et al. (2014). Isolation of prostate cancer-related exosomes. *Anticancer Res.* 34, 3419–3423.

Nakai, W., Yoshida, T., Diez, D., Miyatake, Y., Nishibu, T., Imawaka, N., et al. (2016). A novel affinity-based method for the isolation of highly purified extracellular vesicles. *Sci. Rep.* 6, 33935. doi:10.1038/srep33935

Niu, F., Chen, X., Niu, X., Cai, Y., Zhang, Q., Chen, T., et al. (2020). Integrated immunomagnetic bead-based microfluidic chip for exosomes isolation. *Micromachines (Basel)* 11, 1103. doi:10.3390/mi11050503

Pedersen, K. W., Kierulf, B., Oksvold, M. P., Li, M., Vlassov, A. V., Roos, N., et al. (2013). Isolation and characterization of exosomes using magnetic beads. *BioProbes* 71, 10–13.

Pegtel, D. M., and Gould, S. J. (2019). Exosomes. *Annu. Rev. Biochem.* 88, 487–514. doi:10.1146/annurev-biochem-013118-111902

Rani, S., O'Brien, K., Kelleher, F. C., Corcoran, C., Germano, S., Radomski, M. W., et al. (2011). Isolation of exosomes for subsequent mRNA, MicroRNA, and protein profiling. *Methods Mol. Biol.* 784, 181–195. doi:10.1007/978-1-61779-289-2_13

Raposo, G., and Stoorvogel, W. (2013). Extracellular vesicles: Exosomes, microvesicles, and friends. *J. Cell Biol.* 200, 373–383. doi:10.1083/jcb.201211138

Sharma, P., Ludwig, S., Muller, L., Hong, C. S., Kirkwood, J. M., Ferrone, S., et al. (2018). Immunoaffinity-based isolation of melanoma cell-derived exosomes from plasma of patients with melanoma. *J. Extracell. Vesicles* 7, 1435138. doi:10.1080/20013078.2018.1435138

Sidhom, K., Obi, P. O., and Saleem, A. (2020). A review of exosomal isolation methods: Is size exclusion chromatography the best option? *Int. J. Mol. Sci.* 21. doi:10.3390/ijms21186466

Sioud, M. (2015). RNA interference: Mechanisms, technical challenges, and therapeutic opportunities. *Methods Mol. Biol.* 1218, 1–15. doi:10.1007/978-1-4939-1538-5_1

Song, Z., Mao, J., Barrero, R. A., Wang, P., Zhang, F., and Wang, T. (2020). Development of a CD63 aptamer for efficient cancer immunochemistry and immunoaffinity-based exosome isolation. *Molecules* 25, 276. doi:10.3390/molecules25235585

Sun, J., Han, S., Ma, L., Zhang, H., Zhan, Z., Aguilar, H. A., et al. (2021). Synergistically bifunctional paramagnetic separation enables efficient isolation of urine extracellular vesicles and downstream phosphoproteomic analysis. *ACS Appl. Mat. Interfaces* 13, 3622–3630. doi:10.1021/acsami.0c19400

Swanton, C. (2012). Intratumor heterogeneity: Evolution through space and time. *Cancer Res.* 72, 4875–4882. doi:10.1158/0008-5472.can-12-2217

Tauro, B. J., Greening, D. W., Mathias, R. A., Ji, H., Mathivanan, S., Scott, A. M., et al. (2012). Comparison of ultracentrifugation, density gradient separation, and immunoaffinity capture methods for isolating human colon cancer cell line LIM1863-derived exosomes. *Methods* 56, 293–304. doi:10.1016/j.ymeth.2012.01.002

Taylor, D. D., and Gercel-Taylor, C. (2008). MicroRNA signatures of tumor-derived exosomes as diagnostic biomarkers of ovarian cancer. *Gynecol. Oncol.* 110, 13–21. doi:10.1016/j.ygyno.2008.04.033

Théry, C., Boussac, M., Véron, P., Ricciardi-Castagnoli, P., Raposo, G., Garin, J., et al. (2001). Proteomic analysis of dendritic cell-derived exosomes: A secreted subcellular compartment distinct from apoptotic vesicles. *J. Immunol.* 166, 7309–7318. doi:10.4049/jimmunol.166.12.7309

Tian, Y. F., Ning, C. F., He, F., Yin, B. C., and Ye, B. C. (2018). Highly sensitive detection of exosomes by SERS using gold nanostar@Raman reporter@nanoshell structures modified with a bivalent cholesterol-labeled DNA anchor. *Analyst* 143, 4915–4922. doi:10.1039/c8an01041b

Wortzel, I., Dror, S., Kenific, C. M., and Lyden, D. (2019). Exosome-mediated metastasis: Communication from a distance. *Dev. Cell* 49, 347–360. doi:10.1016/j.devcel.2019.04.011

Yang, D., Zhang, W., Zhang, H., Zhang, F., Chen, L., Ma, L., et al. (2020). Progress, opportunity, and perspective on exosome isolation - efforts for efficient exosome-based theranostics. *Theranostics* 10, 3684–3707. doi:10.7150/thno.41580

Yang, F., Liao, X., Tian, Y., and Li, G. (2017). Exosome separation using microfluidic systems: Size-based, immunoaffinity-based and dynamic methodologies. *Biotechnol. J.* 12. doi:10.1002/biot.201600699

Zarovni, N., Corrado, A., Guazzi, P., Zocco, D., Lari, E., Radano, G., et al. (2015). Integrated isolation and quantitative analysis of exosome shuttled proteins and nucleic acids using immunocapture approaches. *Methods* 87, 46–58. doi:10.1016/j.ymeth.2015.05.028

Zeng, R., Wang, J., Wang, Q., Tang, D., and Lin, Y. (2021). Horseradish peroxidase-encapsulated DNA nanoflowers: An innovative signal-generation tag for colorimetric biosensor. *Talanta* 221, 121600. doi:10.1016/j.talanta.2020.121600

Zhang, P., He, M., and Zeng, Y. (2016). Ultrasensitive microfluidic analysis of circulating exosomes using a nanostructured graphene oxide/polydopamine coating. *Lab. Chip* 16, 3033–3042. doi:10.1039/c6lc00279j

Zhang, X., Yuan, X., Shi, H., Wu, L., Qian, H., and Xu, W. (2015). Exosomes in cancer: Small particle, big player. *J. Hematol. Oncol.* 8, 83. doi:10.1186/s13045-015-0181-x

Zhao, A., Guo, L., Xu, J., Zheng, L., Guo, Z., Ling, Z., et al. (2019). Identification and validation of circulating exosomes-based liquid biopsy for esophageal cancer. *Cancer Med.* 8, 3566–3574. doi:10.1002/cam4.2224

Zhu, L., Sun, H. T., Wang, S., Huang, S. L., Zheng, Y., Wang, C. Q., et al. (2020). Isolation and characterization of exosomes for cancer research. *J. Hematol. Oncol.* 13, 152. doi:10.1186/s13045-020-00987-y

frontiers | Frontiers in Bioengineering and Biotechnology

TYPE Systematic Review
PUBLISHED 29 August 2022
DOI 10.3389/fbioe.2022.976960

OPEN ACCESS

EDITED BY
V. Prasad Shastri,
University of Freiburg, Germany

REVIEWED BY
Xiaoxiao Cai,
Sichuan University, China
Siu Hong Dexter Wong,
Hong Kong Polytechnic University,
Hong Kong SAR, China

*CORRESPONDENCE
Kai Li,
lk516433415@smu.edu.cn
Jia Liu,
liujia0111@live.cn
Yujin Tang,
tangyujin1967@163.com

†These authors have contributed equally to this work

SPECIALTY SECTION
This article was submitted to Tissue Engineering and Regenerative Medicine, a section of the journal Frontiers in Bioengineering and Biotechnology

RECEIVED 23 June 2022
ACCEPTED 08 August 2022
PUBLISHED 29 August 2022

CITATION
Luo Z, Chen S, Zhou J, Wang C, Li K, Liu J, Tang Y and Wang L (2022), Application of aptamers in regenerative medicine.
Front. Bioeng. Biotechnol. 10:976960.
doi: 10.3389/fbioe.2022.976960

Application of aptamers in regenerative medicine

Zhaohui Luo[1,2†], Shimin Chen[3,4†], Jing Zhou[1†], Chong Wang[5], Kai Li[6*], Jia Liu[2*], Yujin Tang[2*] and Liqiang Wang[7]

[1]Youjiang Medical University for Nationalities, Baise, Guangxi, China, [2]Guangxi Key Laboratory of basic and translational research of Bone and Joint Degenerative Diseases, Guangxi Biomedical Materials Engineering Research Center for Bone and Joint Degenerative Diseases, Department of Orthopedics, Affiliated Hospital of Youjiang Medical University for Nationalities, Baise, Guangxi, China, [3]Guangxi Botanical Garden of Medicinal Plants, Nanning, China, [4]Dalian Institute of Chemical Physics, Chinese Academy of Sciences, Dalian, China, [5]School of Mechanical Engineering, Dongguan University of Technology, Dongguan, Guangdong, China, [6]Academy of Orthopedics, Guangdong Provincial Key Laboratory of Bone and Joint Degeneration Diseases, The Third Affiliated Hospital of Southern Medical University, Guangzhou, China, [7]State Key Laboratory of Metal Matrix Composites, School of Material Science and Engineering, Shanghai Jiao Tong University, Shanghai, China

Regenerative medicine is a discipline that studies how to use biological and engineering principles and operation methods to repair and regenerate damaged tissues and organs. Until now, regenerative medicine has focused mainly on the in-depth study of the pathological mechanism of diseases, the further development and application of new drugs, and tissue engineering technology strategies. The emergence of aptamers has supplemented the development methods and types of new drugs and enriched the application elements of tissue engineering technology, injecting new vitality into regenerative medicine. The role and application status of aptamers screened in recent years in various tissue regeneration and repair are reviewed, and the prospects and challenges of aptamer technology are discussed, providing a basis for the design and application of aptamers in long-term transformation.

KEYWORDS

aptamer, tissue regeneration, regenerative medicine, repair of tissue injury, transformation and application

Introduction

Regenerative medicine is closely related to the treatment of injury and aging. The methods and strategies of regenerative medicine involve mainly stem cell technology, tissue engineering technology, and physical and chemical intervention (Fu, 2018; Edgar et al., 2020). Although regenerative medicine based on these strategies has achieved partial success in tissue and organ repair and regeneration, it is still subject to many defects. These defects include difficulty in obtaining exogenous stem cells, immunogenicity, tumorigenicity, low survival rate of exogenous stem cells (Tang, 2019), and high production cost of traditional protein active molecules. In addition, the environmental conditions for their biological activity are harsh (Perwein et al., 2018), and the application elements of tissue engineering technology are outdated (Atala and Forgacs, 2019; Matai et al., 2020).

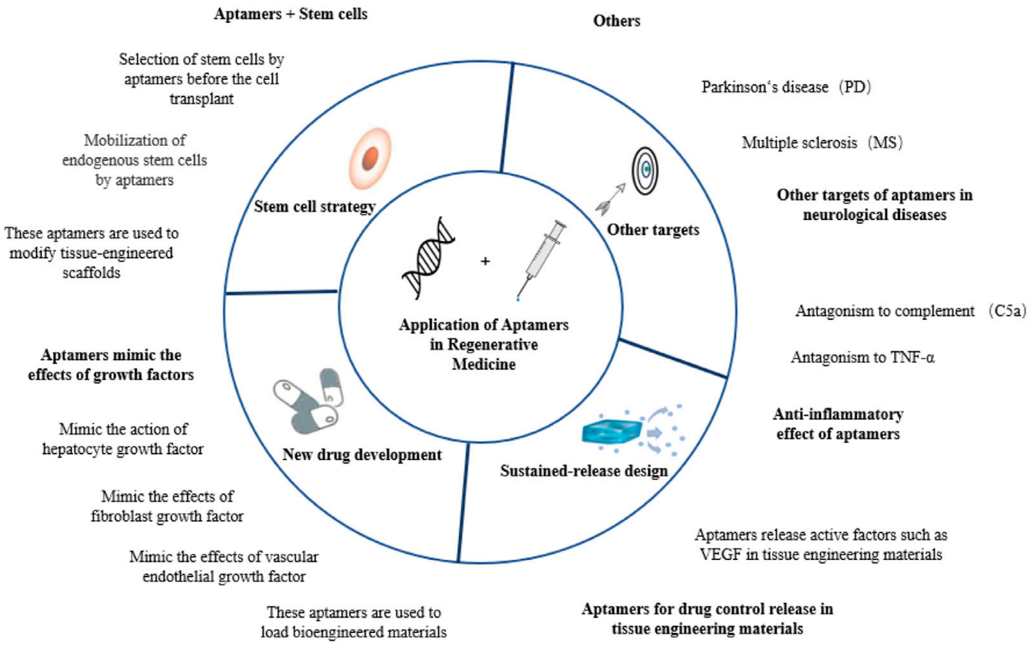

FIGURE 1
Schematic diagram of the partial application of aptamers in regenerative medicine.

Aptamers are a new class of ligand molecules that are manually screened by SELEX (systematic evolution of ligands by exponential enrichment) technology (Saito, 2021). They are short single-stranded DNA or RNA that can be folded into specific spatial structures. Moreover, they can bind to specific target molecules with high affinity and specificity through spatial complementarity, electrostatic attraction, van der Waals force, hydrophobic interaction, π-π stacking, and hydrogen bonding (Cai et al., 2018; Plach and Schubert, 2020). Compared with antibodies, aptamers have lower production cost, higher thermal stability, stronger renaturation after denaturation, easier chemical modification and labeling, wider target range, lower immunogenicity and cytotoxicity, and higher tissue penetration ability (Byun, 2021; Ni et al., 2021). In view of this, they have been widely applied in the biomedical field for testing, diagnosis, and targeted cancer therapy in the form of detection probes and a targeting medium (Zhang et al., 2021a; Mandal et al., 2021; Ni et al., 2021; Riccardi et al., 2021; Ma et al., 2022).

Aptamers have recently been introduced into various regenerative medicine strategies, showing high application value in tissue repair and disease treatment. In this review, aptamers are classified according to their different modes of action, and their applications in tissue regeneration are reviewed. See Figure 1 for a general preview.

Stem cell strategies combining aptamers in regenerative medicine

Stem cells can theoretically divide and proliferate infinitely. They exist widely in various tissues and can be derived and differentiated into various types of cells under specific environmental stimulation. Stem cells have become important resources in regenerative medicine because of their potency and growth capacity, especially for tissues with limited regenerative capacity, such as neural tissues (Gong et al., 2020) and muscle tissues (Roshanbinfar et al., 2021). Currently, stem cell strategies include mainly exogenous stem cell transplantation and endogenous stem cell mobilization and regulation. After arriving at the site of injury, stem cells from different sources play mainly a regenerative and repair role by integrating defects, secreting a variety of bioactive molecules, and partaking in immune regulation (Sarkar et al., 2021).

Aptamer-based stem cell sorting technology can be used to obtain and purify target cells during stem cell transplantation

For exogenous stem cell transplantation, the sorting and collection of various stem cells is the primary problem.

TABLE 1 Aptamers associated with stem cells and their experimental application.

Aptamer name	Aptamer type	Screening targets	Experimental application	References
O-7	Single-stranded DNA	SAOS-2 osteoblasts from human osteosarcoma	The surface of a cell culture plate with aptamer can directly and quickly capture osteoblasts from the cell suspension and enhance cell adhesion. The aptamer-modified titanium alloy surface can rapidly capture osteoblasts from the flowing suspension and enhance cell adhesion	(Guo et al., 2005; Guo et al., 2007)
G-8	Single-stranded DNA	aMSCs from porcine bone marrow	Isolation of aMSCs from porcine bone marrow; transplantation of ischemic myocardium	(Guo et al., 2006; Schäfer et al., 2007)
Aptamer 36	Single-stranded DNA	CD31-positive cells in peripheral blood of pigs	As a coating molecule, endothelial precursor cells (EPCs) with high expression of CD31 in pig blood can be captured *in vitro*. It can be used to isolate EPCs from pig bone marrow, and the isolated EPCs can be used for transplantation treatment in a pig myocardial infarction model	(Hoffmann et al., 2008; Haller et al., 2015)
AT-1	Single-stranded DNA	Purified extracellular domain of human CD31 molecule	It can be used to isolate EPCs from human umbilical cord blood, and the isolated EPCs can be used for transplantation therapy of hind limb ischemia in mice; a coating material for the surface of a vascular stent; vascularization of a bioengineered artificial liver	(Strahm et al., 2010; Yoon et al., 2015; Kim et al., 2021a)
L1-65、L2-2 and L3-3	RNA	Mouse embryonic stem cells (mESCs)	For the differentiation of mouse embryonic stem cells and other differentiated mouse cell lines; tracing the differentiation process of mESCs	Iwagawa et al. (2012)
Aptamer-74	Single-stranded DNA	Progenitor cells with osteogenic induction potential in human jaw membrane cells	Isolation of osteoblast progenitor cells from the human jaw bone periosteal cell population	Ardjomandi et al. (2013)
Apta99	Single-stranded DNA	Human adipose-derived stem cells (ASC)	It can be used to distinguish human fibroblasts from ASCs and purify ASCs	de Melo et al. (2021)
Apt19s	Single-stranded DNA	Human pluripotent stem cells	For the separation and purification of human embryonic stem cells; *in situ* tissue technique for homing mesenchymal stem cells promotes injury repair	(Hou et al., 2015; Hu et al., 2017; Wang et al., 2019a; Wang et al., 2019b; Kuang et al., 2019; Sun et al., 2021)
HM69	Single-stranded DNA	Human embryonic stem cells	*In situ* tissue technique for homing mesenchymal stem cells promotes injury repair	(Wang et al., 2019c; Yang et al., 2021a)

Classical cell sorting methods include immunomagnetic bead sorting (Laghmouchi et al., 2020), flow cytometry (Manohar et al., 2021), and solid surface sorting strategy based on cell adhesion differences (Durand, 2021). The first two methods are based mainly on the immunological principle of antibodies. However, during the sorting operations, cell viability and biological characteristics are often affected by antibody binding, fluid shear force, treatment of related enzymes, temperature changes, and electrical and chemical stimulation. Finally, they become unstable (Yao et al., 2020). For example, the combination of protein antibodies with stem cells can lead to changes in cell Stemness, changing the initial state of the cell and too intense ambient temperature, potential of hydrogen (pH) and electric field intensity can even induce cell degeneration and apoptosis, etc.

The emergence of SELEX technology based on cell or cell-specific markers has enabled aptamers to be used for sorting target cells. It has the advantages of low production cost, strong resistance to enzymatic hydrolysis, high purity, high efficiency, and little influence on cells. Over the past decade, a large number of aptamers with specificity and high affinity for various types of progenitor cells have been identified (Table 1). These include O-7 (a single-stranded DNA aptamer that binds human osteoblasts) (Guo et al., 2005; Guo et al., 2007), G-8 (an aptamer for binding adult mesenchymal stem cells (aMSCs) from pig bone marrow) (Guo et al., 2006; Schäfer et al., 2007), aptamer 36 (for CD31-positive cells in pig peripheral blood) (Hoffmann et al., 2008; Haller et al., 2015), specific binding aptamers of purified human CD31 extracellular domain (Strahm et al., 2010; Yoon et al., 2015; Kim et al., 2021a), specific RNA aptamers (L1-65, L2-2, and L3-3 binding to mouse embryonic stem cells (mESCs)) (Iwagawa et al., 2012), and DNA aptamers ((Aptamer-74) for osteoblast progenitors present in human jaw membrane cell population) (Ardjomandi et al., 2013). They have shown the ability to capture and enrich corresponding stem cells in bone marrow, whole blood, and other cell suspensions, suggesting their potential application in the collection of exogenous stem cells before transplantation and surface modification of biomaterials for

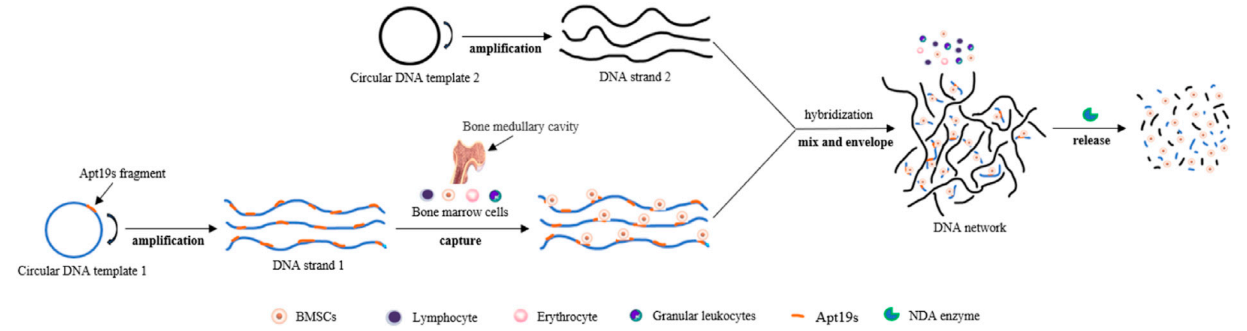

FIGURE 2
Schematic of a DNA cross-linking network designed for harvesting bone marrow mesenchymal stem cells. The process of capturing, enveloping, and releasing bone marrow stem cells (BMSCs). Capturing: DNA strand 1 was incubated with BMSCs, and cell capture was performed by aptamer Apt19s anchoring. Enveloping: Introducing DNA strand 2 into a cell solution containing DNA strand 1 triggers the formation of DNA networks. Releasing: The DNA network can be digested by DNA enzymes, which release BMSCs.

tissue regeneration. Recently, de Melo et al. (2021) used adipose-derived stem cells (ASCs) from human adipose tissue and fibroblasts from skin tissue as screening targets and used Cell-SELEX and quantitative PCR technology to screen and identify an aptamer named Apta99. The aptamer can specifically recognize ASCs and shows a low affinity for fibroblasts, which is expected to be a powerful tool in ASC purification and therapeutic applications. Yao et al. (2020) also reported a cell capture technique beneficial to the survival of bone marrow mesenchymal stem cells (BMSCs). They introduced Apt19s (Hou et al., 2015), a single-stranded DNA aptamer with high specificity and affinity for BMSCs, into another cell-friendly DNA hydrogel system (Nam et al., 2021; Wu et al., 2021) to achieve a specific envelope and capture of stem cells during the formation of a hydrogel 3D DNA network. BMSCs showed uniform spatial distribution and good survival activity in this 3D network, and this system could achieve controlled release of captured cells under the digestion of nuclease. This principle is shown in Figure 2.

Aptamers can capture and enrich endogenous stem cells at the site of tissue injury to promote tissue regeneration and repair

When tissue is damaged, the stimuli can activate the silent stem cells residing *in situ* to divide and proliferate for self-repair. Compared with exogenous stem cells, endogenous stem cells do not have problems with immunogenicity and origin (Yamanaka, 2020). Activating endogenous stem cells facilitate tissue repair. Traditional chemoattractant types have been used to activate and migrate endogenous stem cells and have gained recognition *in situ* tissue engineering techniques (Andreas et al., 2014).

In recent years, aptamers with *in vitro* cell capture ability have also been applied to *in situ* enrichment of endogenous stem cells and promote tissue regeneration. Apt19s (Hou et al., 2015; Wang et al., 2019a) is a single-stranded DNA aptamer derived from the SELEX sequence database of human pluripotent stem cells (PSCs). It shows high specificity and affinity binding to multiple gene-derived progenitor cells *in vitro*. Apt19s can be used as a powerful tool for the isolation, purification, and enrichment of PSCs. The binding target was identified as alkaline phosphatase-ALPL, a membrane protein type highly expressed on the surface of PSCs and its derived progenitor cells. The possibility of applying Apt19s to tissue engineering *in situ*, which facilitates the homing of stem cells, has been explored. In these designs (Hu et al., 2017; Wang et al., 2019b; Sun et al., 2021), the authors chemically coupled amino-modified Apt19s with activated carboxyl groups in various tissue-engineered scaffold components through the dehydration condensation reaction. They expected that the tissue-engineered scaffolds functionalized by this novel "cell catcher" could achieve a better repair effect after implantation at the injured site. The results showed that Apt19s on these scaffolds could recruit bone marrow mesenchymal stem cells and promote injury healing in a rat osteochondral knee joint defect model, rabbit osteochondral knee joint defect model, and critical size rat skull bone defect model. Kuang et al. (2019) produced a functional hydrogel by the covalent combination of Apt19s, which was modified by Acrydite (acrylic phosphoramidite) at the 5′ end of the nucleotide chain with an injectable composite hydrogel whose matrix was mainly composed of dimethylaminoethyl methacrylate (DMAEMA) and 2-hydroxyethyl methacrylate (HEMA). This hydrogel was also found to have obvious endogenous MSC recruitment when implanted into a rat femur bone defect model. Wang et al. (2019c) recently developed a new MSC-targeting aptamer HM69 using whole cell SELEX technology and constructed functional nanoparticles based on this aptamer. Such nanoparticles are essentially oligonucleotides formed by the end-to-end connection of nucleotide chains of the aptamer as independent units. Both HM69 and HM69 functional nanoparticles showed high specificity and affinity binding to MSCs *in vitro*, and such binding properties were evaluated to be superior to Apt19s. They applied the novel nanoparticles to treat a femur bone defect in a rat model and found that nanoparticles reached the bone defect via the circulation and then mediated *in situ* recognition, capture, and enrichment of MSCs. Yang et al. (2021a) also designed a 3D bio-printing dual-function bionic scaffold for *in-situ* cartilage regeneration based on the directional recruitment of MSCs by the HM69 aptamer. MSC cartilage differentiation was enhanced by transforming growth factor, which achieved good results in a rabbit full-layer cartilage injury model of a knee joint. In addition, a large number of designs have been reported that use aptamers to recruit and enrich endogenous repair factors at tissue injury sites (e.g.,vascular endothelial growth factor (VEGF) (Son et al., 2019), fractalkine (FKN) (Enam et al., 2017), etc.) and these designs also take full advantage of the binding specificity and adhesion between aptamers and target molecules.

In conclusion, aptamers play a role as a new cell sorting tool and a new cell chemoattractant and trapping agent in regenerative medicine stem cell strategies. Compared with the traditional application elements represented by active protein molecules, aptamers have more efficient cell sorting efficiency and better adaptability *in vivo*, and are easier to modify and connect with tissue engineering scaffolds. However, there are no reports on human experimental applications.

Aptamer elements in a sustained-release hydrogel system

Aptamers with growth factor-like activity can be introduced into biomedical materials such as hydrogel to prolong the release time of aptamers, compared with using them alone. Moreover, aptamers can also be used as a controlled release device to control the release of other active molecules in sustained-release hydrogels.

Active aptamers in hydrogels

So far, some aptamers with growth factor-like activity have been screened to promote tissue regeneration. They have been combined with various hydrogel materials, showing a good application prospect in the field of tissue engineering. Ueki et al. (2016); Ueki et al. (2019); Ueki et al. (2020) obtained two aptamer dimers, ss-0 and TD0, that simulate the physiological effects of hepatocyte growth factor and basic fibroblast growth factor, respectively. The ss-0 is composed of two DNA aptamer monomers cross-linked by their complementary 5′-end sequences. These two monomers bind specifically and with high affinity to the receptor Met and have strong anti-nuclease stability. *In vitro* experiments have shown that ss-0 binds two Met receptor molecules to mediate intermolecular dimerization, including autophosphorylation of the receptor molecule, which stimulates cell migration and proliferation. After intravenous administration, the aptamer dimer showed ideal tissue distribution and pharmacokinetic characteristics, which are closely related to the G-quadruplex structure of the dimer sequence (see Figure 3). In a mouse model of outbreak hepatitis, ss-0 antagonizes the apoptosis of liver cells and alleviates the inflammatory response by specifically activating Met, proving its biosafety *in vivo*. TD0 specifically activates fibroblast growth factor receptor-1 (FGFR1). TD0 is directly linked by two SL38.2 DNA aptamers that target the extracellular domain of FGFR1 and can simulate the biological role of bFGF *in vitro*. This induces activation of FGFR1 dimerization and subsequent phosphorylation signal transduction pathways, supporting self-renewal and maintenance of stemness in induced pluripotent stem cells (iPSCs). It is noteworthy that SL38.2 also contains a guanine (G)-rich sequence that can form an antiparallel G-quadruplex structure in the physiological environment. This is considered to be key to its anti-nuclease stability and high-affinity binding to FGFR1. In 2015, Ramaswamy et al. (2015) reported a divalent aptamer (AptDivalent) assembled from two AptM80mer monomers, which specifically targets vascular endothelial growth factor receptor-2 (VEGFR2). Binding of AptDivalent to VEGFR2 on the surface of umbilical vein endothelial cells can activate the phosphorylation of receptors, activate the

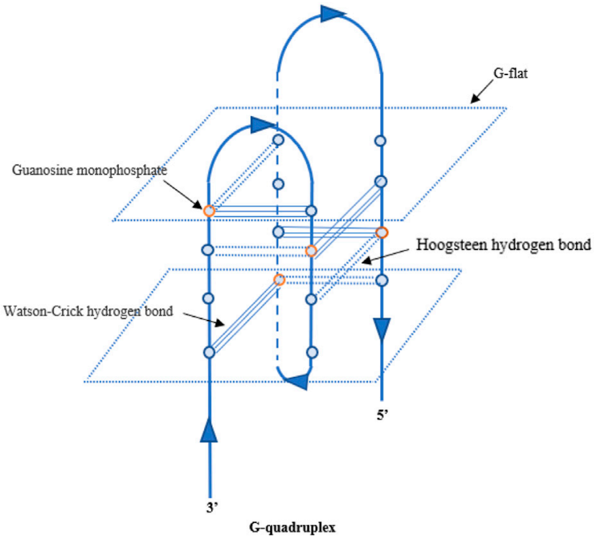

FIGURE 3
Schematic diagram of the G-quadruplex.

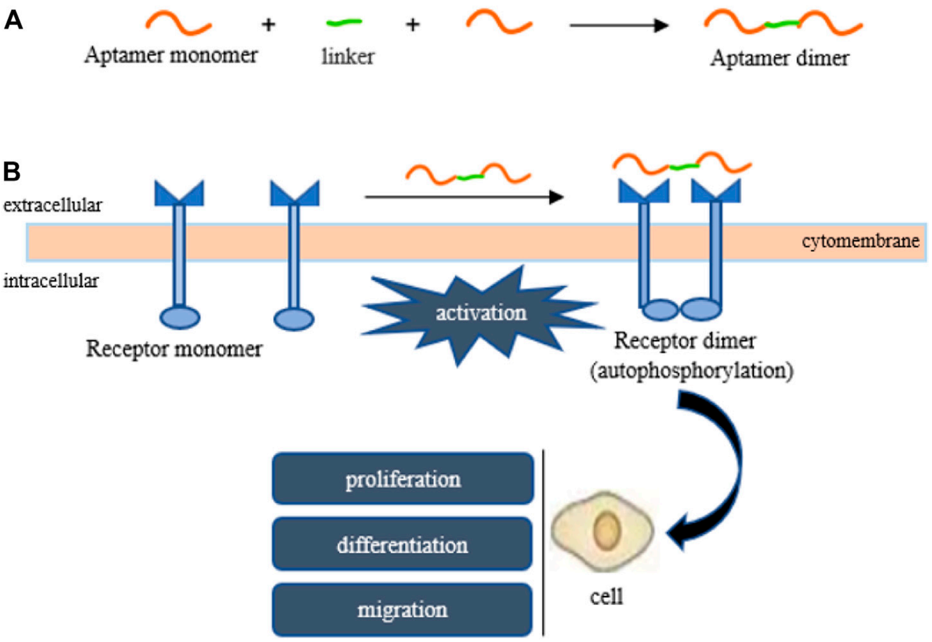

FIGURE 4
Aptamers mimic the activity of growth factors (HGF, bFGF, VEGF). **(A)** The formation of an aptamer dimer, **(B)** receptor-to-receptor dimerization and subsequent activation are both mediated by the aptamer dimer.

downstream Akt pathway, upregulate nitric oxide synthase content in endothelial cells, and ultimately promote endothelial cells to participate in the formation of new capillaries (all *in vitro*). James and Allen (2021) also reported the formation of a tubular phenotype *in vitro* in human umbilical vein endothelial cells (HUVECs) mediated by composite microfibers formed by the self-assembly of this aptamer dimer and collagen. Roy et al. (2021) introduced AptM80mer into a hyaluronic acid hydrogel and realized the functionalization of the hydrogel. They coupled the aptamer whose 5′ end of the nucleotide chain had been modified by an acrydite group to a thiolated-hyaluronic acid in the form of thioether bonds, which are formed under conditions of copolymerization. *In vitro* experiments based on HUVECs demonstrated that AptM80mer plays a similar role in endothelial cell activation and migration mediated by vascular endothelial growth factor (VEGF) in this hydrogel system and promoted angiogenesis. These studies indicate that the aptamer is expected to be an effective biochemical element for the vascularization design of engineering tissues (Figure 4).

Aptamers can control the release of other active molecules in hydrogels

A novel sustained-release hydrogel system has been constructed by using aptamers as the affinity sites for proteins and bioactive oligonucleotides in hydrogels. This sustained-release hydrogel system has been proven beneficial to the long-term and flexible regulation of histopathological repair. In 2019, Abune et al. (2019) designed a double-aptamer-functionalized large-hole polyethylene glycol (PEG) hydrogel. They applied the same bonding method to introduce two DNA aptamers, modified by acrylate and targeting bFGF and VEGF, into the PEG network in the hydrogel system. This design also slowed the release rate of protein factors in the hydrogel and realized the long-term and stable release of active factors. The release mode of the two active factors mediated by this release platform synergistically promoted the migration of HUVECs and the regeneration of blood vessels in the chorioallantoic membrane (CAM) model *in vitro*. Zhao et al. (2019) also developed an aptamer-fibrin (Ap-Fn) hydrogel for controlling VEGF delivery, but the difference was the modification method of the aptamer. They first chemically coupled the mercaptosylated anti-VEGF aptamer with acrydite-modified natural fibrinogen in a copolymerization reaction between mercaptosylation and olefin to synthesize an aptamer-coupled fibrinogen macromolecule monomer. Compared with simple fibrinogen, the overall size and biological activity of this monomer hardly changed, and it could assemble and form a fibrin hydrogel under the action of thrombin and other clotting-related factors. It was proven that the anti-VEGF aptamer could significantly prolong the retention of VEGF in the Ap-Fn hydrogel, thus realizing the sustained release of VEGF. This improved VEGF release modality and promoted p-VEGFR2 expression and cell growth in HUVECs *in vitro*. Compared with the control hydrogels loaded with VEGF (hydrogels without aptamer modification or nonspecific aptamer modification), the Ap-Fn hydrogels loaded with VEGF could more effectively promote the generation of new blood vessels in the mouse skin trauma model and accelerate skin wound healing. The experiment by Juhl et al. (2019) also confirmed that the functional fibrinogen-aptamer did not lead to significant changes in gelation time, mechanical properties, or microstructure of the gel after gelation. However, the introduction of specific aptamers improved VEGF release kinetics in the aptamer-fibrin hydrogels (AFH), reducing the diffusion rate of VEGF compared with non-functional fibrin hydrogels (FH). The release time of VEGF was prolonged. In a mouse skull defect model of critical size, VEGF release mediated by the release platform functionalized by the aptamer increased the degree of vascularization *in vivo* and promoted osteogenesis more significantly than VEGF release mediated by the release platform without the introduction of the aptamer.

It can be seen from the above that aptamers could be used not only as a new bioactive ingredient to load hydrogels and other biological materials to promote tissue regeneration but also as a control device in biological materials to control the release process of other active ingredients. Screening more aptamer molecules for biological activity would be beneficial to regenerative medicine. In addition, we still need to pay more attention to the connection method between aptamers and biomaterial. We must also fully ensure that the biological activity of aptamers does not change after the connection, which is key to the future role of aptamers in the field of regenerative medicine.

Antagonistic aptamers against pro-inflammatory mediators (plays a blocking role in inflammatory mediators)

The immune-inflammatory response plays an important role in the repair of organ and tissue injury. A large number of therapeutic strategies targeting inflammatory factors or inflammatory factor receptors have been attempted for tissue regeneration. As a new type of ligand molecule, aptamers can influence the biological activities mediated by the target after binding with their targets. As a result, a number of aptamers directly involved in the regulation of inflammation have been developed. These aptamers can specifically bind inflammatory mediators, including interleukin-2 (IL-2), IL-6, IL-10, IL-11, IL-17, IL-32, transforming growth factor-β (TGF-β), tumor necrosis factor-α (TNF-α), interferon-γ (IFN-γ), chemokines CCL2, IP-10, and some related receptors (Boshtam et al., 2017), and even some inflammatory autoantigens (Mor-Vaknin et al., 2017; Cao et al., 2021), etc. Here, we focus on several aptamers with immunomodulatory activity developed in recent years. The difference is that they have been studied *in vivo*, and the types of aptamers that regulate complement activity have been developed.

Aptamers that bind TNF-α or TNF receptor

TNF-α is an important member of the TNF superfamily and is derived mainly from monocytes and macrophages. Other cells such as T and B lymphocytes, natural killer cells, mast cells and endothelial cells, neutrophils, smooth muscle cells, and cardiomyocytes can also release this cytokine. TNF-α is also one of the most potent cytokines found in mammals. Its pleiotropy is reflected mainly in its ability to bind both TNFR1 and TNFR2. The binding of TNF-α to TNFR1, one receptor type, leads to a negative inflammatory process or apoptosis. The binding of TNF-α to TNFR2 produces positive repair effects, such as maintaining cell survival and promoting tissue regeneration. These two opposite biological effects of TNF-α are closely related to the mitogen-activated protein kinase (MAPK) signaling pathway (Tseng et al., 2018; Zhang et al., 2020).

The inhibitors represented by TNF-α monoclonal antibodies are thought to effectively block the destructive effect of TNF-α (Mitoma et al., 2018). According to the same principle, a new class of aptamer-based TNF-α inhibitors has been developed. In 2013, Orava et al. (2013) identified a DNA aptamer VR11 that specifically recognizes human recombinant TNF-α. *In vitro* experiments showed that the aptamer could block the binding process between TNFα and TNFα receptor, thus inhibiting the cytotoxicity of TNF-α, which was similar to the action of TNF-α antibody. Kim et al. (2021b) introduced VR11 into a metal nanoparticle that is often used as a carrier material in biomedical applications. This not only enhanced the stability of aptamers but also played a role in capturing TNF-α at the inflammatory site *in vivo* and inhibiting the inflammatory response. Lai et al. (2019) developed a novel TNF-α targeting aptamer (aptTNF-α) and its PEG derivative (aptTNF-α-PEG), which showed good affinity for human/mouse TNF-α *in vitro*. In addition, targeted inhibition of TNF-α was also shown in acute lung injury and acute liver failure mouse models with high TNF-α expression. *In vivo* application of aptTNF-α/aptTNF-α-PEG reduced the degree of the acute inflammatory response in both models and promoted early regeneration of liver tissue. These studies indicate the potential of aptamers as non-immunogenic oligonucleotide inhibitors against TNFα.

Although TNF-α inhibitors inhibit the negative effects of TNF-α, they also eliminate the positive contribution of TNF-α to inflammation. To solve this problem, Zhang et al. (2020) screened specific aptamers for the inflammatory receptor TNFR1 downstream of the TNF-α signaling pathway, hoping to inhibit inflammation and improve the therapeutic effect by selectively inhibiting TNFR1. So far, they have obtained eight aptamers with high affinity for TNFR1 and two with low affinity for TNFR2. However, there are no relevant experimental data in cells and zoology.

Aptamers antagonizing complement (aptamers binding to complement)

Among these aptamers, NOX-D20 (Hoehlig et al., 2013), which binds and blocks complement C5a, has been studied the most. C5a is considered a potent anaphylactic toxin, and excessive C5a demonstrates a cascade of inflammatory destruction (Wood et al., 2018). NOX-D20 is a mirror aptamer synthesized from an unnatural L-oligonucleotide known as Spiegelmers. *In vitro* experiments have shown that NOX-D20 could block the release of elastase from polymorphonuclear leukocytes induced by C5a and the chemotaxis of CD88 expression cell lines. These two pathological events are closely related to pro-inflammation. In rodent sepsis models induced by cecal ligation and puncture, it showed therapeutic effects of reducing inflammation and organ damage, preventing the destruction of the vascular endothelial barrier, and improving the survival rate. The specific binding and inhibitory activity of NOX-D20 on C5a has been proven to be closely related to the G-quadruplex structure of its molecular structure (Yatime et al., 2015). In recent years, people have developed ways of using and treating NOX-D20. Li et al. (2019) combined a framework of nucleic acid (FNA) (Zhang et al., 2021b; Zhang et al., 2021c; Gao et al., 2022) in the form of a DNA origami nanostructure to improve the stability and targeting of NOX-D20 *in vivo*. They used bipyramidal FNA as a drug delivery platform to deliver NOX-D20 to treat cerebral ischemia-reperfusion injury and achieved good results. Zhang et al. (2021d) conjugated NOX-D20 with cerium dioxide nanoparticles (Ni et al., 2019) with active oxygen scavenging activity and formed the complex Ceria@Apt, which not only integrates the anti-inflammatory advantages of both but also makes full use of the liver absorption effect of nanomaterials. This composite material shows great application potential in the repair of liver ischemia-reperfusion injury.

In general, although various inhibitors against C5a have been extensively studied, the types of inhibitors against downstream c5A-related signaling molecules have not been reported.

Aptamer types that act on other pathological targets in neurological diseases

In recent years, studies on the types of aptamers involved in treating several neurological diseases (represented by multiple sclerosis and Parkinson's disease) have become increasingly mature. These have provided ideas for developing new aptamer-based drugs, which are also introduced here.

Aptamers associated with multiple sclerosis

Inspired by the fact that a natural IgM antibody can promote myelin regeneration after binding to oligodendrocytes both in a mouse multiple sclerosis (MS) model infected with Theiler's myeloencephilitis virus (TMEV) (Dubik et al., 2021) and in a mouse model of focal demyelination induced by lysophosphatidylcholine (Bieber et al., 2002), Nastasijevic et al. (2012) identified a small molecule single-stranded DNA aptamer 3064, or LJM-3064 (Wilbanks et al., 2019). This aptamer is smaller than the IgM monoclonal antibody by *in vitro* screening and targets the crude extract of myelin from SJL mice (the myelin preparation is a crude mixture of proteins and lipids). The aptamer contains a guanylate-rich domain and has shown high affinity and specific binding ability to myelin basic protein (MBP) subtypes *in vitro*. Previous studies (Bose, 2021) have shown that the sequence encoded by MBP exon 2 in the MBP subtype is an effective target for myelin regeneration. Their further study found that a streptavidin tetramer could mediate the coupling of four aptamers. This formed the tetramer aptamer complex Myaptavin-3064, which mimics the activity of polyvalent antibodies (Fereidan-Esfahani et al., 2020). The biological stability of the aptamer complex was enhanced compared with that of the aptamer monomer. Intraperitoneal injection of demyelinated mice infected with TMEV enhanced myelin regeneration in the mouse model, while aptamer monomers did not.

In later studies, Smestad and Maher (2013) verified that 26 nucleotides at the 5′ terminal of LJM-3064 (guanylate-rich region) were involved in forming the G-quadruplex through intramolecular folding. They also proved the univalent ion-dependent conformational switching of the G-tetrahedron structure in the physiological environment. Namely, in the absence of sodium and potassium ions, LJM-3064 adopts an antiparallel G-tetrahedron structure. When transferred into a buffer that mimics low potassium concentrations in tissue fluid and plasma, LJM-3064 rapidly transitions into a thermodynamically more stable parallel chain G-tetrahedron conformation. Their data also showed that the parallel G-quadruplex structure of the LJM-3064 monomer still existed in the tetravalent complex Myaptavin-3064. Perschbacher et al. (2015) used quantitative PCR to analyze the effect of the nucleotide sequence structure of LJM-3064 on its pharmacokinetics and the pharmacokinetic characteristics of various LJM-3064 derivatives produced by different modification methods. The results suggest that LJM-3064s tissue penetration and anti-enzymatic activity may be related to the G-rich sequence in its composition structure, and the polyvalent property of MyAPtavin-3064 may more affect the biological activity of myelin regeneration. Wilbanks et al. (2019) truncated and optimized a DNA aptamer LJM-5708 containing only 20 nucleotides based on LJM-3064, which retained the rich G sequence of the G-quadruplex structure formed by the original aptamer. The polyvalent aptamer complex formed by LJM-5708 showed enhanced myelin-binding properties compared with the LJM-5708 monomer, and also showed significant binding ability to human oligodendrocytes cultured *in vitro*. The study also pointed out that the absence of the G-quadruplex formation of the LJM-5708 aptamer results in the loss of myelin binding function of the polyvalent aptamer complex. Heider et al. (2018) designed a streptavidin-free aptamer polymer (named 3064-4WJ-LNA) on the basis of previous work, which is expected to improve immunogenicity.

In addition to studying the role of the LJM-3064 aptamer alone in MS myelin regeneration therapy, LJM-3064 was also conjugated to a mesenchymal stem cell-derived exosome with immunomodulatory functions. Two synergistic biological effects of myelin regeneration and anti-inflammation were achieved in the multiple sclerosis mouse model induced by a myelin oligodendrocyte glycoprotein, which expanded the application of the LJM-3064 aptamer (Hosseini et al., 2019).

In 2020, Fereidan-Esfahani et al. (2020) used flow cytometry and immunocytochemistry to determine the cell-binding properties of Myaptavin-3064 *in vitro*. Myaptavin-3064 shows relatively specific binding to the human oligodendroglioma (HOG) cell line. In particular, the differentiated HOG shows enhanced binding ability with no affinity for lung (L2) or kidney (BHK) cell lines. In addition to HOG cells, Myaptavin-3064 could bind to adult rat oligodendrocytes (OLs) but not to primary cortical cells derived from embryonic mice. The cell-binding properties of Myaptavin-3064 indicate that the target of Myaptavin-3064 exists in the more mature myelin sheath and also support the hypothesis that Myaptavin-3064 induces myelin regeneration through OL binding.

The migration of autoreactive immune cells across the BBB (blood-brain barrier) is considered to be a pathological feature of MS, and it plays a key role in the formation of MS demyelinating plaques (Goverman, 2009). The α4-integrin family mediates the adhesion, exudation, and migration of these inflammatory cells (Mitroulis et al., 2015). Based on the importance of α4-integrin in the pathogenesis of MS, a blocking antibody against α4-integrin, natalizumab, has been used for phase 3 clinical observation in patients with secondary progressive multiple sclerosis (Kapoor et al., 2018). According to a similar concept of action, Kouhpayeh et al. (2019) screened a specific single-stranded DNA aptamer with a high affinity for α4-integrin, which is expected to play a therapeutic effect similar to natalizumab on MS.

Aptamers associated with Parkinson's disease

The α-synuclein (α-syn) is a small natural non-folding protein containing 140 amino acids, existing mainly in the presynaptic terminal in neurons (Burré et al., 2018). In a physiological state, α-syn is a kind of disordered protein in nature. Once stimulated by various injury factors, it tends to form oligomers and aggregates, which may produce toxic effects on neurons through mitochondrial injury, axon transport dysfunction, inflammation, and other mechanisms (Shahnawaz et al., 2020). More importantly, once the abnormal α-syn protein aggregates are absorbed by other normal cells, they can secondarily cause the same pathological process as other normal α-syn proteins in the recipient cells. This leads to intercellular infection and diffusion (Valera and Masliah, 2016), which are important in the formation and progression of PD. Zheng et al. (2018) attempted an aptamer strategy to regulate α-syn toxicity by screening two aptamers with high specificity and affinity for α-syn protein (named F5R1 and F5R2, respectively) using optimized SELEX. Both aptamers could effectively reduce α-syn accumulation in extracellular and intracellular domains, especially in cells. When delivered into human neuroblastoma cells and primary neurons by a carrier peptide, the targeted binding of the two aptamers to α-syn inhibits the formation of pathogenic aggregates and mediates intracellular degradation of α-syn, saving mitochondrial dysfunction and cell damage caused by α-syn overexpression. Ren et al. (2019) studied the *in vivo* effect of these aptamers on PD-related neuropathological defects. They used a neuron-targeting exosome (Alvarez-Erviti et al., 2011) as a loading vehicle for these therapeutic aptamers, achieving efficient delivery of aptamers to neurons *in vivo* and *in vitro*. When co-cultured with primary neurons, aptamer-loaded exosomes significantly reduced the formation of intracellular secondary α-syn insoluble aggregates induced by α-syn fibrils and saved synaptic protein loss and neuronal death. Intraperitoneal injection of this compound in a PD mouse model showed a significant reduction in the pathological aggregates of α-syn in the brain and a significant improvement in the associated motor dysfunction, further confirming the therapeutic ability of these aptamers *in vivo*.

Aptamers associated with Nogo-66 receptor

Myelin-derived inhibitors, represented by Nogo, myelin-associated glycoprotein (MAG), and oligodendrocyte myelin glycoprotein (OMgp), inhibit the growth of neuronal processes by binding to the Nogo-66 receptor (NgR). Using the NgR as the screening target, Wang et al. (2010) obtained a set of RNA aptamers. *In vitro* experiments showed that the binding properties of these aptamers to NgR did not affect neurite growth but could competitively block the inhibition of neurite growth by these three inhibitors. Agrawal et al. (2020) designed a sustained-release hyaluronic acid hydrogel modified by several antisense oligonucleotides, and realized the slow and sustained release of these highly therapeutic aptamers by using the complementary pairing relationship between antisense oligonucleotide sequence and NgR targeted aptamers to varying degrees. It had the same protective effect on the neuronal processes damaged *in vitro*.

Summary and prospects

Regenerative medicine makes full use of various biological techniques and engineering principles to provide better and faster repair of diseases. In the past, stem-cell strategies, tissue engineering techniques, and physicochemical techniques have been applied to regenerative medicine, which has achieved remarkable results. However, in the actual process of operation, people are still faced with many problems, such as difficulties in obtaining stem cells and limited means of regulating cell biological behavior. In addition, there is a lack of development mode and type of new chemical preparations with biological activity, as well as a scarcity of tissue engineering technology application factors.

Aptamers are a kind of ligand nucleic acid molecule with similar binding properties to antibodies. The binding targets are varied, including inorganic ions, amino acids, antibiotics, peptides, proteins, sugars, nucleotides, and their derivatives (Plach and Schubert, 2020). At the same time, these targets can be used as specific markers of bacteria (Yang et al., 2021b), viruses (Lu et al., 2021), cells (Lin et al., 2021), and other living organisms. Aptamers are widely used in various fields of biomedicine, especially in testing, diagnosis, and targeted therapy of cancer, due to their different binding effects with different targets. In a word, aptamers can be called “artificial high quality nucleic acids” because of their universality of application purposes, wide range of action targets, flexibility of action time and space, and diversity of action forms.

From the perspective of tissue regeneration, this article on aptamers in related research in recent years has continued the review and summary. The results show that aptamers can be used alone or crossed with each other through various technical means, such as stem cell technology, biological engineering materials such as hydrogels, nanomedicine, immunotherapy, and so on. Therefore, they show strong plasticity and a broad transformation prospect for applied research in regenerative medicine. At the same time, this paper also provides a reference for the long-term design and utilization of aptamers. Due to the limited amount of literature and the inability to categorize and report, we could not summarize the modification methods of aptamers for therapeutic application.

Many problems still need to be solved for the practical application of aptamers. These include further cost control, development of new aptamer types, improvement in screening efficiency, creation of modifications that improve pharmacokinetics and enhance biological activity *in vivo*, optimization of connection methods with other biomedical materials, and advancing zoological and human experiments. We believe that aptamers can better serve us after these problems have been solved.

Data availability statement

The original contributions presented in the study are included in the article/Supplementary Material, further inquiries can be directed to the corresponding authors.

Author contributions

Study design: LW, JL, and YT. Study procedures and data collection: ZL, SMC, and JZ. Data analysis: ZL and CW. Drafting the manuscript: ZL, CW, and KL. All authors approved the final version of the manuscript and agreed to be accountable for all aspects of the work.

Funding

This work was supported by grants from the National Natural Science Foundation of China (Grant No. 32160209, 82160357, 82071361), Guangxi Key Laboratory of basic and translational research of Bone and Joint Degenerative Diseases (NO. 21-220-06).

Conflict of interest

The authors declare that the research was conducted in the absence of any commercial or financial relationships that could be construed as a potential conflict of interest.

Publisher’s note

References

Abune, L., Zhao, N., Lai, J., Peterson, B., Szczesny, S., and Wang, Y. (2019). Macroporous hydrogels for stable sequestration and sustained release of vascular endothelial growth factor and basic fibroblast growth factor using nucleic acid aptamers. *ACS Biomater. Sci. Eng.* 5 (5), 2382–2390. doi:10.1021/acsbiomaterials.9b00423

Agrawal, N. K., Allen, P., Song, Y. H., Wachs, R. A., Du, Y., Ellington, A. D., et al. (2020). Oligonucleotide-functionalized hydrogels for sustained release of small molecule (aptamer) therapeutics. *Acta Biomater.* 102, 315–325. doi:10.1016/j.actbio.2019.11.037

Alvarez-Erviti, L., Seow, Y., Yin, H., Betts, C., Lakhal, S., and Wood, M. J. A. (2011). Delivery of siRNA to the mouse brain by systemic injection of targeted exosomes. *Nat. Biotechnol.* 29 (4), 341–345. doi:10.1038/nbt.1807

Andreas, K., Sittinger, M., and Ringe, J. (2014). Toward *in situ* tissue engineering: Chemokine-guided stem cell recruitment. *Trends Biotechnol.* 32 (9), 483–492. doi:10.1016/j.tibtech.2014.06.008

Ardjomandi, N., Niederlaender, J., Aicher, W. K., Reinert, S., Schweizer, E., Wendel, H.-P., et al. (2013). Identification of an aptamer binding to human osteogenic-induced progenitor cells. *Nucleic Acid. Ther.* 23 (1), 44–61. doi:10.1089/nat.2012.0349

Atala, A., and Forgacs, G. (2019). Three-dimensional bioprinting in regenerative medicine: Reality, hype, and future. *Stem Cells Transl. Med.* 8 (8), 744–745. doi:10.1002/sctm.19-0089

Bieber, A. J., Warrington, A., Asakura, K., Ciric, B., Kaveri, S. V., Pease, L. R., et al. (2002). Human antibodies accelerate the rate of remyelination following lysolecithin-induced demyelination in mice. *Glia* 37 (3), 241–249. doi:10.1002/glia.10033

Bose, P. (2021). Central pontine myelinolysis and the osmotic demyelination syndromes: An open and shut case? *Acta Neurol. Belg* 121 (4), 849–858. doi:10.1007/s13760-021-01634-0

Boshtam, M., Asgary, S., Kouhpayeh, S., Shariati, L., and Khanahmad, H. (2017). Aptamers against pro- and anti-inflammatory cytokines: A review. *Inflammation* 40 (1), 340–349. doi:10.1007/s10753-016-0477-1

Burré, J., Sharma, M., and Südhof, T. C. (2018). Cell biology and pathophysiology of α-synuclein. *Cold Spring Harb. Perspect. Med.* 8 (3). doi:10.1101/cshperspect.a024091

Byun, J. (2021). Recent progress and opportunities for nucleic acid aptamers. *Life (Basel)* 11 (3). doi:10.3390/life11030193

Cai, S., Yan, J., Xiong, H., Liu, Y., Peng, D., and Liu, Z. (2018). Investigations on the interface of nucleic acid aptamers and binding targets. *Analyst* 143 (22), 5317–5338. doi:10.1039/c8an01467a

Cao, J., Su, J., An, M., Yang, Y., Zhang, Y., Zuo, J., et al. (2021). Novel DEK-targeting aptamer delivered by a hydrogel microneedle attenuates collagen-induced arthritis. *Mol. Pharm.* 18 (1), 305–316. doi:10.1021/acs.molpharmaceut.0c00954

de Melo, M., da Silva Cunha, S. C. P., de Miranda, M. C., Barbosa, J. L., Faria, J. A. Q. A., Rodrigues, M. A., et al. (2021). Selection of DNA aptamers for differentiation of human adipose-derived mesenchymal stem cells from fibroblasts. *Appl. Biochem. Biotechnol.* 193 (11), 3704–3718. doi:10.1007/s12010-021-03618-5

Dubik, M., Marczynska, J., Mørch, M. T., Webster, G., Jensen, K. N., Wlodarczyk, A., et al. (2021). Innate signaling in the CNS prevents demyelination in a focal EAE model. *Front. Neurosci.* 15, 682451. doi:10.3389/fnins.2021.682451

Durand, M. (2021). Large-scale simulations of biological cell sorting driven by differential adhesion follow diffusion-limited domain coalescence regime. *PLoS Comput. Biol.* 17 (8), e1008576. doi:10.1371/journal.pcbi.1008576

Edgar, L., Pu, T., Porter, B., Aziz, J. M., La Pointe, C., Asthana, A., et al. (2020). Regenerative medicine, organ bioengineering and transplantation. *Br. J. Surg.* 107 (7), 793–800. doi:10.1002/bjs.11686

Enam, S. F., Krieger, J. R., Saxena, T., Watts, B. E., Olingy, C. E., Botchwey, E. A., et al. (2017). Enrichment of endogenous fractalkine and anti-inflammatory cells via aptamer-functionalized hydrogels. *Biomaterials* 142, 52–61. doi:10.1016/j.biomaterials.2017.07.013

Fereidan-Esfahani, M., Yue, W. Y., Wilbanks, B., Johnson, A. J., Warrington, A. E., Howe, C. L., et al. (2020). Remyelination-promoting DNA aptamer conjugate myaptavin-3064 binds to adult oligodendrocytes *in vitro*. *Pharm. (Basel)* 13 (11). doi:10.3390/ph13110403

Fu, X. (2018). Regenerative medicine in China: New advances and hopes. *Sci. China Life Sci.* 61 (10), 1135–1136. doi:10.1007/s11427-018-9394-9

Gao, Y., Chen, X., and Tian, T. (2022). A lysosome-activated tetrahedral nanobox for encapsulated siRNA delivery[J]. *Adv. Mater* 2022, e2201731.

Gong, Z., Xia, K., Xu, A., Yu, C., Wang, C., Zhu, J., et al. (2020). Stem cell transplantation: A promising therapy for spinal cord injury. *Cscr* 15 (4), 321–331. doi:10.2174/1574888x14666190823144424

Goverman, J. (2009). Autoimmune T cell responses in the central nervous system. *Nat. Rev. Immunol.* 9 (6), 393–407. doi:10.1038/nri2550

Guo, K. T., SchÄfer, R., Paul, A., Gerber, A., Ziemer, G., and Wendel, H. P. (2006). A new technique for the isolation and surface immobilization of mesenchymal stem cells from whole bone marrow using high-specific DNA aptamers. *Stem Cells* 24 (10), 2220–2231. doi:10.1634/stemcells.2006-0015

Guo, K. T., Scharnweber, D., Schwenzer, B., Ziemer, G., and Wendel, H. P. (2007). The effect of electrochemical functionalization of Ti-alloy surfaces by aptamer-based capture molecules on cell adhesion. *Biomaterials* 28 (3), 468–474. doi:10.1016/j.biomaterials.2006.09.021

Guo, K., Wendel, H. P., Scheideler, L., Ziemer, G., and Scheule, A. M. (2005). Aptamer-based capture molecules as a novel coating strategy to promote cell adhesion. *J. Cell. Mol. Med.* 9 (3), 731–736. doi:10.1111/j.1582-4934.2005.tb00503.x

Haller, C., Sobolewska, B., Schibilsky, D., Avci-Adali, M., Schlensak, C., Wendel, H.-P., et al. (2015). One-staged aptamer-based isolation and application of endothelial progenitor cells in a porcine myocardial infarction model. *Nucleic Acid. Ther.* 25 (1), 20–26. doi:10.1089/nat.2014.0499

Heider, R. M., Smestad, J. A., Lemus, H. N., Wilbanks, B., Warrington, A. E., Peters, J. P., et al. (2018). An assay that predicts *in vivo* efficacy for DNA aptamers that stimulate remyelination in a mouse model of multiple sclerosis. *Mol. Ther. - Methods & Clin. Dev.* 9, 270–277. doi:10.1016/j.omtm.2018.03.005

Hoehlig, K., Maasch, C., Shushakova, N., Buchner, K., Huber-Lang, M., Purschke, W. G., et al. (2013). A novel C5a-neutralizing mirror-image (l-)Aptamer prevents organ failure and improves survival in experimental sepsis. *Mol. Ther.* 21 (12), 2236–2246. doi:10.1038/mt.2013.178

Hoffmann, J., Paul, A., Harwardt, M., Groll, J., Reeswinkel, T., Klee, D., et al. (2008). Immobilized DNA aptamers used as potent attractors for porcine endothelial precursor cells. *J. Biomed. Mat. Res.* 84A (3), 614–621. doi:10.1002/jbm.a.31309

Hosseini, S. F., Alibolandi, M., and Rafatpanah, H. (2019). Immunomodulatory properties of MSC-derived exosomes armed with high affinity aptamer toward mylein as a platform for reducing multiple sclerosis clinical score[J]. *J. Control Release* 299, 149–164.

Hou, Z., Meyer, S., Propson, N. E., Nie, J., Jiang, P., Stewart, R., et al. (2015). Characterization and target identification of a DNA aptamer that labels pluripotent stem cells. *Cell Res.* 25 (3), 390–393. doi:10.1038/cr.2015.7

Hu, X., Wang, Y., Tan, Y., Wang, J., Liu, H., Wang, Y., et al. (2017). A difunctional regeneration scaffold for knee repair based on aptamer-directed cell recruitment. *Adv. Mater* 29 (15). doi:10.1002/adma.201605235

Iwagawa, T., Ohuchi, S. P., Watanabe, S., and Nakamura, Y. (2012). Selection of RNA aptamers against mouse embryonic stem cells. *Biochimie* 94 (1), 250–257. doi:10.1016/j.biochi.2011.10.017

James, B. D., and Allen, J. B. (2021). Self-assembled VEGF-R2 targeting DNA aptamer-collagen fibers stimulate an angiogenic-like endothelial cell phenotype. *Mater. Sci. Eng. C* 120, 111683. doi:10.1016/j.msec.2020.111683

Juhl, O. T., Zhao, N., Merife, A. B., Cohen, D., Friedman, M., Zhang, Y., et al. (2019). Aptamer-functionalized fibrin hydrogel improves vascular endothelial growth factor release kinetics and enhances angiogenesis and osteogenesis in critically sized cranial defects. *ACS Biomater. Sci. Eng.* 5 (11), 6152–6160. doi:10.1021/acsbiomaterials.9b01175

Kapoor, R., Ho, P. R., Campbell, N., Chang, I., Deykin, A., Forrestal, F., et al. (2018). Effect of natalizumab on disease progression in secondary progressive multiple sclerosis (ASCEND): A phase 3, randomised, double-blind, placebo-controlled trial with an open-label extension. *Lancet Neurol.* 17 (5), 405–415. doi:10.1016/S1474-4422(18)30069-3

Kim, D. H., Ahn, J., Kang, H. K., Kim, M.-S., Kim, N.-G., Kook, M. G., et al. (2021). Development of highly functional bioengineered human liver with perfusable vasculature. *Biomaterials* 265, 120417. doi:10.1016/j.biomaterials.2020.120417

Kim, J., Park, H., Saravanakumar, G., and Kim, W. J. (2021). Polymer/aptamer-integrated gold nanoconstruct suppresses the inflammatory process by scavenging ROS and capturing pro-inflammatory cytokine TNF-α. *ACS Appl. Mat. Interfaces* 13 (8), 9390–9401. doi:10.1021/acsami.0c15727

Kouhpayeh, S., Hejazi, Z., Boshtam, M., Mirian, M., Rahimmanesh, I., Darzi, L., et al. (2019). Development of α4 integrin DNA aptamer as a potential therapeutic tool for multiple sclerosis. *J Cell. Biochem.* 120 (9), 16264–16272. doi:10.1002/jcb.28907

Kuang, L., Ma, X., Ma, Y., Yao, Y., Tariq, M., Yuan, Y., et al. (2019). Self-assembled injectable nanocomposite hydrogels coordinated by *in situ* generated CaP nanoparticles for bone regeneration. *ACS Appl. Mat. Interfaces* 11 (19), 17234–17246. doi:10.1021/acsami.9b03173

Laghmouchi, A., Hoogstraten, C., Falkenburg, J., and Jedema, I. (2020). Long-term *in vitro* persistence of magnetic properties after magnetic bead-based cell separation of T cells. *Scand. J. Immunol.* 92 (3), e12924. doi:10.1111/sji.12924

Lai, W. Y., Wang, J. W., Huang, B. T., Lin, E. P.-Y., and Yang, P.-C. (2019). A novel TNF-α-targeting aptamer for TNF-α-mediated acute lung injury and acute liver failure. *Theranostics* 9 (6), 1741–1751. doi:10.7150/thno.30972

Li, S., Jiang, D., Rosenkrans, Z. T., Barnhart, T. E., Ehlerding, E. B., Ni, D., et al. (2019). Aptamer-conjugated framework nucleic acids for the repair of cerebral ischemia-reperfusion injury. *Nano Lett.* 19 (10), 7334–7341. doi:10.1021/acs.nanolett.9b02958

Lin, N., Wu, L., Xu, X., Wu, Q., Wang, Y., Shen, H., et al. (2021). Aptamer generated by cell-SELEX for specific targeting of human glioma cells. *ACS Appl. Mat. Interfaces* 13 (8), 9306–9315. doi:10.1021/acsami.0c11878

Lu, T., Zhang, H., Zhou, J., Ma, Q., Yan, W., Zhao, L., et al. (2021). Aptamer-targeting of Aleutian mink disease virus (AMDV) can be an effective strategy to inhibit virus replication. *Sci. Rep.* 11 (1), 4649. doi:10.1038/s41598-021-84223-8

Ma, W., Yang, Y., and Zhu, J. (2022). Biomimetic nanoerythrosome-coated aptamer-DNA tetrahedron/maytansine conjugates: pH-responsive and targeted cytotoxicity for HER2-positive breast cancer[J]. *Adv. Mater* 2022, e2109609.

Mandal, M., Dutta, N., and Dutta, G. (2021). Aptamer-based biosensors and their implications in COVID-19 diagnosis. *Anal. Methods* 13 (45), 5400–5417. doi:10.1039/d1ay01519b

Manohar, S. M., Shah, P., and Nair, A. (2021). Flow cytometry: Principles, applications and recent advances. *Bioanalysis* 13 (3), 181–198. doi:10.4155/bio-2020-0267

Matai, I., Kaur, G., Seyedsalehi, A., McClinton, A., and Laurencin, C. T. (2020). Progress in 3D bioprinting technology for tissue/organ regenerative engineering. *Biomaterials* 226, 119536. doi:10.1016/j.biomaterials.2019.119536

Mitoma, H., Horiuchi, T., Tsukamoto, H., and Ueda, N. (2018). Molecular mechanisms of action of anti-TNF-α agents - comparison among therapeutic TNF-α antagonists. *Cytokine* 101, 56–63. doi:10.1016/j.cyto.2016.08.014

Mitroulis, I., Alexaki, V. I., Kourtzelis, I., Ziogas, A., Hajishengallis, G., and Chavakis, T. (2015). Leukocyte integrins: Role in leukocyte recruitment and as therapeutic targets in inflammatory disease. *Pharmacol. Ther.* 147, 123–135. doi:10.1016/j.pharmthera.2014.11.008

Mor-Vaknin, N., Saha, A., Legendre, M., Carmona-Rivera, C., Amin, M. A., Rabquer, B. J., et al. (2017). DEK-targeting DNA aptamers as therapeutics for inflammatory arthritis. *Nat. Commun.* 8, 14252. doi:10.1038/ncomms14252

Nam, K., Im, B. I., Kim, T., Kim, Y. M., and Roh, Y. H. (2021). Anisotropically functionalized aptamer-DNA nanostructures for enhanced cell proliferation and target-specific adhesion in 3D cell cultures. *Biomacromolecules* 22 (7), 3138–3147. doi:10.1021/acs.biomac.1c00619

Nastasijevic, B., Wright, B. R., Smestad, J., Warrington, A. E., Rodriguez, M., and Maher, L. J. (2012). Remyelination induced by a DNA aptamer in a mouse model of multiple sclerosis. *PLoS One* 7 (6), e39595. doi:10.1371/journal.pone.0039595

Ni, D., Wei, H., Chen, W., Bao, Q., Rosenkrans, Z. T., Barnhart, T. E., et al. (2019). Ceria nanoparticles meet hepatic ischemia-reperfusion injury: The perfect imperfection. *Adv. Mater* 31 (40), e1902956. doi:10.1002/adma.201902956

Ni, S., Zhuo, Z., Pan, Y., Yu, Y., Li, F., Liu, J., et al. (2021). Recent progress in aptamer discoveries and modifications for therapeutic applications. *ACS Appl. Mat. Interfaces* 13 (8), 9500–9519. doi:10.1021/acsami.0c05750

Orava, E. W., Jarvik, N., Shek, Y. L., Sidhu, S. S., and Gariépy, J. (2013). A short DNA aptamer that recognizes TNFα and blocks its activity *in vitro*. *ACS Chem. Biol.* 8 (1), 170–178. doi:10.1021/cb3003557

Perschbacher, K., Smestad, J. A., Peters, J. P., Standiford, M. M., Denic, A., Wootla, B., et al. (2015). Quantitative PCR analysis of DNA aptamer pharmacokinetics in mice. *Nucleic Acid. Ther.* 25 (1), 11–19. doi:10.1089/nat.2014.0515

Perwein, M. K., Smestad, J. A., Warrington, A. E., Heider, R. M., Kaczor, M. W., Maher, L. J., et al. (2018). A comparison of human natural monoclonal antibodies and aptamer conjugates for promotion of CNS remyelination: Where are we now and what comes next? *Expert Opin. Biol. Ther.* 18 (5), 545–560. doi:10.1080/14712598.2018.1441284

Plach, M., and Schubert, T. (2020). Biophysical characterization of aptamer-target interactions. *Adv. Biochem. Eng. Biotechnol.* 174, 1–15. doi:10.1007/10_2019_103

Ramaswamy, V., Monsalve, A., Sautina, L., Segal, M. S., Dobson, J., and Allen, J. B. (2015). DNA aptamer assembly as a vascular endothelial growth factor receptor agonist. *Nucleic Acid. Ther.* 25 (5), 227–234. doi:10.1089/nat.2014.0519

Ren, X., Zhao, Y., Xue, F., Zheng, Y., Huang, H., Wang, W., et al. (2019). Exosomal DNA aptamer targeting α-synuclein aggregates reduced neuropathological deficits in a mouse Parkinson's disease model. *Mol. Ther. - Nucleic Acids* 17, 726–740. doi:10.1016/j.omtn.2019.07.008

Riccardi, C., Napolitano, E., Platella, C., Musumeci, D., Melone, M. A. B., and Montesarchio, D. (2021). Anti-VEGF DNA-based aptamers in cancer therapeutics and diagnostics. *Med. Res. Rev.* 41 (1), 464–506. doi:10.1002/med.21737

Roshanbinfar, K., Esser, T. U., and Engel, F. B. (2021). Stem cells and their cardiac derivatives for cardiac tissue engineering and regenerative medicine. *Antioxidants Redox Signal.* 35 (3), 143–162. doi:10.1089/ars.2020.8193

Roy, T., James, B. D., and Allen, J. B. (2021). Anti-VEGF-R2 aptamer and RGD peptide synergize in a bifunctional hydrogel for enhanced angiogenic potential. *Macromol. Biosci.* 21 (2), e2000337. doi:10.1002/mabi.202000337

Saito, S. (2021). SELEX-based DNA aptamer selection: A perspective from the advancement of separation techniques. *Anal. Sci.* 37 (1), 17–26. doi:10.2116/analsci.20sar18

Sarkar, A., Saha, S., Paul, A., Maji, A., Roy, P., and Maity, T. K. (2021). Understanding stem cells and its pivotal role in regenerative medicine. *Life Sci.* 273, 119270. doi:10.1016/j.lfs.2021.119270

Schäfer, R., Wiskirchen, J., Guo, K., Neumann, B., Kehlbach, R., Pintaske, J., et al. (2007). Aptamer-based isolation and subsequent imaging of mesenchymal stem cells in ischemic myocard by magnetic resonance imaging. *Fortschr Röntgenstr* 179 (10), 1009–1015. doi:10.1055/s-2007-963409

Shahnawaz, M., Mukherjee, A., Pritzkow, S., Mendez, N., Rabadia, P., Liu, X., et al. (2020). Discriminating α-synuclein strains in Parkinson's disease and multiple system atrophy. *Nature* 578 (7794), 273–277. doi:10.1038/s41586-020-1984-7

Smestad, J., and Maher, L. R. (2013). Ion-dependent conformational switching by a DNA aptamer that induces remyelination in a mouse model of multiple sclerosis. *Nucleic Acids Res.* 41 (2), 1329–1342. doi:10.1093/nar/gks1093

Son, J., Kim, J., Lee, K., Hwang, J., Choi, Y., Seo, Y., et al. (2019). DNA aptamer immobilized hydroxyapatite for enhancing angiogenesis and bone regeneration. *Acta Biomater.* 99, 469–478. doi:10.1016/j.actbio.2019.08.047

Strahm, Y., Flueckiger, A., Billinger, M., Meier, P., Mettler, D., Weisser, S., et al. (2010). Endothelial-cell-binding aptamer for coating of intracoronary stents. *J. Invasive Cardiol.* 22 (10), 481–487.

Sun, T., Meng, C., Ding, Q., Yu, K., Zhang, X., Zhang, W., et al. (2021). *In situ* bone regeneration with sequential delivery of aptamer and BMP2 from an ECM-based scaffold fabricated by cryogenic free-form extrusion. *Bioact. Mater.* 6 (11), 4163–4175. doi:10.1016/j.bioactmat.2021.04.013

Tang, W. (2019). Challenges and advances in stem cell therapy. *Bst* 13 (4), 286. doi:10.5582/bst.2019.01241

Tseng, W. Y., Huang, Y. S., Lin, H. H., Luo, S.-F., McCann, F., McNamee, K., et al. (2018). TNFR signalling and its clinical implications. *Cytokine* 101, 19–25. doi:10.1016/j.cyto.2016.08.027

Ueki, R., Atsuta, S., Ueki, A., Hoshiyama, J., Li, J., Hayashi, Y., et al. (2019). DNA aptamer assemblies as fibroblast growth factor mimics and their application in stem cell culture. *Chem. Commun.* 55 (18), 2672–2675. doi:10.1039/c8cc08080a

Ueki, R., Uchida, S., Kanda, N., Yamada, N., Ueki, A., Akiyama, M., et al. (2020). A chemically unmodified agonistic DNA with growth factor functionality for *in vivo* therapeutic application. *Sci. Adv.* 6 (14), eaay2801. doi:10.1126/sciadv.aay2801

Ueki, R., Ueki, A., Kanda, N., and Sando, S. (2016). Oligonucleotide-based mimetics of hepatocyte growth factor. *Angew. Chem. Int. Ed.* 55 (2), 579–582. doi:10.1002/anie.201508572

Valera, E., and Masliah, E. (2016). Combination therapies: The next logical Step for the treatment of synucleinopathies? *Mov. Disord.* 31 (2), 225–234. doi:10.1002/mds.26428

Wang, M., Wu, H., Li, Q., Yang, Y., Che, F., Wang, G., et al. (2019). Novel aptamer-functionalized nanoparticles enhances bone defect repair by improving stem cell recruitment. *Ijn* 14, 8707–8724. doi:10.2147/ijn.s223164

Wang, X., Song, X., Li, T., Chen, J., Cheng, G., Yang, L., et al. (2019). Aptamer-functionalized bioscaffold enhances cartilage repair by improving stem cell recruitment in osteochondral defects of rabbit knees. *Am. J. Sports Med.* 47 (10), 2316–2326. doi:10.1177/0363546519856355

Wang, X., Zheng, X., Duan, Y., Ma, L., and Gao, C. (2019). Defined substrate by aptamer modification with the balanced properties of selective capture and stemness maintenance of mesenchymal stem cells. *ACS Appl. Mat. Interfaces* 11 (16), 15170–15180. doi:10.1021/acsami.9b03333

Wang, Y., Khaing, Z. Z., Li, N., Hall, B., Schmidt, C. E., and Ellington, A. D. (2010). Aptamer antagonists of myelin-derived inhibitors promote axon growth. *PLoS One* 5 (3), e9726. doi:10.1371/journal.pone.0009726

Wilbanks, B., Smestad, J., Heider, R. M., Warrington, A. E., Rodriguez, M., and Maher, L. J. (2019). Optimization of a 40-mer antimyelin DNA aptamer identifies a 20-mer with enhanced properties for potential multiple sclerosis therapy. *Nucleic Acid. Ther.* 29 (3), 126–135. doi:10.1089/nat.2018.0776

Wood, A., Vassallo, A., Summers, C., Chilvers, E. R., and Conway-Morris, A. (2018). C5a anaphylatoxin and its role in critical illness-induced organ dysfunction. *Eur. J. Clin. Invest.* 48 (12), e13028. doi:10.1111/eci.13028

Wu, J., Liyarita, B. R., Zhu, H., Liu, M., Hu, X., and Shao, F. (2021). Self-assembly of dendritic DNA into a hydrogel: Application in three-dimensional cell culture. *ACS Appl. Mat. Interfaces* 13 (42), 49705–49712. doi:10.1021/acsami.1c14445

Yamanaka, S. (2020). Pluripotent stem cell-based cell therapy-promise and challenges. *Cell Stem Cell* 27 (4), 523–531. doi:10.1016/j.stem.2020.09.014

Yang, M., Chen, X., Zhu, L., Lin, S., Li, C., Li, X., et al. (2021). Aptamer-functionalized DNA-silver nanocluster nanofilm for visual detection and elimination of bacteria. *ACS Appl. Mat. Interfaces* 13 (32), 38647–38655. doi:10.1021/acsami.1c05751

Yang, Z., Zhao, T., Gao, C., Cao, F., Li, H., Liao, Z., et al. (2021). 3D-Bioprinted difunctional scaffold for *in situ* cartilage regeneration based on aptamer-directed cell recruitment and growth factor-enhanced cell chondrogenesis. *ACS Appl. Mat. Interfaces* 13 (20), 23369–23383. doi:10.1021/acsami.1c01844

Yao, C., Tang, H., Wu, W., Tang, J., Guo, W., Luo, D., et al. (2020). Double rolling circle amplification generates physically cross-linked DNA network for stem cell fishing. *J. Am. Chem. Soc.* 142 (7), 3422–3429. doi:10.1021/jacs.9b11001

Yatime, L., Maasch, C., Hoehlig, K., Klussmann, S., Andersen, G. R., and Vater, A. (2015). Structural basis for the targeting of complement anaphylatoxin C5a using a mixed L-RNA/L-DNA aptamer. *Nat. Commun.* 6, 6481. doi:10.1038/ncomms7481

Yoon, J. W., Jang, I. H., Heo, S. C., Kwon, Y. W., Choi, E. J., Bae, K. H., et al. (2015). Isolation of foreign material-free endothelial progenitor cells using CD31 aptamer and therapeutic application for ischemic injury. *PLoS One* 10 (7), e0131785. doi:10.1371/journal.pone.0131785

Zhang, N., Wang, Z., and Zhao, Y. (2020). Selective inhibition of Tumor necrosis factor receptor-1 (TNFR1) for the treatment of autoimmune diseases. *Cytokine & Growth Factor Rev.* 55, 80–85. doi:10.1016/j.cytogfr.2020.03.002

Zhang, T., Tian, T., and Lin, Y. (2021). Functionalizing framework nucleic-acid-based nanostructures for biomedical application[J]. *Adv. Mater* 2021, e2107820.

Zhang, X., Hu, J., Becker, K. V., Engle, J. W., Ni, D., Cai, W., et al. (2021). Antioxidant and C5a-blocking strategy for hepatic ischemia-reperfusion injury repair. *J. Nanobiotechnol* 19 (1), 107. doi:10.1186/s12951-021-00858-9

Zhang, X., Liu, N., Zhou, M., Li, S., and Cai, X. (2021). The application of tetrahedral framework nucleic acids as a drug carrier in biomedicine fields. *Cscr* 16 (1), 48–56. doi:10.2174/1574888x15666200422103415

Zhang, Z., Pandey, R., Li, J., Gu, J., White, D., Stacey, H. D., et al. (2021). High-affinity dimeric aptamers enable the rapid electrochemical detection of wild-type and B.1.1.7 SARS-CoV-2 in unprocessed saliva. *Angew. Chem. Intl Ed.* 60 (45), 24266–24274. doi:10.1002/anie.202110819

Zhao, N., Coyne, J., Xu, M., Zhang, X., Suzuki, A., Shi, P., et al. (2019). Assembly of bifunctional aptamer-fibrinogen macromer for VEGF delivery and skin wound healing. *Chem. Mat.* 31 (3), 1006–1015. doi:10.1021/acs.chemmater.8b04486

Zheng, Y., Qu, J., Xue, F., Zheng, Y., Yang, B., Chang, Y., et al. (2018). Novel DNA aptamers for Parkinson's disease treatment inhibit α-synuclein aggregation and facilitate its degradation. *Mol. Ther. - Nucleic Acids* 11, 228–242. doi:10.1016/j.omtn.2018.02.011

frontiers | Frontiers in Bioengineering and Biotechnology

TYPE Brief Research Report
PUBLISHED 05 September 2022
DOI 10.3389/fbioe.2022.961108

OPEN ACCESS

EDITED BY
Feng-Huei Lin,
National Taiwan University, Taiwan

REVIEWED BY
Silvia Rizzato,
Department of Physical Sciences and Technologies of Matter (CNR), Italy
Chérif Dridi,
Ministry of Higher Education and Scientific Research, Tunisia

*CORRESPONDENCE
Jin Nam,
jnam@engr.ucr.edu

†These authors have contributed equally to this work

SPECIALTY SECTION
This article was submitted to Tissue Engineering and Regenerative Medicine, a section of the journal Frontiers in Bioengineering and Biotechnology

RECEIVED 03 June 2022
ACCEPTED 05 August 2022
PUBLISHED 05 September 2022

CITATION
Banerjee A, Tai Y, Myung NV and Nam J (2022), Non-destructive characterization of bone mineral content by machine learning-assisted electrochemical impedance spectroscopy.
Front. Bioeng. Biotechnol. 10:961108.
doi: 10.3389/fbioe.2022.961108

Non-destructive characterization of bone mineral content by machine learning-assisted electrochemical impedance spectroscopy

Aihik Banerjee[1†], Youyi Tai[1†], Nosang V. Myung[2] and Jin Nam[1,3*]

[1]Department of Bioengineering, University of California, Riverside, University Ave, Riverside, CA, United States, [2]Department of Chemical and Biomolecular Engineering, University of Notre Dame, Notre Dame, IN, United States, [3]UC-KIMS Center for Innovative Materials, University of California, Riverside, University Ave, Riverside, CA, United States

Continuous quantitative monitoring of the change in mineral content during the bone healing process is crucial for efficient clinical treatment. Current radiography-based modalities, however, pose various technological, medical, and economical challenges such as low sensitivity, radiation exposure risk, and high cost/instrument accessibility. In this regard, an analytical approach utilizing electrochemical impedance spectroscopy (EIS) assisted by machine learning algorithms is developed to quantitatively characterize the physico-electrochemical properties of the bone, in response to the changes in the bone mineral contents. The system is designed and validated following the process of impedance data measurement, equivalent circuit model designing, machine learning algorithm optimization, and data training and testing. Overall, the systematic machine learning-based classification utilizing the combination of EIS measurements and electrical circuit modeling offers a means to accurately monitor the status of the bone healing process.

KEYWORDS

bone mineral content, electrochemical impedance spectroscopy, equivalent circuit model, machine learning, bone healing

Introduction

Critical-sized bone defects, generally characterized as a bone loss greater than two times the diameter of the specific bone, pose a significant clinical concern, requiring therapeutic interventions for proper healing (Nauth et al., 2018; Kobbe et al., 2020). Non-union bone healing, which often occurs during the treatment of critical-sized bone defects, is an especially challenging condition, requiring surgical intervention and frequently causing inefficient bone repair with suboptimal clinical outcomes (Wildemann et al., 2021). Thus, the management of critical-sized bone defects remains a major clinical orthopedic challenge and it requires novel and safe therapeutic strategies for enhanced bone regeneration.

Bone healing is a highly dynamic process and continuous monitoring of the efficacy of a therapeutic approach is crucial for ensuring optimal treatment. One promising strategy is to quantify the change in mineral content to correlate it with the healing status in the defect region. To date, however, effective real-time *in situ* monitoring systems for bone healing are highly primitive at best and non-existent at worst (Augat et al., 2014; Rani et al., 2020; Ernst et al., 2021). Current assessment modalities, including X-ray diagnostic radiography, photon absorptiometry, quantitative computed tomography, and magnetic resonance imaging, suffer from many limitations such as low sensitivity for bone mineral content, high cost, the requirement of trained personnel, standardization of image quality/quantification, and radiation overexposure risks (Hak et al., 2014; Wildemann et al., 2021). Moreover, these endpoint qualitative assessments are often subjective, and their accuracy is reliant on the clinician's expertise (Morshed et al., 2008; Claes and Cunningham, 2009; Schwarzenberg et al., 2020).

In this regard, electrochemical impedance spectroscopy (EIS) provides a means to non-destructively assess the bone healing process by characterizing the electrical properties of the tissue. Several studies have demonstrated the feasibility of utilizing EIS for determining bone health, where tissue impedance changes at specific frequencies of the applied alternating current (AC) potential were well correlated to the radiographically determined status of bone regeneration (Kozhevnikov et al., 2016; Afsarimanesh et al., 2016; Dell'Osa et al., 2019a; Dell'Osa et al., 2019b). Particularly, Lin et al. utilized electrode implants to longitudinally monitor bone healing in murine fracture models, where the magnitude of impedance measurements was proportional to the quantified measures of bone volume and bone mineral density (Lin et al., 2015). Such tracking of the longitudinal changes of impedance with respect to those of non-fractured control samples allowed them to distinguish good healing as compared to non-union bone fracture (Lin et al., 2015). This *in vivo* application of EIS demonstrates the potential of the electrochemical analysis for bone fracture monitor and management in the clinic (Lin et al., 2019). However, this approach is semi-quantitative in nature, requiring separate control groups to assess the degree of bone healing.

Herein, we demonstrate the detection of bone mineral contents, a marker for the degree of bone healing, using the EIS technique empowered by machine learning models. Machine learning has emerged as an effective and accurate method to understand complex biological phenomena, especially human diseases and injuries (Yu et al., 2018; Liang et al., 2019; Tekkesin, 2019; Peng et al., 2021). Several studies have used various machine learning approaches to develop equivalent circuit models from EIS data (Tripathi and Maktedar, 2016; Cunha et al., 2019; Babaeiyazdi et al., 2021), but the application of machine learning in diagnosing the degree of bone health has not been attempted. The workflow presented in this study consisted of four main steps—an EIS impedance measurement, equivalent circuit modeling and data fitting, principal component analysis, and machine learning analysis—to gradually build up a bone composition detection strategy with the purpose of automatically formulating multiple impedimetric parameters into a recognition machine that determines the bone mineral content. Three different machine learning algorithms were compared in terms of their performance to categorize the mineral content of rat femur samples. Two types of datasets, one consisting of impedance data at different frequencies only and the other consisting of fitted equivalent circuit model parameters in addition to the impedance values, were used to evaluate the classification models in order to delineate the importance of the feature set used for multiclass classifications. We demonstrate that the machine learning-assisted EIS analysis enables the prediction of the bone mineral content with high accuracy, suggesting its potential for a real-time monitoring modality to assess the bone healing process.

Methods

Bone sample preparation

Femurs were excised from rat cadavers of similar size and age, surpluses from other non-skeletal studies. Bone samples of 6 mm in length, approximately twice the diameter of the as-extracted femurs, were prepared from the diaphysis of the femur by using a diamond saw and both ends were polished with sandpaper to ensure proper electrical contact between the electrode and the sample. For demineralization, the femur samples were incubated in 20% (v/v) Cal-Ex II decalcifier solution (Fisher Scientific) for varying durations to prepare samples containing a specific weight percentage of mineral. Specifically, bone samples having 0, 20, 40, 60, 80, and 100% of mineral contents (as compared to fully demineralized samples) were selected to simulate critical-sized bone defects at different healing stages. The wet weights of the bone samples were recorded after each treatment, which was used to calculate the weight percent of minerals remaining in the samples.

Bone mineral content calculation

The bone mineral content, the wt% of mineral present in the samples after specific durations of demineralization, was indirectly calculated using the following formula,

$$W_{M,lost} = \rho_M \times V_{M,lost} = \rho_M \times \frac{\Delta W_{wet}}{\rho_W - \rho_M}$$

where $W_{M,lost}$ is the weight of mineral lost after decalcifier treatment, ρ_M is the density of hydroxyapatite, which makes up the mineral phase of bone, $V_{M,lost}$ is the volume of mineral lost after decalcifier treatment, ΔW_{wet} is the change in the wet weight of the femur sample, and ρ_W is the density of water. We assumed that the volume of mineral lost is replaced by the volume of media since buffer saturation was used to maintain the net volume.

Surface characterization of bone samples

The morphology of the intact and demineralized bone samples was characterized using a VEGA3 scanning electron microscope (SEM) (Tescan Brno, Czech Republic). The bone samples were subject to a dehydration process for SEM sample preparation by their exposure to a graded ethanol series, followed by a graded ethanol-hexamethyldisilane series as previously described (Nam et al., 2007; Maldonado et al., 2016).

Bone mineral content visualization

Alizarin red S staining (Sigma) was used to colorimetrically determine the mineral content in sectioned bone samples under various demineralization durations as previously described (Homer et al., 2019). The color intensity was quantified under each condition using ImageJ software and five slices were used for quantification for each condition.

Electrochemical impedance spectroscopic (EIS) measurements

The electrochemical impedance measurements were carried out using a CH Instruments 604C electrochemical analyzer (CH Instruments Inc.). A custom-built sample holder and EIS measurement system, consisting of a mini-vise and gold-coated stainless steel disc electrodes with soldered insulated copper wires, was used for EIS signal acquisition. To maintain high humidity and avoid drying of the samples during measurement, a humidity chamber was used to encapsulate the entire measurement assembly. The bone sample was carefully positioned in between the two electrodes for uniform electrode-contact without applying excessive pressure on the sample during clamping. The EIS measurements were performed at 10 mV AC voltage to achieve a pseudo-linear system response (Habekost, 2021; Kretzschmar and Harnisch, 2021), and the impedance (Z) and phase angle (θ) were measured at sixty different frequencies in the range from 1 Hz to 100 kHz (10 data points per decade of frequency). Room temperature was maintained, and a humid chamber was used to prevent bone drying during the entire EIS measurement.

Equivalent circuit modeling and data fitting

An equivalent circuit model was developed based on a physical interpretation of the electrochemical phenomena taking place in our electrochemical system. EIS Spectrum Analyzer software was used to fit the experimental data with the proposed equivalent circuit model. The Nelder-Mead algorithm was utilized for the fitting in order to determine the values of the equivalent circuit model components.

Machine learning algorithms

Machine learning-based classification models were utilized for further analysis of data in order to set up a bone mineral content-based detection system. All the machine learning classifier models were established by the Python based open source visual programming software Orange toolkit (Bioinformatics Laboratory, University of Ljubljana). The detailed algorithm parameters are described in the Supplementary Material.

Results

The flowchart of our machine learning-assisted EIS strategy for the quantitative analysis of bone mineral content is shown in Figure 1. The key points in our approach include, 1) measurement of impedance data from the bone samples of defined mineral content, 2) using the measured impedance data to train and validate a machine learning model, 3) using the trained model to classify bone samples of unknown mineral composition. To the best of our knowledge, this approach of classifying bone samples using a combination of EIS and machine learning is the first used to analyze bone mineral contents, a marker for bone regeneration, potentially offering a non-destructive, quantitative method to track bone regeneration.

To prepare samples of different mineral contents, rat femurs were treated with a demineralization solution for various durations. Fully decalcified bone samples showed a smooth fibrous structure owing to the remaining organic phase, mostly collagen in the bone as compared to intact bone samples (Figures 2A,B). The mineral content linearly decreased as the duration of the demineralization process increased, as shown in Figure 2C. This was further confirmed by alizarin red staining and its colorimetric quantification (Figures 2D,E). The impedances of bone samples with known mineral contents were measured in the longitudinal orientation as shown in Figure 2F. Representative Bode plots and Nyquist plots for bone samples with various mineral contents are shown in Figures 2G–I. As expected, EIS measurements showed a strong frequency dependency; the impedance was considerably higher at

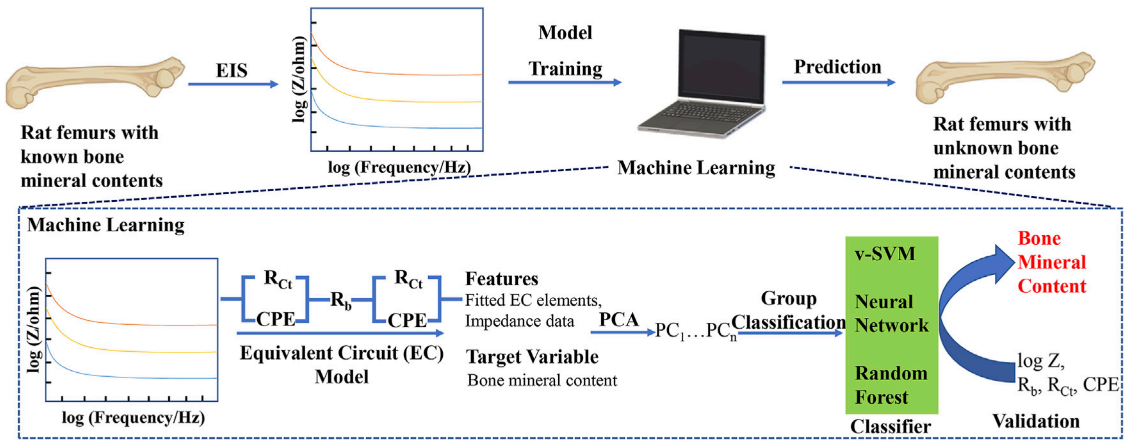

FIGURE 1
Schematic of machine learning-assisted electrochemical impedance spectroscopy (EIS) for the quantitative analysis of bone mineral content. PCA: Principal Component Analysis; v-SVM: Support Vector Machine.

low frequencies than at high frequencies (Figure 2G). At lower frequencies, the signals are both resistive and capacitive (slopes of the curves in the Bode magnitude plot ≈45°, slanted lines), while at higher frequencies the signals become purely resistive with no capacitive contributions to the impedance (slopes of the curves ≈0°, parallel to the abscissa). This decrease is associated with a significant change in the phase shift. The phase is about 60° at low frequencies and drops to values close to zero when the frequency increases (Figure 2H). These observations are in agreement with the results of Balmer et al. (Balmer et al., 2018). The Nyquist plots also show that the real and imaginary components of the impedance decreased as the mineral content decreased, corroborating with the Bode plots (Figure 2I).

An equivalent circuit model was designed to describe the electrochemical processes of the EIS spectra and to deconvolute the impedance contributing factors by fitting the measured impedance data (Figure 3A). Based on the features of the EIS spectra, i.e., the presence of a single prominent peak in the Bode phase plots, a two-layer physical model was employed: bulk bone tissue, and bone surface-metal electrode interface. R_b represents resistance from bulk bone structure, while R_{Ct} and CPE represent interfacial charge-transfer resistance and non-ideal double-layer capacitance (constant phase element) at the bone surface-metal electrode interface, respectively (Figure 3A). The experimental data were fitted into the proposed equivalent circuit model and representative fitting results from the bone sample having a mineral content of 20%, including Bode magnitude, Bode phase angle, and Nyquist, are shown in Figures 3B–D, where the robust goodness of fit values, presented as R^2 values, has been achieved. A complete data sets for various mineral contents are shown in Supplementary Figures S1–S6.

In order to better understand and confirm the physical meanings of the proposed circuit model, the relationship between each equivalent circuit model parameter and corresponding mineral content was further investigated. As expected, the bulk bone structural resistance, R_b, decreases with a decrease in bone mineral content (Figure 3E). Cortical bone mostly contains a mineral phase, which has large resistance, and hence demineralization results in a resistance drop. The interfacial resistance, R_{Ct}, only drops after about 20% demineralization (or 80% mineral content) and then reaches a steady-state value, signifying that the interfacial resistance solely depends on the bone/electrode interfacial electrochemical effects and not on bone structural degradation (Figure 3F). In contrast, the CPE value increases slightly after about 20% mineral removal and then stabilizes, which is similar to the observation by Wang *et al.*, where the capacitance slightly decreased with increased apatite growth (Figure 3G) (Wang et al., 2003). The impedance values at different frequencies were combined with the fitted equivalent circuit parameters to test a simple regression model. Figure 3H shows the performance of the logistic regression model in predicting the bone mineral content, where the classification accuracy of 52.4% with a precision of 43.4% was observed.

To improve the prediction accuracy, various machine learning algorithms were employed. In order to establish an appropriate machine learning classification model and evaluate its performance, the original dataset was divided into a training set and a testing set, where the training set was used to establish prediction models and the testing set was used to verify the validity of the models (Figures 4A,B). A dataset of ninety-one measured impedance signals, corresponding to at least fifteen signals per mineral content category (0, 20, 40, 60, 80, 100 wt%), from multiple samples was prepared. Seventy data instances were randomly selected from the dataset, representing all the six classification categories, as the training dataset, and the remaining twenty-one measurements were utilized as the

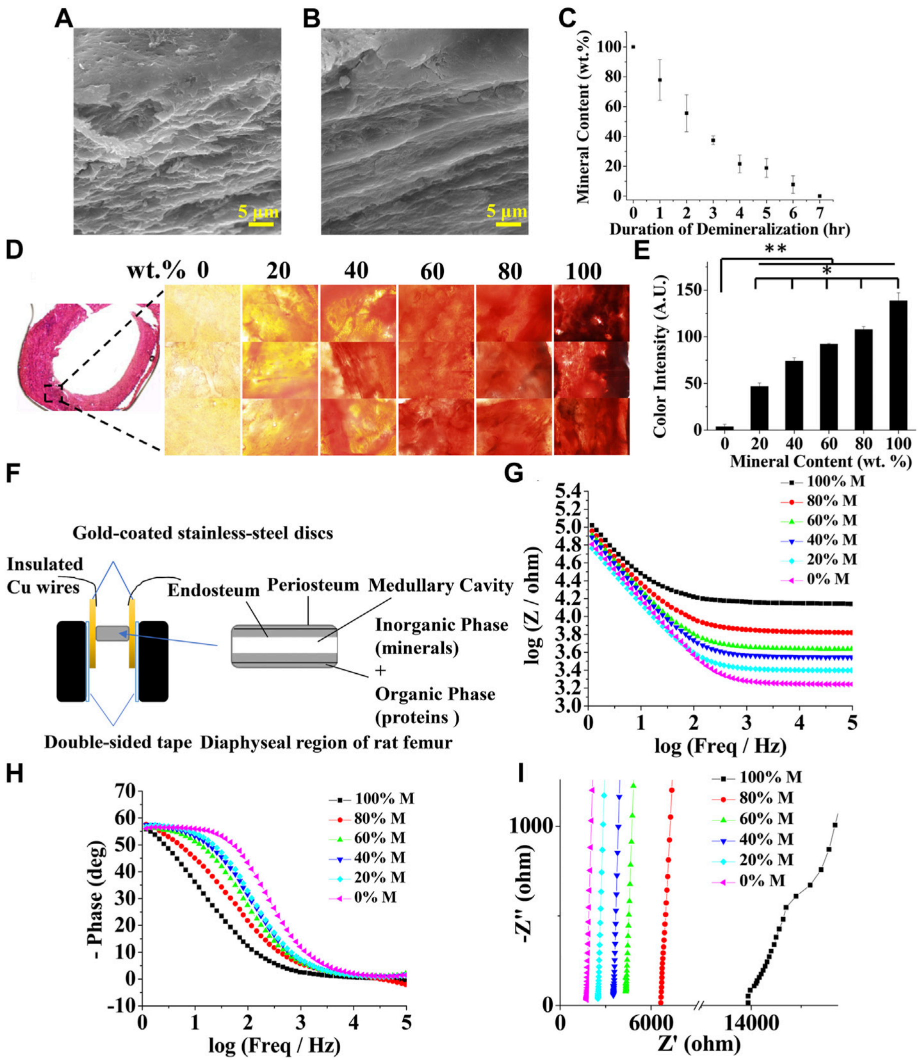

FIGURE 2
Characterization of bone mineral content and electrochemical impedance spectroscopy (EIS) at different levels of mineralization. Scanning electron microscopy (SEM) images of **(A)** intact **(B)** demineralized bone samples **(C)** Bone mineral content as a function of demineralization duration **(D)** Bone cryosection and alizarin red staining at 0, 20, 40, 60, 80, and 100 wt% bone mineral content **(E)** Quantified alizarin red staining intensity as a function of bone mineral content ($n = 5$, * and ** denote statistical significance of $p < 0.05$ and $p < 0.01$, respectively, analyzed by one-way ANOVA with Tukey's posthoc test.) **(F)** Schematic showing an experimental setup for the measurement of EIS spectrum of a bone sample. Representative bone EIS spectra shown as **(G)** Bode magnitude **(H)** Bode phase angle, and **(I)** Nyquist plots.

testing dataset. This dataset splitting ratio was chosen to ensure optimal classification performances of machine learning models (Xu and Goodacre, 2018; Thien and Yeo, 2021).

To avoid problems of overfitting, confusing the algorithms, and high computation cost, we first performed dimensionality reduction on the data using principal component analysis (PCA), instead of directly feeding the original data to the machine learning algorithms. As shown in Figure 4C, the first principal component contributed nearly 90% of the explained variance, and thus was chosen to represent the data with minimal loss of information. Scatter plot analysis of the principal components showed that the six classes of mineral content cannot be clearly distinguished due to the overlapping boundaries by PCA alone (Supplementary Figure S7). Hence, projections of all data features onto the first principal component dimension were then used as the input data for the machine learning models.

In order to find the best algorithm for the bone mineral content prediction, three different machine learning algorithm models—variant of support vector machine (v-SVM), neural network (NN), and random forest (RF) were trained based on the PCA-transformed dataset and compared, based on the classification accuracy and precision of correctly assigning

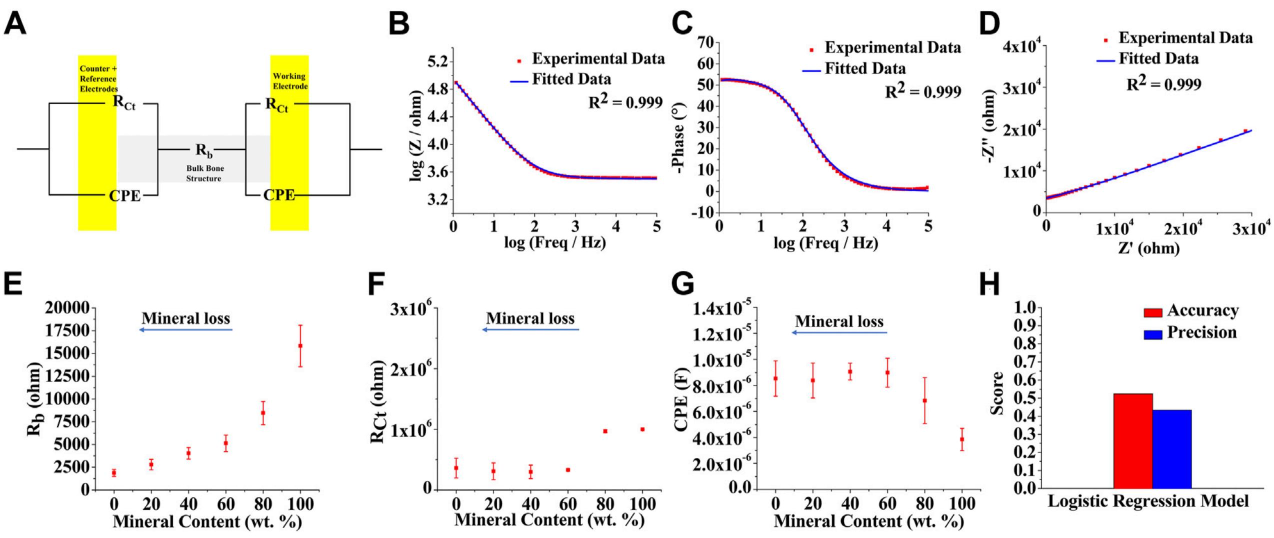

FIGURE 3

Equivalent circuit modeling for the factor deconvolution of electrochemical impedance spectroscopy (EIS) data **(A)** Equivalent circuit model used for fitting the bone EIS spectra. R_b = resistance from bulk bone structure, R_{Ct} = bone surface-metal electrode interfacial charge-transfer resistance, CPE = non-ideal double-layer capacitance (constant phase element) at the bone surface-metal electrode interface or contact region. Representative fitting results (20%) shown as **(B)** Bode magnitude **(C)** Bode phase angle, and **(D)** Nyquist plots. Equivalent circuit model-parametric characterization of bone samples at different levels of demineralization. Plots showing variation of **(E)** R_b **(F)** R_{Ct}, and **(G)** CPE as a function of bone mineral content **(H)** Classification performance of a logistic regression discrimination model using impedance data and fitted equivalent circuit element data for training [*n* (total) = 70; *n* (0 wt%) = 12, *n* (20 wt%) = 12, *n* (40 wt%) = 12, *n* (60 wt%) = 12, *n* (80 wt%) = 9, *n* (100 wt%) = 13] and testing [*n* (total) = 21; *n* (0 wt%) = 4, *n* (20 wt%) = 4, *n* (40 wt%) = 4, *n* (60 wt%) = 3, *n* (80 wt%) = 3, *n* (100 wt%) = 3] datasets.

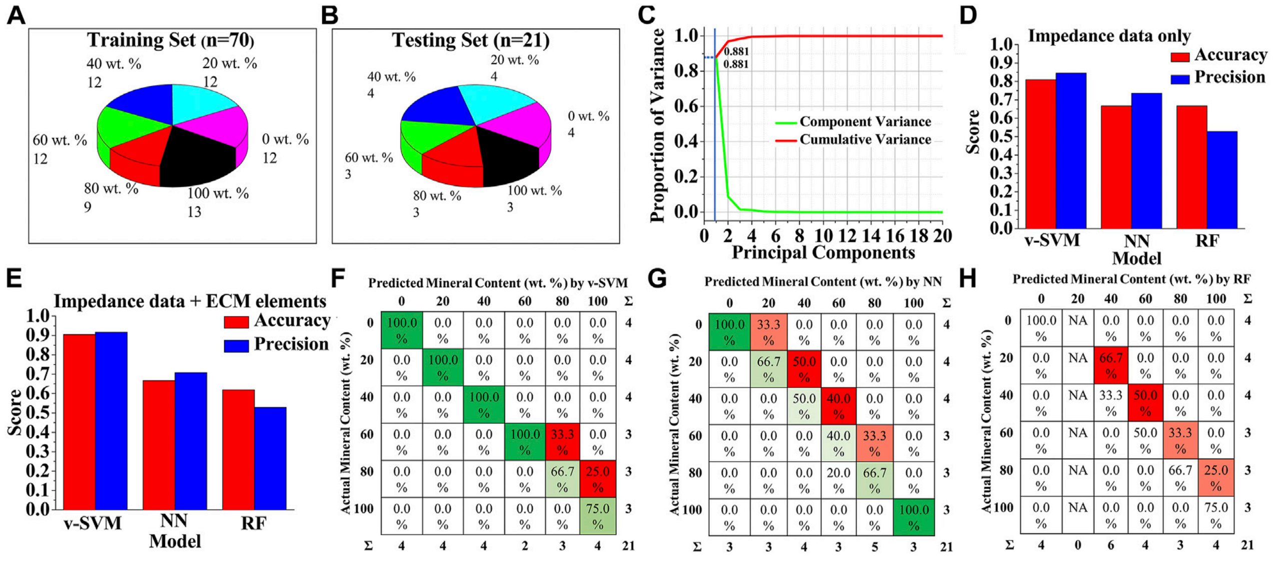

Predicted Mineral Content (wt. %) by v-SVM

Actual Mineral Content (wt. %)	0	20	40	60	80	100	Σ
0	100.0 %	0.0 %	0.0 %	0.0 %	0.0 %	0.0 %	4
20	0.0 %	100.0 %	0.0 %	0.0 %	0.0 %	0.0 %	4
40	0.0 %	0.0 %	100.0 %	0.0 %	0.0 %	0.0 %	4
60	0.0 %	0.0 %	0.0 %	100.0 %	33.3 %	0.0 %	3
80	0.0 %	0.0 %	0.0 %	0.0 %	66.7 %	25.0 %	3
100	0.0 %	0.0 %	0.0 %	0.0 %	0.0 %	75.0 %	3
Σ	4	4	4	2	3	4	21

Predicted Mineral Content (wt. %) by NN

Actual Mineral Content (wt. %)	0	20	40	60	80	100	Σ
0	100.0 %	33.3 %	0.0 %	0.0 %	0.0 %	0.0 %	4
20	0.0 %	66.7 %	50.0 %	0.0 %	0.0 %	0.0 %	4
40	0.0 %	0.0 %	50.0 %	40.0 %	0.0 %	0.0 %	4
60	0.0 %	0.0 %	0.0 %	40.0 %	33.3 %	0.0 %	3
80	0.0 %	0.0 %	0.0 %	20.0 %	66.7 %	0.0 %	3
100	0.0 %	0.0 %	0.0 %	0.0 %	0.0 %	100.0 %	3
Σ	3	3	4	3	5	3	21

Predicted Mineral Content (wt. %) by RF

Actual Mineral Content (wt. %)	0	20	40	60	80	100	Σ
0	100.0 %	NA	0.0 %	0.0 %	0.0 %	0.0 %	4
20	0.0 %	NA	66.7 %	0.0 %	0.0 %	0.0 %	4
40	0.0 %	NA	33.3 %	50.0 %	0.0 %	0.0 %	4
60	0.0 %	NA	0.0 %	50.0 %	33.3 %	0.0 %	3
80	0.0 %	NA	0.0 %	0.0 %	66.7 %	25.0 %	3
100	0.0 %	NA	0.0 %	0.0 %	0.0 %	75.0 %	3
Σ	4	0	6	4	3	4	21

FIGURE 4

Machine Learning-based detection of bone mineral content **(A,B)** Data sets with different bone mineral contents, used for training and testing of machine learning models **(C)** Representative PCA scree plot showing the number of components used (blue line) along with proportion of variance explained. Classification performance of the three types of discrimination models when **(D)** only impedance data were used for training and testing, and **(E)** both impedance data and equivalent circuit-fitted element data were used for training and testing **(F–H)** Confusion matrix for **(F)** v-SVM **(G)** Neural Network, and **(H)** Random Forest algorithms for bone mineral content classification when both impedance data and equivalent circuit-fitted element data were used for training and testing.

categories to the instances in the testing. To further test the importance of the type of data used for model training, one dataset was prepared with only EIS impedance-frequency data, and another dataset contained a combination of fitted equivalent circuit model parameters and EIS impedance-frequency data. The predicting performances of v-SVM, NN, and RF classification algorithm models were compared, when only impedance values at 60 different frequencies in the range of 1 Hz–100 kHz were used as the features of the training and testing datasets (Figure 4D). Results showed that v-SVM exhibited the highest accuracy and precision scores as compared to the other algorithms; while the v-SVM predicted the mineral composition categories with 81% accuracy and 84.5% precision, the accuracy of prediction by the NN and the RF was 66.7% for both. The precision for NN and RF was 73.6 and 52.8%, respectively. Interestingly, when the values of the fitted equivalent circuit model parameters were used in addition to the impedance values as the feature set of training and testing datasets, the performance of the v-SVM markedly increased with classification accuracy reaching approximate 91% with a precision of about 92% (Figure 4E). In the case of the NN, the classification accuracy remained the same at 66.7% with a comparatively lower precision of 70.8%, while for the RF model, the accuracy dropped to 61.9% with the same precision of 52.8%. Therefore, among the three supervised algorithm models, v-SVM exhibited superior accuracy and precision to the other two methods as it can better identify the six classes of bone samples with different mineral levels, especially when the equivalent circuit modeling was employed. It should be also noted that there was a significant improvement in accuracy and precision by all these machine learning algorithms as compared to the logistic regression discrimination model (Figure 3H, Figures 4D,E). Figures 4F–H shows the confusion matrices for v-SVM, NN, and RF, respectively, where each row represents the actual mineral content of samples, and each column represents the predicted mineral content by the respective classification models. The detected values under the v-SVM method corresponded best to the raw data as compared to the other algorithm methods.

Discussion

Treatments of the critical-sized bone defect are challenging due to the frequent surgical intervention and the high risk of causing non-union bone healing (Roddy et al., 2018; Stewart, 2019). To ensure optimal therapeutic treatment, monitoring the bone healing process is crucial. X-ray diagnostic radiography is one of the most used diagnosing and monitoring techniques in clinical settings (Wong et al., 2012). Limitations such as low accuracy, poor quantification, and radio safety, however, still exist. Quantitative computed tomography (QCT), on the other hand, provides a means to assess bone healing by providing high-resolution images and quantitatively measuring the bone mineral content (Augat et al., 1997). However, large signal noise, high cost, and limited accessibility have prevented its further application in the continuous monitoring of bone therapy.

In this regard, EIS provides a means to non-destructively assess bone healing process by characterizing the electrical properties of the tissue in relation to bone mineral content. We showed a decrease in the magnitude of impedance with the decrease in mineral content. In addition, the single peak in the Bode phase plots spreads over a wider frequency range with decreased mineral contents. The shift of this “peak”, corresponding to a time constant (R||C) of the system, indicates that the electrochemical process becomes faster during the progress of demineralization due to the removal of the resistive mineral phase. The observation of the raw impedance values of the bone to assess the mineral content, however, is still semi-quantitative, leading to inaccurate prediction of the mineral content from the overall impedance dataset.

Therefore, equivalent circuit modeling was employed to extract the individual contributing factors from the impedance, including the electrical components of bulk bone tissue and the bone-electrode interfaces. For the purpose of the equivalent circuit modeling, the cortical bones can be assumed to exhibit mostly a resistive behavior and that the bone/electrode phase boundaries result in the appearance of an interfacial capacitance, uncharacteristic of bulk bone tissue (Bauerle, 1969; Mercanzini et al., 2009; Jiang et al., 2016). Furthermore, since the cortical bone samples under study are mostly composed of an inorganic phase, which exhibits low relative permittivity <10, the capacitive behavior of the samples can be neglected for simplicity (Asgarifar, 2012). Apart from the capacitive behavior at the bone-electrode interface, which is typically seen at lower frequencies (<100 kHz), another capacitive contribution to the impedance spectra could result from the stray capacitance of the measurement system at higher frequencies (>100 kHz). However, since the range of frequencies used in this study was from 1 Hz to 100 kHz and precautions were taken to carefully insulate the measurement setup, stray capacitive contributions to the impedance spectra were neglected. In addition, bone tissues can be considered as an inhomogeneous composite material that contains a less conductive mineral phase (hydroxyapatite) and a more conductive hydrated organic phase (mostly collagen). Therefore, the justifications for using CPE instead of a capacitor are two-fold: 1) the inhomogeneity of bone composition coupled with contact-surface roughness, leading to pseudocapacitive behavior at the interface, and 2) a better fit of the simulated data with the experimental data. The conductive charge carriers in the electrochemical system under study are ions and electrons. Thus, the bone/electrode interfacial phenomena are represented by a parallel combination of R_{Ct} and CPE, which is then connected in series to the bulk bone structural resistance, R_b. The interfacial charge transfer resistance R_{Ct} is the resistance for the electron to change the phase, *i.e.*, from the electrode into the hydrated tissue. The equivalent circuit model we designed successfully deconvolute the impedance contributing factors, yet the prediction accuracy solely based on these deconvoluted values remains low due to sample variability. This is especially true if outliers are present in the overall dataset, often observed in the clinical datasets. These experimental error-based subtle ambiguities in the overall dataset cannot be resolved by simple classifiers like regression models as shown in Figure 3H.

In this regard, we utilized the machine learning algorithm models, due to their automation and robustness, as an analytical solution for categorizing bone samples of different mineral contents with multiple impedimetric parameters. The impedance values and their deconvoluted factors obtained from the equivalent circuit model were processed using various algorithm models and the best prediction accuracy was achieved when using the v-SVM, as compared to the other algorithms, including neural network, and random forest. Although small errors still exist due to a relatively small sample size of data being used for training and testing, our approach of random extraction, training, and prediction of the testing data showed that the differences among the data obtained from each group had little effect on the overall results. These results thus indicate that an appropriate equivalent circuit model and an optimal machine learning approach are both necessary for the adaptability and accuracy in bone mineral content detection, providing a means to accurately monitor the healing process of bone.

In this brief research report, we have developed an analytical method combining EIS and machine learning for the quantitative assessment of bone mineral content. We demonstrate that the electrochemical parameters of the bone tissue correlated well with its composition. The classification ability of various algorithms using the EIS data was compared. The results show that the best comprehensive performance is obtained by SVM when equivalent circuit model data were incorporated into raw impedance data. By incorporating multiple impedimetric parameters, the machine learning model enables the accurate determination of bone mineral content. Due to the advantages in adaptability, automation, and accuracy, we anticipate that the method established in this study will find various applications in bone defect management. These results might help further progress on the rapid and longitudinal monitoring of bone healing status and could even be used for the detection and analysis of bone defects. Moreover, this work proves the application potential of machine learning tools in electrochemical research.

Data availability statement

The raw data supporting the conclusions of this article will be made available by the authors, without undue reservation.

Author contributions

AB: Data curation, Formal analysis, Investigation, Methodology, Validation, Visualization, Writing; YT: Data curation, Formal analysis, Investigation, Methodology, Validation, Visualization, Writing; NM: Conceptualization, Formal analysis, Resources, Writing; JN: Conceptualization, Formal analysis, Funding acquisition, Resources, Supervision, Writing.

Funding

This work was supported by UC Riverside and Korea Institute of Materials Science (Research Program PNK7280) through UC-KIMS Center for Innovative Materials for Energy and Environment.

Conflict of interest

The authors declare that the research was conducted in the absence of any commercial or financial relationships that could be construed as a potential conflict of interest.

Publisher's note

Supplementary material

The Supplementary Material for this article can be found online at: https://www.frontiersin.org/articles/10.3389/fbioe.2022.961108/full#supplementary-material

References

Afsarimanesh, N., Zia, A. I., Mukhopadhyay, S. C., Kruger, M., Yu, P. L., Kosel, J., et al. (2016). Smart sensing system for the prognostic monitoring of bone health. *Sensors (Basel)* 16, 976. doi:10.3390/s16070976

Asgarifar, H. (2012). *Application of high voltage, high frequency pulsed electromagnetic field on cortical bone tissue*. Brisbane, QLD: Queensland University of Technology.

Augat, P., Merk, J., Genant, H. K., and Claes, L. (1997). Quantitative assessment of experimental fracture repair by peripheral computed tomography. *Calcif. Tissue Int.* 60, 194–199. doi:10.1007/s002239900213

Augat, P., Morgan, E. F., Lujan, T. J., Macgillivray, T. J., and Cheung, W. H. (2014). Imaging techniques for the assessment of fracture repair. *Injury* 45 (2), S16–S22. doi:10.1016/j.injury.2014.04.004

Babaeiyazdi, I., Rezaei-Zare, A., and Shokrzadeh, S. (2021). State of charge prediction of ev Li-ion batteries using EIS: A machine learning approach. *Energy* 223, 120116. doi:10.1016/j.energy.2021.120116

Balmer, T. W., Vesztergom, S., Broekmann, P., Stahel, A., and Buchler, P. (2018). Characterization of the electrical conductivity of bone and its correlation to osseous structure. *Sci. Rep.* 8, 8601. doi:10.1038/s41598-018-26836-0

Bauerle, J. E. (1969). Study of solid electrolyte polarization by a complex admittance method. *J. Phys. Chem. Solids* 30, 2657–2670. doi:10.1016/0022-3697(69)90039-0

Claes, L. E., and Cunningham, J. L. (2009). Monitoring the mechanical properties of healing bone. *Clin. Orthop. Relat. Res.* 467, 1964–1971. doi:10.1007/s11999-009-0752-7

Cunha, A. B., Hou, J., and Schuelke, C. (2019). Machine learning for stem cell differentiation and proliferation classification on electrical impedance spectroscopy. *J. Electr. Bioimpedance* 10, 124–132. doi:10.2478/joeb-2019-0018

Dell'osa, A., Concu, A., Dobarro, F., and Felice, J. (2019a). *Bone fracture detection by electrical bioimpedance: First non-invasive measurements in* ex-vivo *mammalian femur*. bioRxiv.622936.

Dell'osa, A. H., Felice, C. J., and Simini, F. (2019b). "Bioimpedance and bone fracture detection: A state of the art," in *Journal of physics: Conference series* (Bristol, United Kingdom: IOP Publishing).012010.

Ernst, M., Richards, R. G., and Windolf, M. (2021). Smart implants in fracture care–only buzzword or real opportunity? *Injury* 52, S101–S105. doi:10.1016/j.injury.2020.09.026

Habekost, A. (2021). Fundamentals and applications of electrochemical impedance spectroscopy-a didactic perspective. *World* 9, 14–21. doi:10.12691/wjce-9-1-3

Hak, D. J., Fitzpatrick, D., Bishop, J. A., Marsh, J. L., Tilp, S., Schnettler, R., et al. (2014). Delayed union and nonunions: Epidemiology, clinical issues, and financial aspects. *Injury* 45, S3–S7. doi:10.1016/j.injury.2014.04.002

Homer, C. B., Maldonado, M., Tai, Y. Y., Rony, R. M. I. K., and Nam, J. (2019). Spatially regulated multiphenotypic differentiation of stem cells in 3D via engineered mechanical gradient. *ACS Appl. Mat. Interfaces* 11, 45479–45488. doi:10.1021/acsami.9b17266

Jiang, W. L., Wang, Y. X., Tang, J., Peng, J., Wang, Y., Guo, Q. Y., et al. (2016). Low-intensity pulsed ultrasound treatment improved the rate of autograft peripheral nerve regeneration in rat. *Sci. Rep.* 6, 22773. doi:10.1038/srep22773

Kobbe, P., Laubach, M., Hutmacher, D. W., Alabdulrahman, H., Sellei, R. M., and Hildebrand, F. (2020). Convergence of scaffold-guided bone regeneration and RIA bone grafting for the treatment of a critical-sized bone defect of the femoral shaft. *Eur. J. Med. Res.* 25, 70–12. doi:10.1186/s40001-020-00471-w

Kozhevnikov, E., Hou, X., Qiao, S., Zhao, Y., Li, C., and Tian, W. (2016). Electrical impedance spectroscopy–a potential method for the study and monitoring of a bone critical-size defect healing process treated with bone tissue engineering and regenerative medicine approaches. *J. Mat. Chem. B* 4, 2757–2767. doi:10.1039/c5tb02707a

Kretzschmar, J., and Harnisch, F. (2021). Electrochemical impedance spectroscopy on biofilm electrodes - conclusive or euphonious? *Curr. Opin. Electrochem.* 29, 100757. doi:10.1016/j.coelec.2021.100757

Liang, H., Tsui, B. Y., Ni, H., Valentim, C., Baxter, S. L., Liu, G., et al. (2019). Evaluation and accurate diagnoses of pediatric diseases using artificial intelligence. *Nat. Med.* 25, 433–438. doi:10.1038/s41591-018-0335-9

Lin, M. C., Herfat, S. T., Bahney, C. S., Marmor, M., and Maharbiz, M. M. (2015). "Impedance spectroscopy to monitor fracture healing," in *2015 37th annual international conference of the ieee engineering in medicine and biology society* (Piscataway, NJ: Embc), 5138–5141.

Lin, M. C., Hu, D. E., Marmor, M., Herfat, S. T., Bahney, C. S., and Maharbiz, M. M. (2019). Smart bone plates can monitor fracture healing. *Sci. Rep.* 9, 2122. doi:10.1038/s41598-018-37784-0

Maldonado, M., Ico, G., Low, K., Luu, R. J., and Nam, J. (2016). Enhanced lineage-specific differentiation efficiency of human induced pluripotent stem cells by engineering colony dimensionality using electrospun scaffolds. *Adv. Healthc. Mat.* 5, 1408–1412. doi:10.1002/adhm.201600141

Mercanzini, A., Colin, P., Bensadoun, J. C., Bertsch, A., and Renaud, P. (2009). *In vivo* electrical impedance spectroscopy of tissue reaction to microelectrode arrays. *IEEE Trans. Biomed. Eng.* 56, 1909–1918. doi:10.1109/tbme.2009.2018457

Morshed, S., Corrales, L., Genant, H., and Miclau, T. (2008). Outcome assessment in clinical trials of fracture-healing. *J. Bone Jt. Surg.* Vol. 90a, 62–67. doi:10.2106/jbjs.g.01556

Nam, J., Huang, Y., Agarwal, S., and Lannutti, J. (2007). Improved cellular infiltration in electrospun fiber via engineered porosity. *Tissue Eng.* 13, 2249–2257. doi:10.1089/ten.2006.0306

Nauth, A., Schemitsch, E., Norris, B., Nollin, Z., and Watson, J. T. (2018). Critical-size bone defects: Is there a consensus for diagnosis and treatment? *J. Orthop. trauma* 32, S7–S11. doi:10.1097/bot.0000000000001115

Peng, J. J., Jury, E. C., Donnes, P., and Ciurtin, C. (2021). Machine learning techniques for personalised medicine approaches in immune-mediated chronic inflammatory diseases: Applications and challenges. *Front. Pharmacol.* 12, 720694. doi:10.3389/fphar.2021.720694

Rani, S., Bandyopadhyay-Ghosh, S., Ghosh, S. B., and Liu, G. (2020). Advances in sensing technologies for monitoring of bone health. *Biosensors* 10, 42. doi:10.3390/bios10040042

Roddy, E., Debaun, M. R., Daoud-Gray, A., Yang, Y. P., and Gardner, M. J. (2018). Treatment of critical-sized bone defects: Clinical and tissue engineering perspectives. *Eur. J. Orthop. Surg. Traumatol.* 28, 351–362. doi:10.1007/s00590-017-2063-0

Schwarzenberg, P., Darwiche, S., Yoon, R. S., and Dailey, H. L. (2020). Imaging modalities to assess fracture healing. *Curr. Osteoporos. Rep.* 18, 169–179. doi:10.1007/s11914-020-00584-5

Stewart, S. K. (2019). Fracture non-union: A review of clinical challenges and future research needs. *Malays. Orthop. J.* 13, 1–10. doi:10.5704/moj.1907.001

Tekkesin, A. I. (2019). Artificial intelligence in healthcare: Past, present and future. *Anatol. J. Cardiol.* 22, 8–9. doi:10.14744/AnatolJCardiol.2019.28661

Thien, T. F., and Yeo, W. S. (2021). A comparative study between PCR, PLSR, and LW-PLS on the predictive performance at different data splitting ratios. *Chem. Eng. Commun.*, 1–18. doi:10.1080/00986445.2021.1957853

Tripathi, M. K., and Maktedar, D. D. (2016). "Recent machine learning based approaches for disease detection and classification of agricultural products," in *2016 international conference on computing communication control and automation (ICCUBEA)* (IEEE), 1–6.

Wang, C. X., Wang, M., and Zhou, X. (2003). Nucleation and growth of apatite on chemically treated titanium alloy: An electrochemical impedance spectroscopy study. *Biomaterials* 24, 3069–3077. doi:10.1016/s0142-9612(03)00154-6

Wildemann, B., Ignatius, A., Leung, F., Taitsman, L. A., Smith, R. M., Pesantez, R., et al. (2021). Non-union bone fractures. *Nat. Rev. Dis. Prim.* 7, 57–21. doi:10.1038/s41572-021-00289-8

Wong, L. C. Y., Chiu, W. K., Russ, M., and Liew, S. (2012). Review of techniques for monitoring the healing fracture of bones for implementation in an internally fixated pelvis. *Med. Eng. Phys.* 34, 140–152. doi:10.1016/j.medengphy.2011.08.011

Xu, Y., and Goodacre, R. (2018). On splitting training and validation set: A comparative study of cross-validation, bootstrap and systematic sampling for estimating the generalization performance of supervised learning. *J. Anal. Test.* 2, 249–262. doi:10.1007/s41664-018-0068-2

Yu, K.-H., Beam, A. L., and Kohane, I. S. (2018). Artificial intelligence in healthcare. *Nat. Biomed. Eng.* 2, 719–731. doi:10.1038/s41551-018-0305-z

frontiers | Frontiers in Bioengineering and Biotechnology

TYPE Original Research
PUBLISHED 07 September 2022
DOI 10.3389/fbioe.2022.963996

Bioactive glass-collagen/poly (glycolic acid) scaffold nanoparticles exhibit improved biological properties and enhance osteogenic lineage differentiation of mesenchymal stem cells

Shirin Toosi[1]*, Hojjat Naderi-Meshkin[2], Zohreh Esmailzadeh[2], Ghazal Behravan[3], Seeram Ramakrishna[4] and Javad Behravan[5,6]*

[1]Tissue Engineering Research Group (TERG), Department of Anatomy and Cell Biology, School of Medicine, Mashhad University of Medical Sciences, Mashhad, Iran, [2]Stem Cells and Regenerative Medicine Research Group, Iranian Academic Center for Education, Culture and Research (ACECR), Mashhad, Iran, [3]Faculty of Medicine, Mashhad University of Medical Sciences, Mashhad, Iran, [4]Center for Nanofibers and Nanotechnology, Department of Mechanical Engineering, National University of Singapore, Singapore, Singapore, [5]Biotechnology Research Center, Pharmaceutical Technology Institute, Mashhad University of Medical Sciences, Mashhad, Iran, [6]School of Pharmacy, University of Waterloo, Waterloo, ON, Canada

Today's using tissue engineering and suitable scaffolds have got attention to increase healing of non-union bone fractures. In this study, we aimed to prepare and characterize scaffolds with functional and mechanical properties suitable for bone regeneration. Porous scaffolds containing collagen-poly glycolic acid (PGA) blends and various quantities of bioactive glass (BG) 45S5 were fabricated. Scaffolds with different compositions (BG/collagen-PGA ratios (w/w): 0/100; 40/60; 70/30) were characterized for their morphological properties, bioactivity, and mechanical behavior. Then, biocompatibility and osteogenic differentiation potential of the scaffolds were analyzed by seeding mesenchymal stem cells (MSCs). Scaffolds made with collagen-PGA combined with the BG (45S5) were found to have interconnected pores (average pore diameter size 75–115 μm) depending on the percentage of the BG added. Simulated body fluid (SBF) soaking experiments indicated the stability of scaffolds in SBF regardless of their compositions, while the scaffolds retained their highly interconnected structure. The elastic moduli, cell viability, osteogenic differentiation of the BG/collagen-PGA 40/60 and 70/30 scaffolds were superior to the original BG/collagen-PGA (0/100). These results suggest that BG incorporation enhanced the physical stability of our collagen-PGA scaffold previously reported. This new scaffold composition provides a promising platform to be used as a non-toxic scaffold for bone regeneration and tissue engineering.

EDITED BY
Anna Lange-Consiglio,
University of Milan, Italy

REVIEWED BY
Cijun Shuai,
Jiangxi University of Science and Technology, China
Pei Feng,
Central South University, China

*CORRESPONDENCE
Shirin Toosi,
Toosis@mums.ac.ir
Javad Behravan,
behravanj@mums.ac.ir

SPECIALTY SECTION
This article was submitted to Tissue Engineering and Regenerative Medicine, a section of the journal Frontiers in Bioengineering and Biotechnology

RECEIVED 08 June 2022
ACCEPTED 18 August 2022
PUBLISHED 07 September 2022

CITATION
Toosi S, Naderi-Meshkin H, Esmailzadeh Z, Behravan G, Ramakrishna S and Behravan J (2022), Bioactive glass-collagen/poly (glycolic acid) scaffold nanoparticles exhibit improved biological properties and enhance osteogenic lineage differentiation of mesenchymal stem cells.
Front. Bioeng. Biotechnol. 10:963996.
doi: 10.3389/fbioe.2022.963996

KEYWORDS

bone engineering, scaffold, bioglass, collagen, osteogenic differentiation

Introduction

The science of tissue engineering and regenerative medicine has offered novel approaches for regeneration and repair of tissues and organs which are damaged or lost as a result of trauma, injury or age related conditions (Nerem, 1991). In the most desired condition, a biologically compatible scaffold composite with a well-planned and constructed architecture serves as a temporary structural base for cellular components and guides the differentiation as well as proliferation of tissue forming cell leading to the desired organ or tissue generation. Biomolecules and growth factors can be added into the scaffold, along with the cellular components, to enhance and promote the regulation of cell functions during organ or tissue regeneration (Shea et al., 1999; Babensee et al., 2000; Elisseeff et al., 2001; Mahoney and Saltzman, 2001; Leach et al., 2006; Toosi et al., 2016a; Toosi et al., 2019a) As a general rule, the purpose of this tissue or organ engineering approach is to temporary provide a supporting structure for the cells that contribute to tissue formation enabling them to produce a new tissue with the desired dimensions and shape (Toosi et al., 2016b; Toosi et al., 2018; Toosi et al., 2019b). These investigations have been very fruitful in cellular based bioengineering and regeneration of tissues such as skin (Cooper and Hansbrough, 1991; Hansbrough et al., 1994; Eaglstein and Falanga, 1997; Black et al., 1998), bone (Vacanti et al., 2001; Marcacci et al., 2007; Pishavar et al., 2021)and cartilage (Cao et al., 1997). Figure 1 presents a general schematic bone engineering that includes components used for biocompatible scaffold and cell therapy.

Since the discovery of 45S5 Bioglass® group of materials by Hench (Hench et al., 1971), they have been frequently used as scaffold components for bone repair (Hench et al., 1971; Hench, 1998a; Rahaman et al., 2006; Yunos et al., 2008). BGs are widely recognized for their suitability to support the growth and proliferation of osteoblasts (; Wheeler et al., 1997; Wheeler et al., 1998), and to strongly attach with soft and hard tissues (Hench et al., 1971). Following implantation, BGs undergo very specific types of reactions which lead to the formation of HA (crystalline hydroxyapatite) and ACP (amorphous calcium phosphate) on the glass surface. These specific reactions are shown to be responsible for their strong attachment with the surrounding soft and hard tissue (Fu et al., 2011; Philippart et al., 2015). BGs also release ions that are involved in activation of expression of osteogenic genes (Xynos et al., 2000; Xynos et al.,

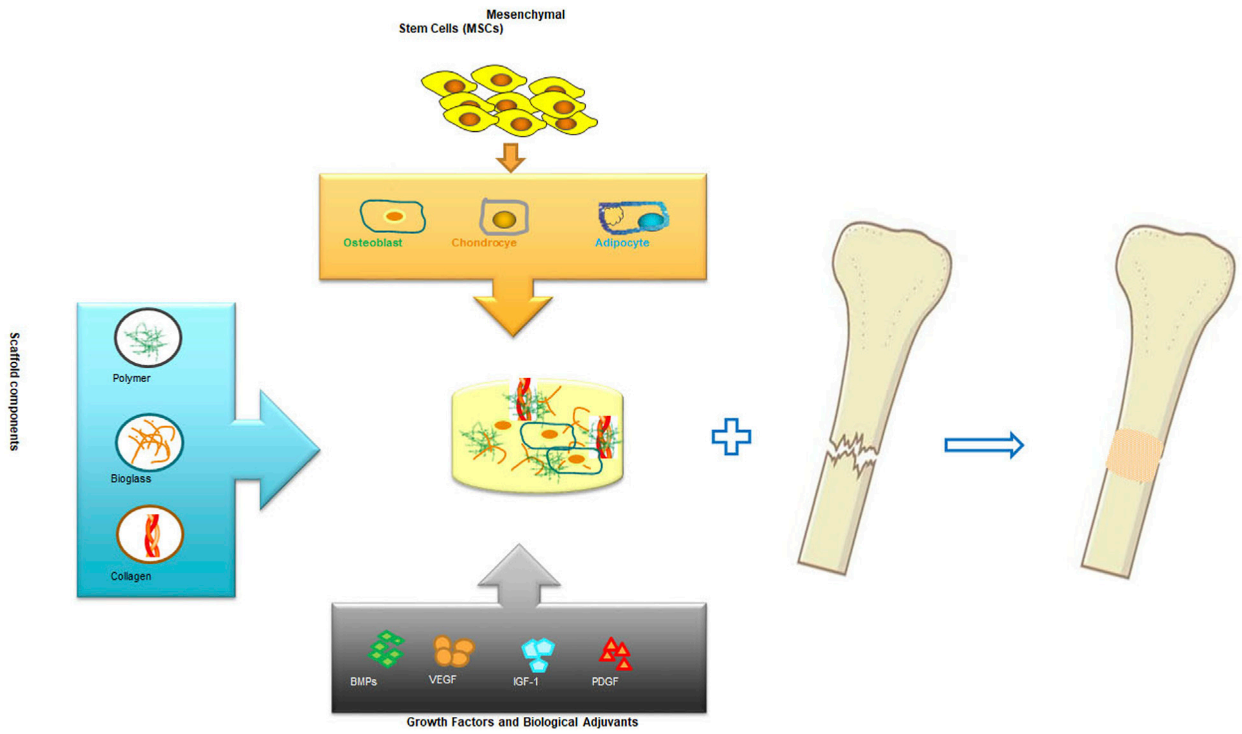

FIGURE 1
Schematic representation of a bone engineering including its major components.

2001), and play important roles in angiogenesis (Leach et al., 2006; Leu and Leach, 2008). The advantages of BGs include ease of management of their chemical composition and control of the rate of their degradation. Both these properties in addition to other advantages make them attractive scaffold component materials. The chemistry and structure of BGs can be designed using a wide range of options for example by changing either composition, or their environmental and thermal processing. Moreover, scaffolds containing BG may be tailored with variable rates of degradation to meet the optional requirements for bone remodeling and ingrowth.

BGs are mechanically weak. It has been shown that during the process of the fabrication of scaffold, BG can partially crystallize if heated to temperatures above 95°C. Moreover, it has been discovered that in a biological environment and at body temperature, this crystalline phase which is mechanically very strong can transform to a biologically degradable amorphous calcium phosphate (Chen et al., 2006). This transformation property of BG makes it possible to design a scaffold which possesses a combination of biodegradability and mechanical strength at the same time (Boccaccini et al., 2007; Detsch et al., 2015).

In our previous *in vitro* and *in vivo* studies we have shown that a collagen: PGA (0.52 w/w) scaffold exhibited a great potential as a suitable scaffold for bone tissue engineering (Toosi et al., 2016c; Toosi et al., 2018; Toosi et al., 2019b). Here in this study we aimed to examine how 45S5 bioglass affects the biological properties of the collagen-PGA scaffold in favor of bone tissue engineering. In addition, we studied the biological behavior of mesenchymal stem cells derived from bone marrow (BM-MSCs) in the new scaffold prepared from collagen-PGA sponge and BG (45S5).

Materials and methods

Collagen sponge fabrication

Type I collagen solution produced by pepsin treatment of porcine tendon (6.33 mg/ml, pH 3.0) in HCl, was obtained from Nitta Gelatin Inc. The fabric of non-woven PGA fiber (20 mm diameter, 0.5 mm thickness, 200–210 g m^{-2}) was purchased from Gunze (Kyoto, Japan). BG (45S5) was obtained from MedZist (Tehran, Iran). Fats and oils were removed by immersing the non-woven fabric of PGA in acetone for 1 hour and then a washing procedure was repeated for three times (10 min at 25°C) with double distilled water. In order to obtain the PGA component, tweezers were used to loosen the PGA fiber. PGA fiber (12 mg) was placed inside each well in a 24-well tissue culture plate, and then 1 ml of collagen containing 40 and 70 (w/w) BG was poured over the PGA fiber inside each well. A dehydro-thermal method was used to fabricate collagen sponges including BG and 12 mg of PGA fiber (Toosi et al., 2016c). The obtained scaffold compositions were frozen for 24 h at −20°C resulting in a collagen sponge containing PGA fiber and BG with the following w/w ratios of BG/collagen-PGA: 0/100; 40/60; 70/30 (collagen: PGA 0.52 w/w). A dehydro-thermal procedure (140°C and under 0.1 torr for 12 h) was used for cross linking of the freeze-dried sponge. This procedure of cross-linking is toxicologically more acceptable compared to the alternative chemical crosslinking. Using collagen solution alone, a similar experimental procedure was conducted to prepare a collagen sponge with no incorporation of PGA. Ethylene oxide (40°C) was used for sterilization of the prepared scaffolds.

Morphological characterization

The infrastructure and appearance of scaffolds [BG/collagen-PGA (w/w): 0/100; 40/60; 70/30] were visualized using a SEM (scanning electron microscopy, Leo, 1450 VP, Germany). A razor blade was used to cut the sponges. The cross sections of the sponges were then coated with gold using E-1010; Hitachi (ion sputterer) 30 s at 5 mA and 50 mTorr. The samples were then visualized using SEM (15 kV). The pictures of the sponge cross sections were used for the calculation of the pore sizes of collagen sponges using the geometric mean values of diameters of the pores (Hu et al., 2008; Mandal and Kundu, 2009; Rahaman et al., 2011).

Sponge characterization

Mercury intrusion porosimetry (MIP) measures the pore volume and geometry. It works by introducing a liquid with non-wetting properties like mercury into the dry sponge under pressure. First the scaffold composites are placed in a penetrometer and then a high vacuum is applied. When the condition of minimal pressure inside the glass penetrometer is achieved, the sample is surrounded by flowing mercury. The initial volume of mercury in the penetrometer is subtracted from the penetrometer total volume (known) and the obtained value is considered as the volume of the test porous sponge if it were a completely solid sample. Subsequently an increasingly incremental pressure is applied on the mercury reservoir in the stem of the penetrometer at several installments. As the pressure is applied the mercury continuously enters in the pores. To determine the overall porosity of scaffold, the mercury volume (total) which is forced into the test sample is measured. For determination of pore size values, the amount of mercury at each pressure interval is used.

Three samples were sliced from three different composite scaffolds and the porosity values were measured with a mercury porosimeter (LLOYD, INSTRUMENTS, An AMETEK Company). Same batch of scaffolds were used for SEM to facilitate correspondence between the calculated values. Initially, a vacuum (50 mm mercury) was applied on each specimen to completely remove air from the test sample. As described above, mercury was then used to surround the sample and introduced into the pores forcing increasing range of pressures from 0.22 to 30 psi. Prior and following of the introduction of mercury, the sample weights in penetrometer were measured. To obtain the total volume used, the weight difference was divided by the mercury density at ambient temperature. By dividing the value of total volume of the pores by the samples external volume, percent pore volume or porosity was determined. For an estimation of the pore size Washburn equation was used:

$$\mathrm{r} = 2s\frac{\cos(\theta)}{p}$$

where r stands for the radius of the pore, s is the value for mercury surface tension, Θ is the value of the mercury contact angle, and p represents the amount of applied pressure. An algorithm that is built in the device automatically calculated the value at various pressure intervals, and after recording all points, the average values were obtained.

Evaluation of bioactivity

To determine the bioactivity of samples, the prepared porous scaffolds were soaked for various time intervals (two, seven, and 14 days) in 5 ml of SBF pH 7.4 at 37°C (at every 2 days the SBF solution was refreshed). The composition of SBF is very similar to blood plasma of human. SBF has been used in bioactivity assays (*in vitro*) extensively. To conduct compositional analysis and morphological examination, the prepared specimens were taken out from SBF and rinsed intensively with deionized water.

Mechanical characterization

The compression test performed based on the international standard for compression testing, ISO 604 using a mechanical testing machine (LLOYD, INSTRUMENTS, AMETEK, West Sussex, United Kingdom). The tested cylinder-shaped scaffold samples had a height of approximately one to 1.2 cm with 2 mm diameter as measured with a digital caliper. For every composition, five porous samples were analyzed at ambient temperature. The used crosshead speed was 0.01 mm.S^{-1} and the loads were added until the sample was compressed to almost seventy percent of its initial length. The curves of compressive stress–strain were prepared and for each sample the mean compressive modulus with the relevant standard deviation (SD) value was obtained. The modulus was defined as the value of slope of the stress–strain curve initial linear portion (Wang et al., 2007).

Cell seeding procedure in the scaffold

BM-MSCs were seeded into the composite scaffolds using the agitated seeding method. Pre-wetted sponges were inserted into a sterile 15 ml tube. Then the cell suspension (1×10^6 in 0.5 ml) was placed into the tube. The sponge–cell mixture culture was shaken on an orbital shaker (VISION, VS-8480, Korea) at 300 rpm for 6 h. Then the culture was placed for 2 hours in a 24-well plate (5% CO_2 incubator) at 37°C. 1 ml of DMEM (Sigma-Aldrich, Milan, Italy) supplemented with FBS (15% w/v) and penicillin (100 U.ml^{-1}) and 100 μg ml^{-1} streptomycin (GIBCO, Invitrogen, Milan, Italy) was added to each culture.

MTT assay

Proliferation of MSCs on sponges was determined by the MTT 3-(4, 5-dimethylthiazol-2-yl)-2, 5-diphenyl-2H-tetrazolium bromide (atocell) assay. The sponges were transferred into a new 24-well plate, and 1 ml of MTT solution (0.5 mg/ml) was added to each well. After incubation at 37°C for 4 h in a 5% CO_2, MTT was taken up by the active cells and reduced in the mitochondria to insoluble purple formazan granules. Subsequently, the medium was discarded and the precipitated formazan was dissolved in DMSO (150 μl/well). The optical density of the solution was evaluated using a microplate spectrophotometer after subtraction of OD 570 nm. The viable cell number was determined using a linear calibration curve between OD and predetermined cell concentration.

Staining for live/dead differentiation

The whole 3D culture was stained with PI/FDA (propidium iodide/fluorescein diacetate) (FDA; Sigma, F73378 and PI; Sigma, 81,845) to demonstrate the viability of cells. Rinsing procedures (three times with PBS) were then followed and the grafts were incubated for 15 min at 37°C with FDA solution (2 μg ml^{-1}). Another rinsing procedure (with PBS for three times) was followed and then the grafts were incubated with PI solution (0.1 mg ml^{-1}) at room temperature for 2 min. A final washing step was followed before the screening of the grafts using a fluorescent microscope (Olympus BX51).

Mesenchymal stem cells derived from bone marrow differentiation towards osteogenic lineage

BM-MSCs were taken from iliac crest bone marrow of healthy donors undergoing bone marrow harvest (approved by medical research ethics committee of Mashhad University

TABLE 1 Characterization of porosity of the collagen/poly (glycolic acid) (PGA) blends containing different amounts of a bioactive glass (45S5).

Collagen/fiber ratio (w/w)	45S5/PGA-collagen 0/100	45S5/PGA-collagen 40/60	45S5/PGA-collagen 70/30
Average pore size (μm)	72.5	113.5	112.5
Porosity (%)	91.39	62.4	73.6

of Medical Sciences (MUMS) project number 951244). To study the osteogenic lineage differentiation of the BM-MSCs, the bone osteocalcin content and ALP (intracellular alkaline phosphatase) activity were evaluated. The cells seeded on BG/collagen-PGA sponge cultured with a similar method as described above. DMEM (low glucose) was supplemented with FBS (10%), ascorbic acid (50 mg ml^{-1}), dexamethasone (10 nM) and 10 mM β-glycerophosphate (differentiation medium) (Toosi et al., 2017). For control experiments DMEM (low glucose) with FBS (10%) was used. ALP activity was assayed with an ALP assay kit (Lot. No. APF; Sigma, Missouri, United States). The cultured sponges were washed three times with PBS, then minced with scissors, and finally homogenized in a lysis buffer consisting of 0.2% triton X-100 (w/v), Tris–HCl (10 mM), $MgCl_2$ (1 mM) and pH 7.5. Two ml of the sample lysate was then centrifuged for 10 min (12,000 rpm at 4°C). Then supernatant ALP activity was measured using the substrate *p*-nitrophenyl phosphate. In order to test for calcium deposition, the cultured grafts were washed (3X with PBS). An aqueous solution of trypsin 0.05% (w/v) and 1 mM EDTA (in 0.1 M PBS), pH 7.4 (GIBCO, Invitrogen, Milan, Italy) was then used to detach BM-MSCs from the cultured scaffold. Attached BM-MSCs to the plates were fixed with formaldehyde 3% (w/v) for 10 min at ambient temperature. The specimens were then placed in alizarin red stain (pH 4, room temperature). The samples were then washed with PBS (3X) for 10 min to visualize the differentiated cells. The stain (alizarin red) was then removed and an equal volume of PBS was added. An Eyepiece camera (AM4023; Dino-lab digital microscope, United States) was used to take pictures.

Statistical analysis

All measured values are shown as mean ± SD (standard deviation). ANOVA (single-factor analysis of variance) was used for statistical analysis. A calculated value of $p < 0.05$ represents a statistically significant value.

Results

Porosity and morphological analysis

Morphological and porosity values of collagen scaffold reinforced with PGA and different amounts of BG are shown in Table 1. Our results indicate that the porosity of collagen-PGA scaffolds was decreased by incorporation of BG to a minimum level at incorporation rate of 40% (w/w) BG. This could be due to the filling of the pores by adding BG and increased interconnectivity of pores.

The pore sizes were found to vary from 75 to 115 μm depending on incorporation percentage of the BG. In particular, the average pore size increased with increasing the bioglass portion. In scaffolds prepared with BG (70% w/w), the average pore size was slightly lower than BG, (40 %w/w) incorporation. This average pore size reduction by higher bioglass incorporation could be attributed to the deposition of BG on the collagen-PGA pore walls and therefore, resulting in the partial occupation of the collagen-PGA matrix free void space. This was subsequently confirmed by SEM) Figure 2. A foam-like morphology presenting with a wide distribution of interconnected pores was observed in the prepared scaffolds (Figure 3).

Bioactivity of the scaffolds

After immersion in SBF, the BG/collagen-PGA composite scaffolds were studied by SEM to investigate the composite surface for its bioactivity properties and the formation of layer of apatite as the interaction between SBF solution and the surface of the composites is expected to cause formation and nucleation of an apatite layer on the scaffold surface.

Figure 3 represents the SEM images of the fractured section of the BG/collagen-PGA scaffold composites after soaking in SBF for two, seven, and 14 days, respectively.

SEM micrographs of the BG/collagen-PGA scaffolds after SBF immersion for different intervals indicated the stability of scaffolds in SBF regardless to the compositions of scaffolds, while they retained their highly interconnected structure.

Mechanical properties characterization

The mechanical characteristics including the compressive strength of the composite sponges were assayed by a mechanical testing machine. By applying a constant compressive load at a fixed speed, the force from stress–strain data was calculated (Figure 4). Table 2 presents the data for stress-strain which was measured for the porous sponges by applying an

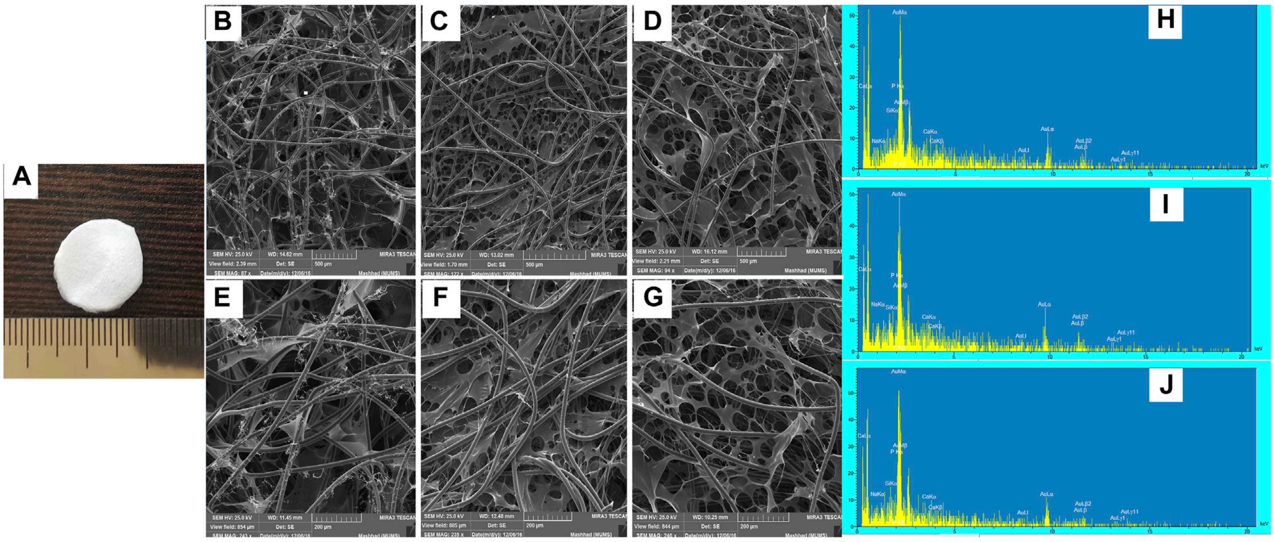

FIGURE 2
Frame structure, SEM micrographs and EDS spectra of BG-Collagen/PGA scaffolds: Physical picture of BG-collagen/PGA scaffold **(A)**. Section of **(B,E,H)** 5S5/PGA and collagen 0/100, **(C,F,I)** 45S5/PGA and collagen 40/60, **(D,G,J)** 45S5/PGA and collagen 70/30. The dispersion of BG nanoparticles in PGA matrix can be seen **(C,F,D,G)**.

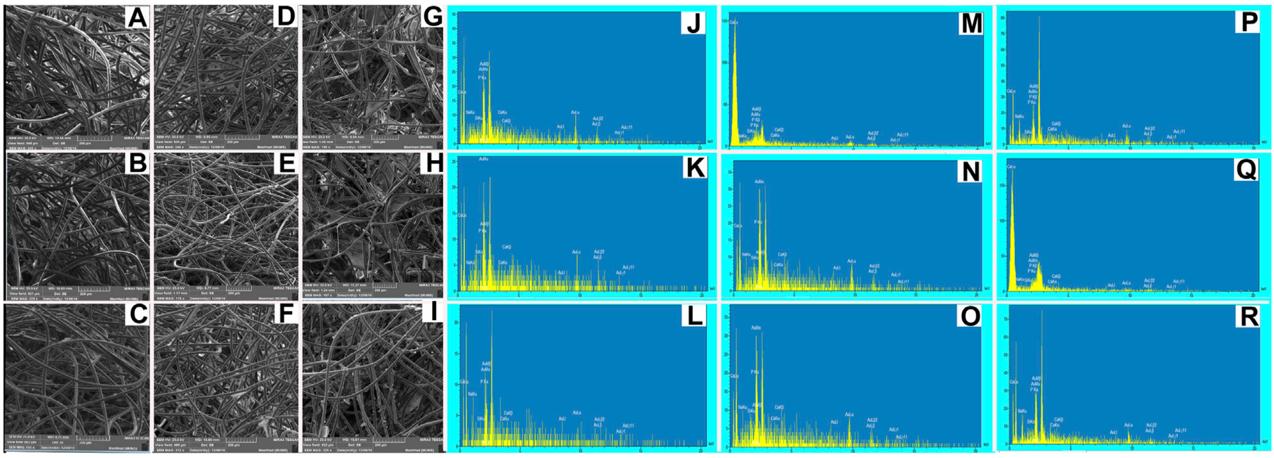

FIGURE 3
SEM micrographs and EDS spectra of BG-Collagen/PGA scaffolds after immersion in SBF for different intervals: after 2 days **(A,J)** 45S5/PGA and collagen 0/100, **(B,K)** 45S5/PGA and collagen 40/60, **(C,L)** 45S5/PGA and collagen 70/30, after 7 days **(D,M)** 45S5/PGA and collagen 0/100, **(E,N)** 45S5/PGA and collagen 40/60, **(F,O)** 45S5/PGA and collagen 70/30, and after 14 days **(G,P)** 45S5/PGA and collagen 0/100, **(H,Q)** 45S5/PGA and collagen 40/60, **(I,R)** 45S5/PGA and collagen 70/30 Figure 4. Stress−strain curves: The porous composite scaffolds compressed at a strain of (0%–70%). The cross-head speed was 0.01 mm.s^{-1}.

excessive compression force at BG (0%–70%). Upon compression, the composite scaffolds underwent a procedure of densification and did not present with any fractures in their structure. Three distinctive regions were used for curves classification: collapse plateau, linear elastic, and densification process. The collapse modulus (E′), collapse strength (s*), elastic modulus value (E*), and strain (ε*) were all obtained from the curves of stress-strain which are presented in Table 2. The elastic moduli of BG/PGA-collagen (40/60) and BG/PGA-collagen (70/30) scaffolds were 1.1 MPa.

The composite scaffold mechanical properties strongly depend on the size of inorganic phase component, the aspect ratio, the

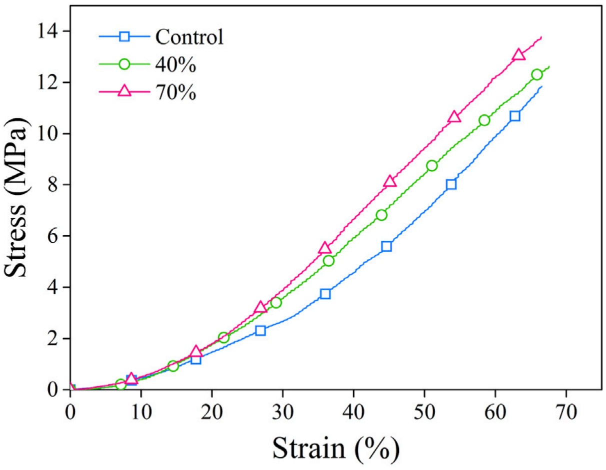

FIGURE 4
Stress–strain curves. The porous composite scaffolds compressed at a strain of (0%–70%). The cross-head speed was 0.01 mm.s^{-1}.

particle amount and the particle-matrix adhesion. By incorporating of nano/micro particles, the sponge modulus can be increased while the strength characteristics depend on the transfer of stress between the particles and the matrix.

The uniformity of BG particles distribution and their appropriate bonding to the collagen matrix are important contributors and responsible for the approximately two folds increase from 2.3 ± 0.18 MPa to 4.1 ± 0.5 MPa and 4.1 ± 0.6 MPa in collapse strength of the designed composites.

The improved mechanical properties of scaffolds can be linked and attributed to the small size and uniform shape of the incorporated inorganic phase and, also to the properly distributed BG particles within the collagen matrix.

Compared to the PGA-collagen sponge, the inclusion of an inorganic phase resulted in two times increase in the scaffolds mechanical properties. The mechanical specifications of the BG/PGA-collagen 40/60 and 70/30 (w/w) scaffolds were significantly improved due to incorporation of BG. However, the sponge composites obtained by freeze drying with collagen incorporation exhibited very high porosity which lowers the collapse strength and elastic modulus of the resulting composite compared to those of the cancellous bone. Therefore, for non-load bearing bone tissue engineering these composite scaffolds may be used.

Cell viability

MTT assay was used to compare cell viability on BG/collagen-PGA ratios (w/w): 0/100; 40/60; 70/30 (Figure 5A). The results showed no significant different between three groups of scaffolds.

The viability of cells in the scaffold composites was assessed by a staining protocol for live-dead (FDA-PI) after 3-weeks of three-dimensional arrangement of the expanded MSCs (Figure 5). Our findings showed that MSCs were homogeneously distributed in all three different types of scaffolds. The green color staining of cellular components proliferation in collagen-PGA sponges, with different amounts of BG, indicates that the MSCs were viable and consisted of almost round-shaped cells. Our finding supports the fact that the prepared composite scaffolds containing BG were biologically compatible as evidenced by MSCs binding to the scaffold, their spreading, and cell viability maintenance within the composites prepared.

Differentiation of mesenchymal stem cells derived from bone marrow towards osteogenic lineage.

Figures 6A–C indicates that MSCs differentiated towards osteocytes. Alizarin red staining used to examine calcium deposits of differentiated cells after 21 days. MSCs differentiation to osteoblasts was confirmed by alizarin red staining with increased ALP activity in collagen-PGA sponge with BG incorporation, in comparison to collagen-PGA scaffold without addition of the BG.

Figure 6D shows ALP activity of MSCs cultured on BG/PGA-collagen ratios (w/w): 0/100; 40/60; 70/30. ALP activity of MSC cultured in the bone differentiation medium was high for BG/PGA-collagen 40/60 and 70/30 (w/w), as compared to BG/PGA-collagen 0/100 (w/w). In induction medium, incorporation of BG enhanced ALP activity.

TABLE 2 Elastic modulus (E^*), collapse modulus (E'), collapse strength (σ^*) and strain (ε^*).

	E^* (MPa)	E' (MPa)	σ^* (MPa)	ε^* (%)
45S5/PGA-collagen 0/100	1.1 ± 0.2	0.9 ± 0.1	2.3 ± 0.18	27 ± 0.7
45S5/PGA-collagen 40/60	1.1 ± 0.4	1.6 ± 0.23	4.1 ± 0.5	32 ± 0.8
45S5/PGA-collagen 70/30	1.1 ± 0.3	1.6 ± 0.25	4.6 ± 0.6	33 ± 0.7

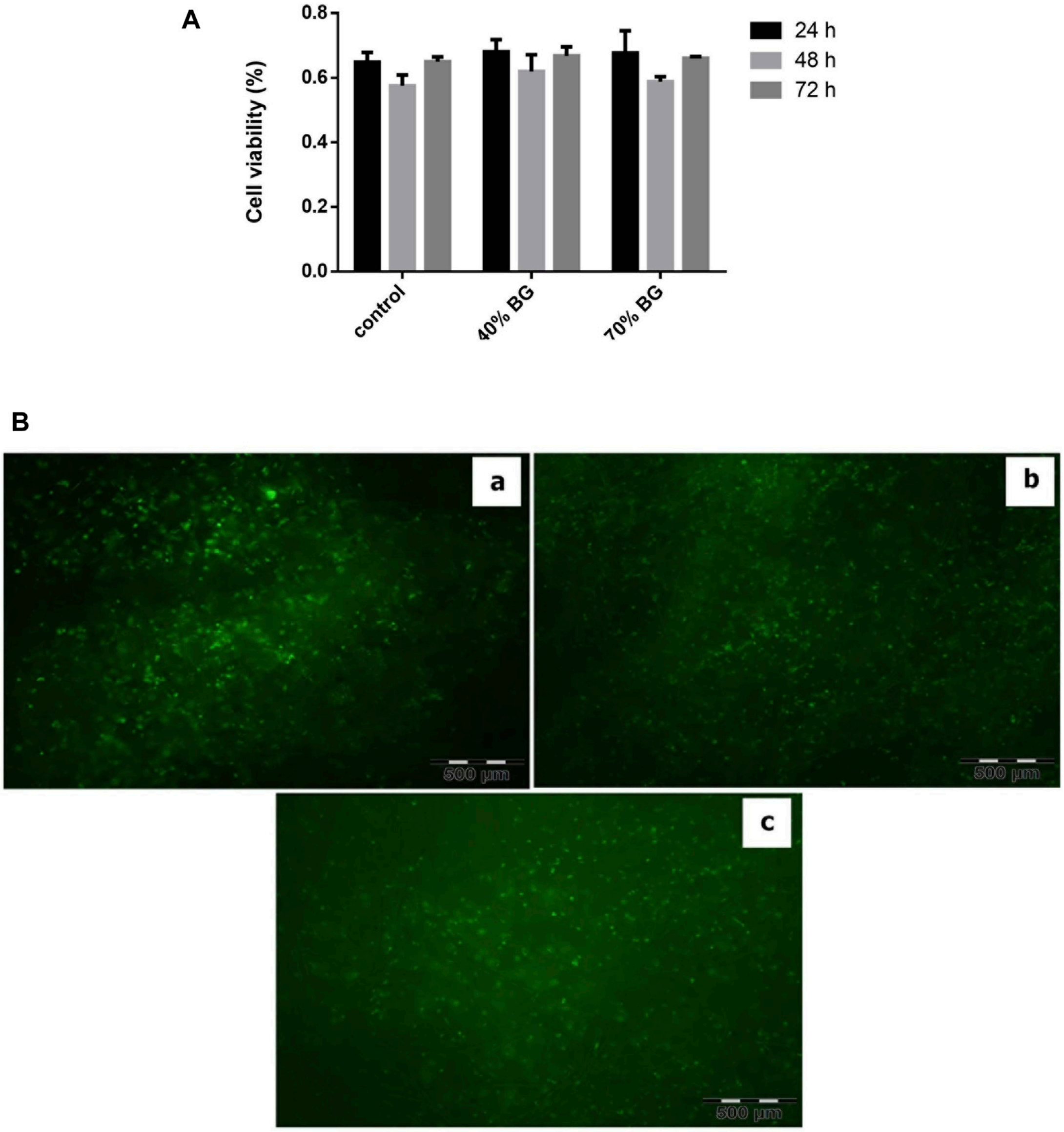

FIGURE 5
Viability assay of BM-MSCs in the sponges using MTT and PI-FDA staining. **(A)** Cell viability on the BG-collagen/PGA scaffolds. The results were expressed as proliferation of MSCs on scaffolds. Each experiment was repeated independently three times in triplicate tests $*p < 0.05$; significant against the viability of cells on collagen/PGA scaffold without BG incorporation. **(B)** Cell viability staining with PI/FDA. **(a)** BG/PGA-collagen 0/100, **(b)** BG/PGA-collagen 40/60, **(c)** BG/PGA-collagen 70/30 w/w. The staining presents with viable cells and homogeneous cell distribution within the scaffold (Magnification 10 X). BG containing scaffolds are biocompatible as evidenced by cell attachment, spreading and maintenance of cell viability within the constructs.

Discussion

Using *in vivo* and *in vitro* experiments, we have previously shown the desirable specifications and bone healing properties of a collagen-PGA scaffold (Toosi et al., 2016c; Toosi et al., 2018; Toosi et al., 2019b). Here, we aimed to enhance the bioactivity, physical, functional and mechanical properties of our previously reported scaffold designed for bone regeneration application by incorporating bioactive glass 45S5.

Porous scaffolds were prepared using various amounts/ratios of BG to collagen-PGA (w/w): 0/100; 40/60; 70/30). Incorporation of BG into the scaffold composites resulted in scaffolds with average pore sizes of 100 μm (75–115 μm). The porous scaffold structures were analyzed for their stability,

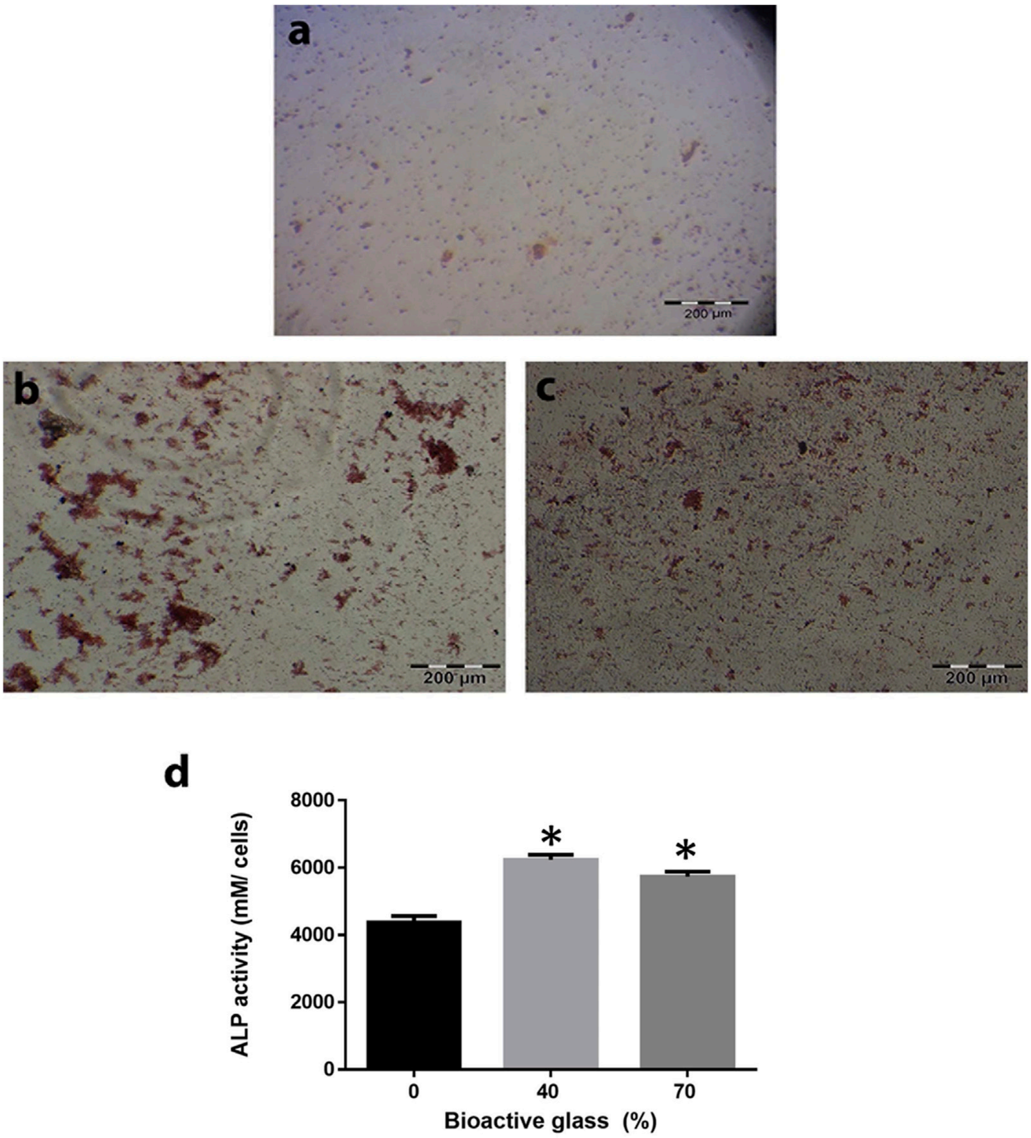

FIGURE 6
Effect of the different scaffold compositions in induction of differentiation of bone marrow mesenchymal stem cells (BM-MSCs) toward osteoblast lineage. Calcium depositions that produced by BM-MSCs have been shown by alizarin red staining for BG/collagen-PGA: **(A)** 0/100; **(B)** 40/60; **(C)** 70/30 w/w cultured in bone differentiation media after 21 days at 37°C in a 5% CO_2. Red nodules are shown the ECM deposition as a result of osteogenesis. **(D)** Alkaline phosphatase activity as an index of osteogenesis was also calculated for BM-MSCs culture within all three types of the scaffold. Each experimental procedure was repeated three times. The data are shown as mean ± SD. $*p \leq 0.05$ was considered as significant. ALP activity was significantly higher in BG/collagen-PGA: 40/60 and BG/collagen-PGA: 70/30 rather than control BG/collagen-PGA: 0/100.

mechanical properties and bioactivity supporting MSCs proliferation, metabolic activity and induction of seeded MSCs towards osteogenic lineage differentiation.

One of the critical and most essential requirements for an artificially prepared composite for bone regeneration applications is its ability to form a bioactive bone-like apatite structure on its surface after exposure with a physiological and suitable environment (Toosi et al., 2018). We have now a vast option of biologically active materials such as bioglass and TCP which have been reported to be used for bone repair clinical procedures (Hench, 1998a). These bioactive composites have been shown to be able to bond with bone tissue by means of a bone-mimicking apatite layer which is formed on the bioactive material surface when implanted into the human (patient) body. Further analysis has confirmed that this formed apatite is composed of carbonate-containing HA. This has not been seen at the interface between bone and bio-inert or non-bioactive materials (Kitsugi et al., 1989). There is an *in vitro*

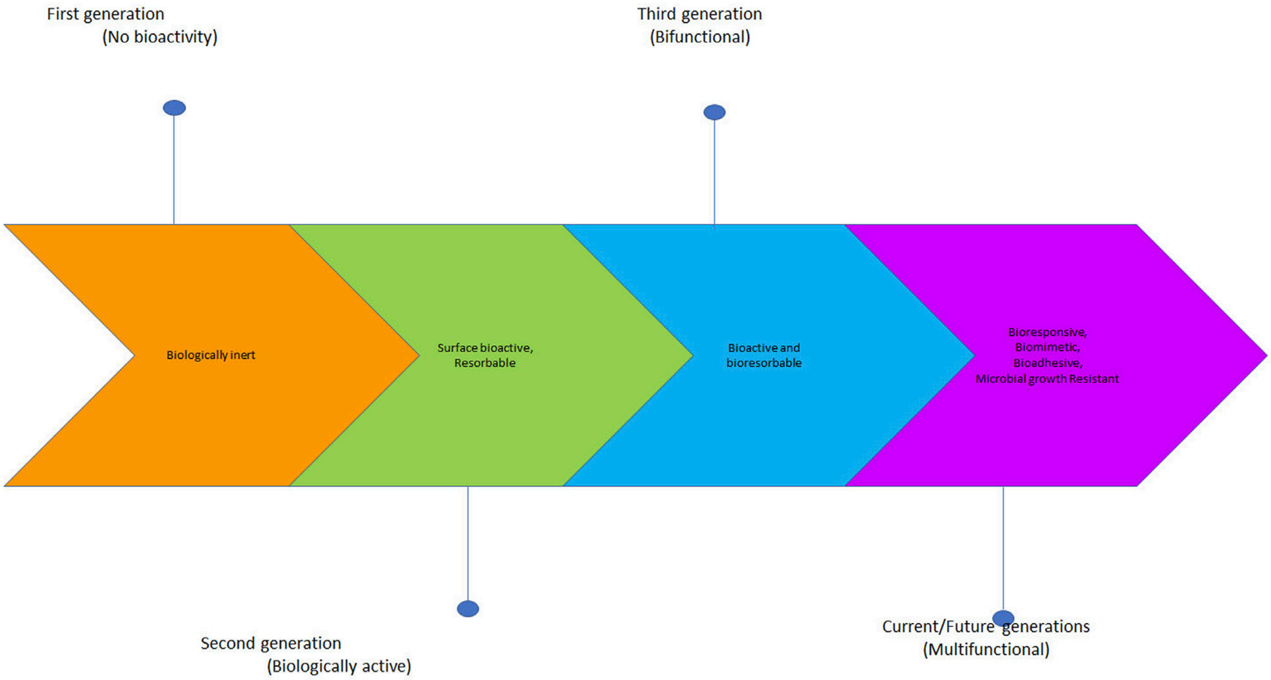

FIGURE 7
The evolving since of bone regeneration scaffolds.

oscillating phenomenon consisting of simultaneous mineral component adsorption and resorption processes that is due to non-stable conditions of SBF. The processes of dissolution and precipitation of bone like apatite happens while the bioactive materials are immersed in SBF. As shown in Figure 3 and supported by other data, in SBF soaking experiments our designed scaffolds were stable and retained their interconnected porous structure. Further *in vivo* analysis is required to assess the bone attachment property that is an essential characteristic of an artificial biomaterial used in bone healing. For bone bonding the *in vivo* formation of bone-like apatite consisting of calcium phosphate is an absolute requirement (Hench, 1998b).

While preparing scaffolds for load-bearing bone tissue engineering application, a scientist needs to deal with two conflicting composite requirements, very high mechanical strength and providing a high porosity. In favor of cell proliferation and growth, the scaffold needs to provide a highly porous structure while this property is generally in conflict with another important property of having a high mechanical strength (Gentile et al., 2012). Moreover, the composite scaffold mechanical properties are highly dependent on the aspect ratio, the size of the added mineral phase, the particle quantifications and the particle-matrix adhesion. By incorporation of nano/micro particles, the modulus of a sponge composite can be increased while the strength of the scaffold structure depends on the transfer of stress between the matrix and the particle (Mikael and Nukavarapu, 2011). Compared to our previously designed collagen-PGA scaffold (used as control here), the BG/collagen-PGA at both ratios (40/60 and 70/30) presented with more advanced mechanical properties.

The BG (45S5) has proved to provide enhanced biological activity and its properties in supporting differentiation of stem cells towards osteoblastic lineage have been reported (Gentile et al., 2012; Detsch et al., 2015). Therefore, its incorporation in a scaffold composite results in a highly mineralized bone matrix formation (Xynos et al., 2001; Gentile et al., 2012). It is considered that BG is osteoinductive and osteoconductive. It is able to support formation of new bone growth along the bone–implant interface and even within the implanted sponges away from the interface of bone–implant (Rahaman et al., 2011). Therefore, as we hypothesized, our new scaffolds with the incorporation of BG showed advanced *in vitro* properties and supported the MSCs differentiation to osteoblasts (Figure 5). This latter property may prove to be very critical *in vivo* and will be examined in our future animal studies.

Induction of ALP expression by the bioactive inorganic incorporation and bioglass polymer composites has been shown elsewhere in the literature (Knabe et al., 2005; Yao et al., 2005; Kim et al., 2006). The products released from 45S5 bioglass ionic dissolution are shown to have effects on the regulation of gene expression profile of human osteoblasts in monolayer cultures (Xynos et al., 2001). Tsigkou and co-workers have shown enhanced differentiation and mineralization of fetal osteoblasts and formation of bone nodules induced by a BG conditioned medium in the absence of other supplements for osteogenic differentiation (Yao et al., 2005; Tsigkou et al., 2007). In another study, El-Gendy *et al.*, have shown that both *in vitro* and *in vivo*, BG containing scaffolds are able to enhance human dental pulp stromal cells differentiation to osteoblasts. This strongly supports the potential use of this bioglass for bone tissue engineering for clinical applications (Reilly et al., 2007; El-Gendy et al., 2012). This is in line with our observations in the design of our BG/collagen-PGA scaffolds. Subsequent plans on implementation and design of *in vivo* studies of the scaffolds are underway.

Overall, our findings indicate that BG incorporation would enhance physical stability and biological activities of our previously reported collagen-PGA scaffold towards bone tissue regeneration applications. The novel scaffold composition may provide a basis for additional *in vivo* and *in vitro* studies of bone repair and bone tissue engineering.

Future works

There is currently an urgent need for methodological studies (design, formulation, and fabrication) of new scaffolds for bone regeneration.

In order to improve the biological and mechanical properties of scaffolds, collagen sponges can be modified by a group of diverse materials. Bioceramics such as BG 45S5, as mineral components are known to be capable to improve the osteointegration, mechanical properties and osteoinduction of composite scaffolds. Moreover, PGA and other polymers enhance the stability and mechanical properties.

One shortcoming in this field is now a lack of reliable and validated experiments *in vivo* to examine the suitability of these scaffolds. Furthermore, there are still challenges in the fabrication of an ideal composite for bone regeneration scaffolds to provide idealistic pore size, mechanical stability and integrity, biocompatibility, osteoinductivity and osteoconductivity. There is also a great need in optimization of scaffolds to provide the required attachment, migration and survival of the cells in volved in bone healing and regeneration.

Following the recent advancements in bone regeneration scaffolds, substantial interest is now growing towards designing multifunctional scaffolds loaded with various molecules and nanomaterials for advanced bone regeneration scaffolds (Figure 7) (Arjunan et al., 2021). For example, in addition to other biofactors and biomolecules, nucleic acids can be added to encode the growth factors that promote bone growth. The discovery of new molecules and bioingredients for manufacturing of future bone generation scaffolds is at the centre of focus and a leading force in studies for bone tissue engineering.

Conclusion

Fabrication of collagen sponges combined with BG and PGA fibers as a scaffold composite for bone tissue engineering was investigated. *In vitro* studies indicated that addition of BG had a great and impressive effect on both physical and mechanical properties of the composite scaffolds and supported differentiation of MSCs cells towards osteoblasts. The results obtained strongly suggest that addition of the already known bioglass 45S5 component which is FDA approved enhances physical stability of the collagen-PGA scaffold and provides further mechanical strength and biological activity. The scaffold composites reported here, may provide advanced functional properties *in vivo* and have the potential to be considered for additional evaluation towards non-union fracture treatment. Further studies including *in vivo* studies are required to evaluate the biological interactions and functionality of these biodegradable composite scaffolds under real conditions.

Data availability statement

The original contributions presented in the study are included in the article/supplementary material, further inquiries can be directed to the corresponding authors.

Author contributions

All the authors listed have made a substantial, direct, and intellectual contribution to the work and approved it for publication.

Funding

Research Council of the Mashhad University of Medical Sciences, Iran for the approval and financial support of this research.

Conflict of interest

The authors declare that the research was conducted in the absence of any commercial or financial relationships that could be construed as a potential conflict of interest.

Publisher's note

References

Arjunan, A., Baroutaji, A., Robinson, J., Praveen, A. S., Pollard, A., and Wang, C. (2021). *Future directions and requirements for tissue engineering biomaterials*. Amsterdam, Netherlands: Elsevier.

Babensee, J. E., McIntire, L. V., and Mikos, A. G. (2000). Growth factor delivery for tissue engineering. *Pharm. Res.* 17 (5), 497–504. doi:10.1023/a:1007502828372

Black, A. F., Berthod, F., L'heureux, N., Germain, L., and Auger, F. A. (1998). *In vitro* reconstruction of a human capillary-like network in a tissue-engineered skin equivalent. *FASEB J.* 12 (13), 1331–1340. doi:10.1096/fasebj.12.13.1331

Boccaccini, A. R., Chen, Q., Lefebvre, L., Gremillard, L., and Chevalier, J. (2007). Sintering, crystallisation and biodegradation behaviour of Bioglass®-derived glass–ceramics. *Faraday Discuss.* 136, 27–44. doi:10.1039/b616539g

Cao, Y., Vacanti, J. P., Paige, K. T., Upton, J., and Vacanti, C. A. (1997). Transplantation of chondrocytes utilizing a polymer-cell construct to produce tissue-engineered cartilage in the shape of a human ear. *Plast. &amp Reconstr. Surg.* 100 (2), 297–302. doi:10.1097/00006534-199708000-00001

Chen, Q. Z., Thompson, I. D., and Boccaccini, A. R. (2006). 45S5 Bioglass®-derived glass–ceramic scaffolds for bone tissue engineering. *Biomaterials* 27 (11), 2414–2425. doi:10.1016/j.biomaterials.2005.11.025

Cooper, M. L., and Hansbrough, J. F. (1991). Use of a composite skin graft composed of cultured human keratinocytes and fibroblasts and a collagen-GAG matrix to cover full-thickness wounds on athymic mice. *Surgery* 109 (2), 198–207.

Detsch, R., Alles, S., Hum, J., Westenberger, P., Sieker, F., Heusinger, D., et al. (2015). Osteogenic differentiation of umbilical cord and adipose derived stem cells onto highly porous 45S5 Bioglass®-based scaffolds. *J. Biomed. Mat. Res. A* 103 (3), 1029–1037. doi:10.1002/jbm.a.35238

Eaglstein, W. H., and Falanga, V. (1997). Tissue engineering and the development of Apligraf®, a human skin equivalent. *Clin. Ther.* 19 (5), 894–905. doi:10.1016/s0149-2918(97)80043-4

El-Gendy, R., Yang, X. B., Newby, P. J., Boccaccini, A. R., and Kirkham, J. (2012). Osteogenic differentiation of human dental pulp stromal cells on 45S5 Bioglass® based scaffolds *in vitro* and *in vivo*. *Tissue Eng. Part A* 19 (5–6), 707–715. doi:10.1089/ten.tea.2012.0112

Elisseeff, J., McIntosh, W., Fu, K., Blunk, T., and Langer, R. (2001). Controlled-release of IGF-I and TGF-β1 in a photopolymerizing hydrogel for cartilage tissue engineering. *J. Orthop. Res.* 19 (6), 1098–1104. doi:10.1016/s0736-0266(01)00054-7

Fu, Q., Saiz, E., Rahaman, M. N., and Tomsia, A. P. (2011). Bioactive glass scaffolds for bone tissue engineering: State of the art and future perspectives. *Mater. Sci. Eng. C* 31 (7), 1245–1256. doi:10.1016/j.msec.2011.04.022

Gentile, P., Mattioli-Belmonte, M., Chiono, V., Ferretti, C., Baino, F., Tonda-Turo, C., et al. (2012). Bioactive glass/polymer composite scaffolds mimicking bone tissue. *J. Biomed. Mat. Res. A* 100 (10), 2654–2667. doi:10.1002/jbm.a.34205

Hansbrough, J. F., Morgan, J., Greenleaf, G., Parikh, M., Nolte, C., and Wilkins, L. (1994). Evaluation of Graftskin composite grafts on full-thickness wounds on athymic mice. *J. Burn Care Rehabil.* 15 (4), 346–353. doi:10.1097/00004630-199407000-00010

Hench, L. L. (1998). Bioactive materials: The potential for tissue regeneration. *J. Biomed. Mat. Res.* 41 (4), 511–518. doi:10.1002/(sici)1097-4636(19980915)41:4<511::aid-jbm1>3.0.co;2-f

Hench, L. L. (1998). Biomaterials: A forecast for the future. *Biomaterials* 19 (16), 1419–1423. doi:10.1016/s0142-9612(98)00133-1

Hench, L. L., Splinter, R. J., Allen, W. C., and Greenlee, T. K. (1971). Bonding mechanisms at the interface of ceramic prosthetic materials. *J. Biomed. Mat. Res.* 5, 117–141. doi:10.1002/jbm.820050611

Hu, K., Cui, F., Lv, Q., Ma, J., Feng, Q., Xu, L., et al. (2008). Preparation of fibroin/recombinant human-like collagen scaffold to promote fibroblasts compatibility. *J. Biomed. Mat. Res. A* 84 (2), 483–490. doi:10.1002/jbm.a.31440

Kim, H., Song, J., and Kim, H. (2006). Bioactive glass nanofiber–collagen nanocomposite as a novel bone regeneration matrix. *J. Biomed. Mat. Res. A* 79 (3), 698–705. doi:10.1002/jbm.a.30848

Kitsugi, T., Yamamuro, T., Nakamura, T., and Kokubo, T. (1989). Bone bonding behavior of MgO CaO SiO2 P2O5 CaF2 glass (mother glass of A W glass ceramics). *J. Biomed. Mat. Res.* 23 (6), 631–648. doi:10.1002/jbm.820230607

Knabe, C., Stiller, M., Berger, G., Reif, D., Gildenhaar, R., Howlett, C. R., et al. (2005). The effect of bioactive glass ceramics on the expression of bone-related genes and proteins *in vitro*. *Clin. oral implants Res.* 16 (1), 119–127. doi:10.1111/j.1600-0501.2004.01066.x

Leach, J. K., Kaigler, D., Wang, Z., Krebsbach, P. H., and Mooney, D. J. (2006). Coating of VEGF-releasing scaffolds with bioactive glass for angiogenesis and bone regeneration. *Biomaterials* 27 (17), 3249–3255. doi:10.1016/j.biomaterials.2006.01.033

Leu, A., and Leach, J. K. (2008). Proangiogenic potential of a collagen/bioactive glass substrate. *Pharm. Res.* 25 (5), 1222–1229. doi:10.1007/s11095-007-9508-9

Mahoney, M. J., and Saltzman, W. M. (2001). Transplantation of brain cells assembled around a programmable synthetic microenvironment. *Nat. Biotechnol.* 19 (10), 934–939. doi:10.1038/nbt1001-934

Mandal, B. B., and Kundu, S. C. (2009). Cell proliferation and migration in silk fibroin 3D scaffolds. *Biomaterials* 30 (15), 2956–2965. doi:10.1016/j.biomaterials.2009.02.006

Marcacci, M., Kon, E., Moukhachev, V., Lavroukov, A., Kutepov, S., Quarto, R., et al. (2007). Stem cells associated with macroporous bioceramics for long bone repair: 6-to 7-year outcome of a pilot clinical study. *Tissue Eng.* 13 (5), 947–955. doi:10.1089/ten.2006.0271

Mikael, P. E., and Nukavarapu, S. P. (2011). Functionalized carbon nanotube composite scaffolds for bone tissue engineering: Prospects and progress. *J. Biomater. Tissue Eng.* 1 (1), 76–85. doi:10.1166/jbt.2011.1011

Nerem, R. M. (1991). Cellular engineering. *Ann. Biomed. Eng.* 19 (5), 529–545. doi:10.1007/bf02367396

Philippart, A., Boccaccini, A. R., Fleck, C., Schubert, D. W., and Roether, J. A. (2015). Toughening and functionalization of bioactive ceramic and glass bone scaffolds by biopolymer coatings and infiltration: A review of the last 5 years. *Expert Rev. Med. devices* 12 (1), 93–111. doi:10.1586/17434440.2015.958075

Pishavar, E., Luo, H., Naserifar, M., Hashemi, M., Toosi, S., Atala, A., et al. (2021). Advanced hydrogels as exosome delivery systems for osteogenic differentiation of MSCs: Application in bone regeneration. *Int. J. Mol. Sci.* 22 (12), 6203. doi:10.3390/ijms22126203

Rahaman, M. N., Brown, R. F., Bal, B. S., and Day, D. E. (2006). "Bioactive glasses for nonbearing applications in total joint replacement," in *Seminars in arthroplasty* (Amsterdam, Netherlands: Elsevier), 102–112.

Rahaman, M. N., Day, D. E., Bal, B. S., Fu, Q., Jung, S. B., Bonewald, L. F., et al. (2011). Bioactive glass in tissue engineering. *Acta biomater.* 7 (6), 2355–2373. doi:10.1016/j.actbio.2011.03.016

Reilly, G. C., Radin, S., Chen, A. T., and Ducheyne, P. (2007). Differential alkaline phosphatase responses of rat and human bone marrow derived mesenchymal stem cells to 45S5 bioactive glass. *Biomaterials* 28 (28), 4091–4097. doi:10.1016/j.biomaterials.2007.05.038

Shea, L. D., Smiley, E., Bonadio, J., and Mooney, D. J. (1999). DNA delivery from polymer matrices for tissue engineering. *Nat. Biotechnol.* 17 (6), 551–554. doi:10.1038/9853

Toosi, S., Behravan, N., and Behravan, J. (2018). Nonunion fractures, mesenchymal stem cells and bone tissue engineering. *J. Biomed. Mat. Res. A* 106, 2552–2562. doi:10.1002/jbm.a.36433

Toosi, S., Esmaeilzadeh, Z., Naderi Meshkin, H., Heirani Tabasi, A., Peivandi, M. T., and Behravan, J. (2019). Adipocyte lineage differentiation potential of MSCs isolated from reaming material. *J. Cell. Physiol.* 234, 20066–20071. doi:10.1002/jcp.28605

Toosi, S., Naderi-meshkin, H., Kalalinia, F., Hosseinkhani, H., Heirani-Tabasi, A., Havakhah, S., et al. (2019). Bone defect healing is induced by collagen sponge/polyglycolic acid. *J. Mat. Sci. Mat. Med.* 30, 33–13. doi:10.1007/s10856-019-6235-9

Toosi, S., Naderi-Meshkin, H., Kalalinia, F., Peivandi, M. T., HosseinKhani, H., Bahrami, A. R., et al. (2016). Comparative characteristics of mesenchymal stem cells derived from reamer-irrigator-aspirator, iliac crest bone marrow, and adipose tissue. *Cell. Mol. Biol.* 62, 68–74.

Toosi, S., Naderi-Meshkin, H., Kalalinia, F., Peivandi, M. T., HosseinKhani, H., Bahrami, A. R., et al. (2016). PGA-incorporated collagen: Toward a biodegradable composite scaffold for bone-tissue engineering. *J. Biomed. Mat. Res. A* 104 (8), 2020–2028. doi:10.1002/jbm.a.35736

Toosi, S., Naderi-Meshkin, H., Kalalinia, F., Pievandi, M. T., Hosseinkhani, H., Bahrami, A. R., et al. (2017). Long bone mesenchymal stem cells (Lb-MSCs): Clinically reliable cells for osteo-diseases. *Cell Tissue Bank.* 18 (4), 489–500. doi:10.1007/s10561-017-9652-3

Toosi, S., Vahednia, E., and Behravan, J. (2016). Ream content a stem cell source for bone defects. *Stem Cell Transl. Investigation* 3. doi:10.14800/scti.1380

Tsigkou, O., Hench, L. L., Boccaccini, A. R., Polak, J. M., and Stevens, M. M. (2007). Enhanced differentiation and mineralization of human fetal osteoblasts on PDLLA containing Bioglass® composite films in the absence of osteogenic supplements. *J. Biomed. Mat. Res. A* 80 (4), 837–851. doi:10.1002/jbm.a.30910

Vacanti, C. A., Bonassar, L. J., Vacanti, M. P., and Shufflebarger, J. (2001). Replacement of an avulsed phalanx with tissue-engineered bone. *N. Engl. J. Med. Overseas. Ed.* 344 (20), 1511–1514. doi:10.1056/nejm200105173442004

Vichery, C., and Nedelec, J-M. (2016). Bioactive glass nanoparticles: From synthesis to materials design for biomedical applications. *Materials* 9, 288. doi:10.3390/ma9040288

Wang, H., Li, Y., Zuo, Y., Li, J., Ma, S., and Cheng, L. (2007). Biocompatibility and osteogenesis of biomimetic nano-hydroxyapatite/polyamide composite scaffolds for bone tissue engineering. *Biomaterials* 28 (22), 3338–3348. doi:10.1016/j.biomaterials.2007.04.014

Wheeler, D. L., Stokes, K. E., Hoellrich, R. G., Chamberland, D. L., and McLoughlin, S. W. (1998). Effect of bioactive glass particle size on osseous regeneration of cancellous defects. *J. Biomed. Mat. Res.* 41 (4), 527–533. doi:10.1002/(sici)1097-4636(19980915)41:4<527::aid-jbm3>3.0.co;2-e

Wheeler, D. L., Stokes, K. E., Park, H. M., and Hollinger, J. O. (1997). Evaluation of particulate Bioglass® in a rabbit radius ostectomy model. *J. Biomed. Mat. Res.* 35 (2), 249–254. doi:10.1002/(sici)1097-4636(199705)35:2<249::aid-jbm12>3.0.co;2-c

Xynos, I. D., Edgar, A. J., Buttery, L. D. K., Hench, L. L., and Polak, J. M. (2001). Gene expression profiling of human osteoblasts following treatment with the ionic products of Bioglass® 45S5 dissolution. *J. Biomed. Mat. Res.* 55 (2), 151–157. doi:10.1002/1097-4636(200105)55:2<151::aid-jbm1001>3.0.co;2-d

Xynos, I. D., Edgar, A. J., Buttery, L. D. K., Hench, L. L., and Polak, J. M. (2000). Ionic products of bioactive glass dissolution increase proliferation of human osteoblasts and induce insulin-like growth factor II mRNA expression and protein synthesis. *Biochem. biophysical Res. Commun.* 276 (2), 461–465. doi:10.1006/bbrc.2000.3503

Yao, J., Radin, S., Leboy, P. S., and Ducheyne, P. (2005). The effect of bioactive glass content on synthesis and bioactivity of composite poly (lactic-co-glycolic acid)/bioactive glass substrate for tissue engineering. *Biomaterials* 26 (14), 1935–1943. doi:10.1016/j.biomaterials.2004.06.027

Yunos, D. M., Bretcanu, O., and Boccaccini, A. R. (2008). Polymer-bioceramic composites for tissue engineering scaffolds. *J. Mat. Sci.* 43 (13), 4433–4442. doi:10.1007/s10853-008-2552-y

frontiers | Frontiers in Bioengineering and Biotechnology

TYPE Brief Research Report
PUBLISHED 29 September 2022
DOI 10.3389/fbioe.2022.969275

Brief communication: Effects of conditioned media from human platelet lysate cultured MSC on osteogenic cell differentiation *in vitro*

Siddharth Shanbhag[1,2]*, Niyaz Al-Sharabi[2], Samih Mohamed-Ahmed[2], Reinhard Gruber[3,4,5], Einar K. Kristoffersen[1,6] and Kamal Mustafa[2]

[1]Department of Immunology and Transfusion Medicine, Haukeland University Hospital, Bergen, Norway, [2]Center for Translational Oral Research, Department of Clinical Dentistry, Faculty of Medicine, University of Bergen, Bergen, Norway, [3]Department of Oral Biology, University Clinic of Dentistry, Medical University of Vienna, Vienna, Austria, [4]Department of Periodontology, School of Dental Medicine, University of Bern, Bern, Switzerland, [5]Austrian Cluster for Tissue Regeneration, Vienna, Austria, [6]Department of Clinical Sciences, Faculty of Medicine, University of Bergen, Bergen, Norway

Culturing mesenchymal stromal cells (MSC) in human platelet lysate (HPL) supplemented media can enhance their osteogenic differentiation potential. The objective of this study was to test the hypothesis that conditioned media (CM) derived from HPL-cultured MSC also have pro-osteogenic effects. Pooled CM was prepared from HPL-cultured human bone marrow MSC (BMSC) of multiple donors and applied on BMSC of different donors (than those used for CM preparation), with or without additional supplementation [HPL, fetal bovine serum (FBS)] and osteogenic stimulation. At various time-points, cell proliferation, alkaline phosphatase (ALP) activity, osteogenic gene expression and *in vitro* mineralization were assessed. BMSC in standard unstimulated growth media served as controls. After 3–7 days, CM alone did not promote BMSC proliferation or ALP activity; supplementation of CM with HPL slightly improved these effects. After 2 and 7 days, CM alone, but not CM supplemented with HPL, promoted osteogenic gene expression. After 14 days, only CM supplemented with FBS and osteogenic stimulants supported *in vitro* BMSC mineralization; CM alone and CM supplemented with HPL did not support mineralization, regardless of osteogenic stimulation. In summary, CM from HPL-cultured BMSC promoted osteogenic gene expression but not *in vitro* mineralization in allogeneic BMSC even when supplemented with HPL and/or osteogenic stimulants. Future studies should investigate the role and relevance of supplementation and osteogenic induction in *in vitro* assays using CM from MSC.

KEYWORDS

mesenchymal stromal cells, conditioned media, platelet lysate, bone tissue engineering, osteogenic differentation

EDITED BY
Anna Lange-Consiglio,
University of Milan, Italy

REVIEWED BY
Jia Xian Law,
Universiti Kebangsaan Malaysia,
Malaysia
Masahiro Nishimura,
Kagoshima University, Japan
Pavel Karalkin,
I.M. Sechenov First Moscow State
Medical University, Russia
Morten Juhl,
Department of Cardiology,
Rigshospitalet, Denmark

*CORRESPONDENCE
Siddharth Shanbhag,
siddharth.shanbhag@uib.no

SPECIALTY SECTION
This article was submitted to Tissue Engineering and Regenerative Medicine, a section of the journal Frontiers in Bioengineering and Biotechnology

RECEIVED 14 June 2022
ACCEPTED 14 September 2022
PUBLISHED 29 September 2022

CITATION
Shanbhag S, Al-Sharabi N, Mohamed-Ahmed S, Gruber R, Kristoffersen EK and Mustafa K (2022), Brief communication: Effects of conditioned media from human platelet lysate cultured MSC on osteogenic cell differentiation in vitro.
Front. Bioeng. Biotechnol. 10:969275.
doi: 10.3389/fbioe.2022.969275

Introduction

Bone tissue engineering strategies are increasingly being used to overcome the limitations of autogenous bone grafts and existing biomaterials to reconstruct complex bone defects (Shanbhag et al., 2019). Conventional tissue engineering strategies involve the transplantation of autologous adult mesenchymal stromal cells (MSC)—usually from the bone marrow (BMSC), in combination with biomaterial scaffolds and/or signaling molecules at bone defect sites. However, certain limitations of this approach have been discussed. Firstly, in a recent meta-analysis, we found the clinical evidence for the effectiveness of this strategy to be limited; the effect sizes of cell therapy over traditional GBR or grafting procedures were relatively small and mainly limited to studies of maxillary sinus augmentation (Shanbhag et al., 2019). Secondly, large scale translation of autologous cell therapy is limited by the need for expensive Good Manufacturing Practice (GMP) grade laboratories for *ex vivo* cell expansion for each patient/production. Thirdly, the traditional hypothesis that MSC exert their bioactivity *via* engraftment, differentiation, and replacement at injury sites, has in recent years been challenged by evidence of a predominantly paracrine mechanism of action (Haumer et al., 2018).

It is now widely believed that MSC exert their effects *via* the secretion of a wide range of bioactive factors, including soluble proteins (growth factors, cytokines, chemokines), nucleic acids and microparticles [extracellular vesicles (EV)] at or near sites of injury (Gnecchi et al., 2016). These factors in turn stimulate tissue-resident progenitor (osteogenesis), endothelial (angiogenesis) and immune cells (immune modulation), to drive subsequent regeneration processes. Moreover, pre-conditioning or "priming" of MSC with various stimulants (growth factors, inflammatory cytokines, etc.) may further enhance their paracrine activity and immunomodulatory potential (Ferreira et al., 2018). These findings provide the biological basis for the development of "cell-free" strategies, which exploit the secretome contained in MSC conditioned media (CM) for tissue regeneration. A major advantage of this strategy is the possibility to produce secretomes on a large scale from a single (or limited) cell expansion cycle(s), and to use these factors as "off-the-shelf" products. The preclinical efficacy of MSC secretomes/CM for bone regeneration has recently been summarized (Veronesi et al., 2018; Benavides-Castellanos et al., 2020).

A critical aspect in the clinical translation of cell therapies is the use of safe and standardized culture conditions resulting in safe-to-use cell constructs. Exclusion of animal-derived supplements, e.g., fetal bovine serum (FBS), in *ex vivo* culture systems is considered important to facilitate clinical translation of cell therapies and is also a recommendation by regulatory health authorities (Bieback et al., 2019). This consideration may also be extended to cell-derivatives such as CM. Pooled human platelet lysate (HPL) has been identified as the optimal "xeno-free" supplement for MSC culture, with particular benefits for MSC osteogenic differentiation (Fekete et al., 2012; Shanbhag et al., 2017). We have recently reported that HPL-cultured MSC demonstrate superior proliferation, osteogenic gene expression and *in vitro* mineralization vs. corresponding FBS-cultured cells (Shanbhag et al., 2020a; Shanbhag et al., 2020b). Indeed, the type of supplement used to culture MSC can influence the composition and efficacy of their CM (Madrigal et al., 2014; Nikolits et al., 2021). In context, few studies have assessed the composition of CM from HPL-cultured MSC or compared the composition of CM from HPL- vs. FBS-cultured MSC (Kehl et al., 2019; Palombella et al., 2020; Kim et al., 2021). Several growth factors related to wound healing, angiogenesis and extra-cellular matrix production were found to be more abundant in the CM of HPL- vs. FBS-cultured BMSC (Kim et al., 2021). Thus, based on these data, it is reasonable to hypothesize that CM from HPL-cultured MSC may be more enriched and potentially pro-osteogenic.

In the context of bone tissue engineering, the efficacy of CM is often studied *in vitro via* its effects on MSC proliferation and osteogenic differentiation. In this regard, previous studies reported that CM promotes MSC osteogenic differentiation; CM in most cases, was derived from FBS-cultured MSC and applied on cells of rodent origin (see review Veronesi et al., 2018). However, for *in vitro* assays, CM is usually supplemented with serum since CM alone does not support longer term cell culture. For differentiation assays, usually lasting 14–21 days, CM is supplemented with both serum and osteogenesis-inducing supplements, i.e., L-ascorbic acid 2-phosphate, dexamethasone and/or β glycerophosphate, in various concentrations (Brauer et al., 2016). To our knowledge, no studies have tested the effects of CM from HPL-cultured human MSC on the osteogenic differentiation of human MSC, which would more closely simulate a clinical scenario. As previously discussed, it is reasonable to hypothesize that CM from HPL-cultured MSC may have pro-osteogenic effects. Thus, the main objective of this preliminary study was to investigate the effects of pooled CM derived from HPL-cultured human BMSC of multiple donors on the *in vitro* proliferation and osteogenic differentiation of allogeneic (different donor) BMSC. A secondary objective was to assess the need for additional supplementation and/or osteogenic stimulation in the *in vitro* assays.

Methods

Cell culture

The use of human cells and tissues was approved by the Regional Committees for Medical Research Ethics (REK) in Norway (2013-1248/REK-sør-øst and 2016-1266/REK-nord). Bone marrow specimens were obtained following parental consent from five independent donors (2 females and 3 males; 8–10 years) undergoing reconstructive surgery at the Department of Plastic Surgery, Haukeland University Hospital, Bergen, Norway; BMSC were isolated and expanded following previous protocols (Shanbhag et al., 2020b). Briefly, cells were cultured in T75 or T175 flasks (Thermo Fisher Scientific, Carlsbad, CA, United States) using sterile filtered growth media (GM) comprising of Dulbecco's Modified Eagle's medium (DMEM, Invitrogen, Carlsbad, CA, United States) supplemented with 5% (v/v) pooled human platelet lysate (HPL; Bergenlys, Bergen, Norway), 1% (v/v) penicillin/streptomycin (GE Healthcare, South Logan, UT, United States) and 1 IU/ml heparin (Leo Pharma AS, Lysaker, Norway). HPL was produced 'in-house' as described elsewhere (Shanbhag et al., 2020b). Cells were sub-cultured and expanded under standard incubation, i.e., 37°C and 5% CO_2, according to a clinically validated protocol with a seeding density of 4000 cells/cm^2 (Rojewski et al., 2019). Passage 1 (p1) and 2 (p2) BMSC were characterized based on immunophenotype and multi-lineage differentiation potential as previously reported (Shanbhag et al., 2020b), and used for CM preparation. In indicated experiments, BMSC from two separate donors (different from those used for CM preparation) were used to study the paracrine effects of CM. BMSC (p2) were seeded in 12-well plates (4000 cells/cm^2) and exposed to CM for various durations in proliferation and differentiation assays. Cell attachment and morphology were regularly monitored under a light microscope (Nikon Eclipse TS100, Tokyo, Japan).

Conditioned media preparation

CM was prepared from BMSC of three independent donors, as previously described (Al-Sharabi et al., 2017). Briefly, p1 and p2 BMSC were expanded in T175 flasks in GM until 70%–80% confluency under standard incubation. At this point, cells were washed three times with phosphate-buffered saline (PBS; Invitrogen) and then cultured in plain DMEM (without HPL or antibiotics) for another 48 h. After 48 h, CM from p1 and p2 BMSC from each of the three donors was collected, pooled, and centrifuged at 4000× *g* for 10 min to remove any debris. The supernatant was aliquoted and stored at −80°C. For all experiments, CM from −80°C storage was thawed overnight at 4°C and sterile filtered (0.2 μm) before use.

DNA quantification and alkaline phosphatase activity assays

BMSC were seeded in 24-well plates at a density of 4000 cells/cm^2 and cultured in GM. After 24 h, corresponding wells were washed with PBS and exposed to CM or CM-HPL (1% HPL); the concentration of HPL was adjusted in comparison to GM (5% HPL) to avoid overconfluency after 24 h. After 3 and 7 days, cells were lysed in 0.1% Triton X-100 (Sigma Aldrich) and DNA quantification and ALP activity assay were performed using the Quant-IT® PicoGreen dsDNA Assay Kit (Thermo Fisher Scientific) and SIGMAFAST BCIP/NBT assay (Sigma-Aldrich), respectively, according to manufacturers' instructions. DNA concentrations (ng/ml), calculated based on known standards, were used to normalize ALP activity of the corresponding cell-lysates.

TABLE 1 Real time qPCR primers.

Gene (human)	TaqMan® assay ID	Amplicon length
References		
GAPDH	Hs 02758991_g1	93
Osteogenesis-related		
RUNX2	Hs01047973_m1	86
COL1A2	Hs00164099_m1	68
OPN (SPP1)	Hs00959010_m1	84
OCN (BGLAP)	Hs01587814_g1	138

GAPDH glyceraldehyde 3-phosphate dehydrogenase, RUNX2 runt-related transcription factor 2, COL1A2 Collagen type 1 alpha 2, OPN/SPP1 osteopontin, OCN/BGLAP osteocalcin.

Gene expression analysis

Expressions of osteogenesis-related genes (Table 1) were assessed after 2 and 7 days *via* quantitative real-time polymerase chain reaction (qPCR) using TaqMan® real-time PCR assays (Thermo Scientific). BMSC in GM were seeded in 12-well plates; after 24 h, corresponding wells were washed with PBS and exposed to different media formulations: GM, CM alone (CM) and CM supplemented with 5% HPL (CM-PL). RNA extraction and cDNA synthesis were performed as previously described (Mohamed-Ahmed et al., 2018) and expressions of genes of interest were normalized to that of a reference gene—glyceraldehyde 3-phosphate dehydrogenase (GAPDH). Data were analyzed by the ΔΔCt method and results are presented as fold changes relative to the reference group (GM) on a log(2)-transformed scale.

In vitro mineralization assay

In vitro mineralization was assessed using the Alizarin red-S assay. BMSC in GM were seeded in 12-well plates; after 24 h, corresponding wells were washed with PBS and exposed to different media formulations with osteogenic induction supplements: growth media (GM+), CM (CM+) and CM with 5% HPL (CM-PL+). To induce osteogenic differentiation, media were supplemented with final

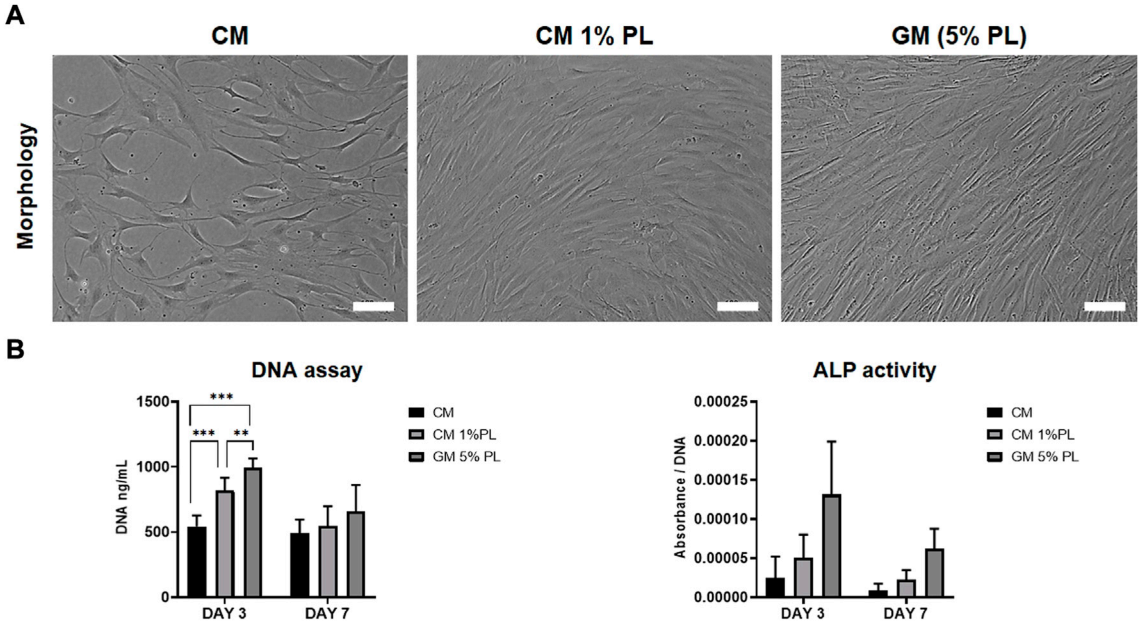

FIGURE 1
Proliferation and ALP activity. **(A)** Representative images of BMSC cultured in CM, CM supplemented with HPL (1% PL) or growth media (5% PL; control) after 3 days, scale bars 100 μm. **(B)** Quantification of total DNA (fluorescence) and ALP activity (absorbance) in BMSC cultured in CM, CM+1% PL and GM after 3 and 7 days (*n* = 2 donors; 3 experimental replicates per donor); $^{**}p < 0.005$, $^{***}p < 0.001$.

concentrations of 0.05 mM L-ascorbic acid 2-phosphate, 10 nM dexamethasone and 10 mM β glycerophosphate (all from Sigma-Aldrich, St. Louis, MO, United States). Additionally, the following groups were included: CM supplemented with 2.5% HPL and osteogenic supplements and CM supplemented with 10% FBS and osteogenic supplements (CM-FBS+). After 14 days, formation of extracellular calcium deposits was assessed *via* Alizarin red S staining, as previously described (Mohamed-Ahmed et al., 2018). Briefly, after fixation with 4% paraformaldehyde, cells were stained with 2% Alizarin red S solution (Sigma Aldrich) for 30 min at RT, then washed and dried, before images were acquired.

Statistical analysis

Statistical analysis was performed using the Prism 9 software (GraphPad Software, San Diego, CA, United States). Data are presented as means (± SD and/or range), unless specified. All linear data are presented as bar graphs. Normality testing was performed *via* the Shapiro-Wilk test. The student *t* test, Mann-Whitney U test, one-way analysis of variance (ANOVA; followed by a *post hoc* Tukey's test) or Kruskal-Wallis test (followed by a *post hoc* Dunn's test) were applied as appropriate, and $p < 0.05$ was considered as statistically significant.

Results

Conditioned media supplemented with platelet lysate did not enhance cell proliferation

The *in vitro* paracrine effects of CM were evaluated *via* proliferation and ALP activity assays using BMSC from two independent donors. DNA content of BMSC was lower in CM vs. GM (5% HPL) after 3 ($p < 0.001$) and 7 days ($p > 0.05$); supplementation of CM with 1% HPL did not attenuate this difference at 3 days (Figures 1A,B). A similar trend was observed for ALP activity between the groups, although without statistical significance (Figure 1B).

Conditioned media supplemented with platelet lysate did not enhance osteogenic gene expression

After 2 d, compared to the reference group (GM), expressions of selected osteogenesis related genes, i.e., runt-related transcription factor 2 (RUNX2), collagen type 1A (COLIA), and osteopontin (SPP1/OPN), were significantly upregulated in BMSC exposed to CM alone after 2 and 7 days ($p < 0.05$ for all genes; Figures 2A,B). In particular, expression of SPP1/OPN was remarkably upregulated in CM. Expression of

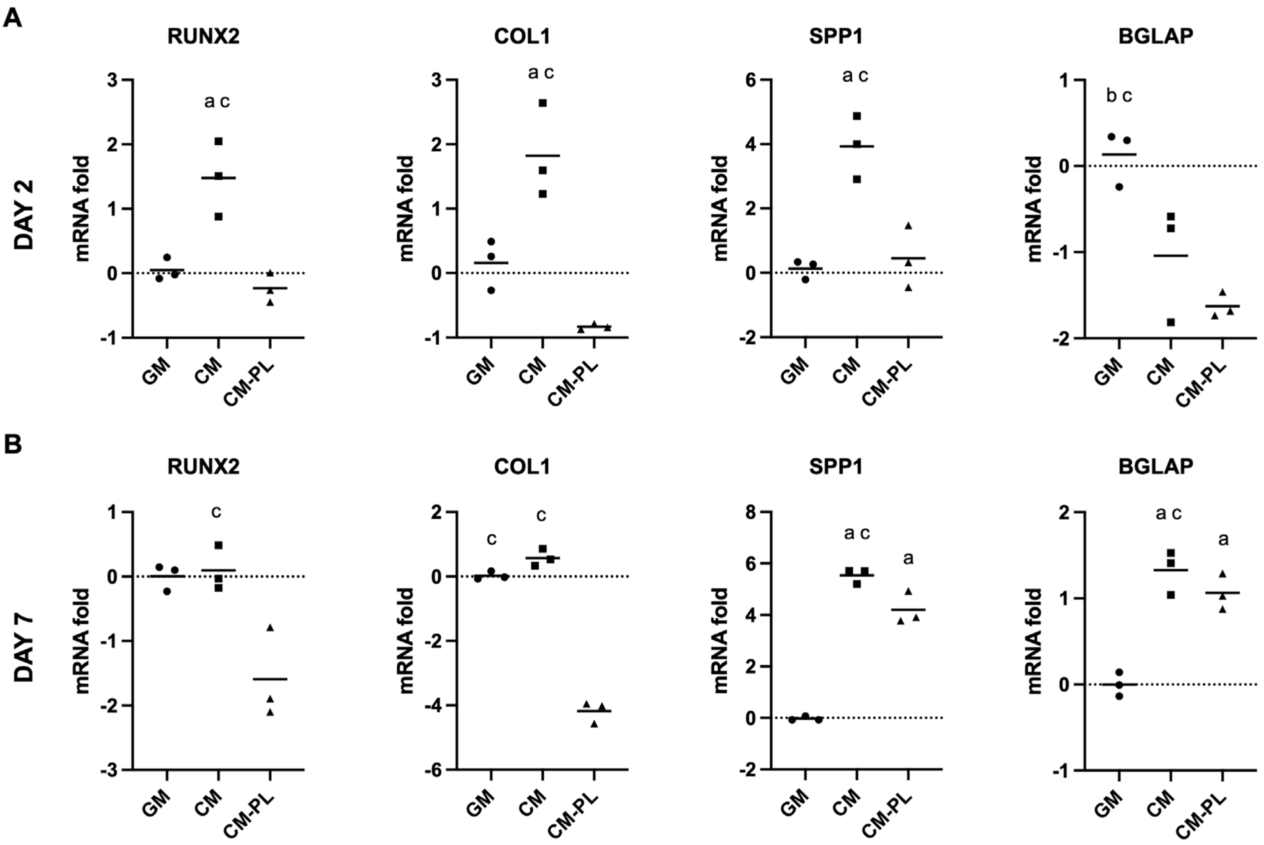

FIGURE 2
Osteogenic gene expression. Relative mRNA fold changes in BMSC after 2 **(A)** and 7 days **(B)**. Data indicate means of 3 experimental replicates for BMSC from one representative donor [Log(2)-transformed y-axis; negative values indicate gene downregulation]. Significance ($p < 0.05$) is denoted by alphabetical letterings: a, compared to GM; b, compared to CM; c, compared to CM-PL; GM, growth media; CM, conditioned media; conditioned media with platelet lysate.

osteocalcin (BGLAP/OCN) was upregulated only after 7 days. When CM was supplemented with HPL (CM-PL), gene expression was either unchanged or downregulated compared to standard GM after 2 days. After 7 days, expressions of SPP1 and BGLAP were upregulated also in CM-PL (Figure 2B).

Conditioned media supplemented with platelet lysate did not promote *in vitro* mineralization

Initially, for the *in vitro* mineralization assay, BMSC were exposed to CM alone or CM supplemented 5% HPL, both with osteogenic stimulants. After 14 days, no mineralization was observed in any of the test groups (Figure 3). Reduction of HPL concentration (from 5% to 2.5%) did not affect the results (data not shown). However, supplementation of CM with 10% FBS (CM-FBS+) revealed *in vitro* mineralization of BMSC comparable to the positive GM control (Figure 3).

Discussion

Since HPL-cultured MSC demonstrate enhanced osteogenic differentiation and the CM of HPL-cultured MSC is more enriched than their FBS-cultured counterparts, the present study hypothesized that the CM of HPL-cultured BMSC has pro-osteogenic effects, i.e., the use of such CM could possibly reduce the need for additional serum/supplementation and/or osteogenic stimulation. Although previous studies have reported that CM promotes MSC osteogenic differentiation (Veronesi et al., 2018; Zhong et al., 2019), these have mainly assessed the effects of CM derived from FBS-cultured cells on MSC of non-human origin. Thus, little is known about the effects of CM from HPL-cultured MSC on allogeneic MSC of human origin. Such an *in vitro* setup would more closely simulate a clinical scenario of CM application, since: 1) current regulations recommend substitution of animal derivatives such as FBS in clinical-grade MSC cultures; and 2) CM would most likely be used as an allogeneic (pooled from multiple donors) "off-the-

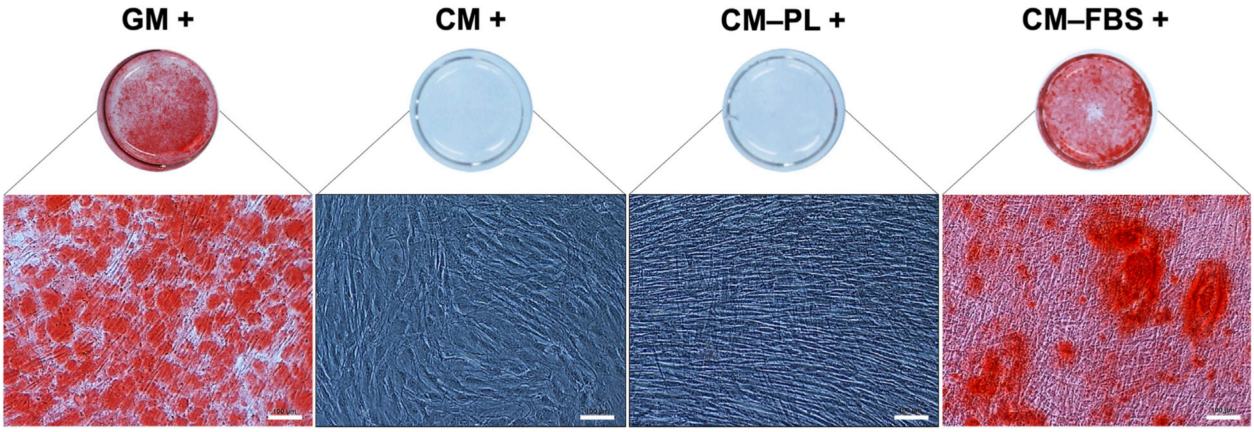

FIGURE 3
In vitro mineralization assay. Representative images of Alizarin red S stained BMSC after 14 days (*n* = 2 donors; 3 experimental replicates per donor), scale bars 100 μm. +, osteogenic induction added; GM, growth media; CM, conditioned media, PL, platelet lysate; FBS, fetal bovine serum.

shelf" product. Therefore, the objective of this preliminary study was to investigate the effects of CM derived from HPL-cultured MSC (pooled CM from multiple donors) on the *in vitro* osteogenic differentiation of allogeneic (different donors) human MSC. The main findings were that: 1) CM alone promoted osteogenic gene expression, but not *in vitro* mineralization of BMSC, and 2) CM supplemented with HPL promoted neither osteogenic gene expression nor *in vitro* mineralization of BMSC.

In the present study, we investigated the influence of CM supplemented with different concentrations of HPL on the *in vitro* proliferation and osteogenic differentiation of BMSC. We observed that pure CM (without HPL) did not have positive effects on BMSC proliferation and *in vitro* mineralization, despite promoting significant upregulation of several osteogenesis-related genes. In previous studies, we showed that HPL-cultured MSC have an enhanced capacity for osteogenic differentiation (Shanbhag et al., 2020a; Shanbhag et al., 2020b). Therefore, we hypothesized that the secretomes of HPL-cultured BMSC (contained in CM) might have a stimulatory effect on cellular metabolic activity and osteogenic differentiation. However, based on the results herein, it seems that CM alone without added supplements (HPL/FBS) might impair the cultured BMSC *via* nutrient deprivation, thus reducing their metabolic activity and functions (Nuschke et al., 2016). It has also been reported that the "serum starvation" method used to collect CM might be associated with the lower content of the specific growth factors with metabolic activity in CM, e.g., hepatocyte growth factor (HGF), brain-derived neurotrophic factor (BDNF), and fibroblast growth factor 2 (FGF-2) (Petrenko et al., 2020). Further investigations to determine the effects of collection methods on the composition and concentrations of secreted molecules in CM are needed.

Cell metabolism and survival are controlled by the action of growth factors and cytokines through inhibition of apoptosis or promotion of cell survival. In previous studies, we have shown that CM from FBS-cultured BMSC contains several growth factors and cytokines with antiapoptotic and antioxidant properties, including platelet-derived growth factor (PDGF) and vascular endothelial growth factor A (VEGFA), and enhances *in vitro* osteogenic differentiation of MSC (Al-Sharabi et al., 2014; Al-Sharabi et al., 2016; Saleem et al., 2021). In context, HPL also contains several growth factors and cytokines, including PDGF, epidermal growth factor (EGF), insulin-like growth factor (IGF), transforming growth factor (TGF), FGF2, stem cell-growth factor-beta (SCGF), interleukin (IL)-1β, IL-2, -6, -10, -12p70, and IL-17A, tumor necrosis factor (TNF)-α and interferon (IFN) (Cañas-Arboleda et al., 2020; Shanbhag et al., 2020a). Therefore, it is reasonable to postulate that CM of HPL-cultured MSC would be correspondingly more enriched. Indeed, in a recent study, the concentrations of important growth factors such as VEGF, TGF-β1, and HGF were found to be significantly greater in the CM of HPL- vs. FBS-cultured MSC (Kim et al., 2021). However, we found that proliferation and osteogenic differentiation rates were insufficient in BMSC treated with 5% vs. 1% HPL-supplemented CM; a 5% concentration was selected based on current recommendations for HPL supplementation for *ex vivo* MSC expansion (Becherucci et al., 2018).

Regarding osteogenic differentiation, previous studies have reported that CM increased osteogenic differentiation and mineralization of MSC in a paracrine manner (Ogata et al., 2015; Zhong et al., 2019). However, most studies have not adequately addressed whether CM alone exerts this effect or whether the addition of FBS or HPL, with or without osteogenic supplements, is necessary. Such information would be important to standardize experimental setups and compare the results across different *in vitro* studies. In the present study, we found that pure CM stimulates neither ALP activity nor *in vitro* mineralization, as detected by Alizarin red staining. This was in line with a study conducted to evaluate proliferation and differentiation of osteoblasts under the induction of different concentrations of CM (Sun et al., 2012). When 1% HPL was added to CM, a slight improvement in ALP activity was detected although this was not equivalent to the control, i.e., GM containing 5% HPL. CM also promoted the expression of osteogenesis-related genes in BMSC, although this effect appears to be insufficient to stimulate *in vitro* mineralization, as no mineralization nodules were detected after 14 days. Thus, despite CM-induced gene upregulation in BMSC (without osteogenic supplementation), the impairment in promoting mineralization (with or without osteogenic supplementation) potentially reflects the safety of using BMSC as sources for CM production for different applications rather than specifically for bone regeneration.

In the context of osteogenic differentiation, we have previously reported that HPL supplementation alone (vs. FBS) enhances the expression of osteogenesis-related genes in MSC, suggesting particular benefits of HPL-supplemented MSC expansion for bone tissue engineering (Shanbhag et al., 2020a). Indeed, in the present study, exposure to CM resulted in an upregulation of osteogenic genes which was greater than that of HPL supplementation. However, the combination of HPL and CM did not exert a synergistic effect in terms of BMSC gene expression. This might indicate that a certain concentration of HPL together with CM might only allow the maintenance of the original microenvironment in BMSC, possibly *via* reduction of overexposure to cytokines and other stimulatory factors (Kandoi et al., 2018). On the contrary, the combination of CM and HPL may have antagonistic effects, which may distort the positive biological activity of CM. Therefore, future molecular research is warranted to study the effects of different combinational ratios of CM and HPL *in vitro* osteogenic differentiation of MSC (Aghamohamadi et al., 2020). Moreover, while the present study focused on osteogenic stimulatory capacity, other pathways of CM bioactivity, particularly angiogenesis (Quade et al., 2020) and immune-modulation (Jin et al., 2022), are also highly relevant for bone regeneration.

Some limitations of the present preliminary study must be acknowledged. The objective herein was to test the hypothesis that CM from HPL-cultured MSC may have pro-osteogenic effects, and not to compare per se CM from HPL- vs. FBS-cultured MSC or the osteogenic effects of CM supplemented with HPL vs. FBS. Therefore, we did not include FBS supplemented CM as a control group in all experiments, but only in the *in vitro* mineralization assay. Secondly, although the CM used herein was produced and pooled from multiple BMSC donors ($n = 3$), which is clinically relevant in terms of scaling up production and minimizing individual donor variations, the number of allogeneic BMSC donors for the *in vitro* assays was limited ($n = 2$). It is well known that BMSC may demonstrate significant donor-related variations in their growth and differentiation potential (Al-Sharabi et al., 2017) and therefore, the experiments should be repeated with BMSC from additional donors to validate the findings. Lastly, in this preliminary study, we did not perform any mechanistic assays, e.g., identification of specific signaling pathways, to determine the molecular basis for reduced mineralization in CM, with or without additional supplements. This would be relevant mainly for future *in vitro* assessments of MSC responses to CM to potentially predict (within the limitations of *in vitro* models) the *in vivo* effects of CM for bone regeneration. Clear descriptions of *in vitro* experimental setups, i.e., addition of serum/supplements and osteogenic stimulants, in future studies of CM efficacy are warranted to allow standardization and comparison of data.

Conclusion

In summary, pooled CM from HPL-cultured human BMSC promoted osteogenic gene expression but not *in vitro* mineralization in allogeneic BMSC, even when supplemented with HPL and/or osteogenic stimulants. The role and relevance of CM supplementation and osteogenic stimulation in *in vitro* assays should be investigated in future studies to better understand the underlying molecular mechanisms and allow standardized comparisons of results.

Data availability statement

The original contributions presented in the study are included in the article/Supplementary Material, further inquiries can be directed to the corresponding author.

Ethical statement

The use of human cells and tissues was approved by the Regional Committees for Medical Research Ethics (REK) in Norway (2013-1248/REK-sør-øst and 2016-1266/REK-nord).

Author contributions

SS and NA-S conceived and designed the study. SS performed the experiments, data collection, data analysis and drafted the manuscript. NA-S and SM-A assisted with experiments, sample preparation, data collection, data analysis/interpretation and/or drafting the manuscript. RG, EK, and KM assisted with data analysis/interpretation, drafting the manuscript and funding acquisition. All authors read and approved the final version of the manuscript.

Funding

This work was supported by the Osteology Foundation, Switzerland (18-152), Helse Vest Research Funding, Norway (F-12124), and Trond Mohn Foundation, Norway (BFS2018TMT10).

Acknowledgments

We thank the Bloodbank at Haukeland University Hospital for assistance with HPL production.

Conflict of interest

The authors declare that the research was conducted in the absence of any commercial or financial relationships that could be construed as a potential conflict of interest.

Publisher's note

References

Aghamohamadi, Z., Kadkhodazadeh, M., Torshabi, M., and Tabatabaei, F. (2020). A compound of concentrated growth factor and periodontal ligament stem cell-derived conditioned medium. *Tissue Cell* 65, 101373. doi:10.1016/j.tice.2020.101373

Al-Sharabi, N., Mustafa, M., Ueda, M., Xue, Y., Mustafa, K., and Fristad, I. (2017). Conditioned medium from human bone marrow stromal cells attenuates initial inflammatory reactions in dental pulp tissue. *Dent. Traumatol.* 33 (1), 19–26. doi:10.1111/edt.12277

Al-Sharabi, N., Xue, Y., Fujio, M., Ueda, M., Gjerde, C., Mustafa, K., et al. (2014). Bone marrow stromal cell paracrine factors direct osteo/odontogenic differentiation of dental pulp cells. *Tissue engineering.Part A* 20 (21-22), 3063–3072. doi:10.1089/ten.TEA.2013.0718

Al-Sharabi, N., Xue, Y., Udea, M., Mustafa, K., and Fristad, I. (2016). Influence of bone marrow stromal cell secreted molecules on pulpal and periodontal healing in replanted immature rat molars. *Dent. Traumatol.* 32 (3), 231–239. doi:10.1111/edt.12246

Becherucci, V., Piccini, L., Casamassima, S., Bisin, S., Gori, V., Gentile, F., et al. (2018). Human platelet lysate in mesenchymal stromal cell expansion according to a GMP grade protocol: A cell factory experience. *Stem Cell Res. Ther.* 9 (1), 124. doi:10.1186/s13287-018-0863-8

Benavides-Castellanos, M. P., Garzon-Orjuela, N., and Linero, I. (2020). Effectiveness of mesenchymal stem cell-conditioned medium in bone regeneration in animal and human models: A systematic review and meta-analysis. *Cell Regen.* 9 (1), 5. doi:10.1186/s13619-020-00047-3

Bieback, K., Fernandez-Munoz, B., Pati, S., and Schafer, R. (2019). Gaps in the knowledge of human platelet lysate as a cell culture supplement for cell therapy: A joint publication from the AABB and the, international society for cell & gene therapy. *Transfusion* 59, 3448–3460. doi:10.1111/trf.15483

Brauer, A., Pohlemann, T., and Metzger, W. (2016). Osteogenic differentiation of immature osteoblasts: Interplay of cell culture media and supplements. *Biotech. Histochem.* 91 (3), 161–169. doi:10.3109/10520295.2015.1110254

Cañas-Arboleda, M., Beltrán, K., Medina, C., Camacho, B., and Salguero, G. (2020). Human platelet lysate supports efficient expansion and stability of wharton's jelly mesenchymal stromal cells via active uptake and release of soluble regenerative factors. *Int. J. Mol. Sci.* 21, 6284. doi:10.3390/ijms21176284

Fekete, N., Gadelorge, M., Furst, D., Maurer, C., Dausend, J., Fleury-Cappellesso, S., et al. (2012). Platelet lysate from whole blood-derived pooled platelet concentrates and apheresis-derived platelet concentrates for the isolation and expansion of human bone marrow mesenchymal stromal cells: Production process, content and identification of active components. *Cytotherapy* 14 (5), 540–554. doi:10.3109/14653249.2012.655420

Ferreira, J. R., Teixeira, G. Q., Santos, S. G., Barbosa, M. A., Almeida-Porada, G., and Goncalves, R. M. (2018). Mesenchymal stromal cell secretome: Influencing therapeutic potential by cellular pre-conditioning. *Front. Immunol.* 9, 2837. doi:10.3389/fimmu.2018.02837

Gnecchi, M., Danieli, P., Malpasso, G., and Ciuffreda, M. C. (2016). Paracrine mechanisms of mesenchymal stem cells in tissue repair. *Methods Mol. Biol.* 1416, 123–146. doi:10.1007/978-1-4939-3584-0_7

Haumer, A., Bourgine, P. E., Occhetta, P., Born, G., Tasso, R., and Martin, I. (2018). Delivery of cellular factors to regulate bone healing. *Adv. Drug Deliv. Rev.* 129, 285–294. doi:10.1016/j.addr.2018.01.010

Jin, Q. H., Kim, H. K., Na, J. Y., Jin, C., Seon, J. K., Kim, H. K., et al. (2022). Anti-inflammatory effects of mesenchymal stem cell-conditioned media inhibited macrophages activation *in vitro*. *Sci. Rep.* 12, 4754. doi:10.1038/s41598-022-08398-4

Kandoi, S., Praveen.kumar, L., Patra, B., Vidyasekar, P., Sivanesan, D., Vijayalakshmi, S., et al. (2018). Evaluation of platelet lysate as a substitute for FBS in explant and enzymatic isolation methods of human umbilical cord MSCs. *Sci. Rep.* 8 (1), 12439. doi:10.1038/s41598-018-30772-4

Kehl, D., Generali, M., Mallone, A., Heller, M., Uldry, A. C., Cheng, P., et al. (2019). Proteomic analysis of human mesenchymal stromal cell secretomes: A systematic comparison of the angiogenic potential. *npj Regen. Med.* 4, 8. doi:10.1038/s41536-019-0070-y

Kim, S. N., Lee, C. J., Nam, J., Choi, B., Chung, E., and Song, S. U. (2021). The effects of human bone marrow-derived mesenchymal stem cell conditioned media produced with fetal bovine serum or human platelet lysate on skin rejuvenation characteristics. *Int. J. Stem Cells* 14 (1), 94–102. doi:10.15283/ijsc20070

Madrigal, M., Rao, K. S., and Riordan, N. H. (2014). A review of therapeutic effects of mesenchymal stem cell secretions and induction of secretory modification by different culture methods. *J. Transl. Med.* 11, 260. doi:10.1186/s12967-014-0260-8

Mohamed-Ahmed, S., Fristad, I., Lie, S. A., Suliman, S., Mustafa, K., Vindenes, H., et al. (2018). Adipose-derived and bone marrow mesenchymal stem cells: A donor-matched comparison. *Stem Cell Res. Ther.* 9 (1), 168. doi:10.1186/s13287-018-0914-1

Nikolits, I., Nebel, S., Egger, D., Kress, S., and Kasper, C. (2021). Towards physiologic culture approaches to improve standard cultivation of mesenchymal stem cells. *Cells* 10 (4), 886. doi:10.3390/cells10040886

Nuschke, A., Rodrigues, M., Wells, A. W., Sylakowski, K., and Wells, A. (2016). Mesenchymal stem cells/multipotent stromal cells (MSCs) are glycolytic and thus glucose is a limiting factor of *in vitro* models of MSC starvation. *Stem Cell Res. Ther.* 7 (1), 179. doi:10.1186/s13287-016-0436-7

Ogata, K., Katagiri, W., Osugi, M., Kawai, T., Sugimura, Y., Hibi, H., et al. (2015). Evaluation of the therapeutic effects of conditioned media from mesenchymal stem cells in a rat bisphosphonate-related osteonecrosis of the jaw-like model. *Bone.* 74, 95–105. doi:10.1016/j.bone.2015.01.011

Palombella, S., Guiotto, M., Higgins, G. C., Applegate, L. L., Raffoul, W., Cherubino, M., et al. (2020). Human platelet lysate as a potential clinical-translatable supplement to support the neurotrophic properties of human adipose-derived stem cells. *Stem Cell Res. Ther.* 11 (1), 432. doi:10.1186/s13287-020-01949-4

Petrenko, Y., Vackova, I., Kekulova, K., Chudickova, M., Koci, Z., Turnovcova, K., et al. (2020). A comparative analysis of multipotent mesenchymal stromal cells derived from different sources, with a focus on neuroregenerative potential. *Sci. Rep.* 10 (1), 4290. doi:10.1038/s41598-020-61167-z

Quade, M., Munch, P., Lode, A., Duin, S., Vater, C., Gabrielyan, A., et al. (2020). The secretome of hypoxia conditioned hMSC loaded in a central depot induces chemotaxis and angiogenesis in a biomimetic mineralized collagen bone replacement material. *Adv. Healthc. Mat.* 9 (2), e1901426. doi:10.1002/adhm.201901426

Rojewski, M. T., Lotfi, R., Gjerde, C., Mustafa, K., Veronesi, E., Ahmed, A. B., et al. (2019). Translation of a standardized manufacturing protocol for mesenchymal stromal cells: A systematic comparison of validation and manufacturing data. *Cytotherapy* 21 (4), 468–482. doi:10.1016/j.jcyt.2019.03.001

Saleem, R., Mohamed-Ahmed, S., Elnour, R., Berggreen, E., Mustafa, K., and Al-Sharabi, N. (2021). Conditioned medium from bone marrow mesenchymal stem cells restored oxidative stress-related impaired osteogenic differentiation. *Int. J. Mol. Sci.* 22 (24), 13458. doi:10.3390/ijms222413458

Shanbhag, S., Mohamed-Ahmed, S., Lunde, T. H. F., Suliman, S., Bolstad, A. I., Hervig, T., et al. (2020a). Influence of platelet storage time on human platelet lysates and platelet lysate-expanded mesenchymal stromal cells for bone tissue engineering. *Stem Cell Res. Ther.* 11 (1), 351. doi:10.1186/s13287-020-01863-9

Shanbhag, S., Stavropoulos, A., Suliman, S., Hervig, T., and Mustafa, K. (2017). Efficacy of humanized mesenchymal stem cell cultures for bone tissue engineering: A systematic review with a focus on platelet derivatives. *Tissue Eng. Part B Rev.* 23, 552–569. doi:10.1089/ten.teb.2017.0093

Shanbhag, S., Suliman, S., Bolstad, A. I., Stavropoulos, A., and Mustafa, K. (2020b). Xeno-free spheroids of human gingiva-derived progenitor cells for bone tissue engineering. *Front. Bioeng. Biotechnol.* 8, 968. doi:10.3389/fbioe.2020.00968

Shanbhag, S., Suliman, S., Pandis, N., Stavropoulos, A., Sanz, M., and Mustafa, K. (2019). Cell therapy for orofacial bone regeneration: A systematic review and meta-analysis. *J. Clin. Periodontol.* 46 (21), 162–182. doi:10.1111/jcpe.13049

Sun, J., Zhou, H., Deng, Y., Zhang, Y., Gu, P., Ge, S., et al. (2012). Conditioned medium from bone marrow mesenchymal stem cells transiently retards osteoblast differentiation by downregulating runx2. *Cells Tissues Organs* 196 (6), 510–522. doi:10.1159/000339245

Veronesi, F., Borsari, V., Sartori, M., Orciani, M., Mattioli-Belmonte, M., and Fini, M. (2018). The use of cell conditioned medium for musculoskeletal tissue regeneration. *J. Cell. Physiol.* 233 (6), 4423–4442. doi:10.1002/jcp.26291

Zhong, S., He, X., Li, Y., and Lou, X. (2019). Conditioned medium enhances osteogenic differentiation of induced pluripotent stem cell-derived mesenchymal stem cells. *Tissue Eng. Regen. Med.* 16 (2), 141–150. doi:10.1007/s13770-018-0173-3

frontiers | Frontiers in Bioengineering and Biotechnology

TYPE Original Research
PUBLISHED 06 December 2022
DOI 10.3389/fbioe.2022.971932

OPEN ACCESS

EDITED BY
Anna Lange-Consiglio,
University of Milan, Italy

REVIEWED BY
Ryan Michael Porter,
University of Arkansas for Medical Sciences, United States
Annunziata Mauro,
University of Teramo, Italy

*CORRESPONDENCE
David A. Lee,
d.a.lee@qmul.ac.uk

SPECIALTY SECTION
This article was submitted to Tissue Engineering and Regenerative Medicine, a section of the journal Frontiers in Bioengineering and Biotechnology

RECEIVED 17 June 2022
ACCEPTED 18 November 2022
PUBLISHED 06 December 2022

CITATION
Heywood HK, Thorpe SD, Jeropoulos RM, Caton PW and Lee DA (2022), Modulation of sirtuins during monolayer chondrocyte culture influences cartilage regeneration upon transfer to a 3D culture environment. *Front. Bioeng. Biotechnol.* 10:971932. doi: 10.3389/fbioe.2022.971932

Modulation of sirtuins during monolayer chondrocyte culture influences cartilage regeneration upon transfer to a 3D culture environment

Hannah K. Heywood[1], Stephen D. Thorpe[1,2,3], Renos M. Jeropoulos[4], Paul W. Caton[5] and David A. Lee[1]*

[1]School of Engineering and Materials Science, Queen Mary University of London, London, United Kingdom, [2]UCD School of Medicine, UCD Conway Institute of Biomolecular and Biomedical Research, University College Dublin, Dublin, Ireland, [3]Trinity Centre for Biomedical Engineering, Trinity College Dublin, Dublin, Ireland, [4]Barts and the London School of Medicine and Dentistry, Queen Mary University of London, London, United Kingdom, [5]Department of Diabetes, School of Life Course Sciences, King's College London, London, United Kingdom

This study examined the role of sirtuins in the regenerative potential of articular chondrocytes. Sirtuins (SIRT1-7) play a key role in regulating cartilage homeostasis. By inhibiting pro-inflammatory pathways responsible for cartilage degradation and promoting the expression of key matrix components, sirtuins have the potential to drive a favourable balance between anabolic and catabolic processes critical to regenerative medicine. When subjected to osmolarity and glucose concentrations representative of the *in vivo* niche, freshly isolated bovine chondrocytes exhibited increases in *SIRT1* but not *SIRT3* gene expression. Replicating methods adopted for the *in vitro* monolayer expansion of chondrocytes for cartilage regenerative therapies, we found that *SIRT1* gene expression declined during expansion. Manipulation of sirtuin activity during *in vitro* expansion by supplementation with the SIRT1-specific activator SRT1720, nicotinamide mononucleotide, or the pan-sirtuin inhibitor nicotinamide, significantly influenced cartilage regeneration in subsequent 3D culture. Tissue mass, cellularity and extracellular matrix content were reduced in response to sirtuin inhibition during expansion, whilst sirtuin activation enhanced these measures of cartilage tissue regeneration. Modulation of sirtuin activity during monolayer expansion influenced H3K27me3, a heterochromatin mark with an important role in development and differentiation. Unexpectedly, treatment of primary chondrocytes with sirtuin activators in 3D culture reduced their matrix synthesis. Thus, modulating sirtuin activity during the *in vitro* monolayer expansion phase may represent a distinct opportunity to enhance the outcome of cartilage regenerative medicine techniques.

KEYWORDS

chondrocyte, cartilage tissue engineering, sirtuin, glucose restriction, pellet culture, nicotinamide adenine dinucleotide

1 Introduction

It is estimated that around 10,000 people in the United Kingdom each year experience cartilage damage that warrants treatment (NICE, 2017). If untreated, such cartilage injuries impair quality of life and increase the risk of osteoarthritis (OA). This has motivated the development of cell-based cartilage repair techniques such as autologous chondrocyte implantation (ACI) and evolving tissue engineering/regenerative medicine approaches (Brittberg et al., 1994; Huang et al., 2016). In many cell-based repair techniques chondrocytes are isolated from a cartilage biopsy and increased in number by maintaining the cells in monolayer culture, such that a much larger cell population can then be re-implanted into the defect to repair the cartilage. However, the capacity of cells to regenerate cartilage upon re-implantation progressively declines during *in vitro* culture due to the process of de-differentiation, with associated loss of expression of cartilage extracellular matrix (ECM) macromolecules such as type II collagen and aggrecan (Dell'Accio et al., 2001; Giovannini et al., 2010; Niemeyer et al., 2012). The development of methods that retain chondrocyte regenerative potential during monolayer culture would provide a major advance for cartilage repair techniques, potentially enhancing clinical outcomes (Saris et al., 2009; Niemeyer et al., 2012).

Sirtuins are a family of seven enzymes (SIRT1-7) which have been established to play a key role in regulating cartilage homeostasis. To date, most studies have focussed on SIRT1 and have revealed that SIRT1 protects against cartilage degradation through multiple mechanisms to delay the onset and progression of both age-associated and instability-linked OA (Matsuzaki et al., 2014). However, transcription and protein levels of SIRT1 decline during ageing and reduced SIRT1 levels correlate with increased severity of OA (Fujita et al., 2011; Li et al., 2016). Importantly, the genetic manipulation of SIRT1 expression has revealed a causal link between SIRT1 deficiency and OA disease progression in animal models (Gabay et al., 2013a; Gabay et al., 2013b). Further studies have demonstrated that SIRT3 and SIRT6 also promote cartilage health (Nagai et al., 2015; Wu et al., 2015; Fu et al., 2016), while a contrasting role was recently revealed for SIRT7 as a negative regulator of cartilage homeostasis, through suppression of the transcriptional activity of pro-chondrogenic SOX9 (Korogi et al., 2018).

The sirtuins are nicotinamide adenine dinucleotide (NAD)-dependent de-acetylases which target histones, transcription factors and enzymes to regulate cell behaviour. SIRT1 de-acetylates the pro-inflammatory nuclear factor-kappa B (NF-κB) transcription factor (Yeung et al., 2004; Lei et al., 2012), inactivating it and thereby inhibiting the pro-inflammatory pathways responsible for cartilage degradation mediated by matrix metalloproteinases (MMPs) and a disintegrin-like and metalloproteinases with thrombospondin motifs (ADAMTS) (Kiernan et al., 2003; Yeung et al., 2004; Matsushita et al., 2013; Moon et al., 2013; Elayyan et al., 2017). SIRT1 also transcriptionally suppresses the senescence marker p16 through epigenetic modification at the p16 promoter (Li and Tollefsbol, 2011) and downregulates pro-apoptotic proteins such as p53 to promote cell survival under stress (Luo et al., 2001; Vaziri et al., 2001; Takayama et al., 2009). Conversely, SIRT1-mediated de-acetylation activates the pro-chondrogenic transcription factor SOX9, promoting expression of key matrix components aggrecan and type II collagen (Dvir-Ginzberg et al., 2008; Fujita et al., 2011; Bar Oz et al., 2016). Thus, sirtuins have the potential to drive a favourable balance between anabolic and catabolic processes that is critical to regenerative medicine. However, the importance of sirtuin activity during monolayer expansion for cell-based repair techniques has not been examined previously.

In vivo, chondrocytes experience high osmolarity conditions and low glucose levels compared to other tissues. In articular cartilage the Donnan osmotic effect of negatively charged proteoglycan in the ECM increases osmolarity of the cartilage niche from ~350 mOsm in the superficial zone to 450 mOsm in the deeper regions, and this is increased further by joint loading (Maroudas and Evans, 1972; Oswald et al., 2008). Culture media has been optimised to replicate the osmotic environment of other tissues with the result that media typically used for *in vitro* chondrocyte culture has a lower osmolarity than these specialised cells experience *in vivo*, at approximately 250–280 mOsm. Conversely, typical culture media contains 10 mM glucose which far exceeds *in vivo* concentrations which can be as low as 1 mM in the deep zone of articular cartilage (Windhaber et al., 2003). The transition from cartilage tissue to monolayer culture is therefore accompanied by a shift from high osmolarity and low glucose to low osmolarity and high glucose. It is well established that glucose restriction promotes sirtuin activity (Lin et al., 2002; Li and Tollefsbol, 2011), and we demonstrated previously that chondrocytes expanded in physiological glucose levels of 1 mM subsequently generated greater tissue mass in pellet culture than 10 mM glucose typical of *in vitro* expansion conditions (Heywood et al., 2014). However, the mechanism remains to be established and the potential role of sirtuins in this phenomenon is not known.

A number of small molecule activators of sirtuins have been reported to ameliorate the decline in sirtuin function in aging and disease. Resveratrol is known to augment sirtuin activity in cartilage and other tissues, although the exact mechanism of action has been debated and it affects many other targets. The activity of sirtuins is regulated by the availability of their common substrate, NAD (Imai and Guarente, 2014). Several NAD precursors have emerged, including nicotinamide riboside (NR) and nicotinamide mononucleotide (NMN) which have been demonstrated to successfully enhance sirtuin activity when supplemented in the diet, or in culture medium of cells *in vitro* (Imai, 2010). In addition, novel potent synthetic activators have been developed, such as the SIRT1-specific activator, SRT1720 (Milne et al., 2007). Therefore, this study tests the hypothesis that activation of sirtuins by supplementation with SRT1720 or NMN during chondrocyte maintenance *in vitro* augments subsequent cartilage regeneration potential. This study demonstrates, for the first time, that treatment with small molecule activators of sirtuin activity during the *in vitro* cell expansion phase may augment the regenerative potential of the expanded chondrocytes. Ultimately, this study aims to enhance the clinical success of cartilage repair procedures such as ACI.

2 Materials and methods

2.1 Ethics statement

Bovine metacarpophalangeal joints were procured as surplus to other food/agricultural use from an abattoir in the United Kingdom, operated under the relevant regulations on animal welfare. This study does not use tissue from animals maintained for research purposes.

2.2 Chondrocyte isolation and seeding

Cartilage was dissected under sterile conditions and chondrocytes were isolated from the tissue by sequential incubation at 37°C in complete Dulbecco's modified Eagle medium (DMEM) supplemented with 20% (v/v) foetal bovine serum (DMEM + 20% FBS) and 5.7 mg/ml pronase for 1 h followed by incubation in DMEM + 20% FBS with 100 U/ml collagenase overnight, as described previously (Heywood and Lee, 2017). All reagents were from Sigma-Aldrich (Poole, United Kingdom). Cells obtained from different donors were isolated and maintained separately, reflecting cell therapy practices, and cultures from each donor allocated to all treatment groups. Freshly isolated chondrocytes were maintained in suspension culture for short term experiments or seeded either into culture dishes or onto serum coated coverslips, at a density of 2×10^4 cells/cm^2 and cultured under standard 5% (v/v) CO_2 conditions in culture media as outlined below.

2.3 Chondrocyte expansion and sirtuin modulation

Control culture media consisted of DMEM+10% (v/v) FBS containing 10 mM glucose and supplemented with 2 mM L-glutamine, 18 mM HEPES buffer, 88 U/ml penicillin, and 88 mg/ml streptomycin (all from Sigma-Aldrich). Media containing 1 mM glucose was supplemented with 9 mM galactose to maintain osmotic balance, as described previously (Heywood et al., 2014). Osmolarity of 10 mM glucose base media was increased through the addition of D-mannitol (Sigma-Aldrich). Osmolarity was confirmed using a freezing-point depression osmometer (model 3250, Advanced Instruments, Norwood, MA). For short term studies on the role of osmolarity or glucose, samples of 1×10^6 freshly isolated chondrocytes were incubated in suspension with appropriate culture media for 5 h or 6 h respectively. Cells were passaged at 85%–90% confluence using trypsin-EDTA (Sigma-Aldrich) to recover the cells, with cell number determined using a haemocytometer, before re-seeding. Cell proliferation at intervening time points was monitored by manually counting cells from representative fields of view from each flask, with phase contrast images captured daily using a microscope-mounted camera. Once the cells had reached a total of 2, 4, 10, and 25 population doublings (PDs), cell extracts for gene expression analysis were collected and cells plated onto coverslips were prepared for immunofluorescent staining. 0 PD cells for gene expression analysis were maintained in culture dishes for 24 h following isolation with treatments as indicated. At 4 PDs cells were detached with trypsin-EDTA, washed and resuspended in fresh culture media before preparation of cell pellets as described below.

Modulators of sirtuin activity were 10 mM nicotinamide (NAM), 100 μM nicotinamide mononucleotide (NMN; both Sigma Aldrich) or 100 nM SRT1720 (Merck, Watford, United Kingdom). Solutions of NAM and NMN were prepared in culture media and SRT1720 was prepared as a stock solution at 25 mM in DMSO before dilution in culture media, such that DMSO represented less than 0.001% v/v at the final concentration of 100 nM. The efficacy of NMN to increase chondrocyte NAD levels was confirmed using a commercial fluorometric NAD assay kit (ab176723, Abcam, Cambridge, United Kingdom) after 4 h exposure using the manufacturer's methods. Chondrocytes supplemented with the nicotinamide phosphoribosyltransferase (NAMPT) inhibitor FK866 (Sigma Aldrich) at 10 nM, which decreases cellular NAD, acted as a negative control (Supplementary Figures S1A,B), whereas the SRT1720 dose was selected from viability dose-response curves (Supplementary Figure S1C) and published efficacy (Milne et al., 2007).

2.4 3D chondrogenic pellet culture

Freshly isolated chondrocytes (0 PD) or chondrocytes cultured to 4 PDs were centrifuged at 380 × *g* such that a cell mass formed at the base of the centrifuge tube. Cell pellets consisting of 0.5×10^6 or 1×10^6 chondrocytes were cultured in 1 ml or 2 ml of control media respectively, with the addition of 50 μM ascorbate (Sigma-Aldrich), such that the treatments applied during the preceding monolayer phase were discontinued. Cell pellets were maintained with loose caps at 37°C and 5% CO_2, with medium replacement every 2–3 days. After culture for up to 28 days, the wet weight of the cell pellets was recorded and the pellets frozen prior to biochemical analysis of ECM constituents. In addition, NMN (100 μM) or SRT1720 (100 nM) were included in the culture media of pellets formed from freshly isolated cells, to examine the effect of treatments on differentiated cells during the 3D culture phase.

TABLE 1 Primer sequences used for quantitative gene expression analysis.

Gene	Accession number	Sense	Antisense	Product size (bp)	Annealing temp. (°C)
ACTB	NM_173979.3	AGC AGT CGG TTG GAT CGA GCA	GGG AAG GCA AAG GAC TTC CTG TAA C	137	60
B2M	NM_173893.3	GGG TGC TAC ATG TCC ATG TTT GAC C	TGC AGA AGA CAC CCA GAT GTT GAT G	118	60
ACAN	NM_173981.2	GAT GCT TCT ATC CCA GCC TCC GC	CGG TCC GGG AAG TGG CGG TAA	125	60
COL2A1	NM_001001135.3	ACG TCC AGA TGA CCT TCC TG	GGA TGA GCA GAG CCT TCT TG	126	60
SIRT1	NM_001192980.3	CCA GCT AGG ACC ATT ACT GCC	AGC ACA AAC ACA GAT CAT GCA A	145	60
SIRT3	NM_001206669.1	CCA CAG ATT AAT GGC GCT GC	GCC CTT CAC ATG GAT CCC AA	145	60

ACTB, β-actin; *B2M*, β2 microglobulin; *ACAN*, aggrecan; *COL2A1*, collagen type II, alpha 1; *SIRT1*, Sirtuin 1; *SIRT3*, Sirtuin 3.

2.5 Biochemical analysis

Samples for biochemical analysis were digested with papain as described previously (Heywood et al., 2004), prior to quantification of sulphated glycosaminoglycan (sGAG) content using the dimethylmethylene blue assay (Farndale et al., 1986), and estimation of collagen content using the hydroxyproline assay (Kafienah and Sims, 2004). DNA content was assessed with a fluorometric assay using Hoechst 33258 (Sigma-Aldrich) as established by Kim et al. (1988).

2.6 qPCR

Gene expression following expansion for up to 25 PDs was determined by quantitative polymerase chain reaction (qPCR). Total RNA of monolayer cells was extracted using TRIzol reagent (Invitrogen) according to the manufacturer's instructions. RNA yield and quality was assessed using a NanoDrop spectrophotometer (Thermo Fisher Scientific). 500 ng of RNA from each sample was reverse transcribed to cDNA using the Thermoscript reverse transcription kit (Invitrogen) with oligo dT primers according to the manufacturer's instructions. Quantitative PCR was performed on samples in parallel using a MX3000P real time PCR machine (Stratagene, La Jolla, CA) with 1 µl of cDNA (or water control) in a 10 µl final reaction volume using hot-start DNA polymerase (Qiagen, Crawley, United Kingdom) in the presence of SYBR green (Sigma-Aldrich), ROX dye (Invitrogen), and 0.25 µM of specific primers (Table 1), with melt curve analysis of the final product. Data were normalised to endogenous control genes, β-2-microglobulin (*B2M*) and/or β-actin (*ACTB*).

2.7 Immunofluorescent staining

Parallel cell cultures seeded onto glass coverslips were fixed at indicated time points in 4% paraformaldehyde for 10 min. After washing in sterile phosphate buffered saline, fixed specimens were stored at 4°C until all time points were collected for a given experimental replicate. Coverslips from all time points were processed in the same batch. Cells were permeabilised with 0.5% Triton X–100 in phosphate buffered saline (PBS) for 5 min and blocked with 5% goat serum in 0.1% BSA-PBS (all Sigma–Aldrich) for 1 h. Cells were incubated with primary antibodies in 0.1% BSA-PBS at 4°C overnight as follows: rabbit polyclonal anti-Sirt1 (Abcam ab13749, RRID: AB_300612) at 1:100, mouse monoclonal anti-H3K27me3 (Abcam ab6147, RRID: AB_449502) at 1:500. Following repeated washing in 0.1% BSA-PBS, cells were incubated with goat anti-rabbit Alexa Fluor 555 (Invitrogen A-21430, RRID: AB_2535851) and goat anti-mouse Alexa Fluor 488 (Invitrogen A-11017, RRID: AB_2534084) conjugated secondary antibodies at 1:1000 for 1 h at room temperature. Nuclei were detected with 1 µg/ml 4′,6-diamidino-2-phenylindole (DAPI; Sigma–Aldrich) in PBS. Following washes in PBS, coverslips were mounted with Fluoromount-G (Cambridge Bioscience, Cambridge, United Kingdom).

Immunofluorescently labelled coverslips were imaged on a Leica DMI4000B fluorescent microscope with a 63x/1.30 oil objective and captured as 16-bit images. A custom script implemented using MATLAB (MathWorks, Cambridge, United Kingdom) was used to identify nuclei and analyse nuclear intensity of SIRT1 and H3K27me3. DAPI labelled nuclei were identified using a Canny threshold. The mean intensity within a region of interest specified by each nucleus was evaluated in each fluorescent channel and output for statistical analysis.

2.8 Statistical analysis

Statistical analyses were performed using Minitab 18 software (Minitab, Coventry, United Kingdom) or Microsoft Excel. When data sets adhered to a normal distribution, two-way *t*-test, ANOVA, or a general linear model for analysis of variance were used with Bonferroni correction or Tukey tests for multiple comparisons. For non-parametric data sets, Mann–Whitney tests were used to compare

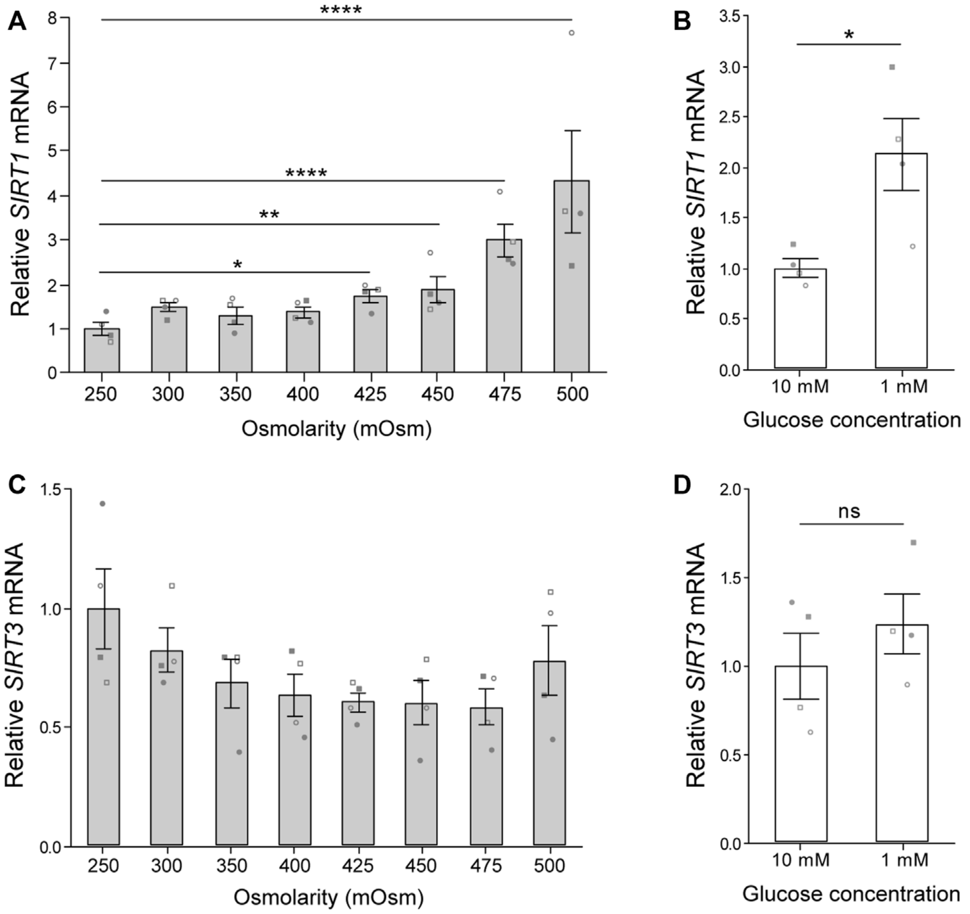

FIGURE 1
Osmolarity and glucose concentration regulate *SIRT1* but not *SIRT3* gene expression. **(A,B)** Gene expression of **(A)** sirtuin-1 (*SIRT1*) and **(B)** sirtuin-3 (*SIRT3*) normalised to β-2-microglobulin (*B2M*) endogenous control and presented relative to 250 mOsm. Mean ± s.e.m., n = 4 donors represented by unique symbols, General linear model with Dunnet multiple comparisons against 250 mOsm: *p = 0.011, **p = 0.005, ****p < 0.0001. **(C,D)** Gene expression of **(C)** *SIRT1* and **(D)** *SIRT3* normalised to β-actin (ACTB) endogenous control and presented relative to 10 mM glucose. Mean ± s.e.m., n = 4 donors represented by unique symbols, paired t-test: *p = 0.030, n. s. P > 0.05. Donors in A,B are distinct from donors in C,D.

conditions. Data quoted in the text are presented as mean ± s.e.m. Details of specific statistical tests and n values can be found in the figure legends.

3 Results

3.1 Physiological glucose and osmolarity enhance *SIRT1* but not *SIRT3* expression

The chondrocyte transition from cartilage tissue to monolayer culture is typically accompanied by a shift from a microenvironment with high osmolarity and low glucose to one with low osmolarity and high glucose. Accordingly we assessed the expression of sirtuins 1 and 3 (*SIRT1* and *SIRT3*) in primary chondrocytes subjected to levels of glucose and osmolarity representative of the *in vivo* niche. Exposure of freshly isolated chondrocytes to media with osmolarity ranging from 250 to 500 mOsm for 5 h induced an osmolarity associated increase in *SIRT1* gene expression (Figure 1A). However, *SIRT3* gene expression was not significantly altered (Figure 1B). Culture of chondrocytes in 1 mM glucose for 6 h increased *SIRT1* expression (Figure 1C), but had little effect on *SIRT3* expression (Figure 1D). Accordingly, *SIRT1* is highly responsive to departures from *in vivo* osmolarity and glucose concentrations typically associated with the switch to monolayer culture.

3.2 SIRT1 expression declines during *in vitro* monolayer expansion

Cell therapies typically involve chondrocyte population expansion by monolayer culture *in vitro* before re-implantation into the damaged site at a high cell density. Population expansion is typically limited to 3–4 population doublings (PDs) due to the concomitant loss of phenotypic expression during monolayer culture. In agreement with previous studies (Dell'Accio et al., 2001; Giovannini et al., 2010), a rapid loss of chondrocyte phenotypic marker gene expression for aggrecan (*ACAN*) and collagen type 2 (*COL2A1*) was observed with monolayer expansion (Figures 2A,B). In a new finding, *SIRT1* expression also decreased with increasing PD number, such that a 51.1 ± 6.1% reduction in *SIRT1* mRNA expression occurred by 4 PDs (Figure 2C), with a similar reduction observed for SIRT1 protein expression assessed using immunofluorescent staining ($p < 0.001$; Figures 2D,E). A positive correlation was observed between the loss of *SIRT1* expression and the phenotypic markers *ACAN* ($r = 0.71$, $p < 0.001$) and *COL2A1* ($r = 0.93$, $p < 0.001$); Figures 2F,G). This supports previous findings relating SIRT1 activity and *COL2A1* expression (Oppenheimer et al., 2014).

3.3 Chondrocytes have similar morphology and proliferation kinetics in the presence or absence of NAM

To assess whether sirtuin activity during population expansion is required to maintain the regenerative capacity of chondrocytes, medium was supplemented with the sirtuin reaction product and physiological pan-sirtuin inhibitor, nicotinamide (NAM), at 10 mM. NAM binds the regulatory C-pocket of sirtuins to inhibit NAD hydrolysis (Bitterman et al., 2002) and is demonstrated to be capable of abolishing sirtuin enzymatic activity at 10 mM (Guan et al., 2014). In addition to enhancing *SIRT1* gene expression (Figure 1B), glucose deprivation is reported to enhance sirtuin activity by a mechanism linked to the induction of mitochondrial respiration upon glucose scarcity that is hypothesised to increase the NAD/NADH ratio (Lin et al., 2002; Heywood et al., 2006; Heywood et al., 2010). Therefore, chondrocytes expanded under 1 mM glucose were also assessed.

Chondrocytes expanded in monolayer exhibited similar morphology regardless of glucose concentration or sirtuin inhibition with NAM (Figure 3A). Population doubling time (PDT) was calculated from the linear proliferation phase up to 4 PDs. NAM did not markedly alter PDT at early timepoints, which was 1.33 and 1.37 days in media containing 10 mM glucose in the presence and absence of NAM, respectively (Figure 3B). Culture under 1 mM glucose conditions slightly increased these respective PDT to 1.65 and 1.57 days in the presence and absence of NAM, respectively (Figure 3C). Thus, expansion in 1 mM glucose resulted in a delay of 1–2 days in reaching four population doublings when compared to 10 mM glucose. Longer term, cells cultured in the presence of NAM treatment initiated proliferative arrest earlier than in the absence of NAM, illustrated by the premature deviation from the linear initial proliferation rate (Figures 3D,E) and consistent with the known role of SIRT1 antagonising senescence (Bitterman et al., 2002; Li and Tollefsbol, 2011).

3.4 Treatment with the sirtuin inhibitor, NAM, during monolayer expansion diminished chondrocyte regenerative capacity

3D pellet cultures recapitulate the re-implantation phase of cell therapy techniques such as ACI, where the cells must be able to regenerate a cartilaginous matrix for clinical success. Cells were recovered from monolayer following 4 PDs and 3D pellets were prepared (Giovannini et al., 2010). The pellets were cultured for a further 28 days, using control media for all groups. The equivalence in population doubling prior to cell pellet formation, illustrated in Figures 3B,C, is important because this is linked to regenerative capacity (Dell'Accio et al., 2001; Giovannini et al., 2010). Cells cultured in monolayer for 4 PDs in the presence of the sirtuin inhibitor, NAM, generated smaller tissue mass after 28 days pellet culture compared with both the untreated control cells and freshly isolated cells that had not been expanded in monolayer prior to pellet formation (0 PD; Figures 4A,B). Wet weight was significantly reduced with expansion in NAM to 44.17 ± 0.02% ($p < 0.001$) of that of untreated controls for 10 mM glucose cultures (Figure 4B). Tissue composition mirrored wet weight, with significantly reduced collagen (41.51 ± 0.08%, $p < 0.05$) and sGAG (45.78 ± 0.03%, $p < 0.001$) content in pellets from cells exposed to NAM treatment during the preceding expansion phase (Figures 4C,D). Glucose deprivation is reported to increase sirtuin activity (Kaeberlein et al., 2002; Lin et al., 2002) and expression (Heywood et al., 2016). Expansion in media containing 1 mM glucose resulted in cells that produced significantly greater tissue mass upon 3D pellet culture compared to cells expanded in media containing 10 mM glucose ($p < 0.05$; Figure 4B). This effect was abolished by the presence of NAM during expansion, providing a significant interaction between glucose concentration and NAM supplementation ($p = 0.002$; Figure 4B). Trends in pellet DNA content at day 28 mirrored ECM, with freshly isolated (0 PD) and control cells proliferating during the 3D pellet phase, with a 58%–102% increase in DNA (Figure 4E). By contrast, NAM treated chondrocytes which proliferated as normal in 2D (Figures 3B,C) failed to demonstrate an increase in DNA on incorporation into 3D pellet culture (Figure 4E). Accordingly, inhibition of sirtuin activity during the monolayer expansion phase is linked to a marked reduction in cartilage tissue regenerated upon transfer to 3D pellet culture.

3.5 SIRT1 expression correlates with epigenetic chromatin modification in monolayer

Treatment with the sirtuin inhibitor NAM, restricted to the monolayer expansion phase, markedly altered regeneration in

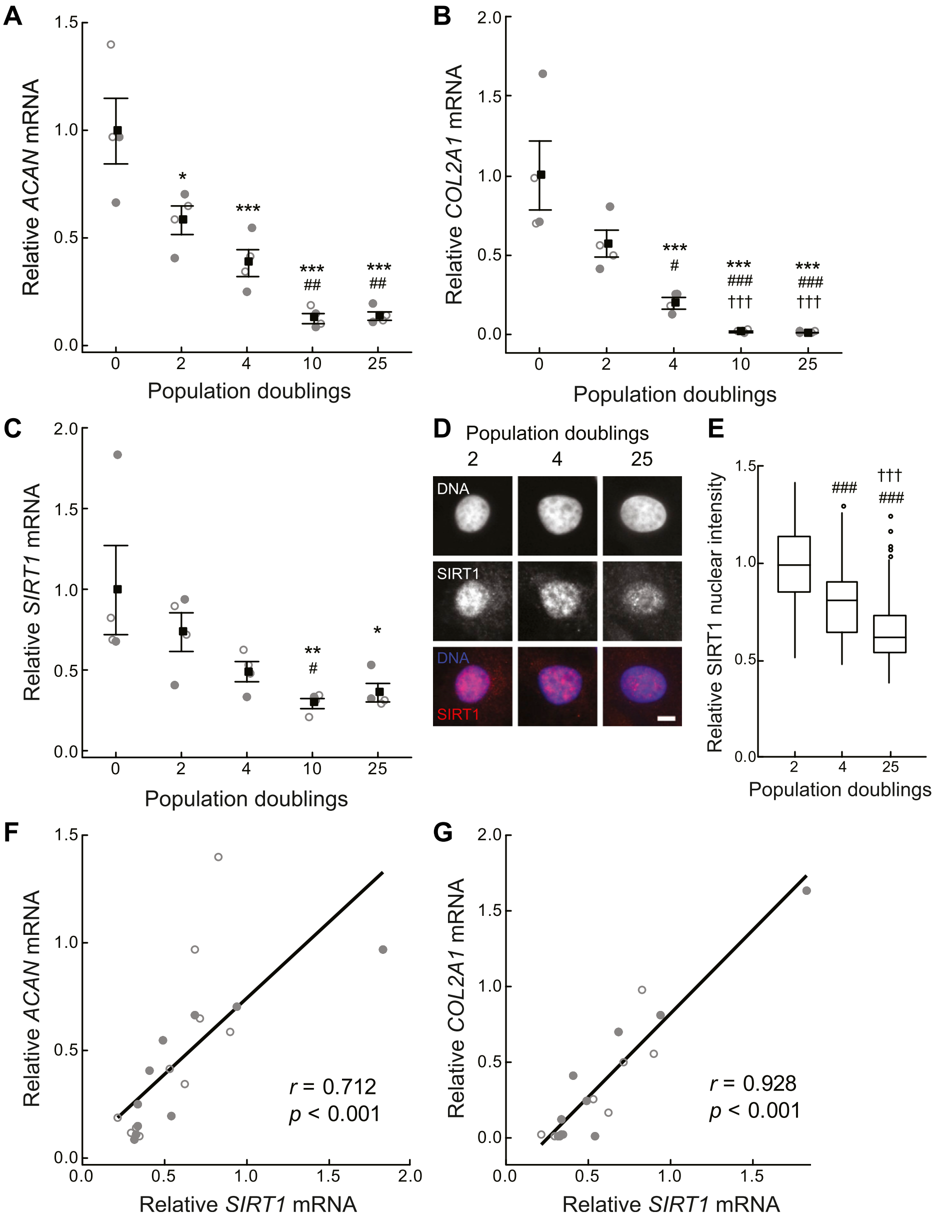

FIGURE 2

Cartilage matrix and sirtuin 1 gene expression declines during *in vitro* monolayer expansion of primary chondrocytes. **(A–C)** Gene expression of **(A)** aggrecan (*ACAN*), **(B)** collagen type II α-1 chain (*COL2A1*) and **(C)** sirtuin 1 (*SIRT1*) is normalised to β-2-microglobulin (*B2M*) and β-actin (*ACTB*) endogenous control genes and presented relative to 0 population doublings (PDs). Mean ± s.e.m., n = 4 from two experiments with individual data points represented by open and closed circles respectively, General linear model with Tukey pairwise comparisons: $^{*}p < 0.05$, $^{**}p < 0.01$ and $^{***}p < 0.001$ vs. 0 PDs, $^{\#}p < 0.05$, $^{\#\#}p < 0.01$ and $^{\#\#\#}p < 0.001$ vs. 2 PDs, $^{\dagger\dagger\dagger}p < 0.001$ vs. 4 PDs. **(D)** Representative nuclear SIRT1 immunofluorescent staining. Scale bar 5 µm. **(E)** Nuclear SIRT1 protein levels relative to 2 PDs. Boxes represent median and interquartile range, with whiskers extending to 1.5 × interquartile range or the max/min data points, n_{2PD} = 140, n_{4PD} = 113, n_{25PD} = 354 cells, General linear model with Tukey pairwise comparisons: $^{\#\#\#}p < 0.001$ vs. 2 PDs, $^{\dagger\dagger\dagger}p < 0.001$ vs. 4 PDs. **(F,G)** Scatter plots of **(F)** *ACAN*, and **(G)** *COL2A1* against *SIRT1* expression. n = 20 from two experiments with individual data points represented by open and closed circles respectively, Pearson correlation coefficient (r) and p-value < 0.001.

the subsequent 3D pellet (Figure 4). However, there was no evidence that the presence of NAM significantly affected the time course of *ACAN* and *COL2A1* gene expression over the preceding 4 PDs in monolayer (Supplementary Figures S2A,B). Therefore, we examined evidence of epigenetic changes, consistent with an enduring cell phenotype. The chromatin

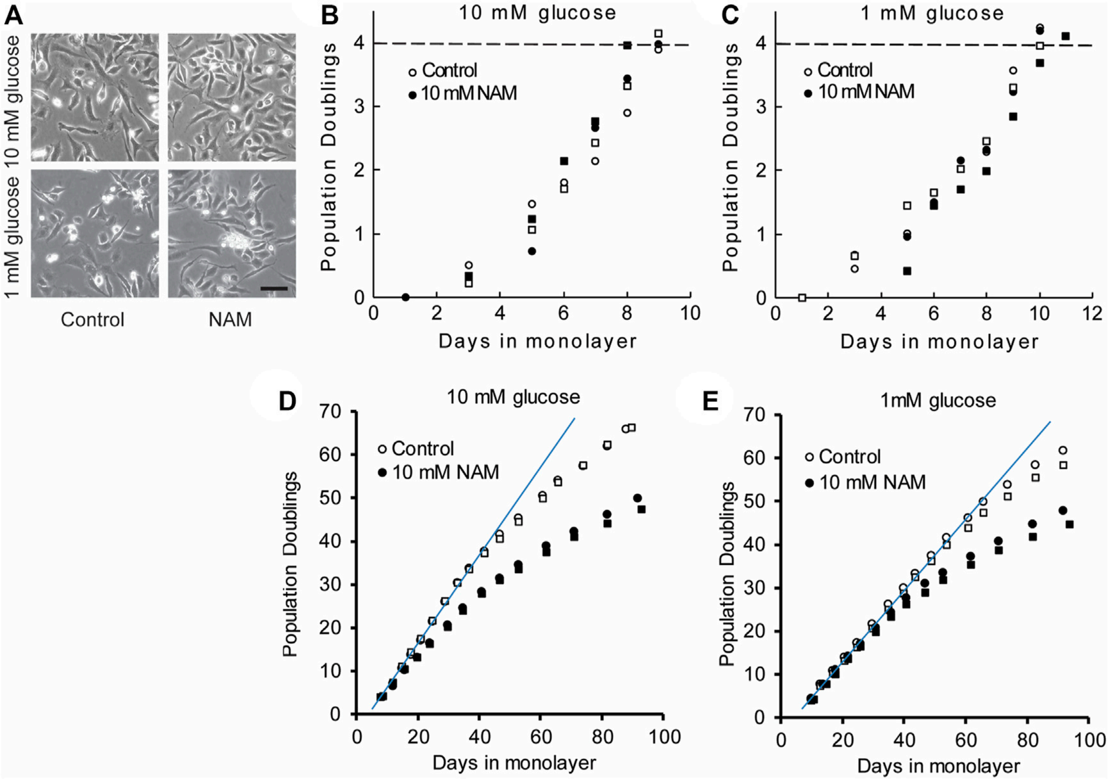

FIGURE 3
Chondrocytes have similar morphology and early proliferation kinetics in the presence or absence of the sirtuin inhibitor, NAM. **(A)** Chondrocytes expanded in monolayer exhibited similar morphology regardless of glucose concentration or sirtuin inhibition with NAM, illustrated by representative images at day 6. Scale bar 100 μm. **(B,C)** Proliferation kinetics data for chondrocytes expanded for 4PD in **(B)** 10 mM glucose and **(C)** 1 mM glucose with and without NAM. Data from two experiments indicated by circles and squares. The population doubling times calculated from the linear region of the population doubling/days in monolayer plots **(B,C)** were 1.49 ± 0.11 and 1.47 ± 0.12 days (mean ± s.e.m.) for control and NAM treated cells respectively. The final population doubling number at which cells were harvested to prepare cell pellets, indicated by the dashed line in **(B)** and **(C)** was 4.06 ± 0.08 and 4.05 ± 0.06 (mean ± s.e.m.) for control and NAM treated cells respectively. **(D,E)** Long-term proliferation kinetics in which a linear fit indicates the trajectory of the initial linear growth phase. During long-term culture, premature proliferative arrest was observed in the presence of NAM treatment for both 10 mM and 1 mM glucose media **(D,E)**, illustrated by earlier deviation from linear growth compared to cells without NAM.

mark H3K27me3 is associated with heterochromatin formation and gene silencing and has an important role in development and differentiation (Kuzmichev et al., 2002; Bosch-Presegue and Vaquero, 2015; Lui et al., 2016). Furthermore, SIRT1 is reported to participate in the polycomb repressive complex 4 (PRC4), a complex with H3K27me3 histone methyltransferase activity (Bosch-Presegue and Vaquero, 2015). In this study, H3K27me3 immunofluorescent intensity correlated positively with SIRT1 expression in the nuclei of chondrocytes cultured in both 10 mM and 1 mM glucose to 4 PDs (Figure 5). Treatment with the sirtuin inhibitor, NAM, during monolayer expansion decreased nuclear levels of both SIRT1 and H3K27me3 (Figures 5A–D) and weakened the correlation between these (Figures 5E,F). These data support the proposal that sirtuins are involved in the maintenance of this chromatin mark during monolayer expansion.

3.6 Pharmacological augmentation of sirtuin activity in monolayer enhances pellet culture mass

Next, we tested whether augmentation of sirtuin activity in chondrocytes during monolayer culture enhances subsequent cartilage tissue generation upon transfer to a cell pellet culture model of re-implantation. 100 μM NMN or 100 nM SRT1720 (Milne et al., 2007), were added during chondrocyte expansion to 4 PDs, at which point 3D pellets were prepared. NMN is anticipated to activate the whole sirtuin family (SIRT1-7) by acting as the precursor of their common sirtuin substrate, NAD (Imai, 2010; Imai and Guarente, 2014), whereas the synthetic sirtuin activator SRT1720 has specificity for SIRT1 (Milne et al., 2007). During expansion, chondrocytes treated with NMN and SRT1720 had similar proliferation rates compared to untreated controls (data not shown). Day 21 pellets are illustrated in

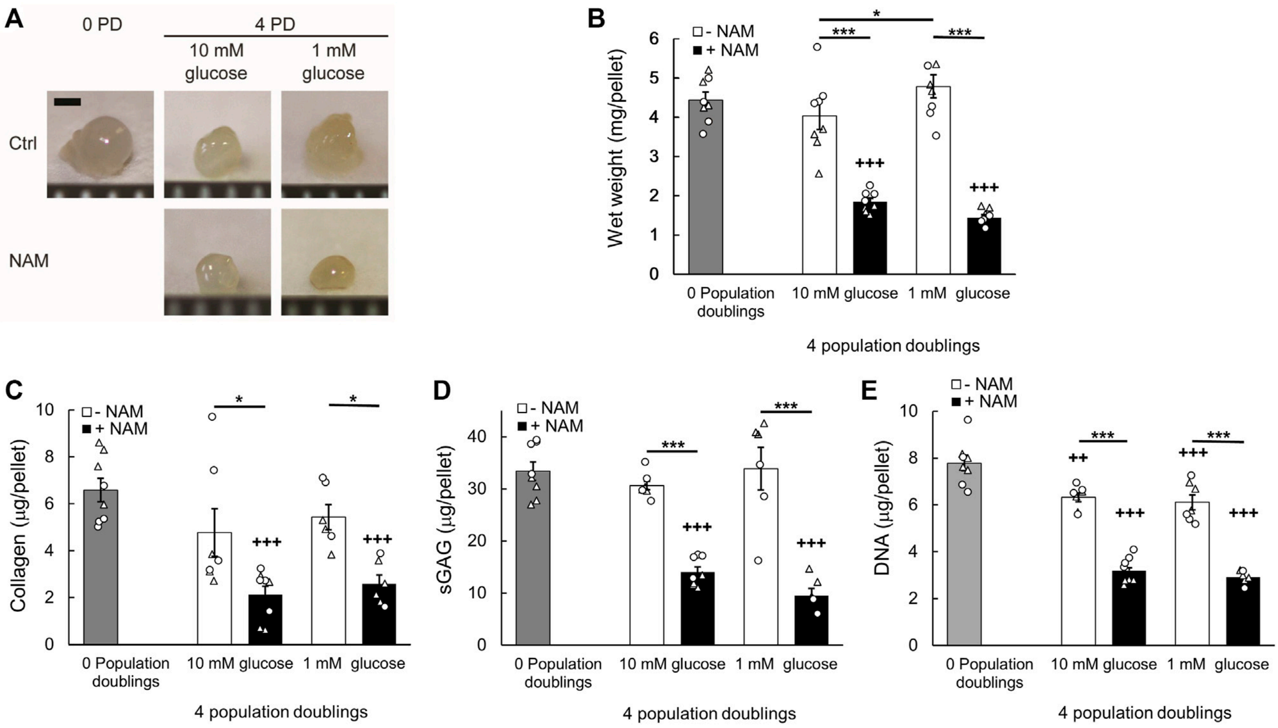

FIGURE 4
Inhibition of sirtuin activity during monolayer expansion abrogates chondrocyte regenerative capacity. **(A)** Representative cell pellets at day 28 of 3D culture created from chondrocytes which were either freshly isolated, 0 population doublings (0 PD), or monolayer expanded for 4 PDs in media containing either 10 mM or 1 mM glucose in the presence or absence of the sirtuin inhibitor nicotinamide (NAM). Scale bar 1 mm. **(B)** Pellet wet weight, **(C)** collagen content, **(D)** sulphated glycosaminoglycan (sGAG) content, and **(E)** DNA content at day 28. Mean ± s.e.m, n_{0PD} = 8 **(B–E)**, $n_{4PD\ 10mM\ Ctrl}$ = 9 **(B)** 7 **(C–E)**, $n_{4PD\ 10mM\ NAM}$ = 10 **(B)** 8 **(C–E)**, $n_{4PD\ 1mM\ Ctrl}$ = 10 **(B)** 6**(C–E)**, $n_{4PD\ 1mM\ NAM}$ = 12 **(B)** 6 **(C–D)** 7 **(E)** from two experiments indicated by symbol shape, General linear model with Tukey pairwise comparisons: *$p < 0.05$, ***$p < 0.001$; $^{+++}p < 0.001$ vs. 0 PD.

Figure 6A and compared to cell pellets which were prepared from the freshly isolated cells (0 PD) to indicate the performance of fully differentiated cells from each donor. The wet weights were significantly greater for cells expanded in the presence of sirtuin activators, being 60% and 34% greater compared to untreated controls, for NMN and SRT1720 respectively ($p < 0.001$; Figure 6B). Analysis of the tissue composition (Figures 6C–E) indicated that the key effect was improved maintenance of cell number during the pellet phase. In untreated cells, measured cell numbers were lower after pellet culture than when seeded within the pellet, suggesting loss of viability (Figure 6E). Additionally, the tissue regenerated by the NMN treatment group had 38% greater collagen content ($p < 0.05$) while sGAG levels were not significantly enhanced.

3.7 The beneficial effects of sirtuin activation are culture context dependent

Freshly isolated chondrocytes (0 PD) were prepared as cell pellets without prior monolayer culture, to examine the effect of sirtuin activation during the 3D culture phase (Figure 7). Unexpectedly, the presence of NMN during 3D pellet culture resulted in a 55% reduction in the tissue mass compared to untreated controls ($p < 0.0001$; Figure 7A). Both NMN and SRT1720 reduced collagen content, by 59% ($p < 0.0001$) and 25% ($p < 0.01$) respectively, while sGAG and DNA content were unaffected. Therefore, treatment of differentiated cells with sirtuin activators in a 3D tissue formation context may be detrimental to tissue regeneration, with implications for approaches that aim to use delivery of activators to enhance repair *in situ*.

4 Discussion

In this study, we examined the potential role of small molecule modulators of sirtuins to augment the regenerative potential of articular chondrocytes, using methods that replicate those adopted for the expansion of cells in regenerative therapies for cartilage repair. This study has demonstrated that *SIRT1* gene expression progressively declines with culture duration during *in vitro* monolayer expansion, and that pharmacological

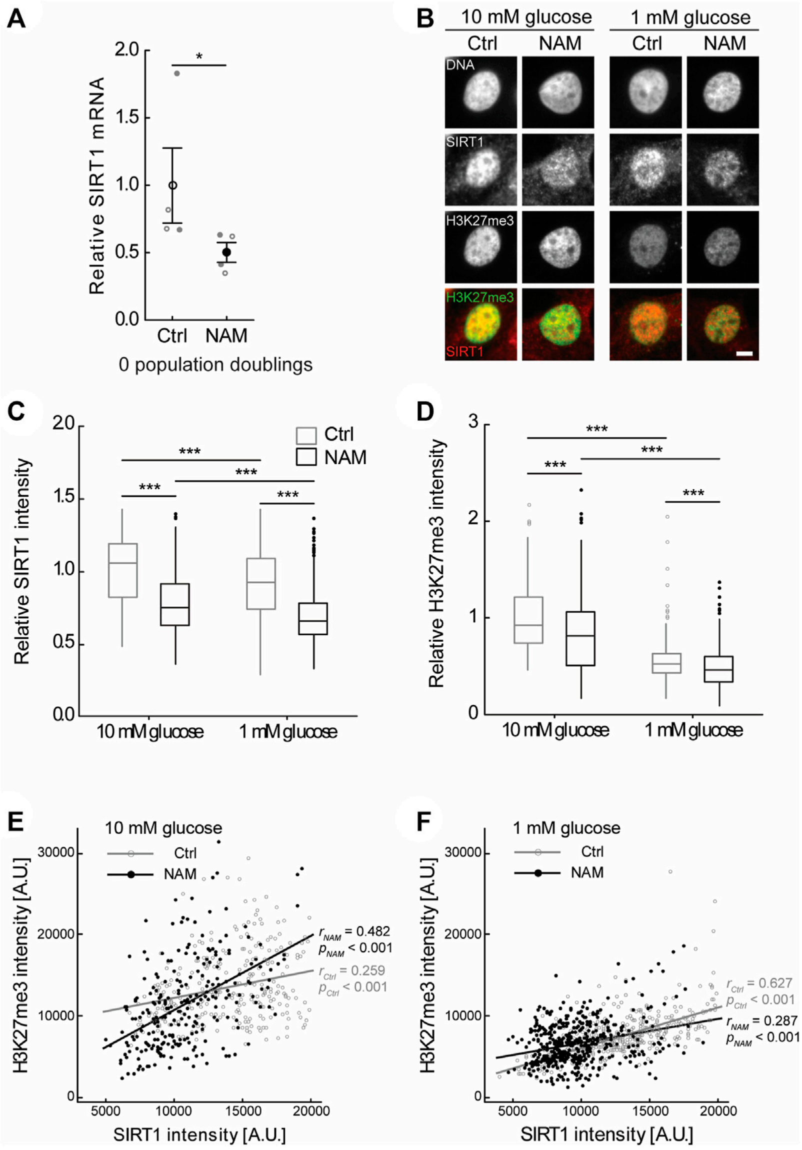

FIGURE 5
Treatment with the sirtuin inhibitor, NAM, decreased expression of SIRT1 and abundance of the epigenetic mark H3K27me3. **(A)** Treatment of primary (0 PD) chondrocytes for 24 h with 10 mM NAM significantly inhibited *SIRT1* gene expression. Mean ± s.e.m., $n = 4$ from two experiments with individual data points represented by open and closed circles respectively, Mann-Whitney test: $^*p < 0.05$. **(B)** Representative SIRT1 and H3K27me3 immunofluorescent nuclear staining in chondrocytes expanded for four population doublings (PDs) in media containing either 10 mM or 1 mM glucose in the presence or absence of the sirtuin inhibitor nicotinamide (NAM). Scale bar 5 μm. **(C)** Nuclear SIRT1 and **(D)** H3K27me3 levels in chondrocytes at 4 PDs relative to 10 mM glucose control cells. Boxes represent median and interquartile range, with whiskers extending to 1.5 × interquartile range or the max/min data points. **(E,F)** Scatter plots of nuclear H3K27me3 against nuclear SIRT1 intensity in 4 PD chondrocytes cultured in **(E)** 10 mM glucose or **(F)** 1 mM glucose in the presence or absence of NAM. $n_{10mM\ Ctrl} = 270$ cells, $n_{10mM\ NAM} = 246$ cells, $n_{1mM\ Ctrl} = 416$ cells, $n_{1mM\ NAM} = 468$ cells from two experiments. **(C,D)** Mann-Whitney test: $^{***}p < 0.001$. **(E,F)** Pearson correlation coefficient (r) and *p*-value presented.

modulators of sirtuin activity during *in vitro* monolayer culture influence the ability of expanded chondrocytes to regenerate a cartilaginous matrix upon transfer to a 3D culture environment. Importantly the regenerative capacity of monolayer-expanded chondrocytes can be manipulated *via* activation or inhibition of sirtuin activity during the expansion phase alone. We observed that SIRT1 gene expression diminishes during monolayer culture (Figure 2). Moreover, inhibition of sirtuin activity during the expansion phase, using NAM, further reduced regenerative capacity during subsequent 3D culture. Accordingly, we tested whether media supplementation during monolayer expansion with known activators of sirtuins would enhance the ability of the

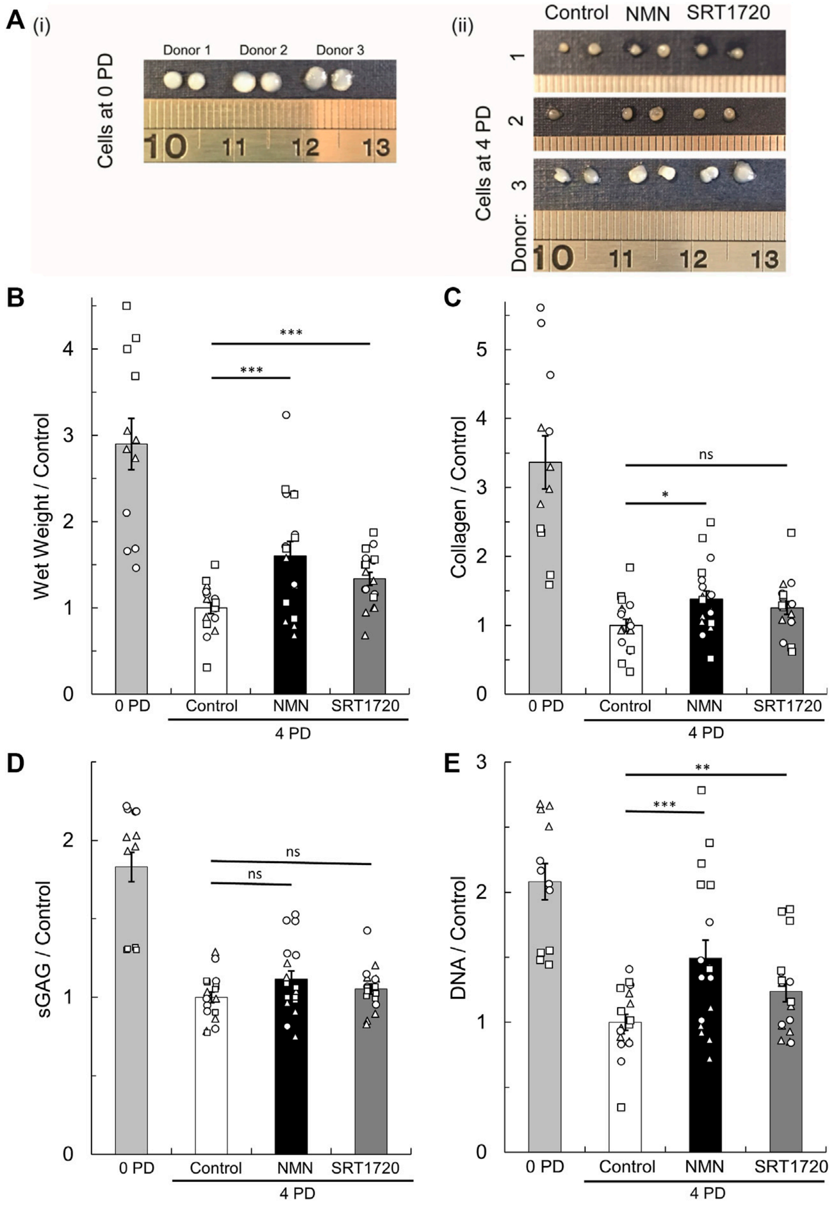

FIGURE 6
Regeneration of cartilage tissue following transfer of monolayer cells to 3D pellet culture. **(A)** Representative tissue masses formed after 21 days culture of cell pellets created from (i) freshly isolated cells (0 PD) or (ii) monolayer expanded for four population doublings (4 PDs) in media containing 10 mM glucose supplemented with the pan-sirtuin activator, 100 μM NMN, or the SIRT1 specific activator, 100 nM SRT1720, or untreated controls. Scale units cm. **(B)** Pellet wet weight, **(C)** collagen content, **(D)** sulphated glycosaminoglycan (sGAG) content, and **(E)** DNA content at day 21 relative to the 4 PD control. Mean ± s.e.m, $n_{0PD} = 12$, $n_{4PD} = 18$ from three donors indicated by symbol shape. 2-factor ANOVA with replication and bonferroni correction: $^{*}p < 0.05$, $^{**}p < 0.01$ $^{***}p < 0.001$, $^{ns}p > 0.05$. The cell number seeded to pellets for each treatment group is shown in Supplementary Figure S3.

cells to synthesise a cartilaginous ECM in 3D, as a novel means of enhancing regenerative medicine approaches to cartilage repair.

Nicotinamide mononucleotide (NMN) is a precursor of the common sirtuin substrate, nicotinamide adenine dinucleotide (NAD), and has been demonstrated by others to enhance sirtuin activity when supplemented in the diet, or in culture medium of cells *in vitro* (Imai, 2010). Its efficacy in enhancing chondrocyte NAD levels *in vitro* was confirmed in our hands (Supplementary Figure S1). In addition, we examined the effect of the synthetic SIRT1-specific activator, SRT1720 (Milne et al., 2007). Cells expanded in the presence of either sirtuin activator generated significantly greater cartilage tissue mass on transfer to 3D

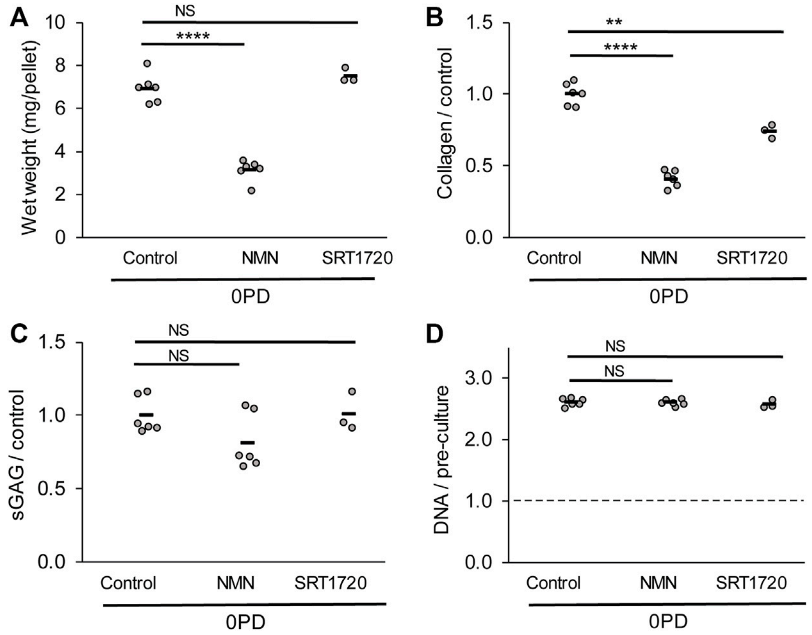

FIGURE 7
Regeneration of cartilage tissue by freshly isolated (0 PD) chondrocytes is impaired by the presence of sirtuin activators during 3D pellet culture. **(A)** Cell pellet wet weights, **(B)** collagen, **(C)** sulphated glycosaminoglycan and **(D)** DNA content after 21 days pellet culture in the presence or absence of sirtuin activators 100 μM NMN or 100 nM SRT1720. DNA content is normalised to pre-culture pellet values at day 0. $n = 6$ for all groups except SRT1720 where $n = 3$. The freshly isolated (0 PD) cells were pooled from four donors before pellet formation. Two-way *t*-test with Bonferroni correction: $^{***}p < 0.001$ $^{****}p < 0.0001$, $^{NS}p > 0.05$.

culture (Figure 6). This was attributed both to an increase in cell number in the mature 3D tissue (NMN and SRT1720 treatments) and an increased accumulation of collagen ECM (NMN treatment) compared to controls. The positive regulation of cartilage-specific matrix gene expression, such as type II collagen, is an established role of SIRT1 in cartilage (Dvir-Ginzberg et al., 2008). However, comparison of the regenerated tissue composition, particularly cellularity (Figure 6E), suggests that the predominant effect of sirtuin activation in this system is to support the survival and proliferation of culture expanded chondrocytes following transfer from monolayer to a 3D environment. Consistent with this, expansion in the presence of the sirtuin inhibitor, NAM, produced the opposite effect, with significantly reduced cell numbers in the regenerated tissues (Figure 4E). Based on 7.7 pg of DNA per chondrocyte (Kim et al., 1988), we observe an approximate two-fold increase in cellularity in the 0 PD and control 4 PD conditions while overall cell number remains unchanged with NAM treatment (Figure 4E). The relative contribution of proliferation and apoptosis to these observations could be explored in the future.

These data are consistent with the pro-survival actions of sirtuins, which are reported to block apoptotic cell death under stress conditions, through a variety of mechanisms including inhibition of the pro-apoptotic protein, p53 (Luo et al., 2001; Vaziri et al., 2001; Takayama et al., 2009; Gagarina et al., 2010), Ku70 (Cohen et al., 2004), forkhead transcription factors (Motta et al., 2004), and p65 (Yeung et al., 2004). Alternatively, sirtuins may promote cell survival through crosstalk with hypoxia-inducible factor 1-α (HIF1α). It is reported that SIRT1 depletion or inactivation hyperacetylates HIF1α and reduces HIF1α accumulation under hypoxic conditions. Chondrocytes become increasingly dependent on oxidative phosphorylation within the aerobic environment in monolayer culture, which contrasts with the highly glycolytic metabolism of primary cells (Heywood and Lee, 2010, Heywood and Lee, 2017). The activation of sirtuins may therefore promote cell survival on transfer to 3D pellet culture *via* HIF1α activation, which adapts cell metabolism to the limited oxygen within the pellet culture. SIRT1 is established to modulate HIF1α activity and expression *via* direct interaction (Laemmle et al., 2012; Joo et al., 2015) or epigenetic modification of the HIF1α promoter (Dong et al., 2016; Luo and Wang, 2018). Further work is required to determine which mechanisms mediate the enhanced cellularity of tissues following cell expansion with sirtuin activators observed in this study.

NAM was used in this study as it is reported to bind to the regulatory C-pocket of sirtuins and inhibit their enzymatic activity (Bitterman et al., 2002; Guan et al., 2014). The supplementation or depletion of NAM is reported to inhibit or activate sirtuins, respectively (Luo et al., 2001; Anderson et al., 2003; Gallo et al., 2004). However, some NAM may be converted into NAD *via* the NAD salvage pathway, the rate limiting step of which is the conversion of NAM to NMN by nicotinamide phosphoribosyl transferase (NAMPT). Therefore, NAM treatment has the potential to indirectly activate sirtuins. However, the present study observed that chondrocytes treated with the putative sirtuin inhibitor NAM had the opposite response to treatment with the NAD precursor, NMN (compare Figures 4, 6). Therefore, the inhibitory effects of NAM treatment appear to outweigh any effects from *de-novo* NAD synthesis in this study. Differences in the efficacy of NAM as a sirtuin inhibitor may occur due to differential expression of NAMPT. For example, normal chondrocytes such as those used in this study are reported to express low levels of NAMPT compared to cells derived from OA tissue used in other studies (Dvir-Ginzberg et al., 2008). Indeed, NAMPT has also been shown to be upregulated in interleukin-1β mediated chondrocyte dedifferentiation, leading to SIRT1 activation (Hong et al., 2011). Further support for NAM as an inhibitor of sirtuins is shown in the long-term proliferation data (Figures 3D,E). As discussed above, sirtuins are established to antagonise cell apoptosis and growth arrest and we observed that the presence of NAM during long-term monolayer culture resulted in premature onset of proliferative growth arrest.

Sirtuins are involved in epigenetic regulation of numerous genes. For example, established SIRT1 targets include histones such as histone H4 lysine 16 (H4K16), histone H3K9, and H3K14 which regulate chromatin structure and biological function (Imai et al., 2000; Bosch-Presegue and Vaquero, 2015). Sirtuins are also involved in histone methylation, by modulating the activity of several methyltransferases (Roth and Chen, 2014; Bosch-Presegue and Vaquero, 2015). For example, SIRT1 associates with enhancer of zeste homolog 2 (EZH2) within polycomb repressive complexes (Kuzmichev et al., 2005), an enzyme with H3K27me3 histone methyltransferase activity (Bosch-Presegue and Vaquero, 2015). H3K27me3 is associated with heterochromatin formation and gene silencing and has an important role in development, differentiation and cell memory (Margueron and Reinberg, 2011; Bosch-Presegue and Vaquero, 2015; Heo et al., 2015; Marasca et al., 2018). H3K27 methylation plays a critical role in chondrocyte proliferation and hypertrophy in the growth plate (Lui et al., 2016), while inhibition of EZH2 histone-lysine N-methyltransferase activity, that leads to reduced H3K27me3, ameliorates OA development (Chen et al., 2016). Consistent with other studies, this study identified a correlation between SIRT1 expression and H3K27me3 (Vazquez et al., 2018) and found that the sirtuin inhibitor NAM reduced H3K27me3 (Figures 5B,D). This is consistent with a role of sirtuins in the maintenance of this chromatin mark during monolayer expansion of chondrocytes. Accordingly, the pharmacological modulation of sirtuin activity during monolayer expansion may leave an epigenetic fingerprint on the cells which could convey persistent effects on cell function following re-implantation.

Such persistence post-expansion may be advantageous as effects gained by *in vitro* treatment with sirtuin activators can be maintained following wash-out of the drug prior to transplantation, thereby avoiding direct exposure of the patient to the sirtuin modulating drugs. Previous reports have suggested that overexpression of sirtuins *in vivo* may have detrimental effects, for example SIRT1 and SIRT7 overexpression is reported to be an indicator of poor prognosis in some cancers (Deng et al., 2018; Ma et al., 2018). Moreover, in this study we observed that primary chondrocytes treated directly in pellet culture with sirtuin activators behaved differently from monolayer-expanded cells with markedly decreased matrix synthesis (Figure 7). Together these finding suggest that restricting modulation of sirtuin activation to the *in vitro* expansion phase of cellular therapies may deliver a number of benefits.

NMN is a common activator for all sirtuins by acting as a precursor for their substrate NAD (Imai, 2010; Imai and Guarente, 2014). By contrast, the synthetic sirtuin activator, SRT1720, has many hundred-fold greater potency for SIRT1 than the closest homologues (Milne et al., 2007). The similar response to each activator illustrated in Figure 6 supports the hypothesis that the effect of sirtuin activation on cartilage regeneration may be attributable, at least in part, to SIRT1. Unexpectedly, this study found that the application of the pan-sirtuin activator, NMN, to freshly isolated chondrocytes in a 3D pellet inhibited tissue regeneration (Figure 7), particularly decreasing wet weight and collagen content. The mechanism is unknown and could be the subject of future studies. One potential cause may be due to the co-activation of SIRT7. In direct contrast to SIRT1 and SIRT6 which are required for cartilage homeostasis (Nagai et al., 2015; Wu et al., 2015; Fu et al., 2016), the selective knockdown of SIRT7 was reported to proportionally increase matrix synthesis in chondrocytes (Korogi et al., 2018). This highlights the importance of specificity of selected activators to sirtuin family members. Smith et al. (2022) recently used pellet culture to induce chondrogenic differentiation in human embryonic stem cells and found that activation of SIRT1 using 5 μM SRT1720 during pellet culture leads to increased collagen type II and aggrecan gene and protein expression, but reduced sGAG accumulation. This contrasts with our findings with mature freshly isolated bovine chondrocytes where we observed a decrease in total collagen with a 50 × lower dose of SRT1720 (Figure 7B), indicating that the response to SIRT1 activation may depend on dose and the differentiation state of the chondroprogenitor cell or chondrocyte. These studies highlight the importance of the context in which sirtuin activators are applied. For example, although sirtuin activators may be beneficial if applied in monolayer or during differentiation, further research is required to determine whether they may be detrimental to healthy cartilage if given systemically to a patient or injected into the joint.

The use of sirtuin activators during the cell processing stage has potential to enhance the outcome of cell-based cartilage repair techniques such as ACI. However, the regenerative capacity of expanded chondrocytes was not restored to that of freshly isolated (0 PD) cells. Further dose-optimisation may be achieved, but the efficacy of small molecule sirtuin activators will be dependent on the retained expression of the target sirtuins, which we have demonstrated to decline *in vitro* (Figures 2C–D). Similarly, the expression of SIRT1 is reported to be reduced in chondrocytes derived from OA tissue (Dvir-Ginzberg et al., 2008). Thus, variations in sirtuin expression may explain the variable response of cells isolated from different donors to sirtuin activators following equivalent population expansion (Figure 6), in addition to other biological variation. Therefore, research effort should be directed toward identifying the physiological conditions that support the retention of sirtuin expression *in vitro*.

The present study demonstrates for the first time that modulation of sirtuin activity during *in vitro* monolayer expansion influences subsequent chondrocyte regenerative potential. Given that *in vitro* monolayer expansion is a requirement of cell therapy-based cartilage repair strategies, these findings have relevance to the clinical success of cartilage repair procedures. Significant increases in regenerated tissue mass, cell survival and collagen content were achieved by supplementing expansion media with selected small molecule sirtuin activators. Importantly, however, the use of these sirtuin activators on differentiated cells *in situ* may be contraindicated.

Data availability statement

The original contributions presented in the study are included in the article/Supplementary Materials, further inquiries can be directed to the corresponding author.

Author contributions

HH designed the study, performed experiments, analysed and interpreted the data and wrote the manuscript. ST designed the study, performed experiments, analysed and interpreted the data, performed statistical tests and critically revised the manuscript. RJ conducted cell culture and performed biochemistry assays with data analysis and reviewed the manuscript. PC devised the study, contributed to scientific discussions and to the manuscript and provided funding. DL devised and supervised the study, contributed to scientific discussions, data interpretation, critically revised the manuscript and provided funding.

Funding

This work was supported by The Dunhill Medical Trust (R339/0214) and the Biotechnology and Biological Sciences Research Council (BB/N018532/1).

Acknowledgments

The authors thank Miss Sabha Asghar and Miss Leila R. Hosseini for assistance with cell proliferation analysis and image analysis.

Conflict of interest

The authors declare that the research was conducted in the absence of any commercial or financial relationships that could be construed as a potential conflict of interest.

Publisher’s note

Supplementary material

The Supplementary Material for this article can be found online at: https://www.frontiersin.org/articles/10.3389/fbioe.2022.971932/full#supplementary-material

References

Anderson, R. M., Bitterman, K. J., Wood, J. G., Medvedik, O., and Sinclair, D. A. (2003). Nicotinamide and PNC1 govern lifespan extension by calorie restriction in *Saccharomyces cerevisiae*. *Nature* 423 (6936), 181–185. doi:10.1038/nature01578

Bar Oz, M., Kumar, A., Elayyan, J., Reich, E., Binyamin, M., Kandel, L., et al. (2016). Acetylation reduces SOX 9 nuclear entry and *ACAN* gene transactivation in human chondrocytes. *Aging Cell* 15 (3), 499–508. doi:10.1111/acel.12456

Bitterman, K. J., Anderson, R. M., Cohen, H. Y., Latorre-Esteves, M., and Sinclair, D. A. (2002). Inhibition of silencing and accelerated aging by nicotinamide, a putative negative regulator of yeast sir2 and human SIRT1. *J. Biol. Chem.* 277 (47), 45099–45107. doi:10.1074/jbc.M205670200

Bosch-Presegue, L., and Vaquero, A. (2015). Sirtuin-dependent epigenetic regulation in the maintenance of genome integrity. *FEBS J.* 282 (9), 1745–1767. doi:10.1111/febs.13053

Brittberg, M., Lindahl, A., Nilsson, A., Ohlsson, C., Isaksson, O., and Peterson, L. (1994). Treatment of deep cartilage defects in the knee with autologous chondrocyte transplantation. *N. Engl. J. Med. Overseas. Ed.* 331 (14), 889–895. doi:10.1056/NEJM199410063311401

Chen, L., Wu, Y., Wu, Y., Wang, Y., Sun, L., and Li, F. (2016). The inhibition of EZH2 ameliorates osteoarthritis development through the Wnt/β-catenin pathway. *Sci. Rep.* 6, 29176. doi:10.1038/srep29176

Cohen, H. Y., Miller, C., Bitterman, K. J., Wall, N. R., Hekking, B., Kessler, B., et al. (2004). Calorie restriction promotes mammalian cell survival by inducing the SIRT1 deacetylase. *Science* 305 (5682), 390–392. doi:10.1126/science.1099196

Dell'Accio, F., De Bari, C., and Luyten, F. P. (2001). Molecular markers predictive of the capacity of expanded human articular chondrocytes to form stable cartilage *in vivo*. *Arthritis Rheum.* 44 (7), 1608–1619. doi:10.1002/1529-0131(200107)44:7<1608:aid-art284>3.0.co;2-t

Deng, Z., Wang, X., Long, X., Liu, W., Xiang, C., Bao, F., et al. (2018). Sirtuin 7 promotes colorectal carcinoma proliferation and invasion through the inhibition of E-cadherin. *Exp. Ther. Med.* 15 (3), 2333–2342. doi:10.3892/etm.2017.5673

Dong, S. Y., Guo, Y. J., Feng, Y., Cui, X. X., Kuo, S. H., Liu, T., et al. (2016). The epigenetic regulation of HIF-1α by SIRT1 in MPP + treated SH-SY5Y cells. *Biochem. Biophys. Res. Commun.* 470 (2), 453–459. doi:10.1016/j.bbrc.2016.01.013

Dvir-Ginzberg, M., Gagarina, V., Lee, E. J., and Hall, D. J. (2008). Regulation of cartilage-specific gene expression in human chondrocytes by SirT1 and nicotinamide phosphoribosyltransferase. *J. Biol. Chem.* 283 (52), 36300–36310. doi:10.1074/jbc.M803196200

Elayyan, J., Lee, E. J., Gabay, O., Smith, C. A., Qiq, O., Reich, E., et al. (2017). LEF1-mediated MMP13 gene expression is repressed by SIRT1 in human chondrocytes. *FASEB J.* 31 (7), 3116–3125. doi:10.1096/fj.201601253R

Farndale, R. W., Buttle, D. J., and Barrett, A. J. (1986). Improved quantitation and discrimination of sulphated glycosaminoglycans by use of dimethylmethylene blue. *Biochimica Biophysica Acta - General Subj.* 883 (2), 173–177. doi:10.1016/0304-4165(86)90306-5

Fu, Y., Kinter, M., Hudson, J., Humphries, K. M., Lane, R. S., White, J. R., et al. (2016). Aging promotes sirtuin 3-dependent cartilage superoxide dismutase 2 acetylation and osteoarthritis. *Arthritis Rheumatol.* 68 (8), 1887–1898. doi:10.1002/art.39618

Fujita, N., Matsushita, T., Ishida, K., Kubo, S., Matsumoto, T., Takayama, K., et al. (2011). Potential involvement of SIRT1 in the pathogenesis of osteoarthritis through the modulation of chondrocyte gene expressions. *J. Orthop. Res.* 29 (4), 511–515. doi:10.1002/jor.21284

Gabay, O., Sanchez, C., Dvir-Ginzberg, M., Gagarina, V., Zaal, K. J., Song, Y., et al. (2013a). Sirtuin 1 enzymatic activity is required for cartilage homeostasis *in vivo* in a mouse model. *Arthritis Rheum.* 65 (1), 159–166. doi:10.1002/art.37750

Gabay, O., Zaal, K. J., Sanchez, C., Dvir-Ginzberg, M., Gagarina, V., Song, Y., et al. (2013b). Sirt1-deficient mice exhibit an altered cartilage phenotype. *Jt. Bone Spine* 80 (6), 613–620. doi:10.1016/j.jbspin.2013.01.001

Gagarina, V., Gabay, O., Dvir-Ginzberg, M., Lee, E. J., Brady, J. K., Quon, M. J., et al. (2010). SirT1 enhances survival of human osteoarthritic chondrocytes by repressing protein tyrosine phosphatase 1B and activating the insulin-like growth factor receptor pathway. *Arthritis Rheum.* 62 (5), 1383–1392. doi:10.1002/art.27369

Gallo, C. M., Smith, D. L., Jr., and Smith, J. S. (2004). Nicotinamide clearance by Pnc1 directly regulates Sir2-mediated silencing and longevity. *Mol. Cell. Biol.* 24 (3), 1301–1312. doi:10.1128/MCB.24.3.1301-1312.2004

Giovannini, S., Diaz-Romero, J., Aigner, T., Mainil-Varlet, P., and Nesic, D. (2010). Population doublings and percentage of S100-positive cells as predictors of *in vitro* chondrogenicity of expanded human articular chondrocytes. *J. Cell. Physiol.* 222 (2), 411–420. doi:10.1002/jcp.21965

Guan, X., Lin, P., Knoll, E., and Chakrabarti, R. (2014). Mechanism of inhibition of the human sirtuin enzyme SIRT3 by nicotinamide: Computational and experimental studies. *PLoS One* 9 (9), e107729. doi:10.1371/journal.pone.0107729

Heo, S. J., Thorpe, S. D., Driscoll, T. P., Duncan, R. L., Lee, D. A., and Mauck, R. L. (2015). Biophysical regulation of chromatin architecture instills a mechanical memory in mesenchymal stem cells. *Sci. Rep.* 5, 16895. doi:10.1038/srep16895

Heywood, H. K., Bader, D. L., and Lee, D. A. (2006). Rate of oxygen consumption by isolated articular chondrocytes is sensitive to medium glucose concentration. *J. Cell. Physiol.* 206 (2), 402–410. doi:10.1002/jcp.20491

Heywood, H. K., Caton, P. W., and Lee, D. A. (2016). SIRT1, an enzyme vital to cartilage homeostasis, is regulated by osmolarity and glucose levels. *Int. J. Exp. Pathol.* 97 (6). A2. doi:10.1111/iep.12211

Heywood, H. K., Knight, M. M., and Lee, D. A. (2010). Both superficial and deep zone articular chondrocyte subpopulations exhibit the Crabtree effect but have different basal oxygen consumption rates. *J. Cell. Physiol.* 223 (3), 630–639. doi:10.1002/jcp.22061

Heywood, H. K., and Lee, D. A. (2017). Bioenergetic reprogramming of articular chondrocytes by exposure to exogenous and endogenous reactive oxygen species and its role in the anabolic response to low oxygen. *J. Tissue Eng. Regen. Med.* 11 (8), 2286–2294. doi:10.1002/term.2126

Heywood, H. K., and Lee, D. A. (2010). Low oxygen reduces the modulation to an oxidative phenotype in monolayer-expanded chondrocytes. *J. Cell. Physiol.* 222 (1), 248–253. doi:10.1002/jcp.21946

Heywood, H. K., Nalesso, G., Lee, D. A., and Dell'accio, F. (2014). Culture expansion in low-glucose conditions preserves chondrocyte differentiation and enhances their subsequent capacity to form cartilage tissue in three-dimensional culture. *Biores. Open Access* 3 (1), 9–18. doi:10.1089/biores.2013.0051

Heywood, H. K., Sembi, P. K., Lee, D. A., and Bader, D. L. (2004). Cellular utilization determines viability and matrix distribution profiles in chondrocyte-seeded alginate constructs. *Tissue Eng.* 10 (9-10), 1467–1479. doi:10.1089/ten.2004.10.1467

Hong, E. H., Yun, H. S., Kim, J., Um, H. D., Lee, K. H., Kang, C. M., et al. (2011). Nicotinamide phosphoribosyltransferase is essential for interleukin-1β-mediated dedifferentiation of articular chondrocytes via SIRT1 and extracellular signal-regulated kinase (ERK) complex signaling. *J. Biol. Chem.* 286 (32), 28619–28631. doi:10.1074/jbc.M111.219832

Huang, B. J., Hu, J. C., and Athanasiou, K. A. (2016). Cell-based tissue engineering strategies used in the clinical repair of articular cartilage. *Biomaterials* 98, 1–22. doi:10.1016/j.biomaterials.2016.04.018

Imai, S. (2010). A possibility of nutriceuticals as an anti-aging intervention: Activation of sirtuins by promoting mammalian NAD biosynthesis. *Pharmacol. Res.* 62 (1), 42–47. doi:10.1016/j.phrs.2010.01.006

Imai, S., Armstrong, C. M., Kaeberlein, M., and Guarente, L. (2000). Transcriptional silencing and longevity protein Sir2 is an NAD-dependent histone deacetylase. *Nature* 403 (6771), 795–800. doi:10.1038/35001622

Imai, S., and Guarente, L. (2014). NAD+ and sirtuins in aging and disease. *Trends Cell Biol.* 24 (8), 464–471. doi:10.1016/j.tcb.2014.04.002

Joo, H. Y., Yun, M., Jeong, J., Park, E. R., Shin, H. J., Woo, S. R., et al. (2015). SIRT1 deacetylates and stabilizes hypoxia-inducible factor-1α (HIF-1α) via direct interactions during hypoxia. *Biochem. Biophys. Res. Commun.* 462 (4), 294–300. doi:10.1016/j.bbrc.2015.04.119

Kaeberlein, M., Andalis, A. A., Fink, G. R., and Guarente, L. (2002). High osmolarity extends life span in *Saccharomyces cerevisiae* by a mechanism related to calorie restriction. *Mol. Cell. Biol.* 22 (22), 8056–8066. doi:10.1128/MCB.22.22.8056-8066.2002

Kafienah, W., and Sims, T. J. (2004). Biochemical methods for the analysis of tissue-engineered cartilage. *Methods Mol. Biol.* 238, 217–230. doi:10.1385/1-59259-428-x:217

Kiernan, R., Bres, V., Ng, R. W., Coudart, M. P., El Messaoudi, S., Sardet, C., et al. (2003). Post-activation turn-off of NF-kappa B-dependent transcription is regulated by acetylation of p65. *J. Biol. Chem.* 278 (4), 2758–2766. doi:10.1074/jbc.M209572200

Kim, Y. J., Sah, R. L., Doong, J. Y., and Grodzinsky, A. J. (1988). Fluorometric assay of DNA in cartilage explants using Hoechst 33258. *Anal. Biochem.* 174 (1), 168–176. doi:10.1016/0003-2697(88)90532-5

Korogi, W., Yoshizawa, T., Karim, M. F., Tanoue, H., Yugami, M., Sobuz, S. U., et al. (2018). SIRT7 is an important regulator of cartilage homeostasis and osteoarthritis development. *Biochem. Biophys. Res. Commun.* 496, 891–897. doi:10.1016/j.bbrc.2018.01.129

Kuzmichev, A., Margueron, R., Vaquero, A., Preissner, T. S., Scher, M., Kirmizis, A., et al. (2005). Composition and histone substrates of polycomb repressive group complexes change during cellular differentiation. *Proc. Natl. Acad. Sci. U. S. A.* 102 (6), 1859–1864. doi:10.1073/pnas.0409875102

Kuzmichev, A., Nishioka, K., Erdjument-Bromage, H., Tempst, P., and Reinberg, D. (2002). Histone methyltransferase activity associated with a human multiprotein complex containing the Enhancer of Zeste protein. *Genes Dev.* 16 (22), 2893–2905. doi:10.1101/gad.1035902

Laemmle, A., Lechleiter, A., Roh, V., Schwarz, C., Portmann, S., Furer, C., et al. (2012). Inhibition of SIRT1 impairs the accumulation and transcriptional activity of HIF-1α protein under hypoxic conditions. *PLoS One* 7 (3), e33433. doi:10.1371/journal.pone.0033433

Lei, M., Wang, J. G., Xiao, D. M., Fan, M., Wang, D. P., Xiong, J. Y., et al. (2012). Resveratrol inhibits interleukin 1β-mediated inducible nitric oxide synthase expression in articular chondrocytes by activating SIRT1 and thereby suppressing nuclear factor-κB activity. *Eur. J. Pharmacol.* 674 (2-3), 73–79. doi:10.1016/j.ejphar.2011.10.015

Li, Y., and Tollefsbol, T. O. (2011). p16(INK4a) suppression by glucose restriction contributes to human cellular lifespan extension through SIRT1-mediated epigenetic and genetic mechanisms. *PLoS One* 6 (2), e17421. doi:10.1371/journal.pone.0017421

Li, Y., Xiao, W., Wu, P., Deng, Z., Zeng, C., Li, H., et al. (2016). The expression of SIRT1 in articular cartilage of patients with knee osteoarthritis and its correlation with disease severity. *J. Orthop. Surg. Res.* 11 (1), 144. doi:10.1186/s13018-016-0477-8

Lin, S. J., Kaeberlein, M., Andalis, A. A., Sturtz, L. A., Defossez, P. A., Culotta, V. C., et al. (2002). Calorie restriction extends *Saccharomyces cerevisiae* lifespan by increasing respiration. *Nature* 418 (6895), 344–348. doi:10.1038/nature00829

Lui, J. C., Garrison, P., Nguyen, Q., Ad, M., Keembiyehetty, C., Chen, W., et al. (2016). EZH1 and EZH2 promote skeletal growth by repressing inhibitors of chondrocyte proliferation and hypertrophy. *Nat. Commun.* 7, 13685. doi:10.1038/ncomms13685

Luo, J., Nikolaev, A. Y., Imai, S., Chen, D., Su, F., Shiloh, A., et al. (2001). Negative control of p53 by Sir2α promotes cell survival under stress. *Cell* 107 (2), 137–148. doi:10.1016/s0092-8674(01)00524-4

Luo, W., and Wang, Y. (2018). Epigenetic regulators: Multifunctional proteins modulating hypoxia-inducible factor-alpha protein stability and activity. *Cell. Mol. Life Sci.* 75 (6), 1043–1056. doi:10.1007/s00018-017-2684-9

Ma, M. C., Chiu, T. J., Lu, H. I., Huang, W. T., Lo, C. M., Tien, W. Y., et al. (2018). SIRT1 overexpression is an independent prognosticator for patients with esophageal squamous cell carcinoma. *J. Cardiothorac. Surg.* 13 (1), 25. doi:10.1186/s13019-018-0718-5

Marasca, F., Bodega, B., and Orlando, V. (2018). How Polycomb-Mediated Cell Memory Deals with a Changing Environment: Variations in PcG complexes and proteins assortment convey plasticity to epigenetic regulation as a response to environment. *Bioessays* 40 (4), e1700137. doi:10.1002/bies.201700137

Margueron, R., and Reinberg, D. (2011). The Polycomb complex PRC2 and its mark in life. *Nature* 469 (7330), 343–349. doi:10.1038/nature09784

Maroudas, A., and Evans, H. (1972). A study of ionic equilibria in cartilage. *Connect. Tissue Res.* 1 (1), 69–77. doi:10.3109/03008207209152058

Matsushita, T., Sasaki, H., Takayama, K., Ishida, K., Matsumoto, T., Kubo, S., et al. (2013). The overexpression of SIRT1 inhibited osteoarthritic gene expression changes induced by interleukin-1β in human chondrocytes. *J. Orthop. Res.* 31 (4), 531–537. doi:10.1002/jor.22268

Matsuzaki, T., Matsushita, T., Takayama, K., Matsumoto, T., Nishida, K., Kuroda, R., et al. (2014). Disruption of Sirt1 in chondrocytes causes accelerated progression of osteoarthritis under mechanical stress and during ageing in mice. *Ann. Rheum. Dis.* 73 (7), 1397–1404. doi:10.1136/annrheumdis-2012-202620

Milne, J. C., Lambert, P. D., Schenk, S., Carney, D. P., Smith, J. J., Gagne, D. J., et al. (2007). Small molecule activators of SIRT1 as therapeutics for the treatment of type 2 diabetes. *Nature* 450 (7170), 712–716. doi:10.1038/nature06261

Moon, M. H., Jeong, J. K., Lee, Y. J., Seol, J. W., Jackson, C. J., and Park, S. Y. (2013). SIRT1, a class III histone deacetylase, regulates TNF-alpha-induced inflammation in human chondrocytes. *Osteoarthr. Cartil.* 21 (3), 470–480. doi:10.1016/j.joca.2012.11.017

Motta, M. C., Divecha, N., Lemieux, M., Kamel, C., Chen, D., Gu, W., et al. (2004). Mammalian SIRT1 represses forkhead transcription factors. *Cell* 116 (4), 551–563. doi:10.1016/s0092-8674(04)00126-6

Nagai, K., Matsushita, T., Matsuzaki, T., Takayama, K., Matsumoto, T., Kuroda, R., et al. (2015). Depletion of SIRT6 causes cellular senescence, DNA damage, and telomere dysfunction in human chondrocytes. *Osteoarthr. Cartil.* 23 (8), 1412–1420. doi:10.1016/j.joca.2015.03.024

NICE (2017). *Autologous chondrocyte implantation for treating symptomatic articular cartilage defects of the knee (TA477)*. London, United Kingdom: National Institute for Health Care Excellence, Resource impact report, 1–9.

Niemeyer, P., Pestka, J. M., Salzmann, G. M., Sudkamp, N. P., and Schmal, H. (2012). Influence of cell quality on clinical outcome after autologous chondrocyte implantation. *Am. J. Sports Med.* 40 (3), 556–561. doi:10.1177/0363546511428879

Oppenheimer, H., Kumar, A., Meir, H., Schwartz, I., Zini, A., Haze, A., et al. (2014). Set7/9 impacts COL2A1 expression through binding and repression of SirT1 histone deacetylation. *J. Bone Min. Res.* 29 (2), 348–360. doi:10.1002/jbmr.2052

Oswald, E. S., Chao, P. H., Bulinski, J. C., Ateshian, G. A., and Hung, C. T. (2008). Dependence of zonal chondrocyte water transport properties on osmotic environment. *Cell. Mol. Bioeng.* 1 (4), 339–348. doi:10.1007/s12195-008-0026-6

Roth, M., and Chen, W. Y. (2014). Sorting out functions of sirtuins in cancer. *Oncogene* 33 (13), 1609–1620. doi:10.1038/onc.2013.120

Saris, D. B., Vanlauwe, J., Victor, J., Almqvist, K. F., Verdonk, R., Bellemans, J., et al. (2009). Treatment of symptomatic cartilage defects of the knee: Characterized chondrocyte implantation results in better clinical outcome at 36 months in a randomized trial compared to microfracture. *Am. J. Sports Med.* 37 (1), 10S–19S. doi:10.1177/0363546509350694

Smith, C. A., Humphreys, P. A., Bates, N., Naven, M. A., Cain, S. A., Dvir-Ginzberg, M., et al. (2022). SIRT1 activity orchestrates ECM expression during hESC-chondrogenic differentiation. *FASEB J.* 36 (5), e22314. doi:10.1096/fj.202200169R

Takayama, K., Ishida, K., Matsushita, T., Fujita, N., Hayashi, S., Sasaki, K., et al. (2009). SIRT1 regulation of apoptosis of human chondrocytes. *Arthritis Rheum.* 60 (9), 2731–2740. doi:10.1002/art.24864

Vaziri, H., Dessain, S. K., Ng Eaton, E., Imai, S. I., Frye, R. A., Pandita, T. K., et al. (2001). hSIR2(SIRT1) functions as an NAD-dependent p53 deacetylase. *Cell* 107 (2), 149–159. doi:10.1016/s0092-8674(01)00527-x

Vazquez, M. J., Toro, C. A., Castellano, J. M., Ruiz-Pino, F., Roa, J., Beiroa, D., et al. (2018). SIRT1 mediates obesity- and nutrient-dependent perturbation of pubertal timing by epigenetically controlling Kiss1 expression. *Nat. Commun.* 9 (1), 4194. doi:10.1038/s41467-018-06459-9

Windhaber, R. A., Wilkins, R. J., and Meredith, D. (2003). Functional characterisation of glucose transport in bovine articular chondrocytes. *Pflugers Arch. - Eur. J. Physiol.* 446 (5), 572–577. doi:10.1007/s00424-003-1080-5

Wu, Y., Chen, L., Wang, Y., Li, W., Lin, Y., Yu, D., et al. (2015). Overexpression of Sirtuin 6 suppresses cellular senescence and NF-κB mediated inflammatory responses in osteoarthritis development. *Sci. Rep.* 5, 17602. doi:10.1038/srep17602

Yeung, F., Hoberg, J. E., Ramsey, C. S., Keller, M. D., Jones, D. R., Frye, R. A., et al. (2004). Modulation of NF-κB-dependent transcription and cell survival by the SIRT1 deacetylase. *EMBO J.* 23 (12), 2369–2380. doi:10.1038/sj.emboj.7600244

Frontiers in
Bioengineering and Biotechnology

Accelerates the development of therapies, devices, and technologies to improve our lives

A multidisciplinary journal that accelerates the development of biological therapies, devices, processes and technologies to improve our lives by bridging the gap between discoveries and their application.

Discover the latest Research Topics

See more →

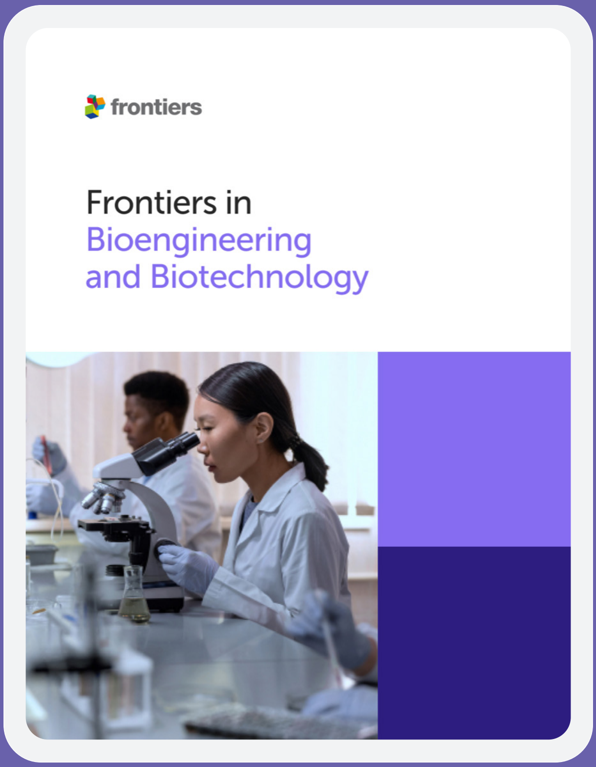

frontiers

Frontiers in
Bioengineering
and Biotechnology

Frontiers

Avenue du Tribunal-Fédéral 34
1005 Lausanne, Switzerland
frontiersin.org

Contact us

+41 (0)21 510 17 00
frontiersin.org/about/contact